2023



High Porosity Cooling Features for Turbine Blade Applications

THESIS SUBMITTED FOR THE DEGREE OF DOCTOR OF PHILOSOPHY

AUGUSTIN WAMBERSIE
ST CATHERINES COLLEGE
UNIVERISTY OF OXFORD

ABSTRACT

Augustin Wambersie

St. Catherine's College, University of Oxford

A thesis submitted for the degree of Doctor of Philosophy, Michaelmas 2023

High Porosity Cooling Features for Turbine Blade Applications

Improving the cooling effectiveness of turbine blades is one of the key drivers in gas turbine engine performance. Transpiration cooling describes an ideal arrangement that maximises this cooling effectiveness through the use of porous structures. High internal surface area and uniform coolant distribution are some of its main benefits. However, physical limitations in manufacturing and materials mean that this arrangement is impractical to implement.

This research identifies some of the key properties that makes transpiration cooling successful and recreate them with geometric features already within the bounds of existing manufacturing capabilities. The use of simple, small round film cooling holes, in tight staggered arrays at varying locations around the blade profile was found to generate exceptional levels of film effectiveness. A series of experimental campaigns were carried out to quantify the effects of different parameters in driving this high film effectiveness. Features placed on the early suction surface of the blade running at low blowing ratios were seen to be perform particularly well, with film effectiveness levels above 90% being maintained to the trailing edge.

Analytical modelling of the results demonstrated that the overall array of film holes generates films that behave similarly to tangential injection slots. A saturated film core was identified, which remained effectively separate from the turbulent boundary layer. Further analysis suggested that the performance of the suction surface films could be explained by these operating in a laminar-like regime, contradicting many commonly held assumptions used for suction surface film modelling.

Investigations into the nature of the interactions between the individual film cooling jets were also carried out using numerical simulations. These illustrated some of the beneficial outcomes of positioning film holes in close proximity to each other. The effects of counter rotating vortex pairs and boundary layer velocity profiles were identified as key mechanisms driving these interactions. Crucially, the magnitude of these interactions was found to outweigh any effect of individual film hole geometry.

The present work culminated in a series of metal effectiveness tests on turbine blade geometries. These were used to obtain a complete measure of the performance of high porosity cooling arrays within a double walled cooling scheme. The aim of these experiments was to showcase the potential breakthrough in film cooling that had been unlocked by the high porosity array approach. Results in this experiment demonstrated that metal effectiveness values for the proposed systems already exceeded those of mature state of the art cooling arrangements.

DEDICATION

Cette thèse est dédiée à mon père et à mes grands-pères

ACKNOWLEDGEMENTS

Professor Peter Ireland must be the first and foremost to be acknowledged, for his relentless support and encouragement throughout the process of this research. He has been an incredible mentor, teacher, and role model and will forever in my mind epitomize the excitement that accompanies the process of scientific research and discovery. This thesis would not have been possible without him.

Next, I must acknowledge my family and particularly my parents, for their infinite support and love. Without their emphasis and investment in my education, a graduate degree at Oxford would have been but a dream. Also, my fiancé Erin who has been an enormous part of my life throughout my journey at Oxford and more recently has confirmed she will continue to be indefinitely, thank you for saying yes.

A special thanks goes to mentors and colleagues Dr. Tsun Holt Wong and Dr. Alex Murray who had the patience and kindness to make sure I was on the right track and then propel me down it with their insights and experience. Equally relevant is a thank you to Dr. Ignacio Mayo, Dr. Janendra Telisighe and the other members of Rolls-Royce Plc. who contributed to the Transpiration Cooling Research. Their genuine interest and enthusiasm in my work as well as their exceptional contributions fuelled the excitement and progress driving my research throughout.

Members of the Osney Thermofluids Institute also deserve to be mentioned: Dave Odell, David Mountain, Craig Parsons, Gregory King, Paul Cox, Hal Surtell, Bill Godfrey, Jason McCluskey, Andreea Dabija, Anna Erillo and others. The success of each and every experimental campaign was either in part or entirely due to the commitment of these people. My typically unreasonable or untimely requests were always somehow met by their hard work and dedication. Peter Walters deserves a special mention for his openness, support and contributions over at the additive manufacturing workshop. Much of this research became possible thanks to his abilities and knowledge in printing incredibly high quality test pieces previously unseen in the lab.

Finally I wish to express thanks for the support provided by both Rolls-Royce PLC and the EPSRC through (EP/P000878/1).

Contents

Abstract **2**

Dedication **4**

Acknowledgements **5**

Nomenclature **12**

List of Figures **14**

1. Introduction **21**

1.1. Overview of Gas turbine engines 21

1.2. State of the art of turbine blade cooling 26

1.3. Risks 28

1.4. Research objectives 30

1.5. Outline of Thesis 30

1.6. Research Achievements 31

2. Literature Review of transpiration and Effusion Cooling **34**

2.1. Early Theoretical considerations 34

2.2. Experimental transpiration cooling research 38

2.3. Recent porous flat plate work 41

2.4. Transition to Effusion cooling or Full coverage film cooling 41

2.4.1. Film cooling review 42

2.4.2. Secondary effects associated with film cooling: heat transfer coefficient 45

2.4.3. Overview of Effusion cooling Experiments 46

2.4.4. Experimental work on FCFC turbine blades 47

2.5. Double wall effusion cooling and Novel cooling strategies under investigation 50

2.5.1. Intersecting, matrix and Lattice systems 53

2.5.2. Dendritic cooling and trench film cooling 54

2.6. Advances in Manufacturing 55

2.7. Summary 57

3. PSP experiments on high porosity cooling geometries 58

3.1. Initial Experiments of Transpiration Cooling Inspired Panel Cooling on a Turbine Blade Yielding Film Effectiveness Levels Over 95% 60

3.1.1. Introduction 60

3.1.2. Literature review 61

3.1.3. Experimental Facility 63

3.1.4. Blade geometry and test regime 63

3.1.5. Results 65

3.1.6. Conclusions 74

3.2. Further Parametric Experimental Study of High Porosity Film Cooling Features on Turbine Blade Geometries 76

3.2.1. Introduction 76

3.2.2. Method 79

3.2.3. Geometries 81

3.2.4. Results- Effect of Blowing ratio 82

3.2.5. Results- Effect of Hole size 93

3.2.6. Results- Effect of Injection angles 98

3.2.7. Conclusions 102

4. Transpiration Cooling Film Effectiveness Correlations for Turbine Blade Applications .. 104

4.1. Introduction 105

4.2. Literature review 108

4.2.1. 1D film cooling models 108
4.2.2. Tangential slot models 109
4.2.3. 2D models 110
4.3. Overview of film effectiveness data and geometries 111
4.4. 1D film effectiveness investigation 112
4.5. 2D Film effectiveness correlation 114
4.5.1. Regression to experimental data 115
4.6. General observations on C_1 and C_2 118
4.7. Discussion 119
4.8. Conclusions 121
5. Study of Interactions between Closely Spaced Films Used in Novel High Porosity Turbine Cooling Designs 124
5.1. Introduction 127
5.2. CFD setup and domain 130
5.3. Results 133
5.3.1. Comparison between basic geometric arrangements 133
5.3.2. Effect of combining film holes – Discussion of the Effective Blowing ratio 135
5.3.3. Effects of interactions between CRVPs 138
5.3.4. Implications of interactions on designs: Effect of spacing 140
5.3.5. Fan shaped holes 143
5.4. Conclusion 145
6. Demonstration of High Porosity Cooling Systems Using Novel Thermochromic Liquid Crystal Method 146
6.1. Introduction 148
6.2. Method 149

6.2.1. Rig 149
6.2.2. Thermochromic liquid crystals 150
6.2.3. Uncertainty analysis 153
6.3. Geometries 154
6.3.1. Design 154
6.3.2. Test Piece manufacture 155
6.4. TLC results 157
6.4.1. TP075TE 159
6.4.2. TP095TE 160
6.4.3. Metal Effectiveness summary plots 160
6.5. Conclusion 164
7. Conclusions and Recommendations 166
7.1. Summary of major themes 166
7.1.1. Experimental investigation of high porosity film features 166
7.1.2. Investigation into the causes of high measured effectiveness 166
7.1.3. Feasibility and performance of a full blade design 167
7.1.4. Challenges 168
7.2. Recommendations 168
7.2.1. Turbulence measurements 168
7.2.2. HTC measurements 169
7.2.3. Further CFD modelling 169
7.2.4. Further Optimization of both individual panels and joint systems 169
7.2.5. Pressure margins 170

7.2.6. Further investigation into shaped holes 170

7.2.7. Mechanical implications 170

Appendix A : Analytical analysis of transpiration cooled turbine blades 172

Approximate Analytic Thermal Solution for Transpiration Cooled Turbine Blades 173

A.1. Introduction 173

A.2. Literature Review 174

A.3. Heat Balance 176

A.4. Analytical Calculation of HTC 176

A.5. Numerical Calculation of HTC 178

A.6. Iterative Process 179

A.7. Example Flow Field 180

A.8. Results 180

A.9. Conclusion 182

A.10. References 183

Appendix B Experimental facility and methods 185

B.1. Rig Description 185

B.1.1. Rig Validation 189

B.1.2. Sensor arrays and camera Setup 190

B.2. Pressure Sensitive Paint methodology for Film Effectiveness measurements 192

B.2.1. Description 192

B.2.2. PSP Characterisation 193

B.2.3. Mass transfer analogy for film effectiveness measurements 195

B.2.4. Implementation 199

B.2.5. Benefits of PSP 200

B.2.6. Limitations of PSP 200

B.3. TLC Crystals for Metal effectiveness measurements 201

B.3.1. Method Overview 202

B.3.2. Implementation 203

B.3.3. Test piece material choice 206

B.3.4. Benefits of TLCs 206

B.3.5. Limitations of TLCs 207

B.4. Uncertainty Analysis 208

References 211

NOMENCLATURE

$\boldsymbol{A}$	Area, $\boldsymbol{m^2}$
$\boldsymbol{b_h}$	Scaled Non-dimensional transpiration blowing parameter with respect to St_0
$\boldsymbol{B_h}$	Scaled Non-dimensional transpiration blowing parameter with respect to St
$\boldsymbol{Bi}$	Biot number
C	Concentration
$\boldsymbol{c_p}$	Specific heat at constant pressure, $J/(kg \cdot \mathrm{K})$
$\boldsymbol{d}$	Film hole diameter, m
$\boldsymbol{G}$	Transpiration blowing mass flux parameter $kg/(s \cdot m^2)$
$\boldsymbol{h}$	Heat transfer coefficient, $W/(m^2 \cdot \mathrm{K})$
$\boldsymbol{I}$	Intensity ration
$\boldsymbol{i}$	Relative pixel intensity
$\boldsymbol{l}$	Characteristic length, m
$\boldsymbol{k}$	Thermal conductivity (W/m.K)
$\boldsymbol{m^*}$	Non-dimensional coolant mass flow Equation (2-7)
$\dot{\boldsymbol{m}}_{\boldsymbol{c}}''$	Coolant mass flow per unit area, $kg/(s \cdot m^2)$
$\dot{\boldsymbol{m}}_{\boldsymbol{c}}$	Coolant mass flow, kg/s
$\boldsymbol{M}$	Film hole blowing ratio
$\boldsymbol{MW}$	Molecular weight
$\boldsymbol{P}$	Pressure, Pa
$\boldsymbol{P_1}, \boldsymbol{P_2}$	Streamwise and spanwise pitch, m
$\boldsymbol{Pr}$	Prandtl Number
$\boldsymbol{PR}$	Pressure ratio
$\boldsymbol{p}$	Partial pressure, Pa
$\dot{\boldsymbol{q}}''$	Heat flux per unit area $J/(s \cdot m^2)$
$\boldsymbol{Re}$	Reynolds number
$\boldsymbol{Re_{\Delta_2}}$	Reynolds number based on enthalpy boundary layer thickness
$\boldsymbol{St}$	Stanton number
$\boldsymbol{St_0}$	Reference Stanton number for solid surface
$\boldsymbol{T}$	Temperature, K
$\boldsymbol{u}$	Streamwsie Velocity, m/s
$\boldsymbol{v}$	Perpendicular Velocity, m/s
$\bar{\boldsymbol{v}}$	Local time-mean velocity in the y direction, m/s
$\boldsymbol{W_c}$	Coolant mass fraction relative to mainstream
$\boldsymbol{X_c}$	Molar fraction
$\boldsymbol{x}$	Distance in Streamwise direction, m

$\boldsymbol{y}$	Distance Perpendicular to wall, m
$\boldsymbol{z}$	Distance in spanwise direction, m
$\boldsymbol{\alpha_H}$	molecular thermal diffusivity, m^2/s
$\boldsymbol{\alpha}$	Streamwise Film hole injection angle, °
$\boldsymbol{\beta}$	Spanwise Film hole injection angle, °
$\boldsymbol{\delta}$	Boundary layer thickness, m
Δ_2	Boundary enthalpy thickness, m
$\boldsymbol{\varepsilon_m}$	Metal effectiveness
$\boldsymbol{\varepsilon_H}$	eddy diffusivity for heat transfer, m^2/s
$\boldsymbol{\theta}$	Fan layback angle, °
$\boldsymbol{\eta_c}$	Cycle efficiency
$\boldsymbol{\eta_{int}}$	Internal cooling effectiveness
$\boldsymbol{\eta_{film}}$	Film cooling effectiveness
$\boldsymbol{\eta}$	Engine cycle efficiency
$\boldsymbol{\rho}$	Density, kg/m^3
$\boldsymbol{\mu}$	dynamic viscosity, kg/ms
$\boldsymbol{\gamma}$	Ratio of specific heats
	Subscripts
$_\infty$	Mainstream condition
$_{\boldsymbol{aw}}$	Adiabatic wall
$_{\boldsymbol{c}}$	coolant
$_{\boldsymbol{ex}}$	exit
$_{\boldsymbol{h}}$	hole
$_{\boldsymbol{in}}$	inlet
$_{\boldsymbol{m}}$	metal
$_{\boldsymbol{ref}}$	Reference
$_{\boldsymbol{w}}$	Wall

LIST OF FIGURES

Figure 1-1 Render of the Rolls Royce Trent 1000 Turbofan, one of the most advanced aircraft engines to date (Copyright: Rolls Royce Plc) 21

Figure 1-2 Schematic of the core section of a gas turbine engine (Rolls-Royce plc, 1986) 22

Figure 1-3 P-V of a real Brayton cycle (Rolls-Royce plc, 1986) 23

Figure 1-4 Illustration of thermal load distribution for high pressure turbine components by Han (2005) 24

Figure 1-5 Advances in turbine entry temperature against release year for different Rolls Royce engine models from Cumpsty (1997) 25

Figure 1-6 Evolution of Turbine blade cooling (Rolls-Royce plc, 1986) 27

Figure 1-7 predicted direction of turbine blade cooling technology from Unnikrishnan & Yang (2022) 27

Figure 1-8 The 10 remaining challenges for hot gas passes according to Bunker (2006). 29

Figure 2-1 Standard blade heat balance for a porous wall section 35

Figure 2-2 Effect of Transpiration on heat transfer coefficient for various conditions with the analytical solution of Kays and Crawford, adapted from Kays & Crawford (1980) 36

Figure 2-3 Results of standard Wall Model with relevant data, adapted from Holland & Thake (1980) 37

Figure 2-4 Photograph (Moskowitz & Lombardo, 1971) schematic (Glassman, 1975) of early transpiration cooled blade using wire form and spar design 38

Figure 2-5 Effect of Oxidation on coolant flow through porous and FCFC blades relative to conventional blade from Esgar, et al. (1970). 39

Figure 2-6 Transpiration Cooling Inserts patent with (a) profile and (b)exploded views (Grylls, et al., 2002) 40

Figure 2-7 Schematic plot of film flow regimes based on film velocity ratio according to Baldauf et al. (2002) 42

Figure 2-8 (a) Coherent and (b) time averaged flow structures due to film-mainstream interactions downstream of a 30 degree inclined holes from Kalghatgi & Acharya (2014). 44
Figure 2-9 Overview of Effusion flat plate studies taken from Natsui, et al (2017) 46
Figure 2-10 Film effectiveness measurements from effusion, from Murray, et al. (2018) 46
Figure 2-11 Schematic (Meitner, 1978) and photograph (Livingood, et al., 1971) of early FCFC blade test pieces 47
Figure 2-12 Right: Cooling Performance of FCFC blade relative to other cooling methods. (Esgar, 1970) Left: Fractured FCFC blade after 110 thermal cycles (Hickel, et al., 1972). 48
Figure 2-13 Film effectiveness levels measured by Narzary, et al. (2012) of a multirow system on a scaled NGV with DR=2.5. 49
Figure 2-14 Film effectiveness contour maps of two different effusion systems on turbine blade geometries with P/d of 5 (Ngetich, 2019) 50
Figure 2-15 Flat plate double wall effusion cooling system by Murray (2017) on the left with application to turbine blade by Ngetich (2019) on the right. 51
Figure 2-16 Sketch of the optimal hexagonal matric geometry (Fletcher, 1997) 53
Figure 2-17 Schematic of dendritic film holes (Luque, et al., 2014) 54
Figure 2-18 Development of film cooling hole AM within a span of 2 years: a 0.5mm diameter cooling hole (a) EDM baseline, (b) taken from Stimpson, et al (2018) (c) and (d) taken from Snyder & Thole (2020) using different print orientations 56
Figure 2-19 Ceramic Porous barrier coating (Arai & Suidzu, 2013) 56
Figure 3-1. (a) Detail of Panel 1 geometry with (b) cross section indicating locations of Panels 1-4 .. 64
Figure 3-2. Film effectiveness of Panel 1 at different coolant mass flow rates (mass fraction). 67
Figure 3-3. Film effectiveness of Panel 2 at different coolant mass flow rates (mass fraction) 67
Figure 3-4. Film effectiveness of Panel 3 at different coolant mass flow rates (mass fraction) 68
Figure 3-5. Film effectiveness of Panel 4 at different coolant mass flow rates (mass fraction) 68
Figure 3-6. Spanwise average film effectiveness of Panels 1, 2, 3 and 4 at different coolant mass flow rates 70

Figure 3-7. Film effectiveness of Panel 5 at different coolant mass flow rates (mass fraction) 71
Figure 3-8 Film effectiveness of Panel 6 at different coolant mass flow rates (mass fraction) 71
Figure 3-9 Film effectiveness of Panel 7 at different coolant mass flow rates (mass fraction) 72
Figure 3-10. Film effectiveness of Panels 1, 5, 6 and 7 at x/d=75 at different average blowing ratios 73
Figure 3-11. Spanwise average of all Panels at 15g/s (1.75%) 74
Figure 3-12 Schematic of experimental test section 78
Figure 3-13 Predicted and measured pressure distribution on test section 79
Figure 3-14 PSP error distribution 80
Figure 3-15 (a) Schematic of test pieces with relevant coordinate system (b) cross section of test section illustrating both PS and SS panels (c) definition of α and β angles 81
Figure 3-16 Film effectiveness plot for different SS XROW geometries 84
Figure 3-17 Spanwise average film effectiveness against BR at different streamwise locations for SSXROW geometries 85
Figure 3-18 Spanwise average film effectiveness against mass flow at different streamwise locations for SSXROW geometries 86
Figure 3-19 Contour plot of film effectiveness for different mass flows and BRs 87
Figure 3-20 Film effectiveness plots for PSXROW geometries 88
Figure 3-21 Spanwise average film effectiveness against BR at different streamwise locations for PSXROW geometries 90
Figure 3-22 Spanwise average film effectiveness against mass flow rate at different streamwise locations for PSXROW geometries 91
Figure 3-23 Contour plot of film effectiveness for different mass flows and blowing ratios on PS 92
Figure 3-24 Film effectiveness plot for different film hole diameters at 12.5g/s on SS panel 94
Figure 3-25 Film effectiveness plot for different film hole diameters at 25g/s 94
Figure 3-26 Effect of film hole diameter at different streamwise locations on SS 95
Figure 3-27 Film effectiveness plot for different hole diameters at 12.5 and 20g/s 97
Figure 3-28 Effect of film hole diameter at different streamwise locations on PS 98

Figure 3-29 Detail of panels at α = 35° and 90° with a coolant mass flow of 25g/s 98
Figure 3-30 Effect of streamwise injection angle α at different streamwise locations on PS 100
Figure 3-31 Film effectiveness plot for different spanwise injection angles β at different streamwise locations on SS..... 101
Figure 3-32 Effect of spanwise injection angle β at different streamwise locations on SS..... 102
Figure 4-1 Demonstration of film effectiveness data obtained with a high porosity panel using 12.5g/s (1.5% of the mainstream) of coolant on both the pressure surface (left) and suction surface (right). Panels are outlined in white. (Wambersie, et al., 2021)..... 107
Figure 4-2 Demonstration of the effect of cooling hole diameter on film effectiveness levels at four different mass flow rates for a pressure surface geometry (Wambersie, et al., 2021) 108
Figure 4-3 Schematic of geometries and locations used in film effectiveness experiments..... 112
Figure 4-4 Film effectiveness levels plotted against scaled streamwise distance with core offset for 12 row staggered geometry on mid Pressure surface. (Wambersie, et al., 2021) 113
Figure 4-5 Film effectiveness against scaled streamwise distance with core offset for 17 row inline late suction surface panel (Wambersie, et al., 2021) 114
Figure 4-6 Best fit of Equation 9 (solid line) with experimental film effectiveness data (dotted line) of a 12-row staggered panel geometry located on the early suction surface..... 115
Figure 4-7 Best fit of Equation 9 (solid line) with experimental film effectiveness data (dotted line) of a 13-row staggered panel geometry located on the mid-pressure surface..... 116
Figure 4-8 C1 values for the suction and pressure surface geometries against velocity ratio (VR) ... 117
Figure 4-9 C2 values for suction and pressure surface geometries..... 118
Figure 4-10 Comparison between film effectiveness levels predicted by correlation and experimental data..... 118
Figure 4-11 C2 values for equivalent geometries across suction surface, pressure surface and flat plate. 119
Figure 4-12 C1 values for flat plate data between pressure surface and laminar suction surface..... 121
Figure 4-13 Conceptual model of high porosity films..... 122

Figure 5-1 (a) Fluid domain and (b) detail of holes and interface 131
Figure 5-2 Comparison between Experimental (left) and numerical CFD (right) film effectiveness levels on the Suction surface for a 7-row panel at M = 1.06 132
Figure 5-3 Hole positioning of main row geometries 133
Figure 5-4 Film effectiveness levels of the four basic geometries and superimposed baseline..... 134
Figure 5-5 Film effectiveness levels of near hole region for different geometric arrangements with $P_1/d = P_2/d = 2.1$ 135
Figure 5-6 Film effectiveness distribution due to different possible interactions between two rows of films 136
Figure 5-7 Variation in velocity downstream of a single film row 0.3*d* above the blade surface 137
Figure 5-8 Static pressure ratio distribution around film holes at high blowing ratios..... 139
Figure 5-9 Streamlines of inline and staggered holes at M = 1 with colour representing film effectiveness 140
Figure 5-10 Cross section of vorticity downstream of the film holes at M= 1 140
Figure 5-11 Effect of Streamwise spacing on film effectiveness for staggered geometry..... 141
Figure 5-12 Detail of film effectiveness distribution with variation of streamwise pitch for P_2/d=2.1 142
Figure 5-13 Variation of film effectiveness with spanwise pitch 143
Figure 5-14 Detail of film effectiveness distribution with variation of the spanwise pitch for P_1/d=3 143
Figure 5-15 Comparison between fanned and circular film holes $\beta = 25°,\ \theta = 7.5°$ 144
Figure 5-16 (a) Summary of principle factors dominating film interactions and (b) Schematic of staggered interactions removing mainstream from the surface..... 145
Figure 6-1 Schematic of the experimental facility with heater mesh..... 150
Figure 6-2 Example of narrowband liquid crystal response applied to test aerofoil with temperatures of principle and secondary contours shown in black and orange respectively..... 151
Figure 6-3 Example of signal response of a pixel between 30.9 and 34.4℃ 152

Figure 6-4 (a) Schematic Cross section of TP095TE and (b) blade surface coordinate system 154
Figure 6-5 Test pieces as manufactured by Laser sintering AM 157
Figure 6-6 Metal effectiveness results for geometry TP075S 158
Figure 6-7 Metal effectiveness distribution of TP075TE 158
Figure 6-8 Metal effectiveness distribution of TP095TE 160
Figure 6-9 Mean metal effectiveness values for leading edge, trailing edge, suction and pressure surfaces 162
Figure 6-10 Mean metal effectiveness values for entire blade surface with data taken from multipass film cooled blade 163
FIGURE A-1:CONTROL VOLUME FOR HEAT BALANCE 176
FIGURE A-2: EXPERIMENTAL DATA OF STANTON NUMBER AGAINST Bh KAYS AND MOFFAT (Kays & Moffat, 1975) 177
FIGURE A-3-3: ITERATIVE LOOP USED TO FIND ISOTHERMAL BLADE TEMPERATURE 180
FIGURE A-4: SIMULATED CASCADE FLOW FIELD SHOWING STATIC PRESSURE 180
FIGURE A-5: FINAL NUMERICAL AND ANALYTICAL SOLUTIONS AT m=0.9 FOR ISOTHERMAL BLADE* 181
FIGURE A-6: PREDICTED COOLING PERFORMANCE OF TRANSPIRATION MODELS COMPARED TO CONVENTIONAL COOLING ARRANGMENTS 181
Figure B-1 Schematic of Cascade Test Section 186
Figure B-2 Static pressure and resulting isentropic Mach number distribution of Rig and compared to design intent. 189
Figure B-3 Visualization of secondary flows within test section at operating conditions using CFD 190
Figure B-4: Original input with detected checkerboard locations and corresponding transformed image 191
Figure B-5 Emission and absorption spectra of UniFIB PSP (Innovative Science Solutions Inc., 2016) 192
Figure B-6 Basic PSP experimental set-up (Quinn, et al., 2013) 193

Figure B-7 Example Calibration Curves taken from UniFIB 194

Figure B-8 2D Film Cooling model showing mass transfer analogy (Han & Rallabandi, 2010) 196

Figure B-9 Schematic of TLC and director orientation (Ireland, et al., 1999) 203

Figure B-10: TLC reference intensity response relative to temperature 205

Figure B-11: Variation in PSP error against film effectiveness 209

1. Introduction

This chapter describes the context within which the present research is set. It begins by giving and brief overview of the systems that would be impacted by this research as well as the potential significance of the solutions proposed. This includes a basic summary of the recent advances within the field of gas turbine engines and the main developments in turbine blade design. It will provide an overview of past and current cooling techniques, moving into a description of the current state of the art, where this research endeavours to contribute. The final sections of the chapter contain an overview of the research goals as well as a list of the achievements realized throughout.

1.1. Overview of Gas turbine engines

Engine efficiency and performance have always been at the core of aircraft development, whether it be the next iteration of ultra-efficient long-range airliners, or a new generation of fighter aircraft. Since the dawn of aviation, engine manufacturers have participated in an ongoing race over who can deliver the next big improvement in engine performance. Originally, the need for military air superiority was the driving force in this evolution (Gunston, 2006), however, growth in the civil aviation market has now led it to become a driving force for the industry as well (Rolls Royce Plc, 2021).

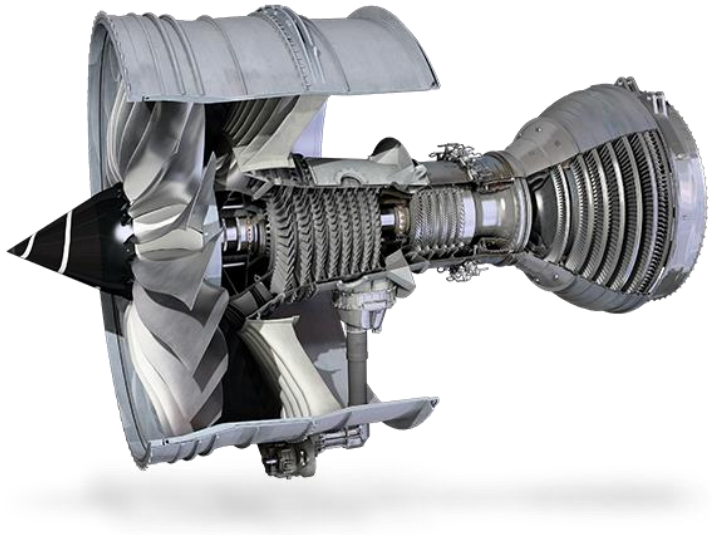


Figure 1-1 Render of the Rolls Royce Trent 1000 Turbofan, one of the most advanced aircraft engines to date (Copyright: Rolls Royce Plc)

As engines have grown in both size and complexity over the years, so has the size of investments and research budgets dedicated to this endeavour, with leaders in the field respected for their engineering achievements, being hailed as points of national pride (Ellis, 2016). Figure 1-1 illustrates one such achievement in the form of the Rolls-Royce Trent 1000.

Gas turbine engines are the principal means of modern aircraft propulsion and exist in many sizes and configurations depending on the needs of the aircraft. It should be noted that turboprops, turbofans, propfans or afterburning supersonic turbojets, all are dependent on the same core system illustrated in Figure 1-2. Whilst both the performance and complexity of gas turbines have made enormous leaps, the basic principles powering the latest generation of turbofan engines have remained mostly unchanged since its conception by Frank Whittle in 1928 (Whittle, 1930).

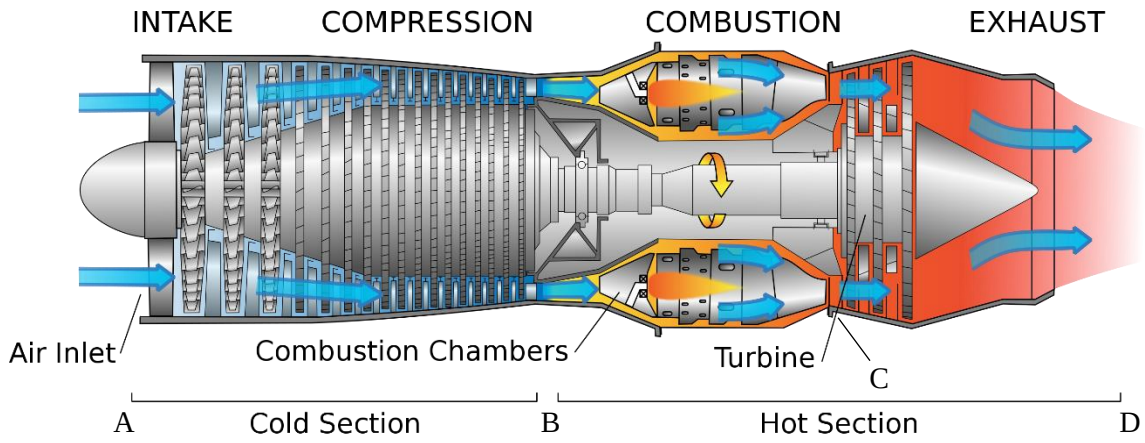


Figure 1-2 Schematic of the core section of a gas turbine engine (Rolls-Royce plc, 1986)

The principal metric of jet engine efficiency is thrust-specific fuel consumption (TSFC), meaning the mass of fuel burned by an engine per unit of thrust developed. This value has a direct impact on aircraft range, speed and payload. With the added backdrop of climate change and CO_2 emissions, reducing this number is of even greater importance for the long-term sustainability of air travel.

Gas turbines operate similarly to a theoretical Brayton thermodynamic work cycle, characterised by an isentropic compression and expansion as well as an isobaric heat addition. Losses within the compression, heat addition and expansion stages lead to some divergence from this cycle, pictured in

Figure 1-3. However, designers are now able to keep these inefficiencies to within a few percent. The efficiency of the ideal Brayton cycle can be characterised by Equation

$$\eta_c = 1 - \left(\frac{P_B}{P_A}\right)^{\frac{\gamma-1}{\gamma}} \quad \textbf{(1-1)}$$

where γ is defined as the ratio of specific heats and A and B refer to the stations in Figure 1-2. By increasing the compression ratio, the thermodynamic efficiency can be improved. However, this has the added consequence of raising the maximum temperature, known as the turbine entry temperature (TET) at station C in Figure 1-2 and 1-3. Once the different stage losses are included, increasing the TET is also found to directly improve the efficiency of a real gas turbine power cycle. The maximum values for TET are set by both the physical limitations of the materials found in the engine as well as the emissions caused by excessively high gas temperatures resulting in the formation of nitrous oxides.

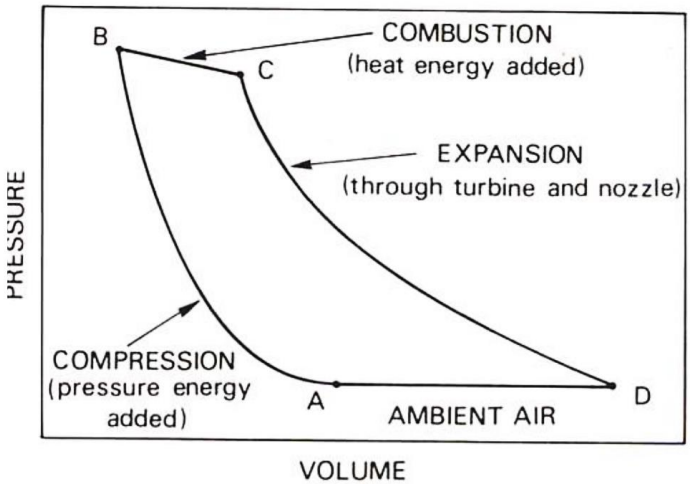


Figure 1-3 P-V of a real Brayton cycle (Rolls-Royce plc, 1986)

The components within the engine most affected by the TET are the combustor lining as well as the high-pressure turbine blades and nozzle guide vanes (NGVs). Both NGVs and turbine blades experience by far the highest heat loads due to the high-speed turbulent flow within the turbine stage, with thermal loads illustrated in Figure 1-4. Turbine blades specifically face even higher cooling requirements because of the higher mechanical stresses experienced due to the unsupported blade tip and high centrifugal forces caused by high shaft RPMs.

Due to the cycling of extreme mechanical and thermal loads, coupled with the necessity to maximise performance, precisely modelling and managing the temperature of high pressure turbine blades and NGVs is of utmost importance for the success and longevity of an engine. Blade life can be reduced in half by metal temperatures only 30K above expected values (Han, 2005). Even when blades are properly maintained, material fatigue within turbine blades requires them to be regularly replaced, resulting in high operational costs.

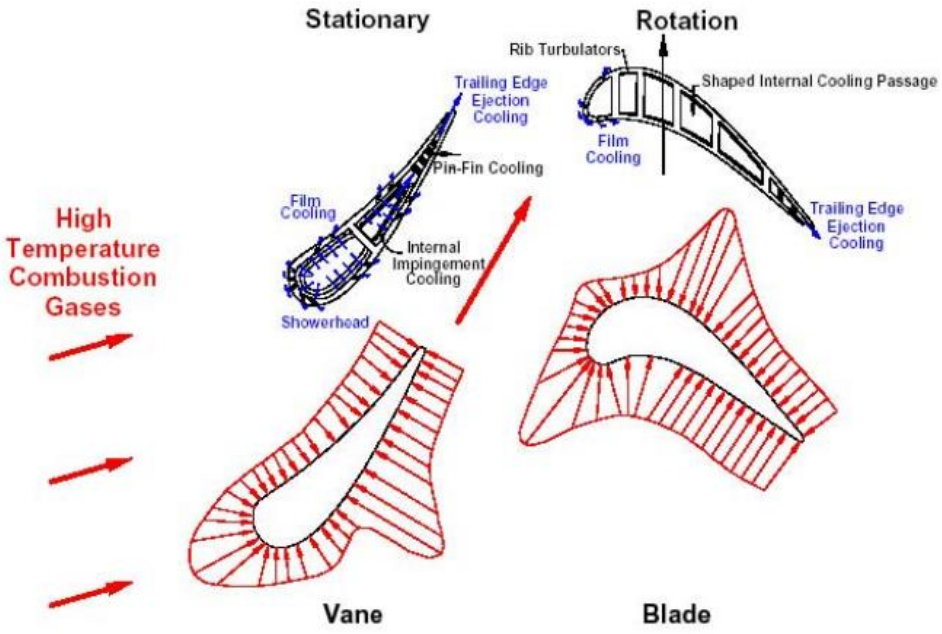


Figure 1-4 Illustration of thermal load distribution for high pressure turbine components by Han (2005)

The ability to sustain higher TETs has been continuously improved thanks to the development of new materials, coatings and technologies as shown in Figure 1-5. The technology cycle typically follows a pattern of innovation, leading to a step change in TET, followed by a period of consolidation in which further diminishing returns are extracted from a given technology. Some of the noteworthy developments have been the introduction of new alloys such as single crystal Nickel superalloys and thermal barrier coatings (TBCs) with the recent development of ceramics adding even further room for development.

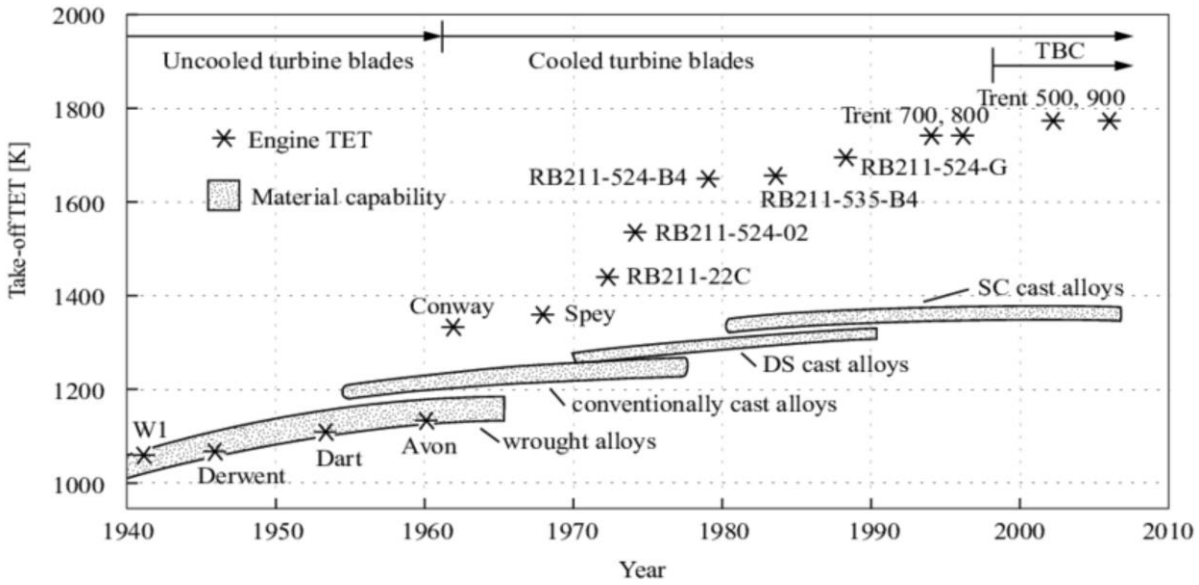


Figure 1-5 Advances in turbine entry temperature against release year for different Rolls Royce engine models from Cumpsty (1997)

One of the most important advances in terms of TET has been the development of cooling systems which has allowed engine temperatures to significantly outpace the development of materials. By bleeding air from the compressor and using it to cool the most vulnerable parts of the engine, such as the combustor and high pressure turbine blades, components can be kept within their operating temperatures, well below the TET. The fraction of air diverted from the core flow of the engine is known as the coolant fraction and the effectiveness of a cooling design can be quantified by Equation (1-2) where T_∞ and $T_{c,in}$ are given as the mainstream and coolant gas feed temperatures respectively.

$$\varepsilon_m = \frac{T_\infty - T_m}{T_\infty - T_{c,in}} \tag{1-2}$$

Whilst increasing the mass flow of air diverted towards cooling proves to be a successful approach to increasing TET, it also reduces the mass flow of working fluid used to drive the turbine. Furthermore, significant losses can be associated with coolant streams such as leakage, aerodynamic mixing losses and outright dilution of the hot mainstream. Studies have shown that coolant fractions must be limited in order to balance the effects of improving the TET and cycle efficiency, against coolant system induced losses (Holrock, et al., 2001). The potential for environmental regulations capping

NOx generation further limits any increase in TET and also favours the reduction in coolant mass fractions as a means to improving engine efficiency. Therefore, novel cooling techniques should aim to not only improve the turbine blade cooling efficiency, but also reduce the consumption of coolant.

1.2. State of the art of turbine blade cooling

Turbine blade cooling has evolved significantly over the years as manufacturing, testing and modelling capabilities have all been expanded. Early cooled turbine blades contained simple cylindrical passages in which cold air was blown into and then ejected either at the tip or root of the blade. As passages became more complex and elaborate, the internal convective cooling effectiveness, defined by Equation (1-3) also improved.

$$\eta_{int} = \frac{T_m - T_{c,ex}}{T_m - T_{c,in}} \tag{1-3}$$

However, a fundamental limitation of internal cooling is that for heat to be removed from the blade by the coolant, it must have already entered the blade and increased the temperature of the metal. The cooler a blade already is, the less benefit internal cooling can have. This means that for high cooling performances of ε_m above 0.5, exceptionally large mass flows of coolant would be required. By contrast, the next developments attempt to insulate the blade from the mainstream of hot gases altogether.

By ejecting the coolant from holes on the blade surface, the boundary layer temperature between the cooled blade and the hot mainstream gas can be reduced. In order to have sufficient pressure margin to eject coolant directly into the mainstream region of the blade, multi feed systems were developed in conjunction to match the new requirements of the coolant systems as illustrated in Figure 1-6. The film effectiveness is given by Equation (1-4).

$$\eta_{film} = \frac{T_\infty - T_{aw}}{T_\infty - T_{cex}} \tag{1-4}$$

where T_{aw} is the adiabatic wall temperature, or the gas temperature at which no heat transfer would occur between the wall and boundary layer.

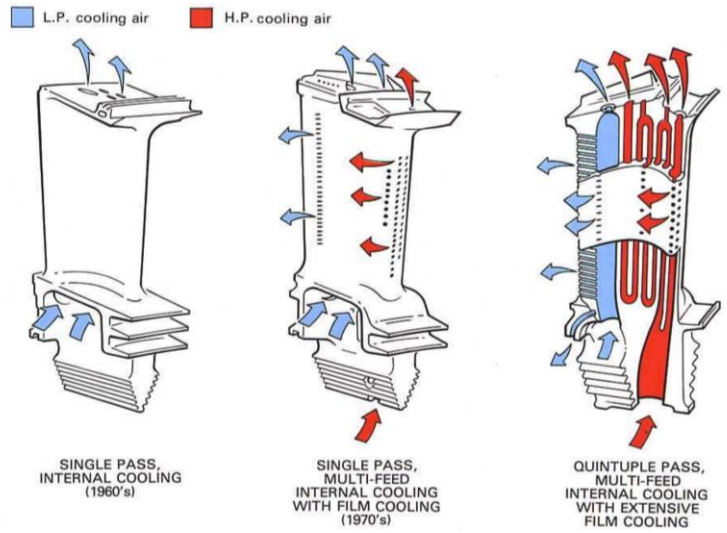


Figure 1-6 Evolution of Turbine blade cooling (Rolls-Royce plc, 1986)

As film cooling developed, the number of film cooling features was increased and geometries were optimized to improve coverage, particularly around areas of the blade under higher heat loads such as the leading and trailing edge. The development of tangential injection holes and slots further improved film effectiveness near trailing edge regions of the blade, with these benefiting from favourable angles to minimise mixing with the remainder of the boundary layer. Together, these improvements have resulted in films not only diluting the boundary layer enthalpy but also beginning to create a physical film barrier between the blade and the mainstream.

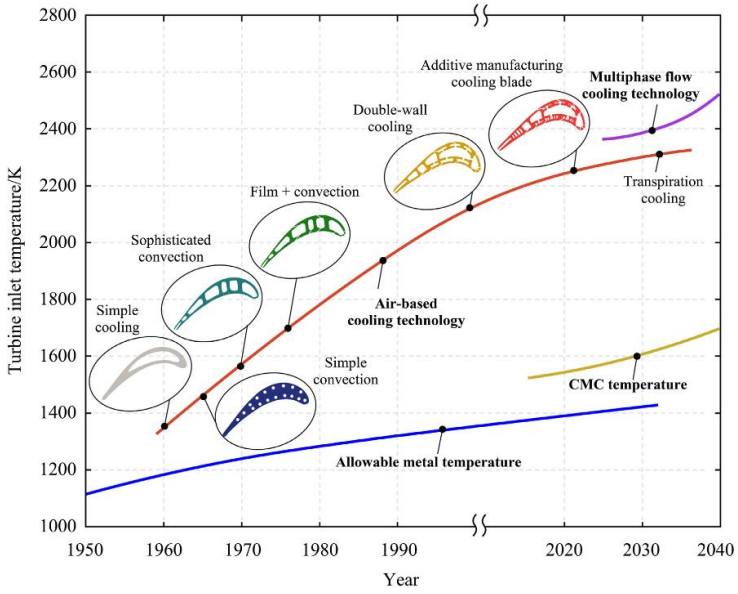


Figure 1-7 predicted direction of turbine blade cooling technology from Unnikrishnan & Yang (2022)

As manufacturing and materials have advanced further, greater flexibility has been afforded to aerothermal designers; this freedom has resulted in the design of multi-walled and effusion-cooled turbine blades as illustrated by Figure 1-7. The trajectory of turbine blade cooling designs is anticipated to achieve transpiration cooling and multiphase cooling within the next ten years.

Effusion cooling stretches the concept of film cooling by further distributing smaller film holes across the entire blade surface. By continuously reinjecting coolant into the boundary layer, a more even and elevated film effectiveness can be established. Moreover, the increase in internal hole area, combined with other features within multi walled systems such as lattices and impingement holes improve the convective efficiency of the blade even further.

This concept can be taken even further through transpiration cooling. By replacing discrete holes with a homogenous porous wall, the distribution of coolant achieved is fully uniform. When ejecting coolant at every location of the blade surface, the mainstream is physically pushed off, resulting in exceptionally high local film effectiveness. Internal cooling is similarly greatly improved. Whilst conceptualised very early on, transpiration cooling remains mainly a theoretical approach due to the limitations of most porous materials and the risks associated with blockage. However, a wide range of novel designs has attempted to mimic this to a degree.

Therefore, the principal aim of the present research is to move the current stage of turbine blade cooling along the curve in Figure 1-7 from double-walled blades towards more advanced schemes that approach transpiration cooling.

1.3. Risks

The development of new high-performance cooling schemes will not come without risks. There are still unknowns with regards to the functional performance of many of the most recently developed cooling schemes, including those investigated in the present research. The implementation of a novel cooling concept into a modern gas turbine is a long and stringent process, often many years in the making.

There is also a significant reliance on a multitude of other fields, equally under development. These include the ever-mentioned challenges with manufacturing, particularly additive manufacturing, the unknowns of thermal and mechanical stressing of lower-density materials as well as the challenges of blockage due to particle ingestion and surface degradation.

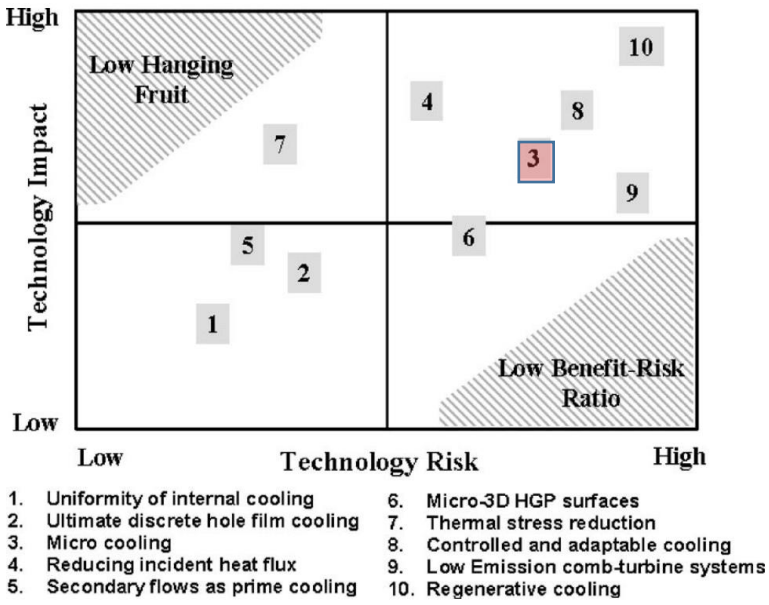


Figure 1-8 The 10 remaining challenges for hot gas passes according to Bunker (2006).

Despite the reasonable risks involved in carrying our research in this area, Bunker (2006) described the successful development of micro cooling features such as transpiration-effusion hybrids as a potentially high-impact field. When discussing the scope of the unexplored thermal and fluid design domains the possibility of additional risks but also the potential for opportunities was highlighted. Other lower risk alternatives also exist, emphasising developments brought about by more modest advances such as core casting developments, resulting in the enhancement of existing designs within current constraints (Bunker, 2017).

Similarly, it was concluded by Krewinkel (2013) in his review of the current state of research that the field of effusion cooling was yet to be fully understood and that the application of previous fundamental research to these new designs would not suffice. Whilst a wide range of high resolution cooling studies has been carried out on flat plates with an emphasis on individual feature performance, experiments on the overall performance and system sensitivity within a turbine blade flow are sparse

and far between. Therefore, it was argued that research must be carried out within this field directly in order to advance it.

1.4. Research objectives

The overarching objective of this research is to advance the effusion and double-walled cooling schemes developed within the University, whilst furthering our knowledge of transpiration cooling and its potential applications to turbine blades. This can further be broken down into 7 areas

- To carry out a review of past research in advanced effusion and transpiration cooling as well as the state of existing novel high effectiveness cooling schemes.
- To comprehend the limitations and maximum theoretical potential of transpiration-cooled turbine blades.
- To enhance the existing experimental facilities at Oxford University in order to better investigate the different relevant aspects of novel blade cooling concepts.
- To advance the effusion and double wall cooling schemes developed by colleagues and predecessors, further towards transpiration cooling and micro cooling. Meanwhile rectifying limitations highlighted by previous designs.
- To carry out PSP experiments on high porosity transpiration cooled blades within a representative high-speed flow
- To better understand the nature of interactions between closely packed cooling features.
- Quantify and accurately model the film cooling performance of high porosity cooling blades.
- Demonstrate the potential of high porosity cooling features within a blade system.

1.5. Outline of Thesis

Chapter 2 contains a review of film cooling designs currently in use as well as other advanced cooling concepts that have been researched. It then goes on to cover certain research pertinent to the proposed designs.

Chapter 3 presents the adiabatic film effectiveness results obtained from two PSP experimental campaigns of high porosity panels at different locations around a blade in the form of two papers. The first paper initially explores the effect of increasing local surface porosity. Meanwhile, the second paper investigates the most significant geometries in greater detail.

Chapter 4 attempts to find correlations to characterise the behaviour of high porosity cooling panels and in doing so better understand the nature of the coolant flow around the blade.

Chapter 5 serves as an investigation, in the form of a research paper, into the performance of and interaction between films using reduced domain numerical simulations.

Chapter 6 presents the results of metal effectiveness tests on the best designs determined by chapter 8. These are also compared to conventional multipass film cooled blades. This is presented in the form of a research paper.

Chapter 7 summarises the research and provides recommendations for future work based on the progress made in the present work.

1.6. Research Achievements

- An analysis and optimization of the potential cooling performance of a theoretical transpiration cooled blade was carried out using both analytical and simple numerical models with the aim to set an upper limit for what could theoretically be achieved using air cooling. This resulted in the submission and admission of a conference paper GT2020-15405 to the 2020 ASME conference held in London, England.
- This research has experimentally demonstrated the potential of high porosity panel cooling concepts over an extensive range of parameters and arrangements using Pressure Sensitive Paint. This has resulted in submissions of two conference papers, ETC2021-680 and ETC2023-297 to the 2021 and 2023 European Turbomachinery Conference, the first of which has been accepted into the International Journal of Turbomachinery Propulsion and Power 2021.

- The present work has provided a detailed CFD analysis of the different interactions of closely packed films on the suction surface of turbine blades, highlighting two different modes of interaction with significant implications on high porosity feature design. Said work has resulted in the submission of a conference paper ETC2023-298 to the 2023 European Turbomachinery Conference held in Budapest, Hungary.
- As a consequence of the extensive experimental work carried out, it was possible to develop correlations using physics-based models to help better describe and understand the mechanisms behind the film effectiveness levels of high porosity cooling features. This has resulted in the submission of a conference paper ETC2023-295 to the 2023 European Turbomachinery Conference held in Budapest, Hungary.
- This work has demonstrated the metal effectiveness and comprehensive cooling capabilities of high porosity cooling systems as well as the development of a basic double wall panel system. This includes the testing of a cast, single crystal CMSX4 test piece, a first to the author's knowledge. This has resulted in the submission of a conference paper ETC2023-296 to the 2023 European Turbomachinery Conference held in Budapest, Hungary.
- The present research was able to demonstrate a potentially significant increase in both film and metal effectiveness relative to previous effusion and industry-standard multipass film cooling designs. This has highlighted the profile of the potential of high porosity cooling schemes, particularly to partners within the industry.
- Within the scope of the work carried out, the experimental facility was developed in order to greatly expand the capabilities and throughput of the rig. This includes the development of the multiband TLC method which made it possible to obtain rapid metal effectiveness measurements of comprehensive blade designs. Other firsts in the rig include density ratio measurements, downstream aerodynamic measurements using a traverse, the addition of a multi-inlet system to accommodate multi-feed designs, and improvements to the control and safety rating of the facility.

- The present work has contributed to the overall progress of the Transpiration Cooling project, an endeavour funded by the Engineering and Physical Sciences Research Council (ESPRC). This research was carried out in close collaboration with Rolls-Royce Plc. and embodying their primary aim is to develop UK knowledge and capabilities towards novel air cooling systems, primarily for turbine and hypersonic flight applications. The ongoing success of the project resulted in the continuation of the research under an new program called CORDITE as well as and under the Rolls-Royce Bristol managed programme TAPAS.

2. Literature Review of transpiration and Effusion Cooling

Transpiration cooling serves as the inspiration and starting point of the present research. However, the topic has long been studied as a potential avenue for advancing turbine blade cooling. This chapter will summarise the development of transpiration cooling research as well as highlight the gaps in existing research. The focus of both this chapter and this body of work as a whole is on the process of developing novel cooling schemes and their progress through experimental campaigns.

As advances in manufacturing techniques are in part responsible for the renewed debate in transpiration cooling and the shift towards novel micro-cooling structures, these developments will also be examined in this chapter.

2.1. Early Theoretical considerations

The first studies on transpiration cooling attempted to find analytical solutions to heat transfer within the transpired boundary layer with the most significant boundary condition being the non-zero perpendicular velocity condition at the wall as illustrated in Figure 2-1. Different models were proposed by Rannie (1947), Friedman (1949), Rubesin (1954) and Spalding et al. (1964) amongst others, each improving on existing solutions. Differences between the models were based on different flow assumptions and assumed boundary conditions. However as experimental data at the time was sparse, a consensus was not immediately reached. Nonetheless, it was made obvious by these early attempts at modelling the transpired boundary layer that transpiration could significantly reduce the heat transfer coefficient of the transpired surface.

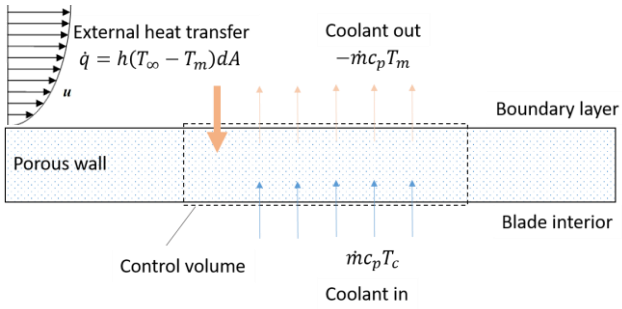


Figure 2-1 Standard blade heat balance for a porous wall section

Finally Kays and Crawford (1980), with the support of extensive flat plate data by Kays & Moffat (1975), developed an elegant solution using Couette flow approximations. By assuming no pressure gradients and constant mainstream velocity, Equation (2-1) can be obtained from the energy equation for the turbulent boundary layer using the boundary conditions outlined in Equation (2-2).

$$\bar{v}\frac{d\bar{T}}{dy} = \frac{d}{dy}\left[(\alpha_H + \varepsilon_H)\frac{d\bar{T}}{dy}\right] \tag{2-1}$$

$$y = 0 \qquad \bar{T} = T_m \qquad \dot{q''} = \rho c_p(\alpha_H + \varepsilon_H)\left(\frac{d\bar{T}}{dy}\right)_m$$
$$y = \delta \qquad \bar{T} = T_\infty \tag{2-2}$$

This form was able to fit practically any flow conditions on flat surfaces, with the reduction in non-dimensional heat transfer coefficient at a given streamwise coordinate being defined as

$$\frac{St}{St_0} = \frac{b_h}{e^{b_h} - 1} \tag{2-3}$$

where

$$b_h = \frac{\dot{m}_c'' / G_\infty}{St_0} \qquad \text{or} \qquad B_h = \frac{\dot{m}_c'' / G_\infty}{St} \tag{2-4}$$

The solution is even able to fit data with significant pressure gradients as shown in Figure 2-2 (Kays & Crawford, 1980). Georgiou and Louis (1985) further affirmed the effect of increasing the blowing parameter until the heat transfer became effectively zero at b_h>16 at which point the blow off

condition was met and the mainstream boundary layer becomes completely removed from the blade surface.

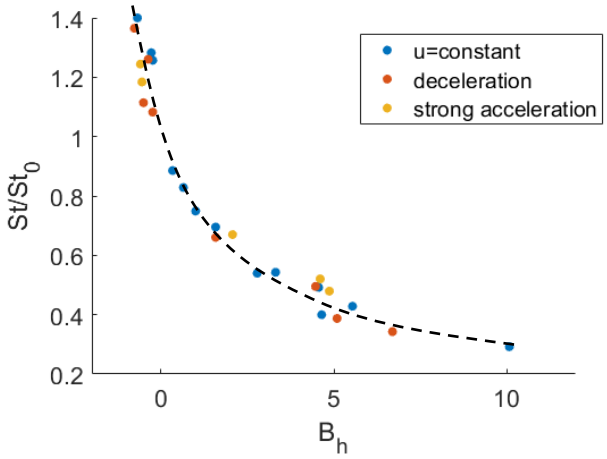


Figure 2-2 Effect of Transpiration on heat transfer coefficient for various conditions with the analytical solution of Kays and Crawford, adapted from Kays & Crawford (1980)

Early considerations of applying such transpiration cooling solutions to entire turbine blades began with the development of the standard blade model such as implemented by Eckert & Livingood (1954). The objective of the model is to determine the steady state blade temperature. The approach consists of a simplified heat balance within an idealised wall block whose control volume is shown in Figure 2-1 and computed in by Equation **(2-5)**. The perfect internal cooling effectiveness of transpiration cooling allows for a relatively simple heat balance between the incoming heat from the hot gas surface, against the heat removed by the internal cooling of the hot gas. Analytical boundary layer solutions are used to determine the outer surface heat transfer coefficient.

$$h(T_\infty - T_{aw}) = c_{p,c}\dot{m}_c(T_m - T_{c,in}) \tag{2-5}$$

In a simplified standard blade model analysis, Holrock (2001) found the potential metal effectiveness of a transpiration cooled system to be given by

$$\varepsilon_m = 1 - \frac{1}{\exp(m^*)} \tag{2-6}$$

allowing for a simple comparison between different cooling approaches to be visualised in Figure 2-3, where the nondimensional coolant supply is given by m^* in Equation **(2-7)**. m^* consists of the ratio between the cooling capacity of the system to the overall external heat load on the blade, where h_o is

the reference heat transfer coefficient of an uncooled surface and A refers to the external blade surface area. Note that m^* is very similar to b_h, with the former referring to an overall blade system, independent of its cooling strategy, and the latter referring to a local region of transpiration cooled boundary layer.

$$m^* = \frac{\dot{m}_c c_p}{\int h_o dA} \tag{2-7}$$

Figure 2-3 also includes the performances of real turbine blades as well as the theoretical performance of internal convenction cooled blades at given mass flows and internal cooling effectiveness levels.

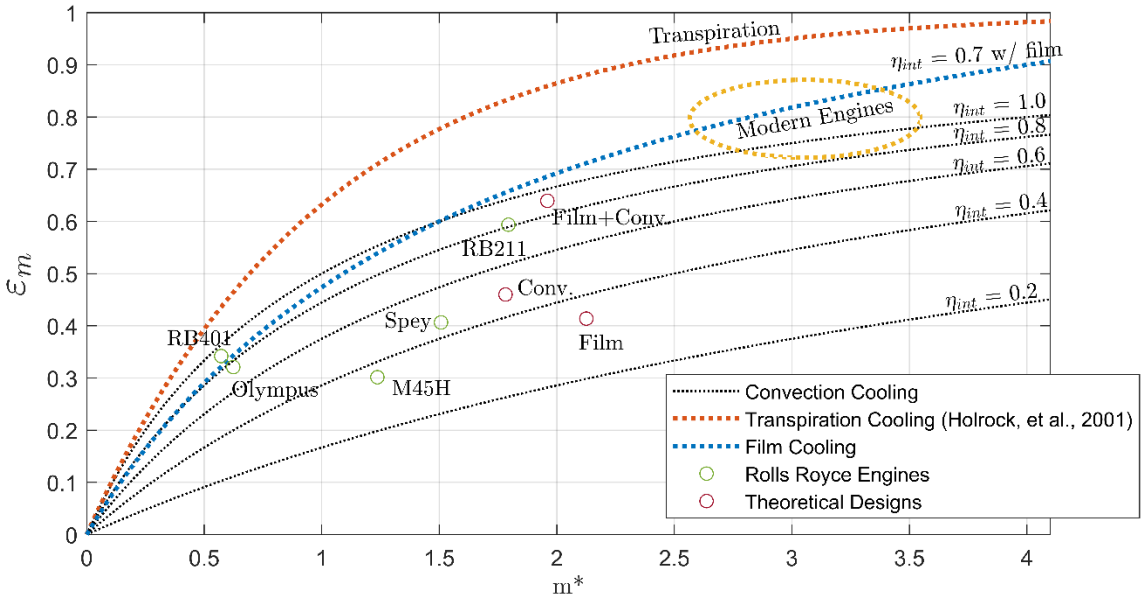


Figure 2-3 Results of standard Wall Model with relevant data, adapted from Holland & Thake (1980)

In addition to the effect on local heat transfer coefficient, the addition of coolant into the boundary layer also reduces adiabatic wall temperature, resulting in the development of a film downstream of the transpiration region. Goldstein et al. (1965) demonstrated that the film effectiveness downstream of flat plate porous section of length l could be accurately described by

$$\eta_{film} = 0.94\left(Re_{\Delta_2}\right)^{0.39}\left(\frac{x}{Ml}\right)^{-0.88} \tag{2-8}$$

Closely matching film cooling models developed by others based on a range of other 2D film cooling geometries (Goldstein, 1971) and together with the boundary layer solutions by Kays and Crawford, form the basis of any analytical transpiration modelling.

2.2. Experimental transpiration cooling research

Whilst analytical models were being developed, NASA and the US Department of Defence engaged in a series of programs, exploring the feasibility of porous transpiration cooled blades, with Poroloy wire mesh blades. These were similar to those patented by Eckert (Eckert, 1953), and quickly found their way into test rigs (Lauziere, 1960). Early tests showed promise, with high blade cooling being reported by Moskowitz & Lombardo (1971) as well as short term resistance to oxidation and blockage (Wolf & Moskowitz, 1983). Different porous structures were tested including wire wound porous material shown in Figure 2-4, Lamiloy (Nealy, et al., 1969) and porous sintered materials.

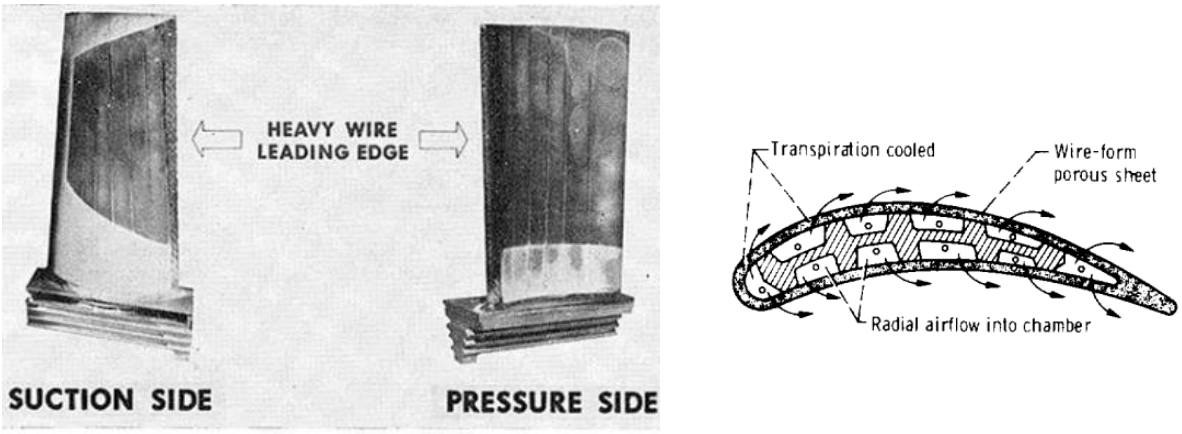


Figure 2-4 Photograph (Moskowitz & Lombardo, 1971) schematic (Glassman, 1975) of early transpiration cooled blade using wire form and spar design

However, the outcome of these research programs highlighted that despite high cooling effectiveness levels of over 0.7 and potential reductions in coolant mass flow of up to 50% relative to internal cooling (Esgar, et al., 1970), full coverage film cooling would offer a more reliable and practical solution to turbine blade cooling needs of $\varepsilon_m > 0.5$ (Moffit, et al., 1976). Porous geometries were seen to have relatively low structural strengths suffer from potential oxidation of the materials (Glassman, 1975), and long-term operation and maintenance were questioned as hole blockage of very small pores became an issue (Raj, 1983).

The resultant degradation would reduce the coolant throughput as illustrated in Figure 2-5, preventing the blade from being cooled. Whilst material oxidation could be reduced through alloy development, at the time these came at the expense of further reduced material strength. Bayley noted that in order to mitigate blockage and oxidation, pore size should be maintained over 100 microns (Bayley, et al., 1973) meaning little was to be gained relative to small film holes within the same magnitude. High-temperature gradients caused by low cooling towards the leading edge also resulted in poor lifing due to high thermal stresses (Hickel, et al., 1972).

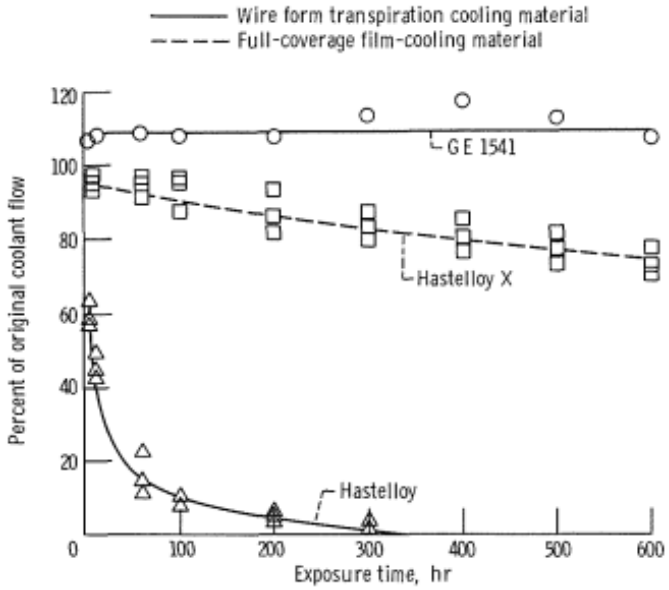


Figure 2-5 Effect of Oxidation on coolant flow through porous and FCFC blades relative to conventional blade from Esgar, et al. (1970).

Furthermore, aerodynamic performance was also seen to be lacking behind convection and film-cooled blades due to the normal velocity coolant injection, and the possibility of leading edge ingestion at low mass flow rates (Behning, et al., 1971). While these studies have provided a valuable consensus on the (im)practicality of a fully porous transpiration cooled blade, the reported data is mainly limited to overall performance, offering only some insight into the nature of transpired films their cooling performances and their interactions with the blade surface.

It was highlighted that the knowledge gained of transpiration cooling could be used in applications requiring shorter timescales and higher cooling requirements such as in missiles and re-entry vehicles (Stepka, 1981), as well as lower stress environments such as combustor liners (Acosta, 1987).

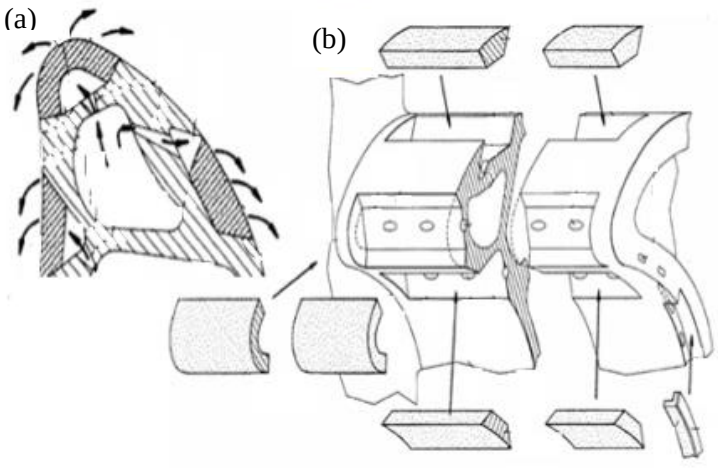


Figure 2-6 Transpiration Cooling Inserts patent with (a) profile and (b)exploded views (Grylls, et al., 2002)

More recently, patents concerning the manufacturing of porous turbine blade cooling schemes such as the ones illustrated in Figure 2-6, have been filed (Battisti, 2002) (Grylls, et al., 2002) but limited work on turbine blade testing with porous features has recently made it into research and the public domain.

Newer lower fidelity studies have revisited some of these designs in scaled rigs with better imaging methodologies in order to obtain in situ measurements of the blade surface, though similar conclusions were reached. Kim et al. (2022) tested a fully porous sintered NGV next to a micro-cooled effusion blade and noted that the strong pressure gradient between the LE and suction surface affected the coolant and temperature distribution around the blade leaving the leading edge relatively under-protected (Kim, et al., 2021). Mean cooling effectiveness levels were measured at 0.6 and 0.4 for the transpiration and effusion blades respectively. Even without external flow field variations, it was demonstrated by Huang & He (2019) that non-uniformities in pore distribution could easily have a large effect on external cooling and temperature gradients.

2.3. Recent porous flat plate work

Porous cooling features have meanwhile found a niche in leading-edge cooling for re-entry vehicles with a large portion of flat plate transpiration cooling research now aimed at supersonic flows and applications. The uniquely high heat loads found in these regions warrant the use of exotic porous materials which would otherwise be prohibitively expensive for turbine blade applications.

Nonetheless, these experiments have demonstrated the possibilities of new porous materials called ceramic matrix composites consisting of Carbon/Carbon and C/SiC (Glass, 2008). They illustrate how weaves of carbon-based fibres are able to create an incredibly rigid yet porous matrix. Langener, et al. (2012) demonstrated that a modified version of an analytical model of Kays and Crawford (Kays & Crawford, 1980) could still be applied to weaved porous carbon features in supersonic flows (Langener, et al., 2010). Dahmen, et al. (2017) outline the advances in modelling the dual domain system of a porous body and external mainstream. These studies have demonstrated the potential of newer composite materials relative to more conventional sintered and metal wire structures. However, some challenges remain: Xu et al. (2015) demonstrated the importance and sensitivity to different weaves when using metal wires, and how results typically fall far short of analytical predictions. Liu et al. (2013) also demonstrated the effects of porosity grain size, highlighting that because a material appears to be porous, it might not match the theoretical performance of transpiration cooled features.

Studies into different leading edge shapes such as on struts by Jiang, et al. (2017) and cones by Zhao et al. (Zhao, et al., 2014) have provided insight, not only into transpiration cooling but also into aerodynamic performances and internal flows within a porous object with cross flow.

2.4. Transition to Effusion cooling or Full coverage film cooling

Whilst analytically a very simple setup, the challenges of developing open porous structures with acceptable blockage resistance and structural strength have pushed research in another direction. In order to circumvent many of the challenges of transpiration cooling, Effusion cooling, or Full Coverage Film Cooling (FCFC) was developed. By covering critical components with small discrete film holes, many of the features of transpiration cooling, such as high internal surface area and uniform film

cooling could be recreated. Eckert and Cho (1994) developed an analytical approach, which attempted to model effusion-cooled systems as modified transpiration systems, accounting for the effect of larger discrete channels with larger pitches.

Similarly, Le Brocq et al. (1973) found that for low pitch to diameter ratios of 2, the perforated plates behaved very much like a sintered porous surface which was also tested. However, when increasing the pitch to diameter ratio to 8, the behaviour of the coolant films was very different and behaved like films. Andrews et al. (1986) similarly demonstrated that the film effectiveness of full coverage film cooled plates, with pitch to hole diameter ratios of 1.9 could almost match sintered porous plates at low mass flow rates, a phenomenon recently reproduced by Huang et al. (2015). It was surmised that for these high porosity effusion features at low coolant mass flows, the predominant difference between effusion cooling and transpiration cooling was in the internal cooling effectiveness.

2.4.1. Film cooling review

As effusion cooling diverges from transpiration cooling with larger pitch to diameter ratios, film cooling becomes the primary vehicle through which external heat transfer is reduced. This section offers a short overview of the basics of film cooling, particularly with regards to turbine blade effusion cooling systems.

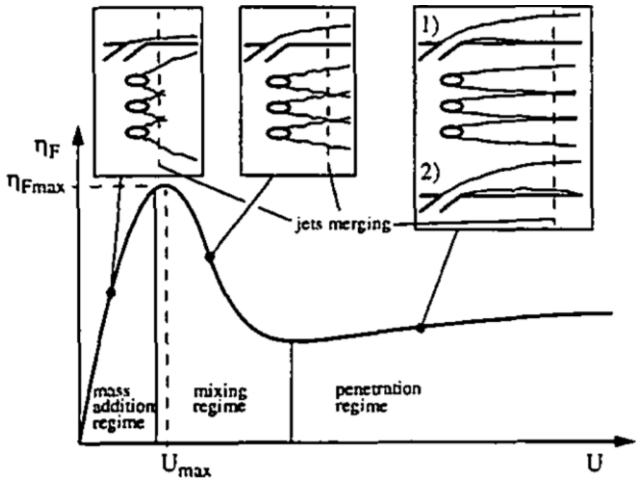


Figure 2-7 Schematic plot of film flow regimes based on film velocity ratio according to Baldauf et al. (2002)

Film cooling involves injecting coolant through a hole on the blade surface into the mainstream cross flow. As the film is blown downstream and mixed into the boundary layer, the downstream surface is protected by a cooler layer of film. The reduction in temperature experienced by the downstream surface is quantified by the film effectiveness given by Equation (1-4).

Whilst area averaged coolant mass flow might remain comparable between effusion and transpiration systems, the individual film holes will have blowing ratios multiple orders of magnitude above transpiration equivalents. The parameters such as blowing ratio (Equation **(2-9)**) and injection angle have a significant effect on how these discrete films interact with the mainstream.

2D film cooling has been extensively studied on flat plates and can be modelled to a high degree of accuracy using analytical models alone. Goldstein (1971) provides an extensive derivation of these models as well as a summary of relevant data sets which remain relevant to this day.

Baldauf et al. (1997) attempted to generate overarching and all-encompassing correlations for cylindrical holes on flat plates with others such as Colban et al. (2010) attempting the same for shaped holes. However, the ability of these approaches to model films in more complex 3D flows remains a challenge as it has been shown that the effects of mainstream flow field curvature (Schwarz, et al., 1990), acceleration and turbulence (Bons, et al., 1994) all play a significant role. Moreover, the behaviours of films, even within flat plate studies are highly non-linear, with films behaving in one of three different regimes: the mass addition regime, the mixing regime and the penetrating regime as illustrated by Baldauf, et al. (2002) in Figure 2-7.

$$M = \frac{\rho_c u_c}{\rho_\infty u_\infty} \tag{2-9}$$

A combination of multiple rows of films over a blade surface is often desired in order to improve film cooling. The temperature field of these films can be superimposed into a single solution using the method described by Sellers (1963), however, interactions between films can have significant effects on individual film performances. One of the main drivers of these interactions is the multiple vortexes and wake patterns that are a result of the interaction of the coolant jet into the mainstream. This includes the counter-rotating vortex pair (CRVP) illustrated in Figure 2-8 (a) Coherent and (b)

time averaged flow structures due to film-mainstream interactions downstream of a 30 degree inclined holes.

Interactions between films have demonstrated varied, and at times less predictable, effects on film effectiveness whether films are next to each other, (Baldauf, et al., 2002), inline (Saumweber & Schulz, 2004) (Yoon, et al., 2019) (Wang, et al., 2020), or in staggered rows (Jiang, et al., 2018). In order to avoid these interactions, films can be spaced out, particularly in the streamwise direction beyond their development length; a term used by Jubran & Brown (1985) to describe the distance required for the boundary layer velocity profile to return to a 2D profile. However, whilst a convenience for modelling, these constraints are highly inappropriate for effusion cooling designs, meaning film interactions are either ignored at the penalty of increased errors (Ngetich, 2019), modelled using simplified correlations (Arcangeli, et al., 2008) or fully accounted for with significant additional complexity (Jiang, et al., 2019). As the complexity of cooling schemes is expected to continue to increase, so are the computational requirements needed to model them. Alternatively, experimental methods remain a necessity in being able to validate the complex fields and structures developed by multiple film features.

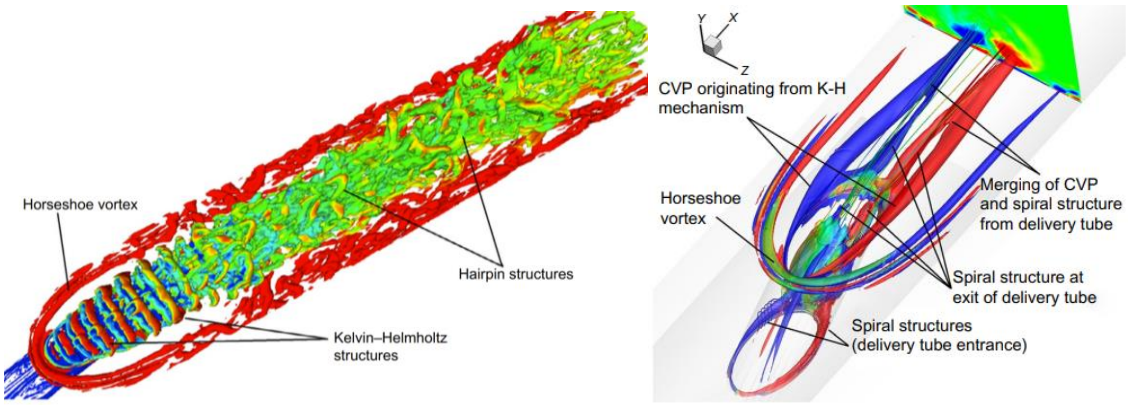


Figure 2-8 (a) Coherent and (b) time averaged flow structures due to film-mainstream interactions downstream of a 30 degree inclined holes from Kalghatgi & Acharya (2014).

With new imaging techniques such as PSP being developed, high resolution film effectiveness data can be acquired from turbine blade geometries in realistic engine flows with Mhetras & Han (2006) being one of the first to do so. Before this development, much of the research in advanced film cooling methods were either theoretical (Battisti, et al., 2006) or of low experimental resolution as measurement

techniques such as liquid crystals did not have the resolution to properly examine intricate cooling distributions (Guo, et al., 1998).

With these experimental developments, flat plate and cylindrical body studies of individual film holes have for the most part all been repeated in representative turbine blade or NGV flows (Waye & Bogard, 2007)**.** As a whole, these have demonstrated the significance of testing on a blade geometry versus on a flat plate (Bunker, 2017). Furthermore, it has highlighted the challenges faced by CFD in matching experimental results. Experimental work will always be required to calibrate numerical simulations and determine the sensitivity and setup required (Johnson, et al., 2010).

2.4.2. Secondary effects associated with film cooling: heat transfer coefficient

While film cooling results in a reduced adiabatic wall temperature, the presence of jets ejecting into the boundary layer can also have effects on the heat transfer coefficient. At lower blowing ratios, with films within the mass addition regime, the heat transfer coefficient remains mainly unchanged. However, when BRs are increased and films penetrate through the boundary layer and into the mainstream, the disruption of the boundary layer increases the HTC around the hole injection (Baldauf, et al., 1999). Film hole size relative to the boundary layer thickness was also measured to have a significant effect as larger jets ($\delta/d < 0.15$) will penetrate further into the boundary layer, increasing the overall HTC, whereas smaller diameter holes ($\frac{\delta}{d} > 0.5$) have the opposite effect (Bunker, 2005).

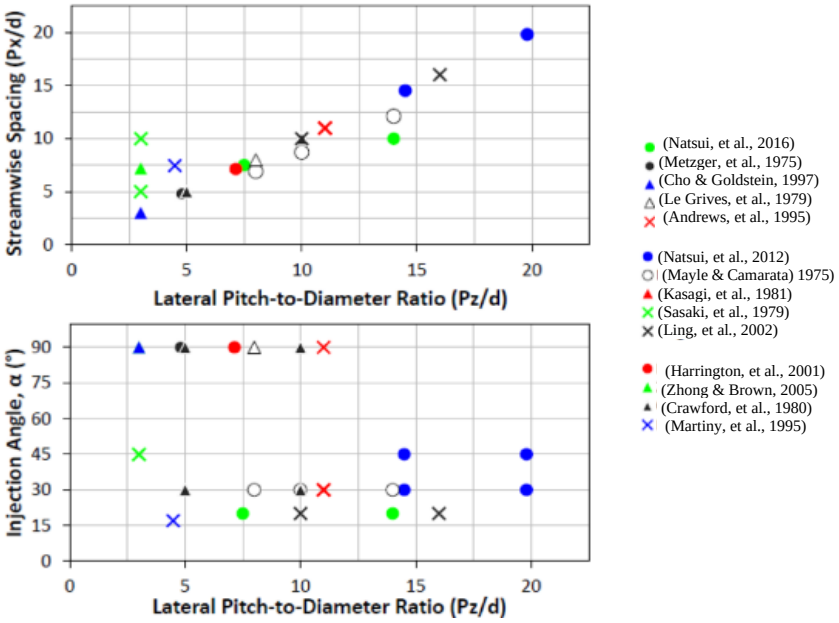


Figure 2-9 Overview of Effusion flat plate studies taken from Natsui, et al (2017)

2.4.3. Overview of Effusion cooling Experiments

With the basics of film cooling covered, attention can now be redirected towards developing turbine blade cooling schemes. The cooling performance of full-coverage film cooling schemes has been extensively studied. Much of the early work was carried out at Stanford University (Choe, et al., 1976) where the main parameters: BR, Temperature ratio, mainstream conditions and angles were studied (Crawford, et al., 1980). This laid down the groundwork to develop numerical boundary layer solvers that bridged the gap from transpiration cooling to FCFC (Crawford, et al., 1980) called STAN5 (Kays, 1976) and later developed into TEXSTAN (Crawford, 2008).

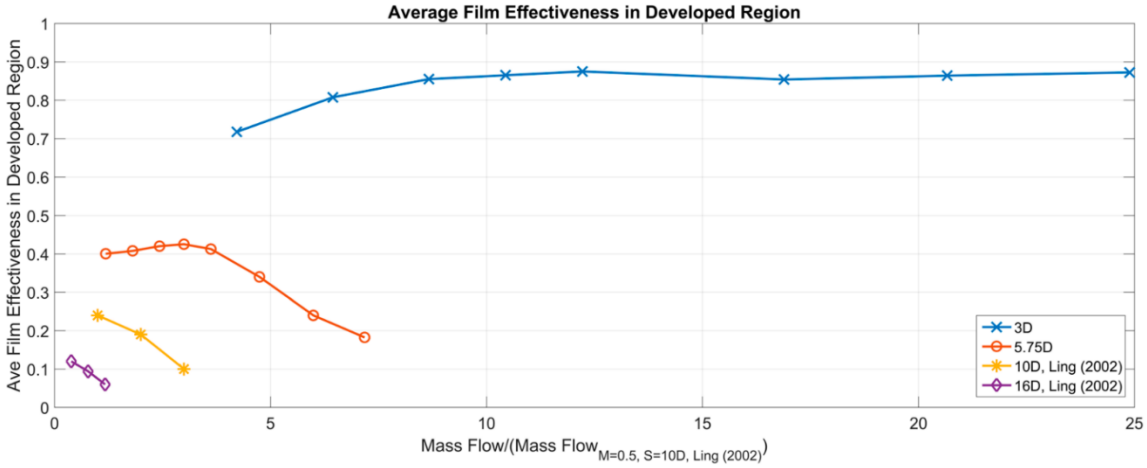


Figure 2-10 Film effectiveness measurements from effusion, from Murray, et al. (2018)

More recently, Natsui et al. (2016) included fans to this range of parameters. A sample of the wide range of effusion studies already carried out is illustrated in Figure 2-9. In addition to the same conclusions as film cooling, pointing towards the importance of BR and injection angle, FCFC studies have consistently shown that the reduction of pitch to diameter ratio, as well as the hole size relative to the boundary layer thickness is crucial in order to improve both film and overall cooling performance. Oguntade, et al. (2015) demonstrated that a reduction of hole diameters and pitches by a factor of 3, resulted in a 50% reduction in coolant consumption at identical cooling effectiveness levels. Mean-while, a comparison between results by Murray, et al. (2018) and Ling, et al. (2002) given in Figure 2-10 indicates that a 33% reduction in pitch to diameter ratios results in a doubling of film effectiveness down to P/D =3 at effectiveness levels exceeding 0.85.

2.4.4. Experimental work on FCFC turbine blades

Much like for porous transpiration cooled blades, NASA tested a wide range of FCFC blades at elevated engine temperatures. Blades tested had pitch to diameter ratios of approximately $P_{1,2}/d = 7$ with both staggered (Figure 2-11) and inline geometries. Results showed better resistance to wear and blockage relative to porous blades despite a slow degradation in coolant throughput with coolant rates dropping by 20% after 600hrs of operation (Esgar, et al., 1970). Metal effectiveness levels of above 0.7 could be obtained by matching previous transpiration-cooled blades with coolant fractions of 5% (Esgar, 1970).

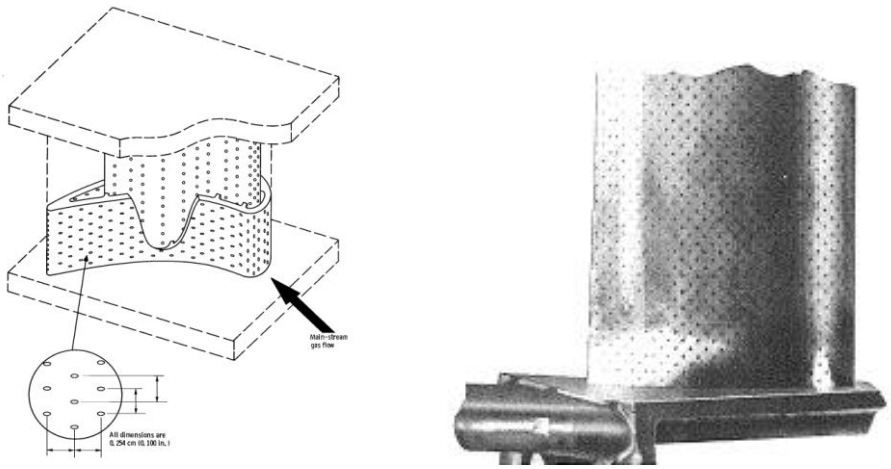


Figure 2-11 Schematic (Meitner, 1978) and photograph (Livingood, et al., 1971) of early FCFC blade test pieces

However, the stress concentrations around the small diameter holes, coupled with the low strength of the laminated perforated sheets being used resulted in the blade failures shown in Figure 2-12 (Hickel, et al., 1972). As a result, multirow film cooling blades continued as the preferred cooling method. The aerodynamic performance of FCFC blades also suffered relative to the convection and film-cooled blades (Behning, et al., 1971), as coolant ejected into the high-speed mainstream of the suction surface incurs a high aerodynamic penalty (Hartsel, 1972).

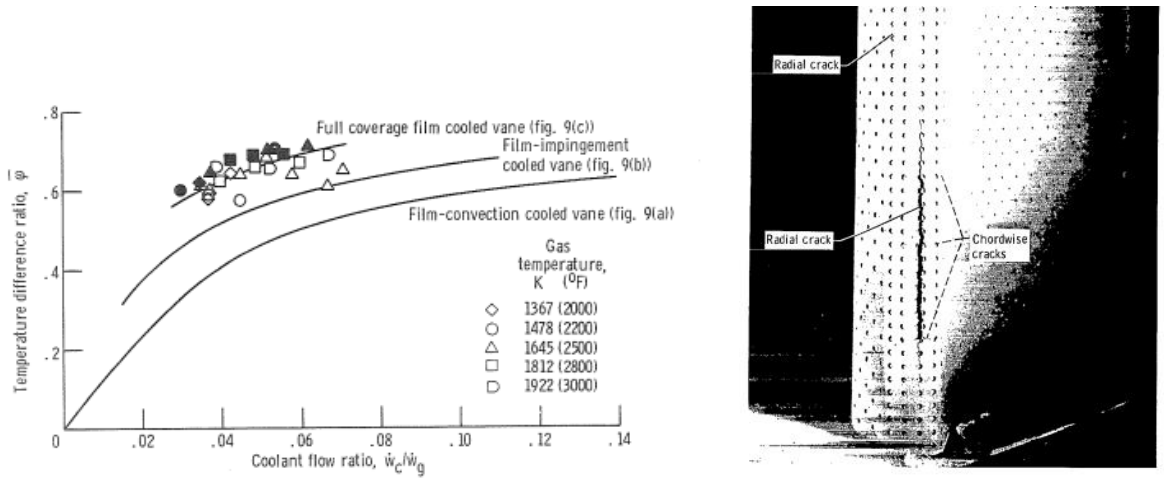


Figure 2-12 Right: Cooling Performance of FCFC blade relative to other cooling methods. (Esgar, 1970) **Left: Fractured FCFC blade after 110 thermal cycles** (Hickel, et al., 1972)**.**

Gao, et al. (2008) were some of the first to measure the film effectiveness of multi-row schemes by making use of new imaging techniques. Others such as Han & Rallabandi (2010) Narzary, et al., (2012) Naik, et al. (2014) followed suit (Figure 2-13). Particular focus was given to the LE, with multi-row schemes being dubbed showerhead cooling, by Gao and Han, (2009), Nathan (2012), and then Moore et al. (2021) who focused on the particulars of hole geometry within this design.

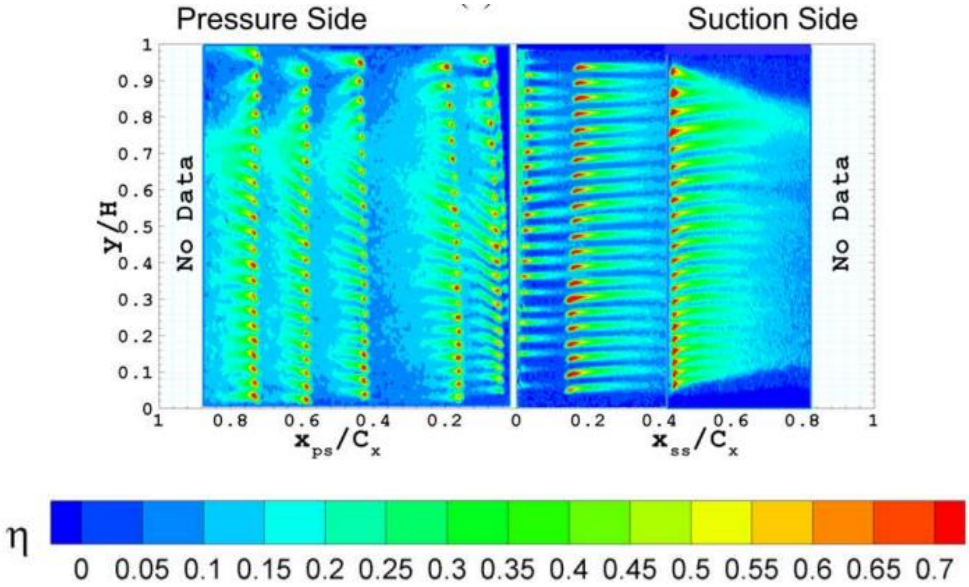


Figure 2-13 Film effectiveness levels measured by Narzary, et al. (2012) **of a multirow system on a scaled NGV with DR=2.5.**

However, the designs tested so far would be labelled as multi-row film cooling by most, as opposed to pure effusion cooling. More recently Li, et al. (2018) and Zhang, et al. (2021) have studied more genuine effusion geometries on NGV geometries with $P_{1,2}$/d ratios of 5 and 6 respectively. Similarly, Ngetich (2019) studied effusion cooling schemes on a turbine blade with $P_{1,2}$/d ratios of 5 and 10, illustrated in Figure 2-14. These experiments have shown somewhat mixed results with regard to film effectives as the cylindrical holes used had a high tendency to lift off. An improvement over initial fanned multi row cooling systems was not quite achieved without the use of excessive volumes of coolant due to widespread ingestion on the pressure surface at lower pressure ratios.

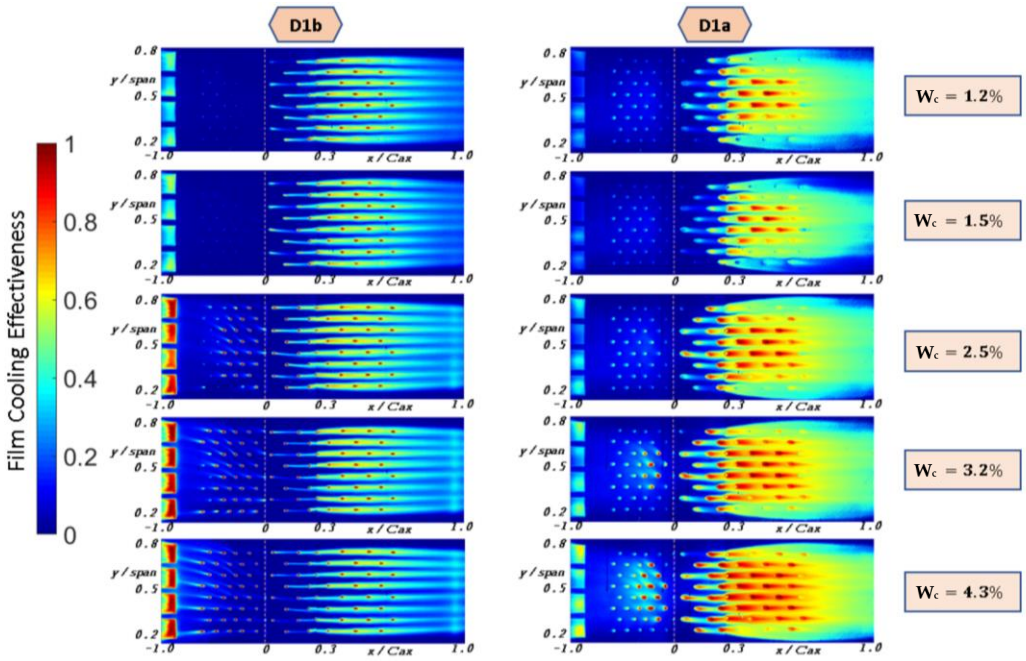


Figure 2-14 Film effectiveness contour maps of two different effusion systems on turbine blade geometries with $P_{1,2}$/d of 5 (Ngetich, 2019)

2.5. Double wall effusion cooling and Novel cooling strategies under investigation

One of the principal avenues of research for advanced cooling architectures is that of double wall effusion-cooled systems. These multiwall systems have evolved as a means to improve internal cooling as well as boasting beneficial mechanical properties, with the inner load bearing wall remaining close to coolant temperatures. These designs aim to reduce coolant consumption by 15-20% whilst possibly improving cooling effectiveness as well, with geometries within reach of existing manufacturing techniques (Bunker, 2017).

Novel double wall cooling schemes have also allowed for the easy integration of effusion cooling resulting in Double Walled Effusion Cooling (DWEC). A host of parametric studies have already been carried out highlighting the importance of internal features such as pedestal shape (Murray, et al., 2021), pedestal height and pitch (Murray, 2017), coolant hole orientation (Sweeney & Rhodes, 2000) amongst other geometric considerations and combinations (Rogers, et al., 2017). External film geometry has also been shown to be of particular significance, both to the external cooling performance and the internal aerothermal properties; the relative effects of spanwise spacing, streamwise spacing and

overall porosity being studied by Courtis, et al. (2021). The effect of reducing hole sizes and increasing the overall number of holes at a fixed pitch to diameter ratio is also seen to be significant (El-Jummah, et al., 2017). Overall, the consensus is that the greater the internal surface area and the greater the film cooling feature density, the more the overall wall system behaves as a porous wall and the better the cooling performance.

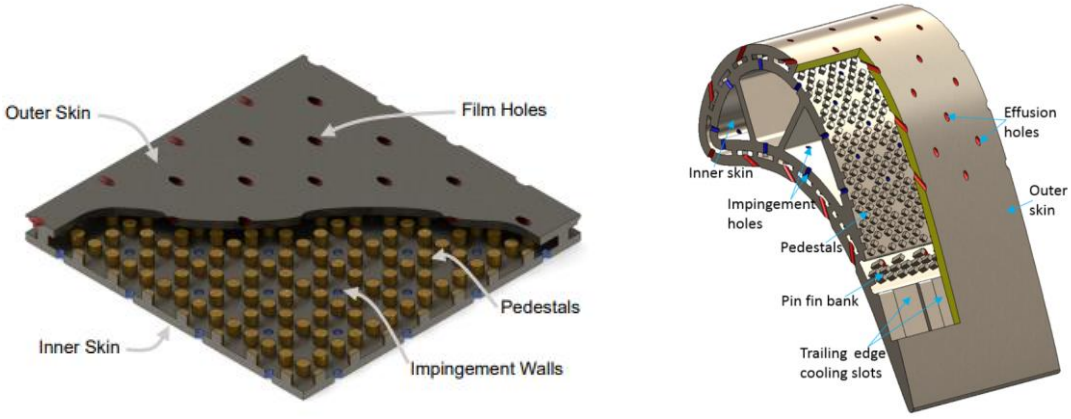


Figure 2-15 Flat plate double wall effusion cooling system by Murray (2017) on the left with application to turbine blade by Ngetich (2019) on the right.

In this vein, Murray, et al. (2020) demonstrated the possibility of modelling the wall as a quasi-homogenous feature of smaller periodic wall block structures illustrated in Figure 2-15 (left). Individual repeating unit cells are modelled to a high degree of accuracy in order to have well defined aerothermal internal flow properties. External film cooling would be modelled in parallel using conventional film and effusion cooling models (Murray, et al., 2018), resulting in a decoupled unit cell conjugate method. The unit cell approach has also been applied to structural considerations (Skamniotis & Cocks, 2021), resulting in a system that has been relatively well analysed in flat plate form within a short period of time. Issues such as blockage have also been investigated and whilst concerns have arisen around the impingement holes, these have been found to be mitigatable at appropriate geometries and pressure ratios (Land, et al., 2010).

The application of these findings to a full blade geometry with its associated flow fields was carried out by Ngetich (2018), demonstrating the potentially high turbine cooling performances achievable by such a system. Figure 2-15 (right) illustrates how the double wall scheme was applied to the

blade geometry. Both conjugate heat transfer and isolated wall block studies indicated that the double wall cooling geometries proposed could achieve metal effectiveness levels of almost 0.7 at non dimensional mass flows of $m^* = 4$. External surface porosity was also shown to have a linear correlation with overall cooling effectiveness.

However, experimental studies also re-illustrated some of the practical challenges associated with using an effectively porous blade with a high-pressure loading (Ngetich, 2019), with ingestion and flow migration marring some of the cooling benefits previously mentioned. Whilst the wall block prediction method was reasonably precise for the full blade model and significantly faster, the fully conjugate numerical simulations were still seen to remain the most accurate method in predicting the thermal performance of the cooling scheme. The presence of holes on the late suction surface further adds to the range of pressures at which films eject to, as well as leading to lift-off and high aerodynamic losses. As the number of film cooling features is increased, so then does the sensitivity to variations in pressure, both spatial and temporal. As the use of coolant must be limited, the internal pressure ratio cannot simply be increased further to avoid ingestion. In order to manage this some studies have examined the possibility of increasing the internal losses within certain holes with the added benefit of improving internal heat transfer.

These have prompted studies on the flows within the double wall cavity (Jackowski, et al., 2021), on the particular effects of cross flows (Ligrani, et al., 2019) and how flow migration can be controlled by internal features (van de Noort & Ireland, 2022). Whilst able to reduce migration to a degree, the preferred method for preventing coolant from migrating excessively from the pressure to suction surface remains the addition of spanwise baffles, breaking up the region between walls into several compartments as highlighted by recently patented designs by (Campbell & Morrison, 2012) and (Devore & Paauwe, 2009).

Whilst flat plate studies have been able to successfully highlight the potential effectiveness and gains to be had from double wall systems, their full practical implementation still requires further development, with the current state of the art only allowing for the partial or limited implementation of double wall cooling systems to turbine blades.

2.5.1. Intersecting, matrix and Lattice systems

Other novel cooling approaches with similar effects include matrix and intersecting hole geometries as shown in Figure 2-16. Basic implementations of these schemes, typically designed for the stagnation region and trailing edge involve simple intersecting film holes as investigated by Nowlin (Nowlin, 2009). Increasing the number of intersections within each hole results in a matrix structure with a high number of internal junctions as investigated by Fletcher (Fletcher, 1997). As the holes become larger and the spacings between them are reduced, the overall feature can result in a geometry similar to the double walled schemes just mentioned if contained within a planar volume.

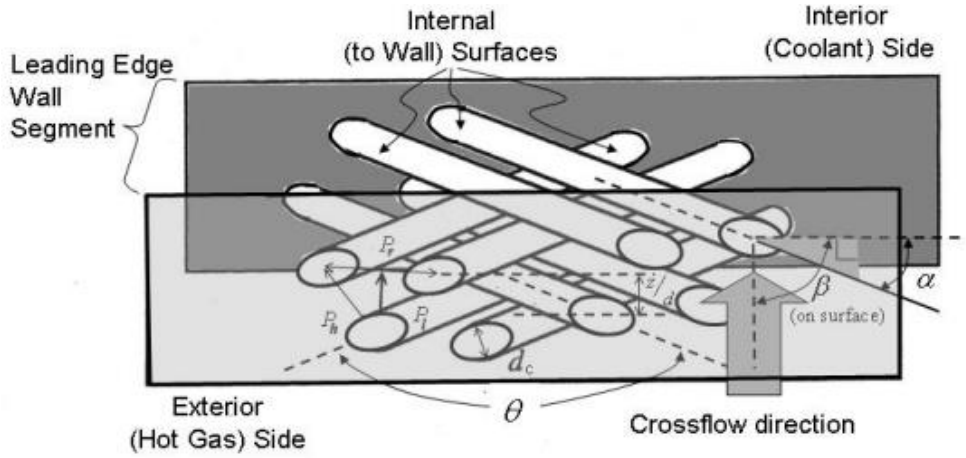


Figure 2-16 Sketch of the optimal hexagonal matric geometry (Fletcher, 1997)

The intersecting channel geometry is designed to increase the internal heat transfer coefficient as the interaction between the two streams can be tailored to increase turbulence and internal vorticity, particularly when streams interact with an offset. The predominant parameters that contributed to the increased heat transfer were injection angle, hole length, diameter, offset and number of interactions. Nowlin found improvements in internal convection to improve by 50% for certain geometries. Significantly, the pressure drop across each interaction was also found to be highly dependent on the geometry and inlet flow conditions of the intersection with losses equating to up to 3 dynamic heads. Whilst this was highlighted as a concern with respect to overall system losses, the ability to tailor both heat transfer coefficients and discharge coefficients remains an asset (Gillespie & Ireland, 1999). Similar relation-

ships were established with lattice cooling schemes which also benefit from intersecting cooling passages. (Gillespie, et al., 2000). It was then shown that the intersecting film trajectories outside of the blade, resulting from matrix schemes, could have further beneficial properties as noted by Holgate et al. (2020).

2.5.2. Dendritic cooling and trench film cooling

Other novel geometries being investigated include dendritic wall cooling where film holes bifurcate within the blade wall, illustrated in Figure 2-17. Thanks in part to advances in manufacturing capabilities, these new designs result in an increased external porosity relative to the internal wall (Luque, et al., 2014). Sometimes also referred to as blood vessel-shaped designs (Min, et al., 2019), these geometries have shown promise in both flat plate and NGV blade studies where a reduction in approximately 10% cooling mass flow was achieved for the same cooling performance.

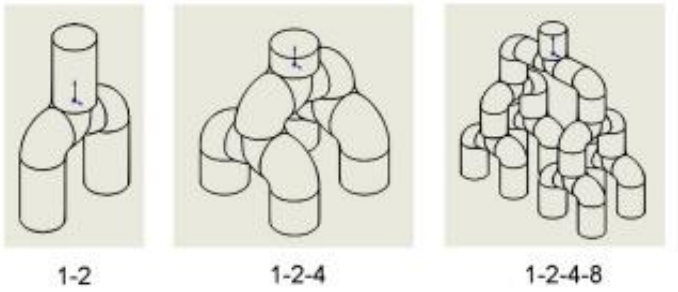


Figure 2-17 Schematic of dendritic film holes (Luque, et al., 2014)

Finally, the most recent family of geometries that have attracted more attention has been trenched film cooling holes (Song, et al., 2021). By including the film holes within a trench perpendicular to the mainstream flow, the trench fills up with coolant which slowly flows out, providing high levels of coverage. Resultant film effectiveness distributions are very similar to 2D slot cooling with the destructive CRVPs also being successfully suppressed (Wang, et al., 2022). Aerodynamic measurements have shown that the trenches can result in large losses, however, these are significantly reduced when located on the slow-moving regions of the concave pressure surface (He, et al., 2019).

2.6. Advances in Manufacturing

In order to keep up with ever more complicated cooling schemes, manufacturing methods have also needed to improve. Developments in laser sintering additive manufacturing (AM) have opened up new avenues in effusion and transpiration cooling as the usual geometric constraints of casting no longer apply. The ability to successfully manufacture turbine blades for industrial turbines with AM was demonstrated by Adair et al. (2019). Once combined with post-processing techniques such as pulsed electrochemical machining, blades without cracks were manufactured from turbine blade grade materials within appropriate tolerances. Krewinkel, et al. (2020) achieved a similar result for NGVs with internal cooling passages. After 70 hours of engine tests, it was found using thermal history paint that the printed blades had effectively the same temperatures and cooling effectiveness as existing cast and machined pieces. It was concluded that it was likely that AM was already mature enough to manufacture NGVs in small scale industrial turbines.

Other studies have managed to demonstrate the manufacture of intricate small passages without post processing (Snyder & Thole, 2020). Figure 2-18 illustrates just how far AM has progressed in a short amount of time. Print quality and its effects on aerothermal performance still remain an issue to be studied (Snyder & Thole, 2020) with many different parameters being investigated such as grain size and print orientation (Snyder, et al., 2016). While the technology continues to mature in terms of reliability and capability, laser sintering additive manufactured parts have already found their way into high porosity cooling studies (Stimpson, et al., 2018). Calderon et al. (2018) tested leading edge cooling concepts with porosities of 0.57 and tortuous lattice holes whilst Min et al. (2019) tested a range of different flat macro porous designs with porosities reaching up to 0.23. With some AM parts already making their way into commercial turbofan engines, the likelihood of laser sintering AM being used for direct turbine blade manufacturing is becoming almost certain (Najmon, et al., 2019).

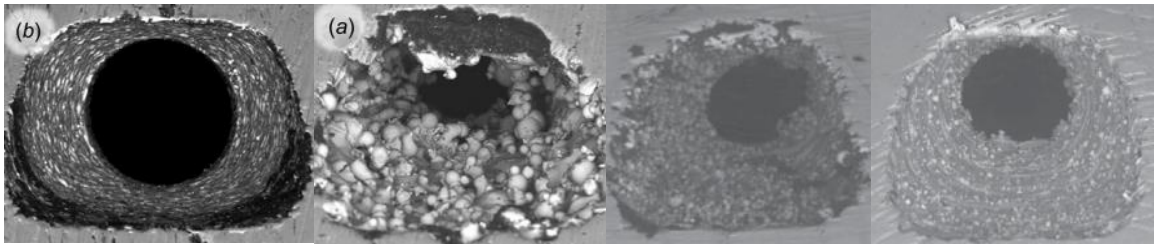


Figure 2-18 Development of film cooling hole AM within a span of 2 years: a 0.5mm diameter cooling hole (a) EDM baseline, (b) taken from Stimpson, et al (2018) (c) and (d) taken from Snyder & Thole (2020) using different print orientations

Even conventional casting manufacturing techniques have benefited from advances in additive manufacturing, as the 3D printing of ceramic cores allows for designs to increase in complexity (Liu, et al., 2017). Coupled with an overall improvement in casting technology (Broomfield, et al., 1998), the existing design space for turbine cooling geometries will expand even before the takeover of full AM (Bunker, 2017).

Other promising advances in materials and manufacturing include Poroform, developed by (Battisti, et al., 2006) and uses galvanic electroforming in order to control the surface geometry of the blade and develop more durable full coverage film cooling solutions. Alternatively Arai & Suidzu (2013) began investigating the use of porous ceramic barrier coatings to develop an effusion, porous hybrid with materials capable of resisting oxidation as illustrated in Figure 2-19.

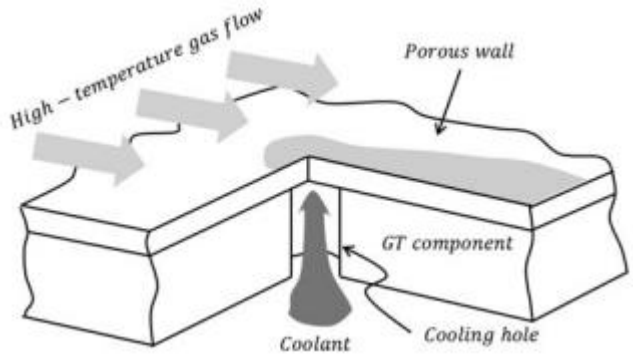


Figure 2-19 Ceramic Porous barrier coating (Arai & Suidzu, 2013)

Lastly, ceramic matrix composites, first tested for hypersonic purposes have been reconsidered for turbine blade applications by Wilkins, et al. (2021a). These have recently been tested to include film holes for turbine blade applications (Wilkins, et al., 2021b);

2.7. Summary

As transpiration cooling has been studied since the inception of gas turbines, a large volume of experimental, numerical and analytical work has already been carried out. However, the vast majority of this work has been carried out on flat plates with limited modern data existing on its actual performance on the surface of a turbine blade. Whilst research in the 60s and 70s attempted its implementation directly into engines, the maturity of materials and designs were not evolved enough for this endeavour to be successful.

Hybrid schemes have shown the most promise with regard to advancing turbine blade cooling performances towards the potential levels idealised by successful transpiration cooling. Advances in manufacturing, particularly in the field of AM, coupled with the development modern imaging techniques has greatly expanded the breadth of geometries that can be considered for investigation.

Current hybrid designs however remain relatively distant from their goal, with many of the most effective flat plate effusion cooling designs having yet to be implemented into turbine blade geometries. For example the beneficial effect of the pitch to diameter ratios around 2 and film features with high porosities requires further investigation in engine representative flows. Successfully adapting genuine effusion schemes to work within a blade flow remains to be done, particularly with regard to external blade cooling.

3. PSP experiments on high porosity cooling geometries

Theoretical analysis on a transpiration cooled blade, such as the one included in Appendix A, illustrates the lack of any experimental data of high porosity cooling features other than from flat plate studies. This results in the validation of turbine blade transpiration cooling models being exceptionally challenging if not impossible. The objective of this chapter was to begin the investigation into transpiration flows in turbine blades by isolating the effect of film cooling effectiveness from variations in heat transfer coefficient or internal convection.

This chapter contains two papers detailing extensive PSP campaigns carried out in two distinct phases. The first paper, contained in section 3.1, was published in the 2021 International Journal of Turbomachinery Propulsion and Power (IJTPP 60220016) and presents the first series of experiments carried out on high porosity geometries. The motivation behind this first paper was to characterise the film effectiveness of significantly higher porosity cooling features within turbine blade flows. Increasing the porosity of previous "full coverage" schemes such as the ones summarised in Chapters 1 and 2 had been attempted but proved to be unsuccessful due to challenges with pressure margin management and ingestion, with porosities above 2-3% requiring unrealistic mass flow rates and pressure ratios to avoid the ingestion of mainstream gas. Appendix B contains a more detailed overview of the experimental facilities used.

This paper was written under the supervision of Professor Peter Ireland and Ignacio Mayo from Rolls-Royce PLC. Experiments were carried out with the assistance and supervision of Dr. Tsun Holt Wong.

The findings of the first paper, notably the very high film effectiveness levels on the suction surface as well as the effect of staggering the film holes, prompted further investigation into the different parameters causing the high levels of film cooling effectiveness. A second, much larger, series of experiments are detailed in the second paper contained in section 3.2. An emphasis is placed on the geometries that were seen to be most successful in the section 3.1. This paper was presented at the 15th

European Turbomachinery Conference (ETC2023-297) in Budapest Hungary April 2023 and was written under the supervision of Professor Peter Ireland.

3.1. Initial Experiments of Transpiration Cooling Inspired Panel Cooling on a Turbine Blade Yielding Film Effectiveness Levels Over 95%

Augustin Wambersie [1], Holt Wong [1], Peter Ireland [1], Ignacio Mayo [2,*]

[1] Department of Engineering Science, University of Oxford, Oxford OX1 3PJ, UK;
[2] Rolls-Royce PLC, Derby DE24 8BJ, UK; mayo@Rolls-Royce.com
* Correspondence: augustinwambersie@eng.ox.ac.uk ;

† This paper is an extended version of our paper published in Proceedings of the European Turbomachinery Conference ETC14 2021, Paper No. 680

Abstract

Panels were tested at different locations around the blade, on both suction and pressure surfaces. Three different surface porosities were also tested. Results demonstrated that the approach can be very successful with high levels of film cooling effectiveness exceeding 95% achieved using low coolant mass flow rates. Increasing the surface porosity also proved to be an important parameter in the panel's performance. Additionally, staggering the film holes lead to significant positive interactions between individual films, resulting in much improved panel performance.

Keywords: Transpiration cooling; turbine blade; film cooling, pressure sensitive paint

3.1.1. Introduction

The need to design turbine blades able to endure the ever increasing temperatures found in the next generation of turbine engines has long motivated continuous improvement in cooling and material technology. However, despite the impressive progress made over the past 80 years, most gains have been slow, incremental improvements of existing technology, with film cooling, thermal barrier coatings and CMC being the only significant innovations.

While transpiration cooling is not a new concept, it has long been predicted to deliver a step change in cooling performance relative to conventional systems [1]. The very high internal surface area, positive effect on heat transfer coefficient and uniform distribution of cooling films make it theoretically ideal for turbine blade applications. Recent advances in porous C/C-SiC and CMC have led to a revival in the field of transpiration in aerospace for uses such as rocket nozzle cooling [2] yet momentum in turbine blade technology has lagged behind. While this may be due to the significant constraints in

blade design arising from the high thermal, mechanical and cyclical loading, a fundamental understanding of the true potential of transpiration cooling as applied to turbine blades remained mostly unexplored before the present research.

The development of high resolution, non intrusive measurement techniques has facilitated the study of more complicated external cooling flows, allowing much greater understanding of cooling phenomena in representative conditions. By making use of Pressure Sensitive Paint (PSP) to measure the film effectiveness of transpiration cooling feature on turbine geometries, this paper will attempt to demonstrate how such cooling flows behave in engine representative conditions.

Two separate studies are considered in this paper. The first looks at the performance of a transpiration panel over different locations around the blade, on both suction and pressure surfaces. The second looks to compare several variants of the same panel at the same location. While transpiration cooling has benefits far beyond external film effectiveness, the simplicity of this type of experiment allows for a large number of geometries to be quickly sampled, making it a sensible starting point.

3.1.2. Literature review

In previous work by Ngetich [3], the effectiveness of full coverage effusion cooling schemes on full turbine blade geometries was tested but with limited success. The introduction of large numbers of large holes across the entirety of the blade surface resulted in a significant flow migration towards the latter portion of the suction surface due to the high pressure gradient across the blade. Combined with the effects of secondary flows, this resulted in very low effectiveness on the pressure surface. Reducing the pitch and increasing the number of holes was seen to noticeably improve the external film effectiveness, though large mass coolant fractions of above 4% were required.

Several studies have demonstrated the film effectiveness of arrays of more tightly packed holes and porous media, albeit on flat plates. In a study by Murray et al.[4] the effect of hole pitch of effusion cooled plates demonstrated that the for a given coolant output per unit area, reducing the pitch between coolant holes greatly improved the average film effectiveness of the studied plate. Reducing the pitch to hole diameter ratio from 5.75 to 3 more than doubled the effectiveness. When compared to results by

Ling et al. [5] in which higher pitch to diameter ratios were used, the improvement in film effectiveness from a pitch of 10d to 3d was almost seven fold for the same non dimensional mass flow. CFD modeling of the same domain remains a challenge though with so many interactions between closely spaced films proving difficult to predict. With each additional film row, divergence from experimental data as well as computing time was greatly increased. While simplified analytical approaches such as the one suggested by Sellers [6] can greatly reduce computing time, accuracy remains a challenge, leaving experimental data as the most reliable approach.

In another flat plate study by Huang et al. [7] the metal effectiveness of perforated plates was compared to that of sintered porous media in a low speed wind tunnel. Here, it was shown that while perforated plates with higher porosities performed better those with lower porosities, the sintered plates did not have a noticeable improvement in performance despite being almost twice as porous. This suggests that downsizing cooling features is only beneficial up to a point, at which the individual cooling jets become smaller than the boundary layer characteristic length.

While flat plate studies provide a level of insight into the behavior of transpired coolant flows, the nature of the flow around a turbine blade can lead to significant divergence from flat plate studies, particularly in the case of low blowing ratios. Schwarz et al. [8] examined the effect of the curvature to film hole size ratio 2r/d on film effectiveness by studying high speed flows around a cylindrical section. It was observed that for highly convex surfaces at low film momentum ratios of 0.5, the measured film effectiveness was over twice as high as that measured on a flat plate and this increase was closely correlated to the 2r/d ratio.

The adverse effect of curvature on film effectiveness was found to be true on concave surfaces. El-Hady & Verma [9] argue that this is due to additional secondary flows, namely Taylor-Gortler vortices, which have a significant effect on the boundary layer stability and film effectiveness of concave surfaces, due to an increase in film to mainstream mixing.

Winka et al. [10] took the study of convex surfaces further and examined how the non uniform curvature of an airfoil affected film effectiveness. By comparing several different combinations of hole location and size, it was possible to deduce that the local curvature r, local curvature ratio 2r/d and

curvature of the entire downstream region play a significant role in the film to mainstream mixing. In this study, a momentum ratio of 0.2 was measured to be the most effective for convex surfaces.

Another effect not considered by either of these studies is the effect of acceleration on the boundary layer. Vinton & Wright [11] subjected films to favorable pressure gradients resulting in a reduction in the boundary layer thickness, forcing the film core closer to the test surface and leading to improved film effectiveness.

3.1.3. Experimental Facility

Experiments were conducted at the Oxford Thermofluids Institute of The University of Oxford. A detailed description of the test apparatus and its operating conditions can be found in the work by Nget-ich [3]. The airfoil profile used was a scaled up midsection profile of a high pressure turbine blade. The walls of the cascade are made of thick Perspex for optical access and were designed to acheive the periodic boundary conditions defined by the midpitch streamline in the engine. The facility was de-signed to match engine Reynolds numbers, as well as match the Mach number distribution predicted by a CFD infinite cascade simulation. The mainstream mass flow rate was calculated to be 1.43 kg/s.

The test pieces were painted with PSP and monitored using three high resolution CCD cameras. Each being positioned so that their overlapping fields of view could be stitched into a single image covering the entirety of the blade surface. The data capture, processing and uncertainty measurements were carried out as described by Gurram et al. [12].

3.1.4. Blade geometry and test regime

The test pieces were fabricated in house by 3D additive manufacturing techniques. The interior of the blades were completely hollow and void of any features. The coolant inlet was a large simple cut into the side of the blade. For this experiment, only the middle 60mm of the span was used in order to avoid end wall effects at either end the blade span. The default wall thickness of the blades were kept high, at 5mm in order to reduce strain under aerodynamic loading, but was reduced at the panel location in order to produce representative blade wall thickness.

Each test piece contained a panel formed by a large array of 0.5mm diameter holes spanning an area of 60x18mm. The spanwise pitch was always equal to the streamwise pitch and the holes were always angled at 45 degrees from the surface. The panel was tested at four different locations around the blade, indicated by Figure 3-1. For the second part of the study, the film hole pitch was changed in order to vary the panel porosity. Lastly a final panel was tested with staggered rows. The full description of all geometries can be found in Table 3-1 and a detail of Panel 1 can also be found in Figure 3-1.

The test pieces were fitted with dedicated channels for thermocouples spaced at every 20mm along the surface for PSP calculations as well as with pressure tappings to measure the internal plenum pressure.

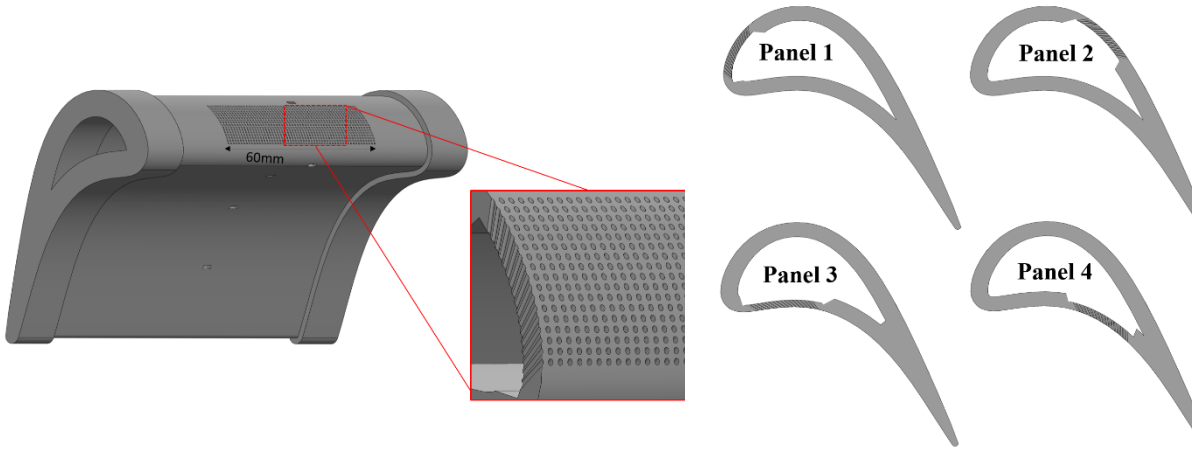


Figure 3-1. (a) Detail of Panel 1 geometry with (b) cross section indicating locations of Panels 1-4

Each geometry was tested at eight different mass flow rates covering the typical range of mass coolant fractions representative of engine designs. The coolant mass flow rates tested were 5, 7.5, 10, 12.5, 15, 17.5, 20 and 25g/s. This equates to a coolant to mainstream mass fraction ranging from 0.58% to 2.91%. Turbine blade cooling requirements can range from 2% to 6% but most modern first stage HP turbine blades now require a cooling fraction of approximately 4.5% [13]. Sensor data and the camera inputs were averaged over a period of 5 seconds for every measurement in order to obtain a time-averaged result.

Table 3-1 **Summary of geometries tested.**

Panel	Surface	Pitch (mm)	d (mm)	Pitch/d	L_h (mm)	L_h/d	Streamwise distance from LE over chord	Approximate Porosity (%)	Hole arrangement
1	SS	1.05	0.5	2.1	3	6	0.1	25	Inline
2	SS	1.05	0.5	2.1	3	6	0.64	25	Inline
3	PS	1.05	0.5	2.1	3	6	0.1	25	Inline
4	PS	1.05	0.5	2.1	3	6	0.33	25	Inline
5	SS	1.20	0.5	2.4	3	6	0.1	20	Inline
6	SS	0.95	0.5	1.8	3	6	0.1	30	Inline
7	SS	1.05	0.5	2.1	3	6	0.1	25	Staggered

3.1.5. Results

3.1.5.1. *Varying Panel Location*

The test pieces were fabricated in house by 3D additive manufacturing techniques. The interior of the blades were completely hollow and void of any features. The coolant inlet was a large simple cut into the side of the blade. For this experiment, only the middle 60mm of the span was used in order to avoid end wall effects at either end the blade span. The default wall thickness of the blades were kept high, at 5mm in order to reduce strain under aerodynamic loading, but was reduced at the panel location in order to produce representative blade wall thickness.

First, the film effectiveness map of Panels 1-4 across four different blowing rates are shown in Figure 3-2 to 3-5 respectively. The charts show the entire width of the blade surface from the start of the panel at x/d=0 down to the trailing edge. The ratio Pr between the coolant and mainstream inlet total pressures is also shown. The plots are arranged so that the coolant is always being fed from the right side of the image.

For all panels at low blowing rates, film distributions are uneven with coolant only being ejected from certain sections of the panels. This is mainly due to the significant external static pressure variation along the streamwise dimension of the panels. This favors flow towards the trailing edge of Panel 1, 2 and 4, and towards the leading edge of Panel 3, where a mild adverse pressure gradient occurs. The low internal pressure results in significant ingestion across the panels. Furthermore, variations in internal static pressure and coolant velocity within the blades lead to uneven spanwise distributions.

As the coolant flow rate is increased, the distribution is first matched in the spanwise direction and as the internal blade pressure is further increased, coolant is observed being ejected by every row.

Due to the high resolution of the PSP, the films of the individual holes can be differentiated from the bulk of the coolant. These individual features mix out within a short distance of the end of the panels. On the other hand, the bulk of the panels form a much more robust sheet film.

At the highest mass flows, Panel 1 demonstrates an almost continuous unbroken film, with the entire region downstream of the panel being of a similar film effectiveness. Once above 5g/s and the entire span of the panel is fed with coolant, increasing the coolant fraction raises the film effectiveness uniformly across the entire area. This is a sharp contrast to Panel 2, where a higher film effectiveness is achieved immediately downstream of the panel but quickly falls off. Increasing the coolant fraction slowly extends the film further downstream, requiring a higher coolant fraction in order to obtain high levels of film effectiveness at the trailing edge.

The difference in films between the two panels can in part be explained by the differences in local mainstream flow. Panel 1, shown in Figure 3-2, is located in a region of high convex curvature and a significant portion of the downstream region is also convex. Furthermore, these films experience a very high favorable pressure gradient near the panel region. These two effects, combined with the low blowing ratio of the individual holes, results in the films remaining very close to the surface of the blade, with minimal decay. Any disturbances created by the small film jets are small enough to be stabilized by the larger dominant behavior of the mainstream flow. The rate of film decay only begins to increase near the trailing edge region where the curvature flattens out and the flow begins to slow down, increasing the boundary layer thickness as well as the turbulent mixing, resulting in a loss of measured film effectiveness. Evidence of this can be seen in both Panels 1 and 2, the films appear to narrow near the trailing edge as the boundary layers of the sides of the rig grow and push the films toward the middle.

As Panel 2 is positioned further back, it can be seen from Figure 3-3 that it does not benefit from the early features of the suction surface. On top of the reversal of the pressure gradient, the Mach number at Panel 2 approaches 0.8 resulting in much more significant film to mainstream interactions within the panel itself.

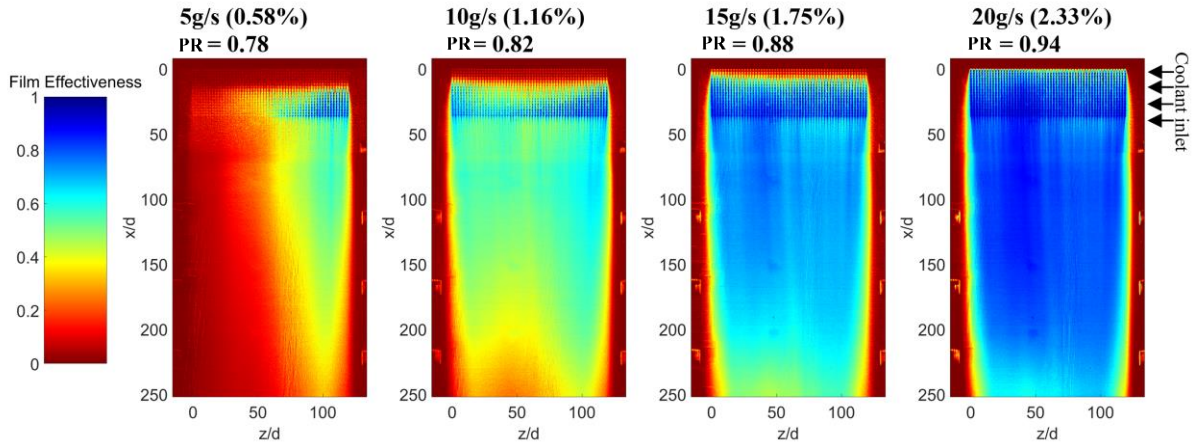


Figure 3-2. Film effectiveness of Panel 1 at different coolant mass flow rates (mass fraction).

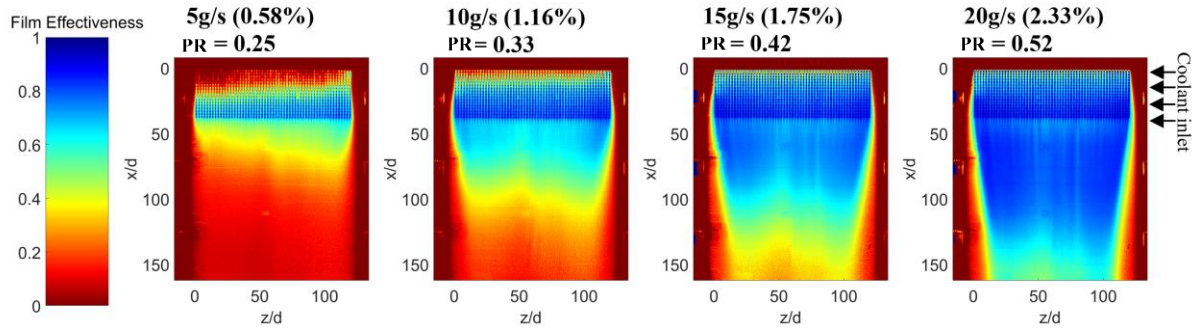


Figure 3-3. Film effectiveness of Panel 2 at different coolant mass flow rates (mass fraction)

The two pressure surface panels share a similar trend and distribution with a few notable differences. Both significantly favor the left side, most likely due to the higher internal static pressure inside this half of the blade, opposite the coolant feed. At higher mass fractions, the films start at very high levels but drastically fall off, particularly in Panel 3. This suggests the films follow a trend similar to the wall jet model, with a section of strong potential core in which the film remains mostly untouched by the mainstream, followed by a region of turbulent mixing, which typically dominates most conventional film behavior.

Figure 3-4 of Panel 3 demonstrates high levels of lateral mixing as the film does not manifest any features reminiscent of the individual holes. In contrast, Figure 3-5 demonstrates that Panel 4 behaves more like the suction surface panels, with definitive streaks being visible, particularly at the higher mass fractions. This behavior is indicative of the high mainstream flow velocity and strong pressure gradient which dominates the flow. Beyond demonstrating a lack in lateral film spreading, the streaks are also indicative that the panels are not entirely successful in pushing the mainstream away from the surface

of the blade as is typically expected in transpiration designs. The square arrangement of holes allows for streams of mainstream air to penetrate through the panels. This is best illustrated in Panel 4 at 15 and 20g/s, where visible wakes of mainstream air can be seen compromising a large portion of the downstream film.

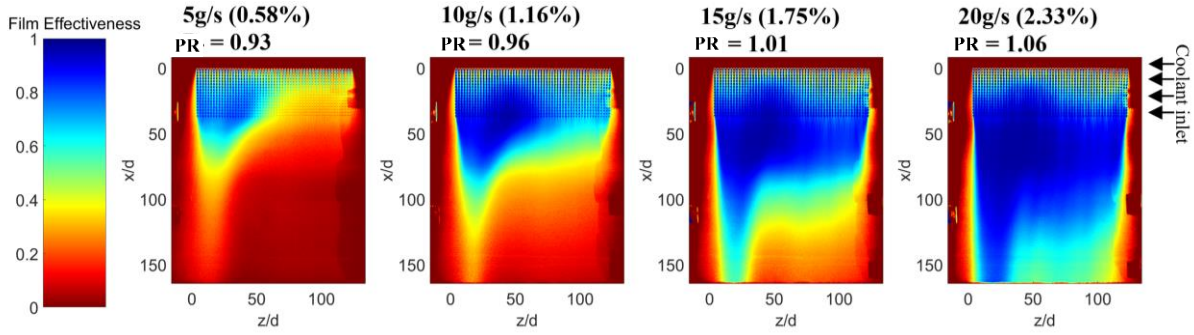


Figure 3-4. Film effectiveness of Panel 3 at different coolant mass flow rates (mass fraction)

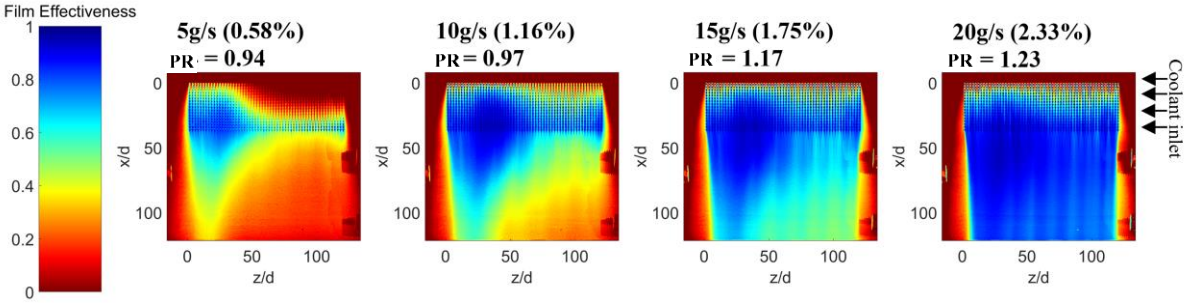


Figure 3-5. Film effectiveness of Panel 4 at different coolant mass flow rates (mass fraction)

Despite these limitations, the overall film effectiveness of all panels remains high for even modest mass flow rates. Once the bulk film is established over the entire span of the panel, a very high average effectiveness is achieved by the spanwise uniformity of the film. This differs from typical film cooling designs that contain hot streaks between film cooling holes, greatly increasing the film to main-stream contact area.

The spatial data can be averaged out laterally, pixel by pixel, in order to obtain a spanwise average of the films as shown by Figure 3-6. The averages are only performed over the 120 z/d midspan of the blade containing the transpiration panel. These plots allow for a greater analysis in the behavior of the films. In these plots the panel location is also indicated by the shaded area.

Immediately downstream of the panels, particularly on the suction surface, film lift off can be observed. While the average blowing ratios of either panel does not exceed 0.3, the rows furthest downstream have a higher blowing ratio and the films require approximately 15d to recover.

When compared to the other panels, Panel 1 undergoes a much lower rate of film decay, to the point at which the film effectiveness at the trailing edge is higher for Panel 1 than for Panel 2 for the same mass flow rates. Naturally, the blowing ratio of Panel 2 is lower than that of Panel 1 due to the higher mainstream velocity, yet the fact remains that the suction surface trailing edge is better served by Panel 1 than Panel 2, suggesting a fundamental difference in the structure and stability of the films.

Panels 3 and 4 follow a similar pattern to Panel 2, with some notable differences. Panel 3 is seen to benefit from a much smaller streamwise pressure gradient resulting in no visible ingestion near the leading edge, even at the lowest blowing rates. Panel 4 is seen to perform better than Panel 3, possibly due to the high positive pressure gradient and larger radius of curvature, minimizing the relative effects of destabilizing secondary flows.

The overall shape of the films is also not typically what is expected, with most analytical models predicting an exponential like decay. The results suggest more of a logarithmic decay, particularly in the case of higher blowing rates with the rate of film decay accelerating, instead of leveling off. One possible explanation is that the individual film rows reattach themselves one by one, rebuilding the film after a short period of film lift off. On the other hand, the strong positive correlation between coolant mass flow rate and film effectiveness across all panels indicates that film lift of is not yet the dominant mechanism at higher mass flows as is often the case for conventional film holes.

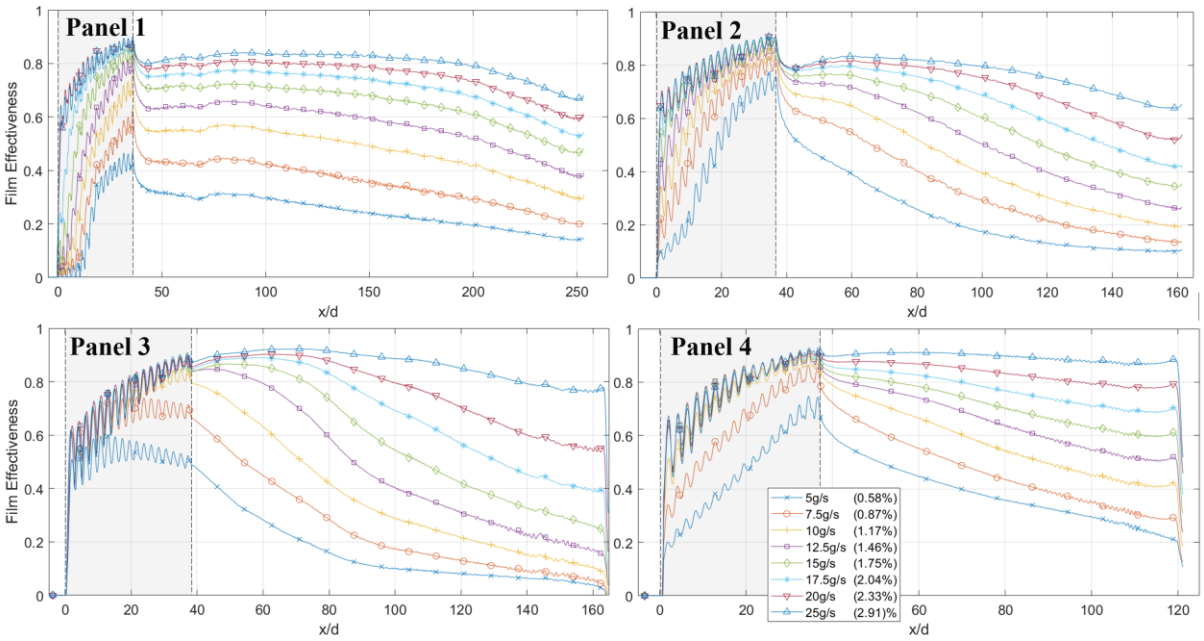


Figure 3-6. Spanwise average film effectiveness of Panels 1, 2, 3 and 4 at different coolant mass flow rates

Another possible reason for the behavior is contained within the tangential injection model for films by Seban and Back [14]. This comparison is not unreasonable given the similarity in performance in flat plate tests between tangential injection and transpiration films as highlighted by Goldstein [15]. According to this model, the films first form a wall jet region in which the films remain intact and only mix with the mainstream flow through diffusion mechanisms. This region is then followed by a region of turbulent boundary layer mixing where film effectiveness is expected to drop off dramatically.

Further justification can be found when considering the secondary flows within the panel films. Conventional films are typically dominated by strong coupled vortex pairs which lift off and then dissipate into the mainstream, as well as allow hot mainstream air to be pulled underneath the film. The quasi 2D behavior of the panel films delays mainstream gas from being pulled in from the sides, resulting in a tangential jet like film effectiveness distribution, particularly when good spanwise distribution is achieved.

3.1.5.2. Varying Panel Configuration

In the second part of the study, different permutations of panel designs were tested in the same location as Panel 1. By changing the hole pitch within the panel, the effective porosity was varied. The effectiveness data of these panels is shown in Figure 3-7 and 3-8.

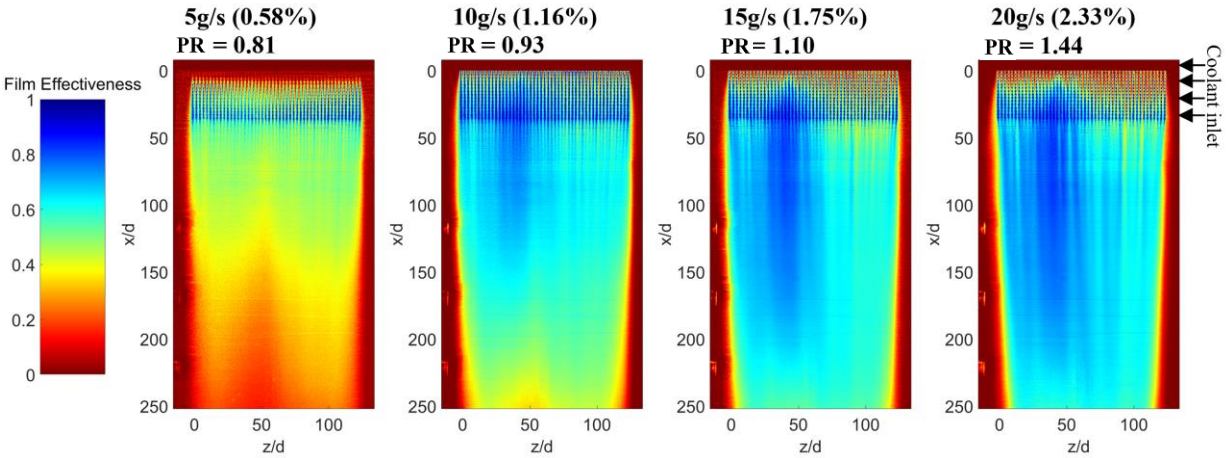


Figure 3-7. Film effectiveness of Panel 5 at different coolant mass flow rates (mass fraction)

Increasing the pitch, as is the case for Panel 5 reduces the number of holes in the panel. This leads to a more uniform film distribution at a coolant mass flow of 5g/s. As coolant mass fraction is increased, the film effectiveness plateaus at a relatively low value. The film is also dominated by significant variations in spanwise effectiveness, which appears as very predominant streaks. With greater spacing in between holes, there is more space for mainstream gas to push its way between the coolant jets and mix with the coolant. This effect is magnified as more coolant is added, with the right side of the panel performing worse at 15 and 20g/s than at 10g/s, with defined lines of film effectiveness below 0.4 visible.

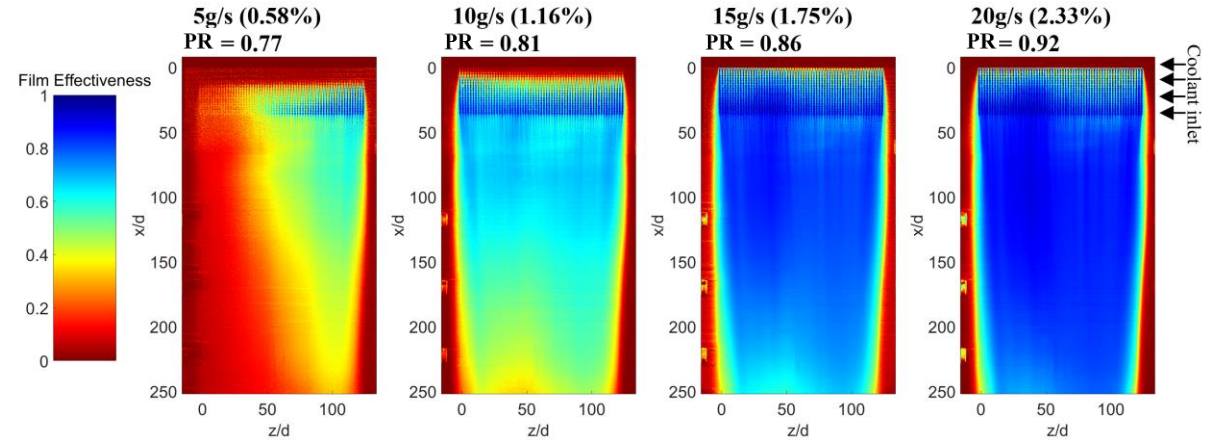


Figure 3-8 Film effectiveness of Panel 6 at different coolant mass flow rates (mass fraction)

Reducing the hole pitches has the opposite effect, with Panel 6 reaching a higher maximum film effectiveness than Panel 1. It is worth noting that the improvement of Panel 6 over Panel 1, is much less

than that of Panel 1 over Panel 5, indicating diminishing returns as the porosity is increased and the near wall boundary layer becomes saturated with coolant.

The final panel tested was Panel 7, and is shown in Figure 3-9. Here the pitch was kept the same as Panel 1 but every other row was shifted by half a pitch. Here the film effectiveness rate was measured to be highest across all panels, despite having the same number of holes and blowing ratio as Panel 1. Here the effect of individual holes can no longer be discriminated and the film appears much more uniform, as there is no path for the mainstream gas to push through the panel. Higher film effectiveness values are also achieved in between the holes of the panel, with the downstream region of the panel essentially obscured from view and saturated at the higher mass fractions. The significant improvement of Panel 7 over the others can also be attributed to the fact that the films are interacting more constructively. With the streamwise pitch essentially doubled, the film jets do not push each other off the surface as is the case with the non-staggered arrangement.

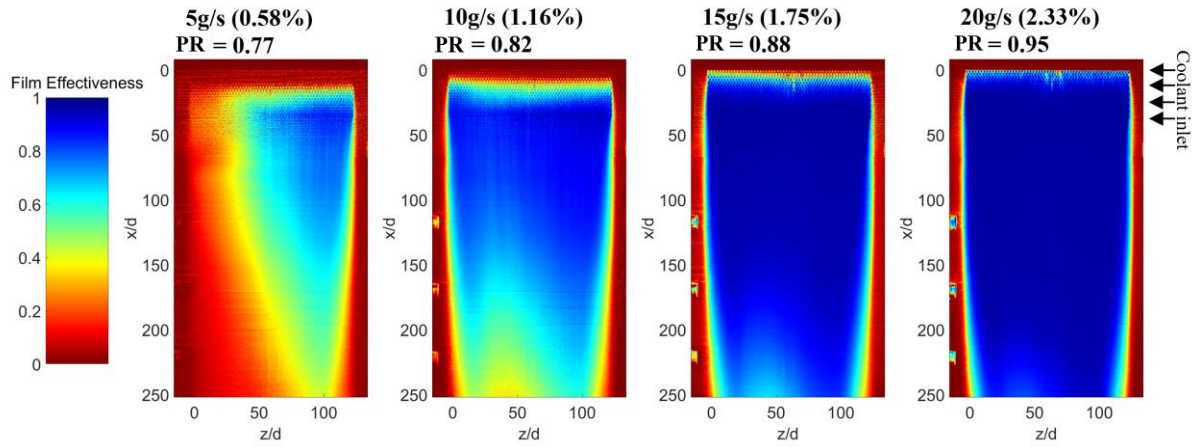


Figure 3-9 Film effectiveness of Panel 7 at different coolant mass flow rates (mass fraction)

Figure 3-10 compares the film effectiveness of these panels at x/d = 75 against the calculated average blowing ratio of each panel.

A clear correlation between pitch and film effectiveness can be observed. While Panel 5 has a higher film effectiveness than Panel 1 at mean blowing ratios below 0.1 due to a better spanwise distribution, the maximum film effectiveness achieved does not exceed 0.65.

The effectiveness of all panels is observed to level off at a mean blowing ratio of approximately 0.2. This is significantly lower to most conventional film geometries, which tend to reach maximum

effectiveness at a blowing of about 0.8. Additionally, this effectiveness does not drop back down as blowing ratio continues to increase indicating that overall, film lift off does not yet dominate the coolant flow.

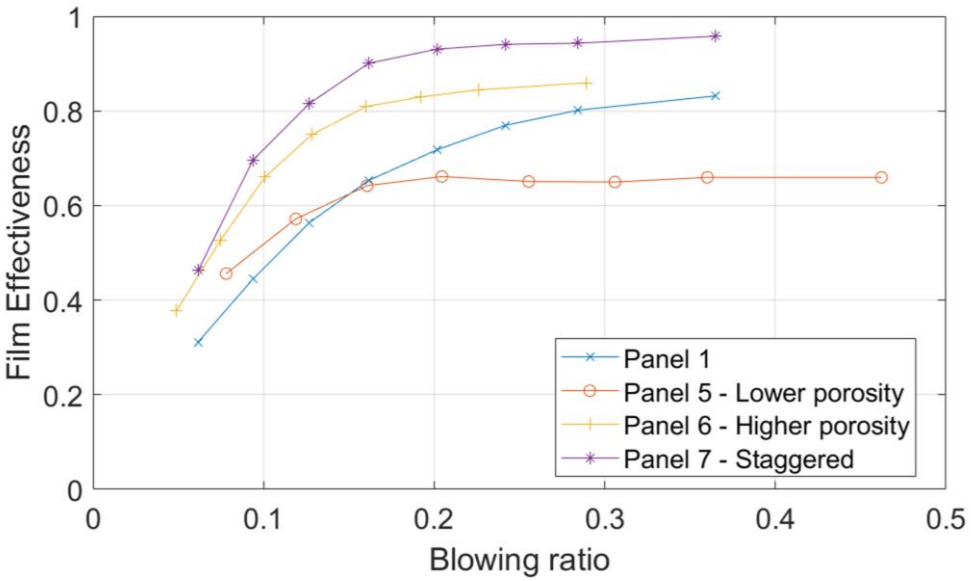


Figure 3-10. Film effectiveness of Panels 1, 5, 6 and 7 at x/d=75 at different average blowing ratios

While not necessarily lifting off, it still can be assumed that the films have reached a saturation point at higher mass flows and that additional coolant would not lead to an improvement in film effectiveness. Therefore the discriminating factor between Panels 1,5,6 and 7, is not the ability to add coolant to the boundary layer, but the ability to push the mainstream off of the blade surface. In conventional film theory, this would be equivalent to reducing the mass fraction of mainstream gas within the near wall boundary layer at the end of the panel.

The consequence of this is that instead of diluting the entrained hot air in the boundary layer with ever increasing mass flows of coolant, a high coolant to mainstream ratio can be achieved with much lower mass flows.

When comparing all of the different Panels at a mass flow for which the film is fully developed, further similarities and differences can be established. As shown by Figure 3-11, all inline Panels with pitch to diameter ratios of 2.1 share approximately the same film effectiveness at x/d =40. At this stage the film effectiveness is dominated by the Panels ability to add coolant to the boundary layer and fend off the mainstream gas. Once past this point, behavior becomes dominated by the particularities of the

local mainstream flow such as the rate of boundary layer mixing and mainstream turbulence, with the film cooling geometry having only a minor effect due to the very low blowing ratios used. This is best exemplified by the near parallel behavior of Panels 1 and 5-7, showing that each is affected by the mainstream flow equally.

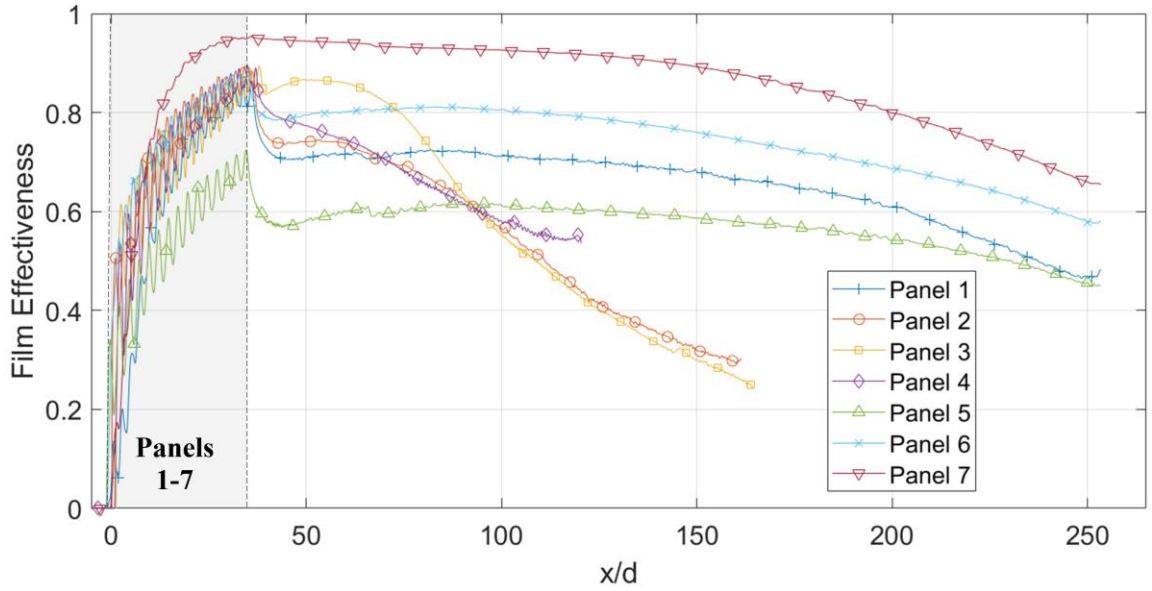


Figure 3-11. Spanwise average of all Panels at 15g/s (1.75%)

3.1.6. Conclusions

Very high cooling effectiveness was achieved around the entire blade at very low mass coolant fractions. Films perform particularly well on the early suction surface, which benefits from the effects of curvature and acceleration, resulting in very constant film coverage downstream of the panel. The ability to cool the entire suction side of the blade almost uniformly with a modest coolant fraction is a significant achievement which could warrant diverting additional coolant and attention to this area. While performance on the pressure surface is more modest, particularly around Panel 3, large regions of high film effectiveness were still attained. Divergence from conventional film hole cooling models also implicates that the behavior of a large array of small holes cannot be simply extrapolated from single hole studies. Comparisons between different pitches and hole arrangements confirmed that minimizing the spacing between holes can greatly improve the film effectiveness and suggest that both interactions between individual films and the influence on the mainstream may have a significant impact on film performance. However, it has also been established that the nature of the mainstream flow

around a turbine still dominates film cooling behavior once beyond the immediate region of the cooling geometry, particularly on the pressure surface.

The relative simplicity of the designs used leads to a hopeful assumption that transpiration inspired cooling features are not as remote a concept as previously imagined, though practicalities of implementing transpiration cooling will remain a challenge with issues such as uniform distribution and ingestion still to be solved. Nonetheless, a clear demonstration of its potential has been achieved.

Author Contributions: Conceptualization, Augustin Wambersie and Peter Ireland; methodology, Holt Wong.; investigation, Augustin Wambersie and Holt Wong.; writing—original draft preparation, Augustin Wambersie.; writing—review and editing, Peter Ireland and Ignacio Mayo.; supervision, Peter Ireland and Ignacio Mayo; All authors have read and agreed to the published version of the manuscript."

Funding: This work is supported by Rolls Royce plc. and the Transpiration Cooling Systems for Jet Engine Turbines and Hypersonic Flight Programme Grant (EP/P000878/1).

Acknowledgments: The authors wish to thank the technicians at the Oxford Thermofluids Institute for their contributions in running experiments, as well as Peter Walters for his contributions in improving the additive manufacturing process

Conflicts of Interest: Rolls-Royce PLC as the funding sponsor provided input to the general scope of interest in the study and the decision to publish the results. They had no direct role in the collection, analyses or interpretation

3.2. Further Parametric Experimental Study of High Porosity Film Cooling Features on Turbine Blade Geometries

A. Wambersie – P.T. Ireland

Department of Engineering Science, University of Oxford
Oxford OX1 3PJ, UK
Email: augustin.wambersie@eng.ox.ac.uk

Abstract

High porosity arrays of film cooling holes have recently shown promise as a means to improving turbine blade film cooling effectiveness. The complexity of the flow field means that relatively little is known about which parameters are most influential in determining porous panel performance. This paper examines a range of geometries to gain a better understanding of the effects of high porosity film cooling features. Blowing ratio, hole diameter, panel array length and hole angles are varied to examine the sensitivity to such parameters. Experiments are carried out using Pressure Sensitive Paint within a highspeed linear cascade at engine representative conditions. Results indicate that significant improvements in film effectiveness can be achieved by developing geometries that incorporate low blowing ratios and small hole diameters. Injection angles were measured to be less significant with all angles still achieving impressive film effectiveness levels above 90% over significant regions of the blade surface.

Keywords: Film Effectiveness, PSP, Transpiration cooling, High porosity

Nomenclature

A	Area (m^2)	W_c	Coolant mass fraction
d	Film hole diameter (m)	α	Streamwise hole angle (˚)
$\dot{m}_c$	Coolant mass flow (kg/s)	β	Spanwise hole angle (˚)
M	Blowing ratio	ρ	Density (kg/m^3)
PR	Pressure Ratio	SS	Suction surface
u	Velocity (m/s)	PS	Pressure surface
x	Streamwise distance (m)	LE	Leading Edge
z	spanwise distance (m)		

3.2.1. Introduction

Earlier experiments of high porosity film cooling features on turbine blades with engine representative flows have demonstrated a potential for unparalleled levels of adiabatic film effectiveness (Wambersie, et al., 2021). However, due to the novelty of this approach and the scarcity

of existing data, further investigation into the mechanisms behind the success of this approach is required.

The cooling geometries tested by Wambersie, inspired by the predominantly theoretical concept of transpiration cooling, feature a large number of tightly packed film cooling holes operating at low blowing ratios (BR). Both hole diameters and pitches are kept very small, with diameters below approximately 0.25mm at engine scale. The resultant spacing between holes results in both very even spanwise distributions as well as a significant level of interactions between the flow ejected from separate holes. The geometric staggering of film holes was seen to further reduce film separation and maximize film performance when compared to inline geometries.

As CFD studies of these types of geometry have yet to be successful in accurately modelling film effectiveness levels, further experiments for these geometries remain a requirement to enable them to be considered for real applications.

Limited research, experimental or numerical has been carried out on these cooling features on aerofoil geometries or in engine representative flows. However, an extensive number of parametric flat plate, adiabatic film cooling studies on effusion systems exist. The latter cover a wide range of pitch to diameter ratios from 19-14 (Natsui, et al., 2012) to 13-6 (Mayle & Camarata, 1975) and 3 (Cho & Goldstein, 1997) amongst many others. The predominant trends indicate that reducing the pitch to diameter ratio results in an improved film effectiveness. By varying the spanwise and streamwise pitch independently, Courtis (2021) further demonstrated the spanwise pitch was particularly influential, with the streamwise pitch to diameter ratio becoming less important if not detrimental below values of 2. Comparisons between large (Ngetich, 2019) and aforementioned small, pitch to diameter ratios on aerofoil geometries also demonstrate the benefit of a localized region of high porosity cooling features as opposed to a full coverage film cooling. This is due to a combination of reduced film lift off as well as the practical necessity with regards to managing coolant to free stream pressure ratios around an aerofoil

geometry. In other words, a single plenum can only extend so far around the aerofoil to feed multiple rows if the coolant can only differ from the free stream by a small amount.

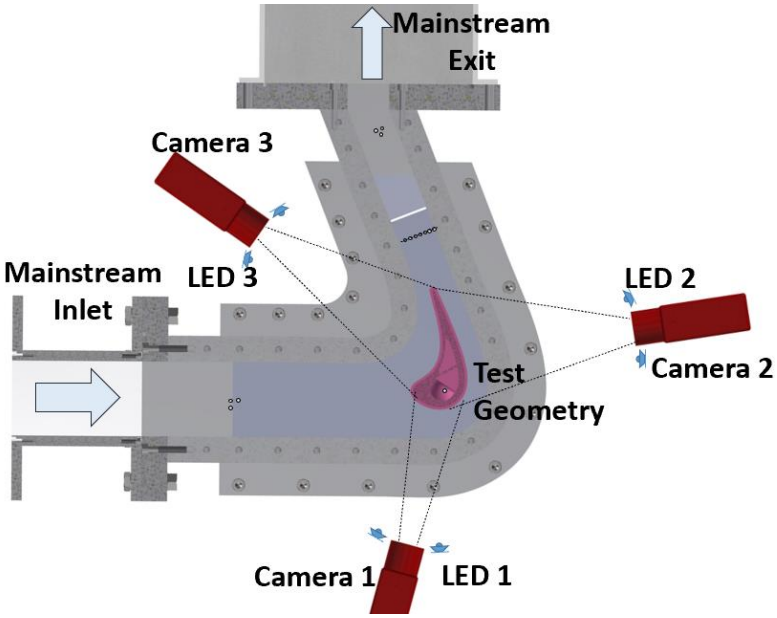


Figure 3-12 Schematic of experimental test section

In the present study, the pitch to diameter ratio of all geometries is kept at 2.1:1. This places it close to, if not at the very bottom of the range for all flat plate effusion cooling studies. The pitch is equal in both the streamwise and spanwise direction, primarily for the purposes of minimizing the streamwise pressure variation across a single cooling feature.

Similarly, a range of studies have been carried out on the effect of injection angle. Reducing the angle between the mainstream and film hole is seen to have a positive effect on both the film cooling, by improving film attachment, as well as on internal cooling by increasing the hole length (Crawford, et al., 1980) (Natsui, et al., 2017). However, it was noted by Andrews (1995) that the effect of reducing the streamwise injection angle would become more limited as the pitch to diameter ratio was decreased. The effect of spanwise injection angle was seen to be detrimental in effusion cooling studies, despite individual film holes benefiting from this effect, at least in the region immediately downstream of the hole (Schmidt, et al., 1996).

When considering the effect of hole size, previous studies do not usually account for variations in porosity and changes in hole size which often also affect the blowing ratio at a given mass flow

(Andrews, et al., 1985). Nonetheless, it has been demonstrated that multiple small holes perform better than individual large film holes (Sohn, 2019) due to the reduction in jet penetration into the mainstream and reduced mixing induced into the boundary layer.

3.2.2. Method

The test facility is a high-speed, low temperature single blade passage, first designed and built by Gurram et. al. (2016). The facility is designed around the mid-pitch streamlines of a modern high pressure turbine blade, and includes Perspex walls to allow full optical access to the blade surface. The facility was designed to simulate engine representative Mach numbers and Reynolds numbers at 2.3 times engine scale. Further details on the facility can be found in Wambersie, Ireland, & Mayo (2021) and is illustrated by Figure 3-12. Pressure sensitive paint was used due to its reliability and high spatial resolution. Gregory et. al. (2008) provides a detailed description of PSP with the implementation of PSP for film effectiveness measurements detailed by Han et al. (2010). This method was chosen due to its accuracy

The static pressure distribution and isentropic Mach number around the blade surface are given presented in Figure 3-13. A close agreement between predicted and measured values is achieved, with the greatest discrepancy occurring on the faster moving suction surface, where boundary layer drag from the rig wall result in slower mainstream flows than expected.

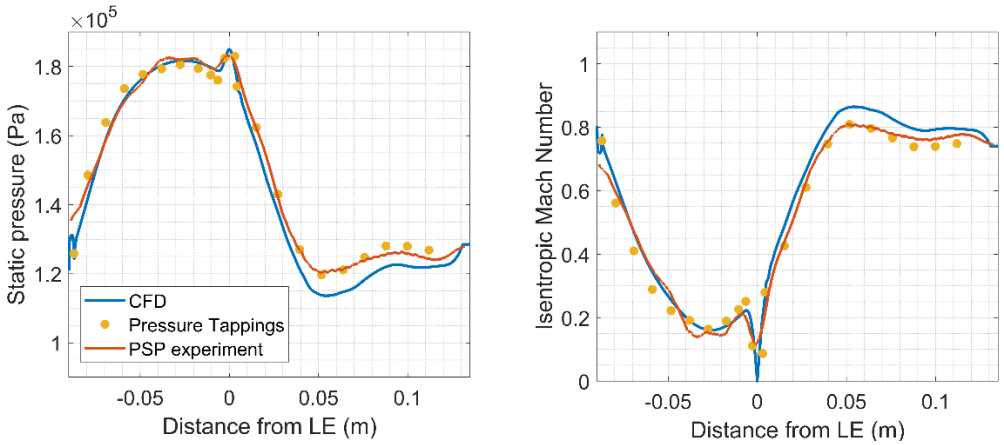


Figure 3-13 Predicted and measured pressure distribution on test section

3.2.2.1. CALCULATION OF BLOWING RATIOS

In order to compare the blowing ratios between geometries, the mean blowing ratio for each panel was calculated. By measuring the static pressure distribution on the surface of the blade and calculating the isentropic Mach number, the mean mainstream velocity and density on the blade surface at the panel location could be measured. Determining the numerator of Equation 1as achieved by dividing the overall hole area by the overall coolant mass flow, measured using an orifice plate as defined by defined by ISO 5167-3 (2020). Whilst it is acknowledged that the blowing ratio of individual holes might vary significantly within a panel, the mean BR allows for comparison between panels and is given by Equation 3-1.

$$M = \frac{\rho_c u_c}{\rho_m u_m} = \frac{\dot{m}_c / A}{\rho_m u_m} \qquad \textbf{3-1}$$

3.2.2.2. UNCERTAINTY ANALYSIS

In order to determine the uncertainty of the different experimental methods, the perturbation method of Moffat (1988) was used. For the orifice plate mass flow calculation, the overall uncertainty measurement of the arrangement due to all of the measurement uncertainties totaled 1.75%.

In order to quantify uncertainty in film effectiveness values, the uncertainty in the measured light intensity is estimated using the standard deviation in intensity ratio across all relevant pixels at nominal values using a calibration rig. As the relationship in between film effectiveness and light intensity is exponential, the uncertainty in film effectiveness varies significantly across the range of the experiment, as indicated by Figure 3-14.

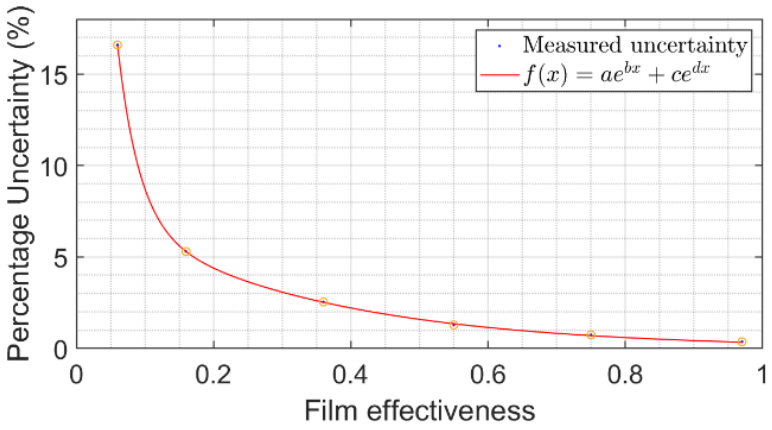


Figure 3-14 PSP error distribution

3.2.3. Geometries

The test pieces were manufactured from high strength polycarbonate-like plastic called VisiJet M2R-TN using a 3D Systems ProJet MJP 2500 additive manufacturing machine with a print resolution of approximately 30 microns (3D Systems, 2020), allowing for very small film cooling features to be accurately manufactured. In order to mitigate potential hole blockage during either manufacturing or PSP application, the holes were subsequently reamed before testing in order to ensure proper hole diameter.

The geometries are grouped into four separate series in Table 3-2. The first series was included in order to examine the effect of blowing ratio and number of rows on both the pressure and suction surface. In the second series, the effect of hole diameter is examined on both aerofoil surfaces with diameters of 0.35mm, 0.75mm and 0.95mm tested in addition to the previous diameter of 0.5mm. This range was selected to encompass values both above and below existing manufacturing capabilities for real engine parts. The combination of number of film rows and hole diameters was selected in order to maintain blowing ratios across geometries of different film hole diameters. The local surface porosity of these geometries within the arrays, defined as the portion of external blade surface occupied by film holes within the panel area, is calculated to be 25%. Finally, the streamwise and spanwise injection angles are examined on the suction surface in the last two series, with stream wise and spanwise angles defined in Figure 3-15c.

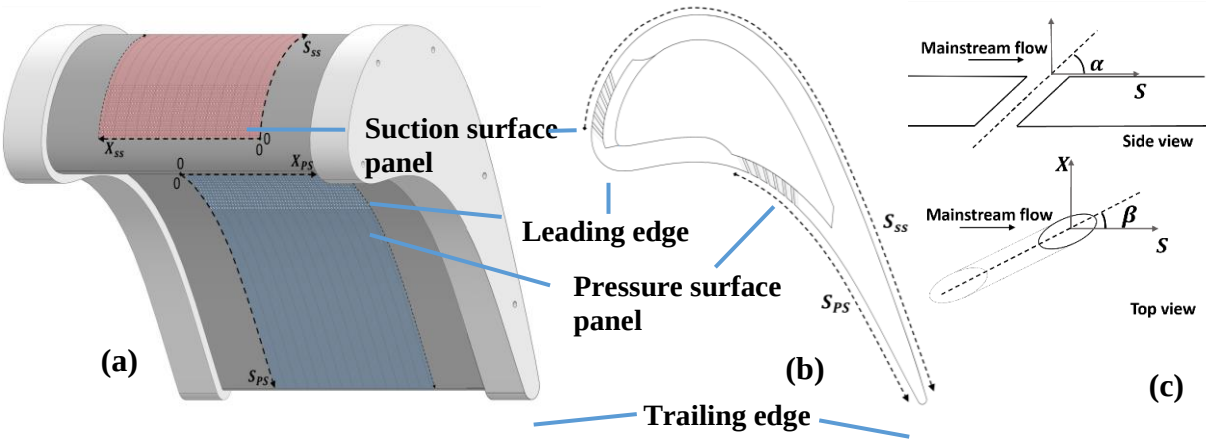


Figure 3-15 (a) Schematic of test pieces with relevant coordinate system (b) cross section of test section illustrating both PS and SS panels (c) definition of α and β angles

Locations of the panels are shown in Figure 3-15a, were maintained constant from previous experiments, with SS panels positioned at 7.5mm from the LE and PS panels kept at 25mm from the LE. This panel location was chosen as was seen to result in the highest levels of film effectiveness.

Configuration	P/D	Number of rows	D (mm)	α (°)	β (°)	Aerofoil Surface	Total normal hole area $\sum \pi r^2$ (mm^2)
SS3 ROW	2.1	3	0.5	45	0	SS	33.6
SS7 ROW	2.1	7	0.5	45	0	SS	78.3
SS12 ROW	2.1	12	0.5	45	0	SS	134
SS17 ROW	2.1	17	0.5	45	0	SS	190
PS5 ROW	2.1	5	0.5	45	0	PS	55
PS9 ROW	2.1	9	0.5	45	0	PS	100
PS13 ROW	2.1	13	0.5	45	0	PS	150
PS17 ROW	2.1	17	0.5	45	0	PS	190
SS035D	2.1	24	0.35	45	0	SS	188
SS075D	2.1	11	0.75	45	0	SS	189
SS095D	2.1	9	0.95	45	0	SS	191
PS035D	2.1	19	0.35	45	0	PS	149
PS075D	2.1	9	0.75	45	0	PS	151
PS095D	2.1	7	0.95	45	0	PS	149
SSa35	2.1	17	0.5	35	0	SS	190
SSa60	2.1	17	0.5	60	0	SS	190
SSa90	2.1	17	0.5	90	0	SS	190
SSb15	2.1	17	0.5	45	15	SS	190
SSb30	2.1	17	0.5	45	30	SS	190
SSb45	2.1	17	0.5	45	45	SS	190

Table 3-2 Definition of geometries

3.2.4. Results- Effect of Blowing ratio

In order to isolate the effects of mass flow from blowing ratio, the first set of geometries varies the cumulative hole area of the film hole array. This was achieved by changing the number of rows. While this would also impact the number of interactions between different holes, the panels remain large homogeneous features with repeating and identical local geometries.

The number of film rows were chosen in order to cover an appropriate range of blowing ratios, from 0.1 to 1.5 on the suction surface and from 0.2 to 2.7 on the pressure surface with the higher blowing ratio on latter being a natural consequence of much slower mainstream velocities in this region.

3.2.4.1. Suction Surface panel experiments

For the suction surface series SS3ROW to SS17ROW, panels containing 3, 7, 12 and 17 staggered rows were tested and the results are given in Figure 3-16. The mass flow was limited to 12.5g/s in

SSROW3 order to avoid over pressurizing the test piece. Several trends can be identified when comparing the results from different geometries. Firstly, the maximum film effectiveness is seen to occur at higher mass flow rates from the larger panels. SSROW3 reaches its peak film effectiveness at 7.5g/s, with SSROW7 achieving its maximum at approximately double the mass flow. Both larger panels perform best at maximum mass flow rates.

The effective saturation of film effectiveness achieved by the larger three panels is also significant in that the mainstream appears to have been completely pushed away from the blade surface with practically no mainstream gas being able to penetrate through the film from the cooling panel.

The leveling off and reduction of effectiveness with massflow for the two smaller panels is indicative of film lift off. However, as the film effectiveness does not drop off significantly as expected from single rows of films, this implies that the interactions between films prevent the coolant from detaching from the aerofoil.

The high resolution of the PSP highlights the lift off and interactions of the individual film holes at blowing ratios exceeding 0.6 at the leading edge of the panel. The first two rows are always seen to lift off completely. However, at the beginning of the third row, the films are seen to reattach resulting in a very significant and almost discrete step in film cooling across the entire panel span. The remarkable uniformity and sharpness of this distribution indicates the importance of the spacing and interactions between rows. This observation, coupled with the lack of complete lift off, confirms observations made previously in literature that a second row of staggered film holes can reattach films from the first row due to interactions between the vortex structures (Jiang, et al., 2017).

The development of discernable streaks resulting in variations effectiveness across the span is also noticeable at higher blowing ratios. These streaks demonstrate instabilities caused by the increase in blowing ratio at or above 0.6. These irregular localized regions of lift off suggest local non uniformities within the panel. The overall width of the film is also seen to narrow towards the trailing edge, indicating greater decay near the lateral edges either due to vortices or increased turbulence.

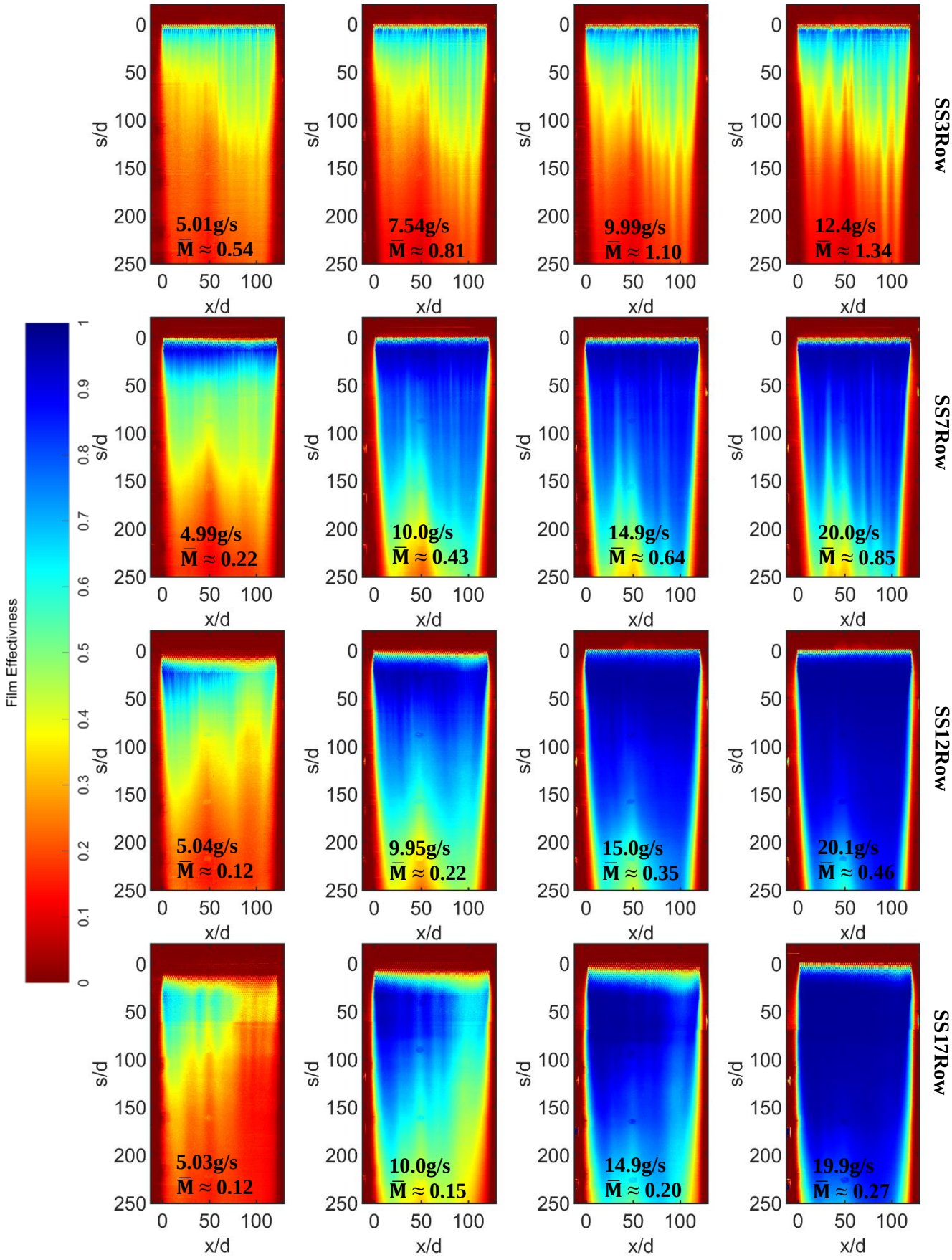


Figure 3-16 Film effectiveness plot for different SS XROW geometries

For the larger panels at lower blowing ratios, the coolant can be seen to favor the left hand side of the charts. This is due to coolant feed mechanism of the blade which supplies coolant from the left side of the blade on the graph. As significant ingestion occurs within the first few rows of the blade, coolant concentrations within the blade plenum are expected to be higher close to the feed inlet. However, at higher mass flow rates and BRs, the variation spanwise film effectiveness is reduced as ingestion in avoided. These panels are then able to saturate the film by the panel edge. Increasing the coolant mass flow has the effect of extending this saturation region further downstream.

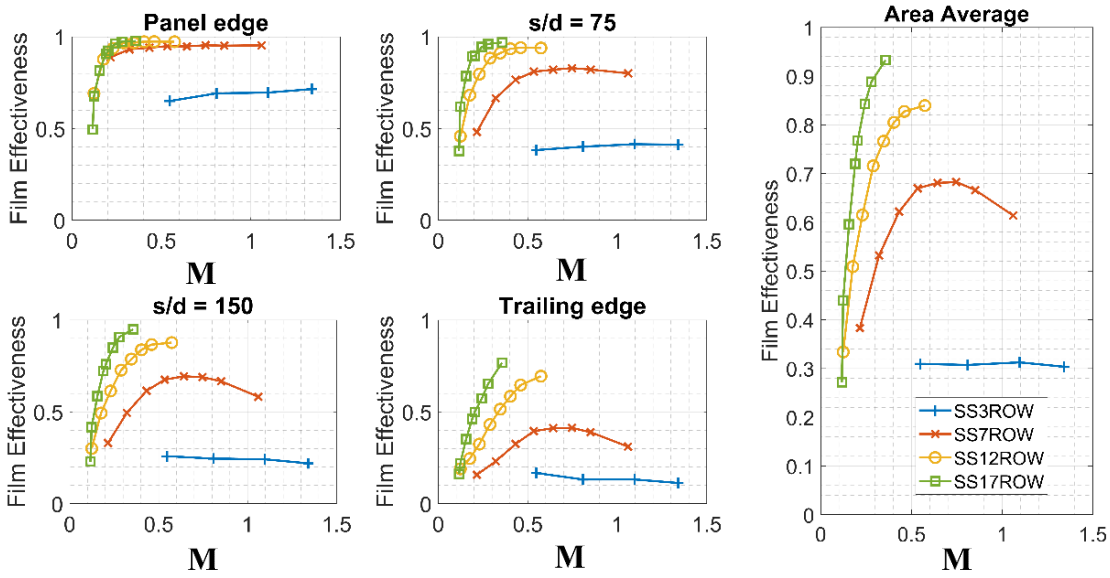


Figure 3-17 Spanwise average film effectiveness against BR at different streamwise locations for SSXROW geometries

Figure 3-17 shows the spanwise average effectiveness measured at four different streamwise locations: the downstream edge of the panel, the trailing edge, and two intermediate locations x/d = 75 and x/d = 150. The area average is also calculated by averaging the region within the span of the panel, between the LE row of holes and the trailing edge.

With the exception of the 3 row panel, all of the geometries reach the same maximum effectiveness value of about 0.95 at the panel edge. This demonstrates the importance of exceeding a minimum number of rows in saturating the film and pushing the mainstream away from the blade.

The spanwise plots at intermediate locations and area averaged plot suggest that the optimal blowing ratio for each geometry lies between 0.6 and 0.8.

Plotting the same results against coolant mass flow in Figure 3-18 indicates that TE film effectiveness exhibits a near linear relationship between mass flow and film effectiveness below a BR of 0.5. Above the latter value the film effectiveness begins to drop off, indicating an increase in mixing as a consequence of film liftoff and jet penetration into the mainstream. This cut off aligns well with reports in the literature suggesting range of the mass addition regime, as defined by Baldauf et al. (1997). Above this point, increasing BR leads to greater mixing between the coolant and mainstream gases.

Figure 3-19 contains a contour plot combining the results for effectiveness at different mass flow rates and blowing ratios for all the suction surface geometries. Mass flow is given as a percentage of the overall mainstream flow. These plots are useful for the purposes of design and optimization allowing a straightforward interpretation of the different effects of both blowing ratio and total coolant mass flow. The design solution that maximizes effectiveness for minimum coolant mass fraction can be identified.

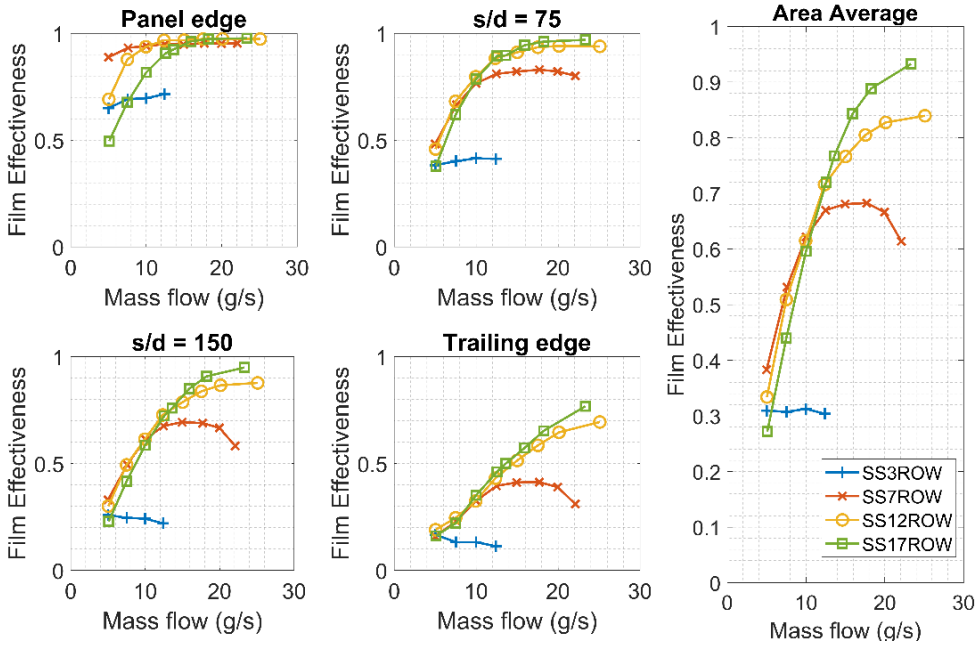


Figure 3-18 Spanwise average film effectiveness against mass flow at different streamwise locations for SSXROW geometries

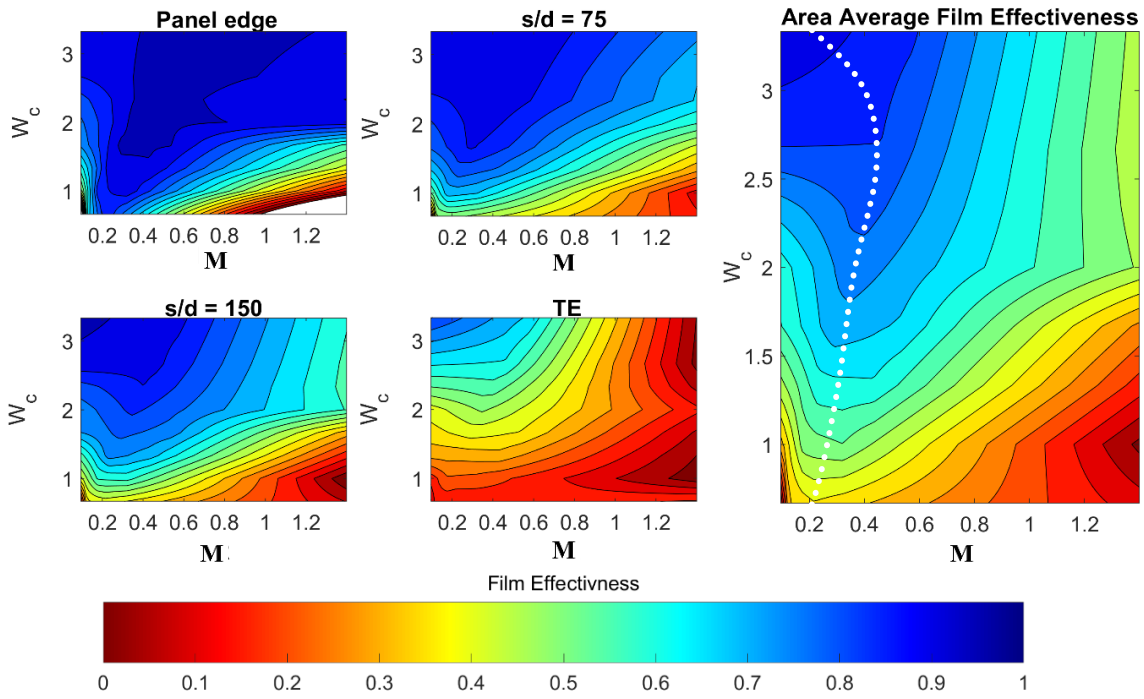


Figure 3-19 Contour plot of film effectiveness for different mass flows and BRs

Overall, the charts show that decreasing blowing ratio and increasing mass flow lead to increased film effectiveness. However, when blowing ratios are below 0.2, ingestion and spanwise maldistribution are significant and reduce the film effectiveness, particularly close to the panel. The optimal blowing ratio to maximize effectiveness for any given mass flow is highlighted by the white dotted line which runs along the ridge of the contour plot in the rightmost chart. The pronounced ridge indicates a clear benefit of operating at the correct blowing ratio, which for these geometries is between 0.2 and 0.4, well within the mass addition regime.

It is worth noting that this BR corresponds with the film effectiveness plots in Figure 3-16 that have both uniform coolant ejection in the first row, yet do not show any signs of lift off. This corresponds to 7.5-10 g/s for SS7ROW, 15g/s for SS12ROW and 25g/s for SS17ROW.

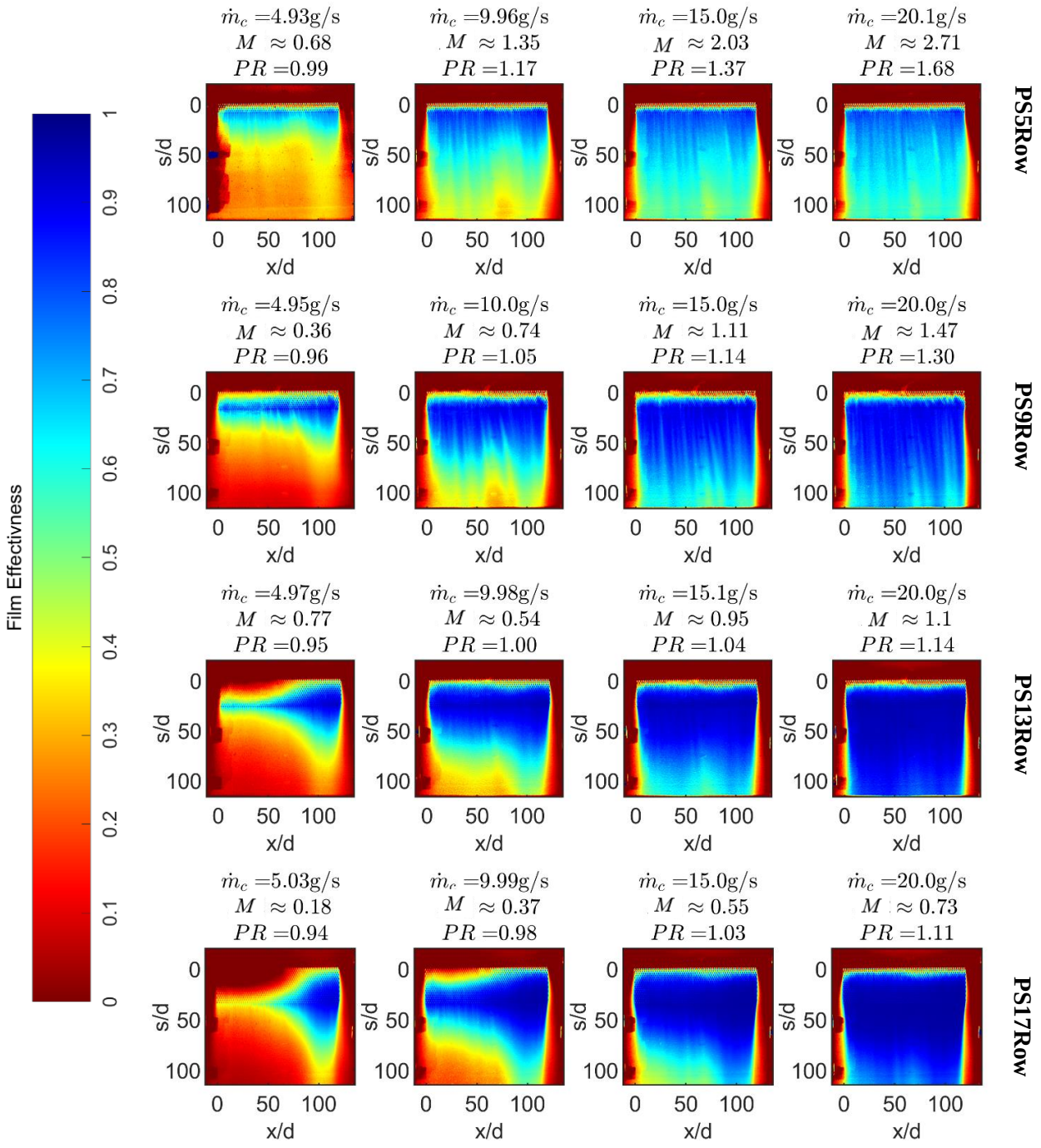


Figure 3-20 Film effectiveness plots for PSXROW geometries

3.2.4.2. Pressure surface panel experiments

On the pressure surface, geometries with 5, 9, 13 and 17 staggered rows were tested and the results are presented in Figure 3-20. Similarly to SS3ROW, PS5ROW is observed to reach a maximum film

effectiveness at moderate mass flows of 12.5g/s whilst maintaining high levels of spanwise uniformity at low mass flow rates.

The maximum film effectiveness levels are observed between 0.8 and 0.9 and the film does not attain levels above ninety percent. This indicates the geometry is not able to fully push the mainstream away from the wall, due to the limited number of film rows. Additionally the reduction in film effectiveness at the highest mass flows suggests that the films begin to lift off and penetrate into the mainstream. However, the films are still seen to remain mostly present despite exceeding BRs of 2, at which point individual rows would have certainly lifted off completely. The interactions between the vortices of different staggered rows allows the bulk of the panel to remain attached far above expected values.

Again, the first 2 to 3 rows of the panel appear to lift off completely before abruptly reattaching around the 3rd row. The local film effectiveness in the early rows is seen to be close to zero in between the holes. This phenomenon is visible for nearly all geometries at BRs above 0.8. The film then reattaches itself downstream of the second or third row.

Non periodic variations in film effectiveness across the span can be observed in the geometries with 5 and 9 rows respectively. Interactions between uneven films due to blockage and manufacturing errors at high BRs are the likely causes of these features. An imbalance between neighboring films would also likely result in more liftoff occurring and a reduction in film cooling.

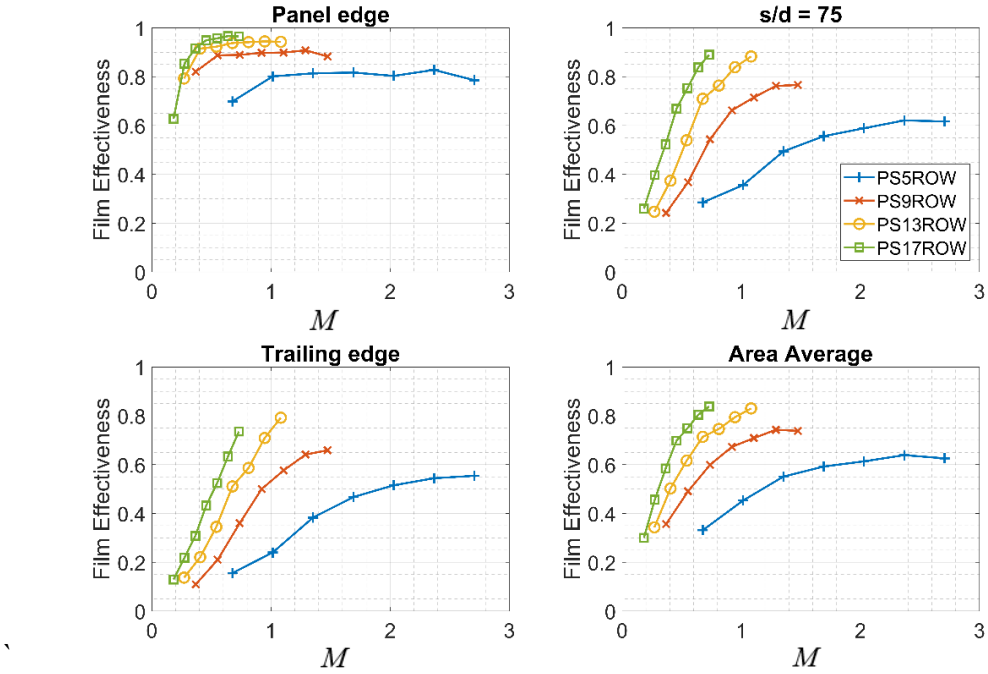


Figure 3-21 Spanwise average film effectiveness against BR at different streamwise locations for PSXROW geometries

Further increasing the number of rows to 13 improves the uniformity by both lowering the BR and saturating the film as a result of a greater number of superimposed films. At mass flows above 10g/s, the data shows the panels achieve film effectiveness levels of very close to unity.

A final observation of the difference between the 12 and 17 row panel results is that while the larger panel achieves a higher film effectiveness level plateau near the panel edge, the smaller panel is able to produce a film which lasts longer and does not decay as much at the TE.

Again, the larger panels at low blowing ratios suffer from significant levels of ingestion, resulting in film higher film effectiveness levels near the coolant inlet, this time on the right hand side of the charts.

Spanwise averaged film effectiveness data is plotted against blowing ratio for the different PS geometries in Figure 3-21. At the panel edge, it can be noted that the larger panels reach higher asymptotic film effectiveness levels than the smaller panels. Each panel reaches its maximum value by a mass flow of 7.5 to 10g/s and this is maintained regardless of how much

more coolant is added. This indicates the importance of the film ejection geometry on effectiveness levels near to the panel edge, with film effectiveness being a strong function of geometry and independent of mass flow.

By comparison, the film effectiveness at the trailing edge shows almost the opposite behavior exhibiting an almost linear dependance on mass flow as shown in Figure 3-22. This suggests that by the trailing edge, any differences in film features resulting from the specifics of the injection geometry will have become dissipated by the turbulent nature of the boundary layer. The exception to this rule is at higher BRs above 1 where additional mainstream gas is entrained into the boundary layer due to greater jet penetration into the mainstream, resulting in a leveling off of effectiveness levels.

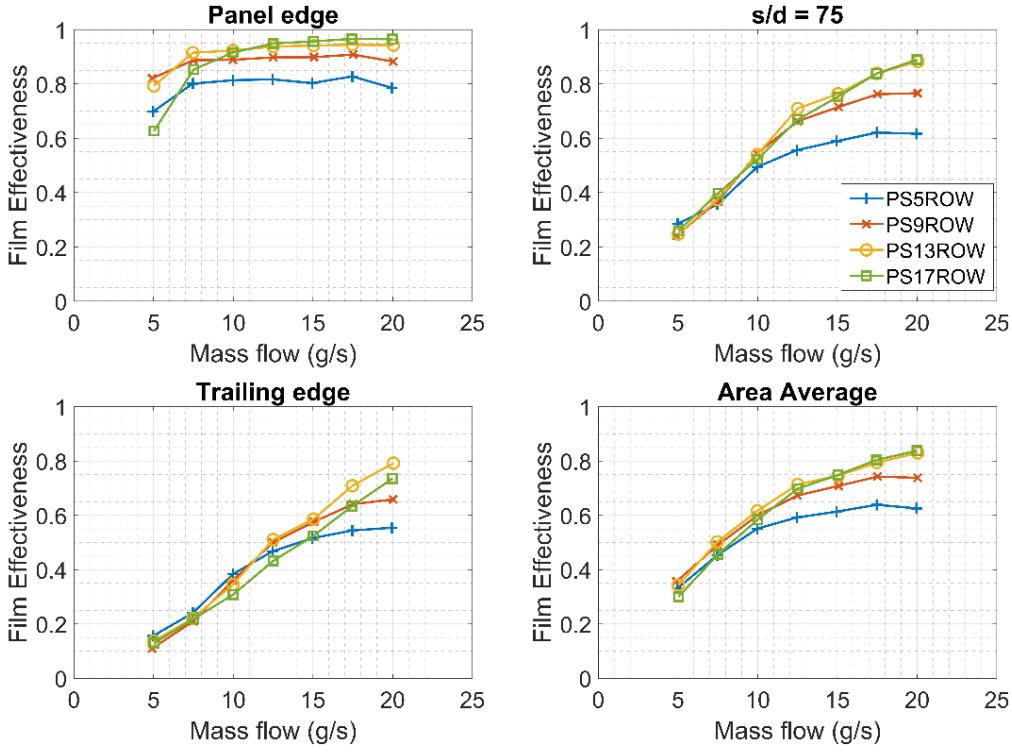


Figure 3-22 Spanwise average film effectiveness against mass flow rate at different streamwise locations for PSXROW geometries

At other streamwise positions as well as for the area average, the superposition of both effects can be noticed. As a whole, it is apparent that the geometries with more rows perform better. It is also apparent that high blowing ratios lead to higher film cooling for each geometry. However, the blowing

ratio at which film effectiveness peaks is much higher than that compared to the suction surface. This can be attributed to the benefit concave curvature can have on high blowing ratio films, with any increase in streamwise momentum ratio leading to an improvement in film attachment. It can also be suggested that the interactions between films in the panel contribute to reducing film lift off that would occur when the blowing ratio exceeds 1.

Combining the results into a single contour plot for each location and the area average results in Figure 3-23 which implies that the optimal film effectiveness lies between 0.3 and 0.6 for most mass flows. Reducing blowing ratios further is again seen to be problematic due to ingestion and a spanwise distribution issues.

Similar trends are observed at intermediate spanwise locations. At the panel edge, the lowest blowing ratios perform the best. However, at the trailing edge, the effects of blowing ratio are less pronounced and mass flow is much more significant. It is worth noticing that, for low mass flows, the film effectiveness at the trailing edge benefits from relatively higher blowing ratios.

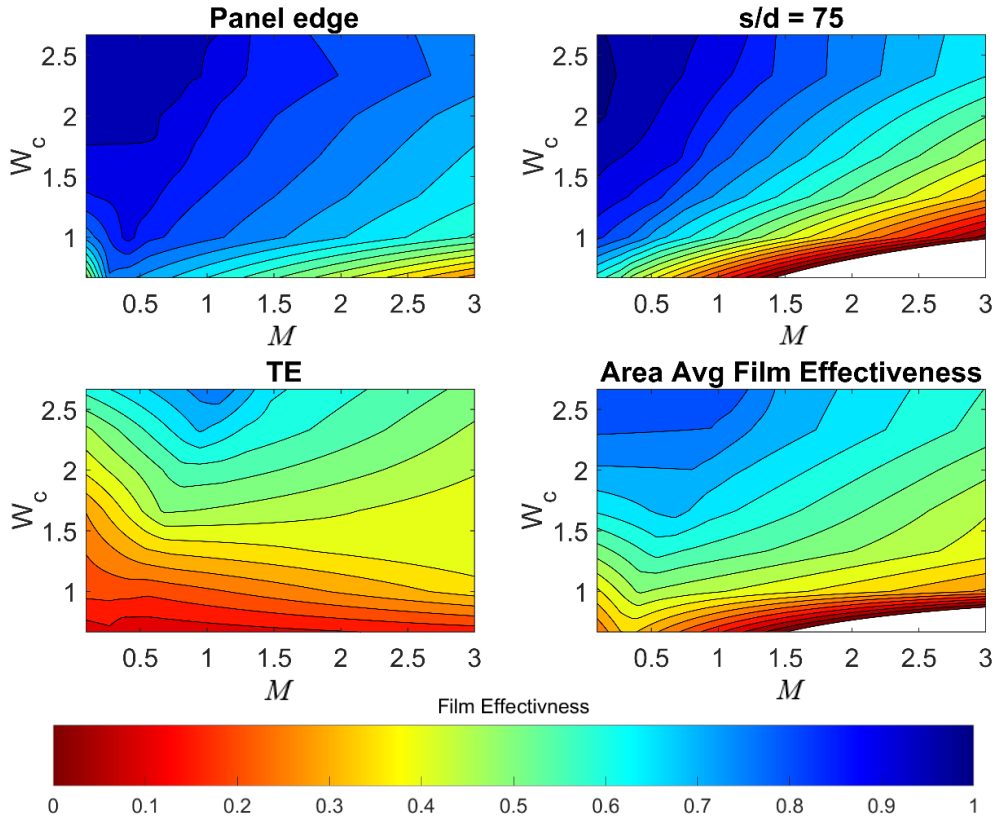


Figure 3-23 Contour plot of film effectiveness for different mass flows and blowing ratios on PS

3.2.5. Results- Effect of Hole size

One of the challenges of transpiration cooling and similar micro effusion cooling approaches have been limitations in manufacturing capability and the possibility of blocking such very small cooling features. In order to measure the sensitivity of hole size on panel cooling effectiveness, four different hole diameters were tested on either side, with the largest hole diameter exceeding typical industry film hole dimensions at engine scale. In order to maintain porosity, the pitch to diameter ratio was kept the same for all the geometries. Due to the discrete nature of film holes, the exact total sum of film hole area could not be kept identical but film hole diameters were selected so that this number would not vary from the baseline by more than 1%, as indicated in Table 3-2. Pressure ratio values are also included and are defined as the ratio between the total coolant feed pressure and the total mainstream pressure.

3.2.5.1. Suction Surface hole diameter experiments

The film effectiveness distributions at an intermediate mass flow rate of 12.5g/s for the geometries SS35D, SS12ROW, SS75D and SS95D with 0.35mm, 0.5mm, 0.75mm and 0.95mm hole diameters respectively are given in Figure 3-24. The film effectiveness distributions indicate the benefit of reducing hole size with the smaller diameters showing higher film effectiveness. Furthermore, SS35D achieves a more even spanwise distribution at these mass flow rates. Figure 3-25 shows the same geometries at 25g/s where the film is fully saturated. At this stage the films show a very similar behavior with the film for the SS095D building up the most gradually with distance.

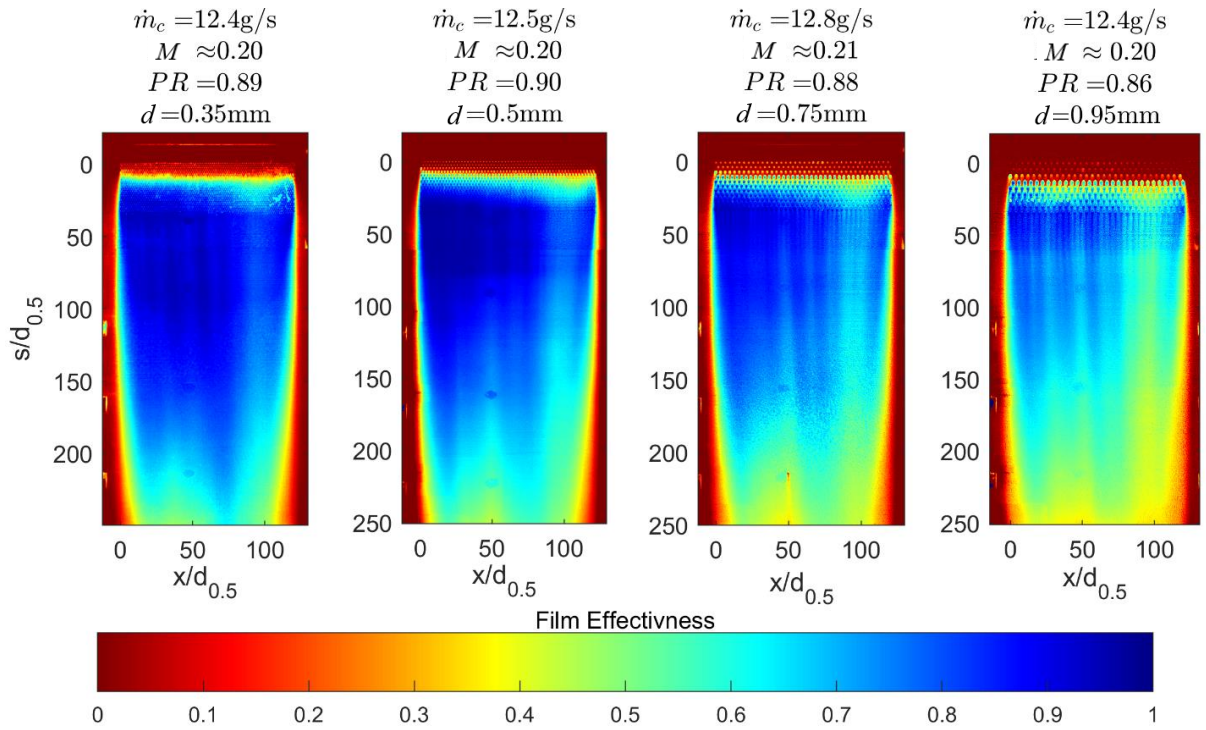


Figure 3-24 Film effectiveness plot for different film hole diameters at 12.5g/s on SS panel

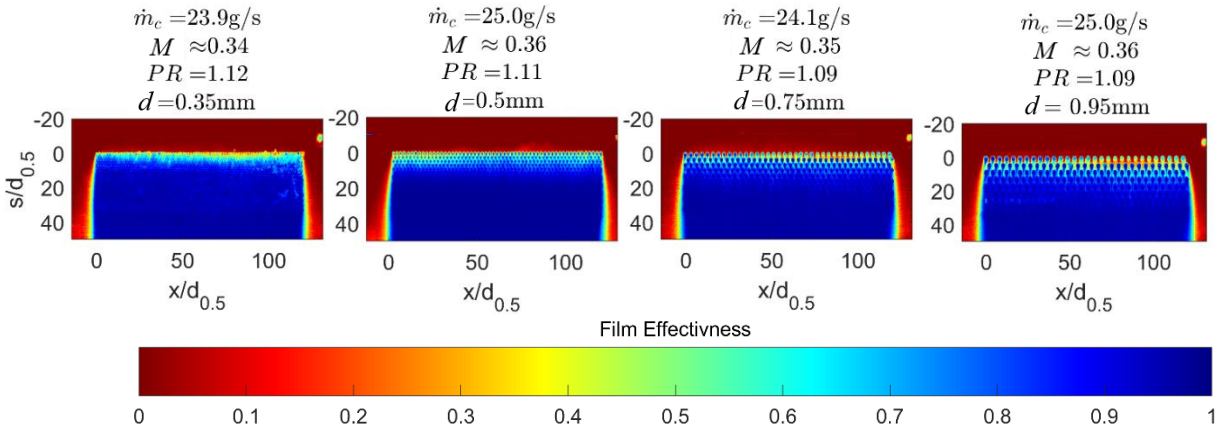


Figure 3-25 Film effectiveness plot for different film hole diameters at 25g/s

Comparing the spanwise averages of film effectiveness at discrete locations downstream presented in Figure 3-26 shows a clear positive correlation between hole size and film effectiveness. Additionally, the greatest sensitivity to hole size occurs at low and intermediate mass flow rates between 5g/s and 15g/s with all geometries achieving saturation at the highest mass flow rates. The difference between film effectiveness levels is also most pronounced at the intermediate streamwise locations, whilst the geometries achieve similar film effectiveness levels at the trailing edge. This indicates that, by the time

the coolant has been able to reach the trailing edge, the detail of the injection geometry becomes less significant, with all geometries remaining in the mass addition regime and avoiding significantly increasing mixing due to film lift of or jet penetration.

Figure 3-26 also demonstrates that the relationship between hole size to film effectiveness follows a trend of diminishing returns as the hole diameters are reduced. The effect of minimizing hole diameter is also diminished at higher mass flow rates where the film effectiveness reaches saturation.

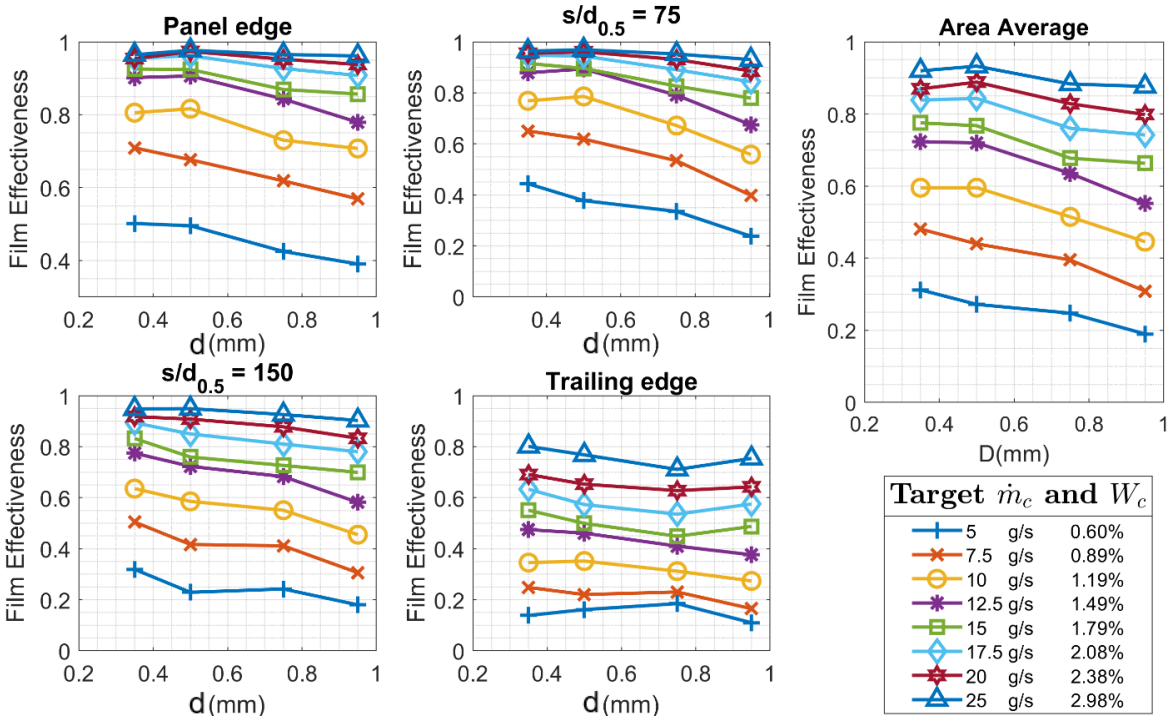


Figure 3-26 Effect of film hole diameter at different streamwise locations on SS

3.2.5.2. Pressure Surface hole diameter experiments

The film effectiveness distributions for the PS35D, PS50D, PS75D and PS95D geometries are shown in Figure 3-27 which first shows an improvement in spanwise distribution for smaller hole diameters at lower mass flows. As the smaller holes have increased pressure drops than the larger holes, the total feed pressure was confirmed to be higher for the smaller diameters at the same mass flow. This has the benefit of distributing the coolant across the span more efficiently, leading to overall better cooling performances.

As the mass flow is increased however, the difference between geometries is less noticeable. A feature unique to the PS35D geometry is the presence of streaks of low film effectiveness. At smaller hole diameters, the sensitivity to hole imperfections and potential blockage are higher, leading to a more localized, yet seemingly random variation across the spanwise distribution.

The film at the first two rows of every geometry always lift off due to the higher blowing ratios on the pressure surface. However the films reattach by the third row and this effect particularly evident for the larger diameters where blockage and manufacturing imperfections are less significant. As all rows share the same pitch to diameter ratio, this results in a later reattachment point for the larger film hole geometries.

The hole size sensitivity is summarized in Figure 3-28. For each location, a linear relationship exists between hole size and film effectiveness at lower mass flow rates, with the initial benefits of smaller holes leading to diminishing returns at higher mass flows where the film level becomes saturated.

At the panel edge, the smaller diameter geometry performs significantly better at lower mass flows due to better spanwise spacing. This improvement occurs as the internal pressure is higher because of the greater losses within the film holes. Geometries PS35D and PS50D reach saturation values of over 0.9 at mass flows of 7.5g/s with PS75D and PS095 requiring 10g/s and 12.5g/s to reach these values respectively.

`At the trailing edge, the film effectiveness is seen to be a weaker function of hole diameter, indicating that, by this point, the nature of the injection geometry again is less important. The trailing edge film effectiveness is also seen to be equal for all geometries at the lowest mass flow rate.

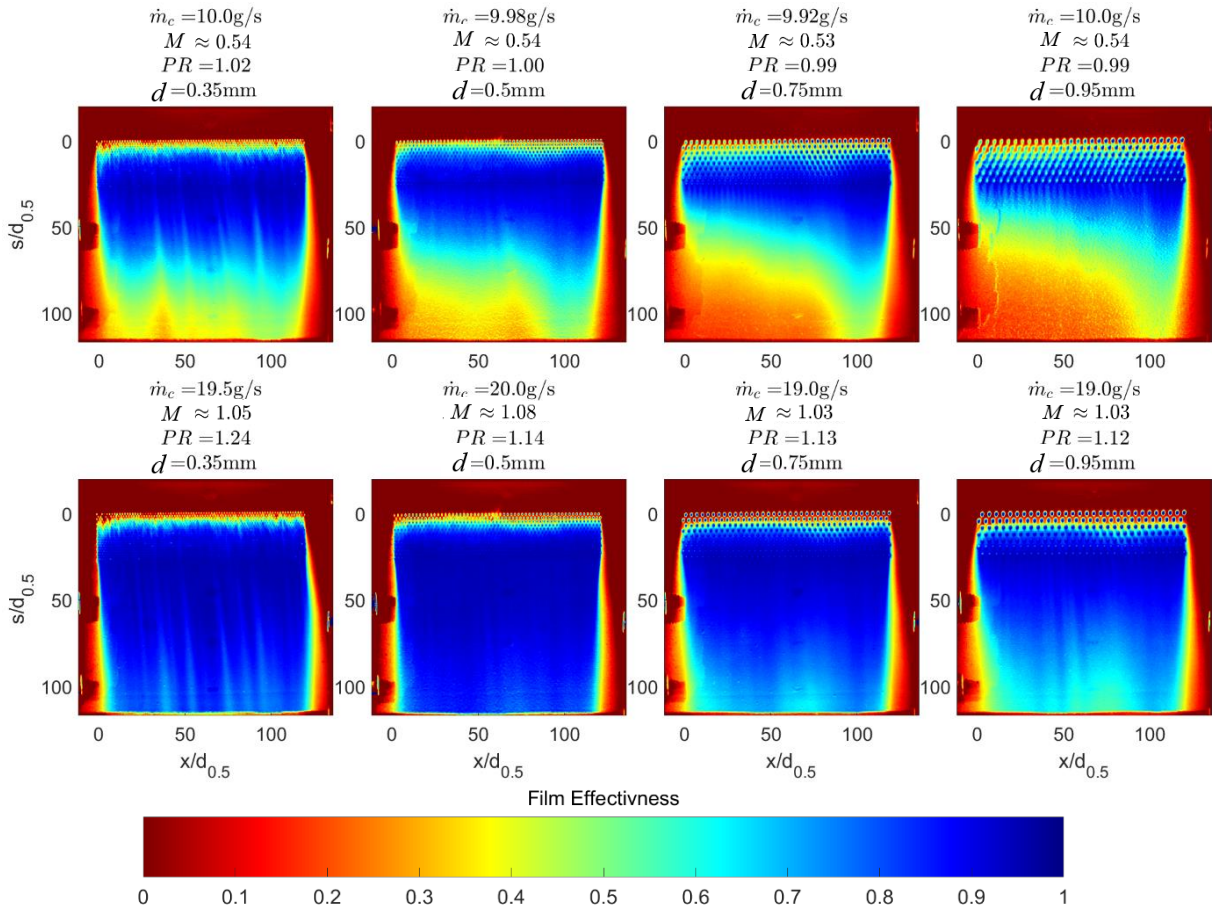


Figure 3-27 Film effectiveness plot for different hole diameters at 12.5 and 20g/s

When taking the area average film effectiveness, the different trends balance each other out. This results in a linear relationship between film effectiveness and hole diameter with each step yielding a 3 to 5% difference in film effectiveness over the entire surface, with the differences being proportionate to the steps in hole diameter.

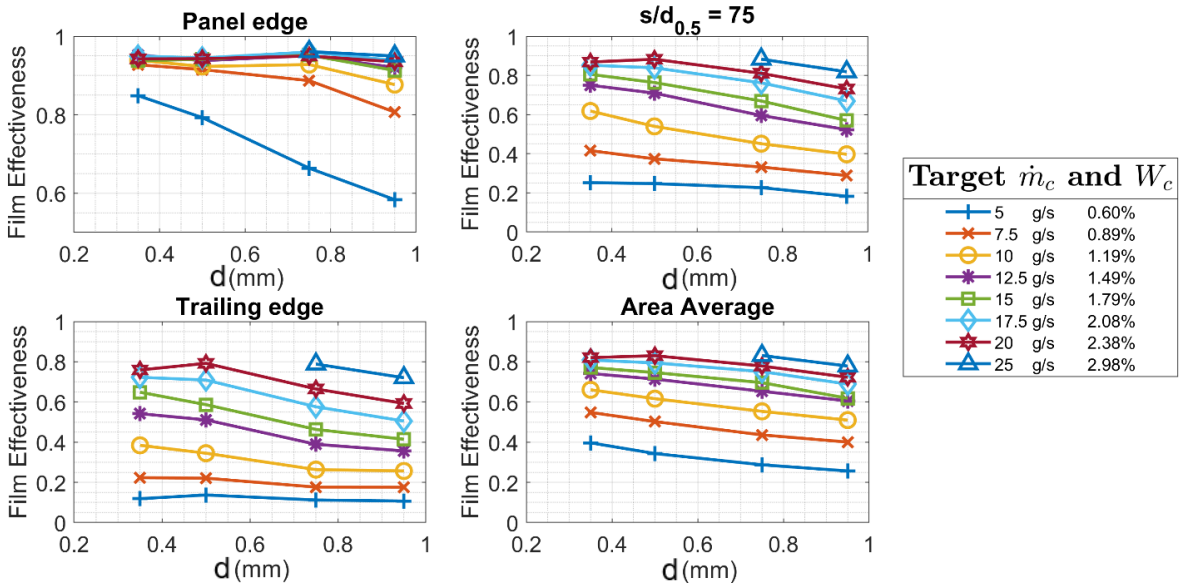


Figure 3-28 Effect of film hole diameter at different streamwise locations on PS

3.2.6. Results- Effect of Injection angles

3.2.6.1. Streamwise angles

Geometries SS35a, SS45a, SS60a and SS90a were tested in order to examine the effects of varying the streamwise film angle, α, with all other parameters kept constant for these geometries.

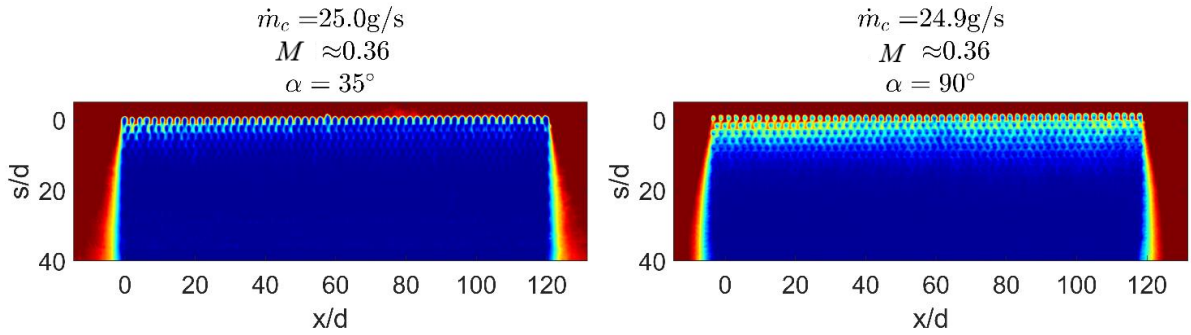


Figure 3-29 Detail of panels at α = 35° and 90° with a coolant mass flow of 25g/s

Film distributions given between geometries were generally similar. The main differences in specific film coverage occur in the vicinity of the first few coolant holes highlighted in Figure 3-29. The film of the most inclined holes becomes saturated within 2 to 3 rows, particularly at higher mass flow rates. By comparison, the first 7 to 8 individual film holes remain discernible for SS90a up to a mass flow of 25g/s. This is mainly due to the fact that perpendicular films tend to penetrate further into the mainstream flow, resulting greater mixing between the film and mainstream as well as increasing the likelihood of individual films lifting off. This keeps the mainstream within the panel much longer

than the shallow angles of SS35a which remain attached and better remove the mainstream from the blade surface. However, despite a perpendicular injection angle for SS90a, a separation bubble cannot be observed downstream of the panels, indicating that the interactions between films are still sufficient to maintain the film bulk attached to the surface.

Figure 3-30 shows the averaged film effectiveness level at given locations on the blade surface. SS35a achieves asymptotic film effectiveness levels at the panel edge at a very low mass flow of 12.5g/s. The high film effectiveness is also maintained at unrivalled levels through to the trailing edge. By contrast, SS45a, SS60a and SS90a demonstrate a more limited sensitivity to injection angle. despite confirming that of shallower angles lead to higher film effectiveness values. SS90a shows similar values to the intermediate geometries at both low and high mass flow rates but falls behind mostly at intermediate mass flow rates between 10-17g/s.

Again the trailing edge region experiences a near linear relationship between film effectiveness and mass flow, with the film effectiveness for different geometries following similar trends despite a constant offset in effectiveness.

Overall, the sensitivity of the panel film effectiveness to streamwise injection angles of individual film holes is much less that what is typically expected in individual rows of film holes. Even at perpendicular injection angles, the lift off of films is effectively absent. This can be explained due to the combination of low blowing ratios, resulting in low perpendicular coolant momentum, as well as the beneficial interactions that can be attributed to staggered hole arrangements.

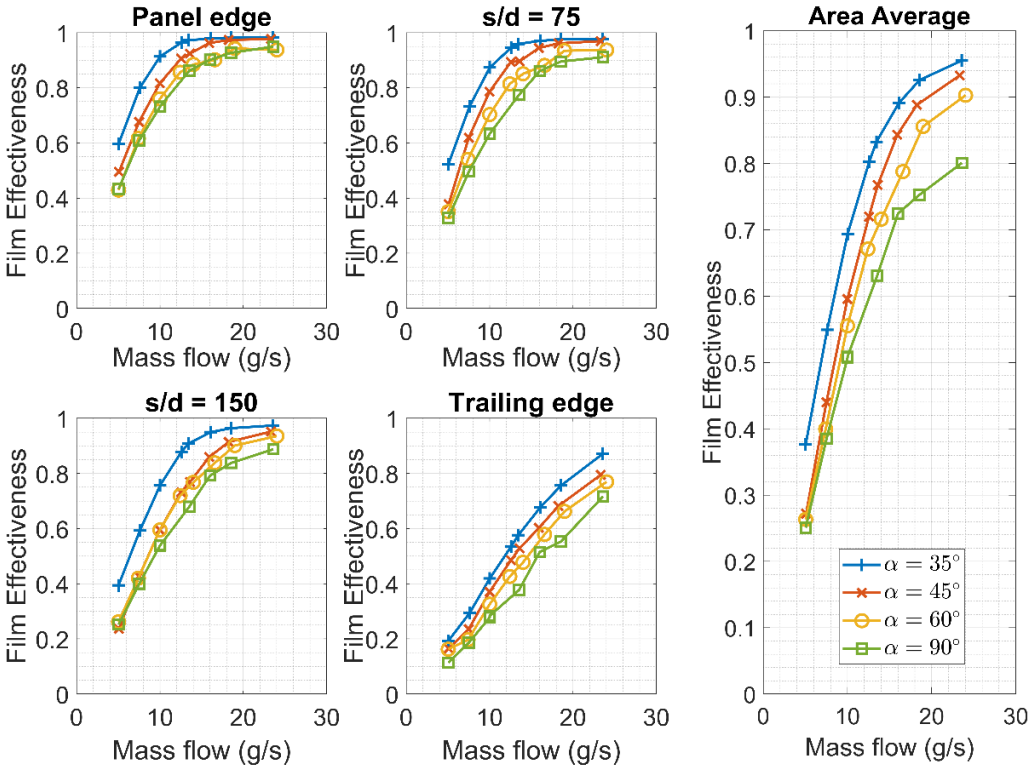


Figure 3-30 Effect of streamwise injection angle α at different streamwise locations on PS

3.2.6.2. Spanwise angles

The film effectiveness ratios for geometries SS0b, SS15b, SS30b and SS45b are shown in Figure 3-31 and examine the effects of varying the spanwise angle β. As the angle and coolant mass flow rates are increased, the film bulk begins to sweep away from the centreline and out of the field of view. This has a significant effect on the measurable film effectiveness as a large portion of coolant has moved beyond the visible region. This migration is more significant than is typically experienced by compound angle films as the downstream rows are sheltered from the fast moving mainstream, resulting in a greater relative radial momentum component.

Accounting for the lateral external migration of the films, geometries SS0b, SS15b and SS30b behave relatively similarly. SS45b however demonstrates a much more significant degradation of film effectiveness, even when accounting for the curvature in the film trajectory. SS45b also has the property of its holes once again being effectively inline with respect to the coolant trajectory, at 45 degrees from the mainstream flow. At higher mass flows, the flow within the panel is turned significantly enough that

the films begin to behave closer to an inline geometry, with mainstream streaks penetrating further into the panel.

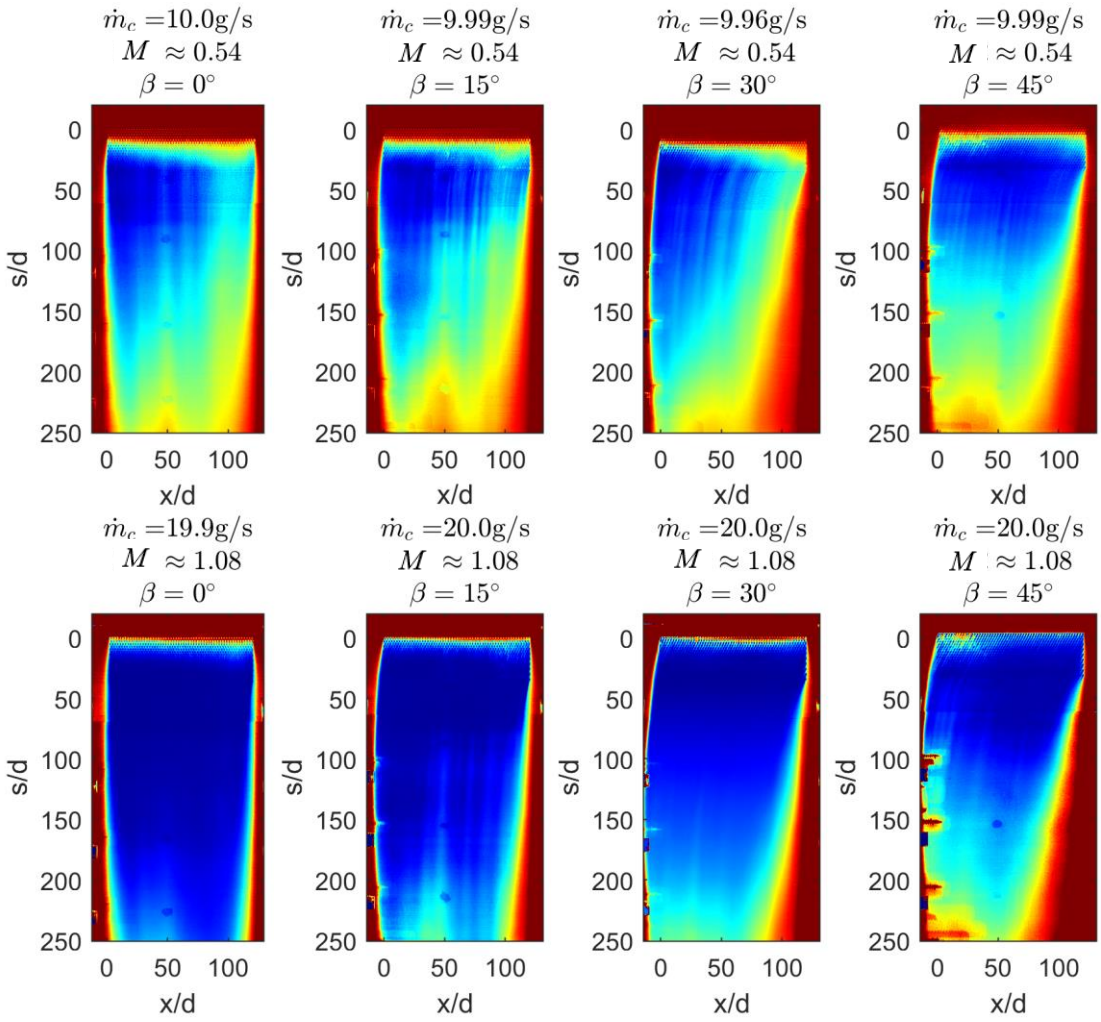


Figure 3-31 Film effectiveness plot for different spanwise injection angles β at different streamwise locations on SS

Spanwise average plots given by Figure 3-32 confirm that SS45b demonstrates a significant drop in effectiveness past 12.5g/s, however this is in part due to the fact that the coolant is swept out of view completely. Between the other geometries, a weak negative correlation between spanwise hole angle and film effectiveness can be established at x/d=150, the TE and for the area average. This correlation is inversed however at the panel edge, particularly at lower mass flows. This is in line with literature as compound angles lead to immediate lateral spacing and improved film cooling effectiveness, at the expense of greater mixing between the mainstream and coolant.

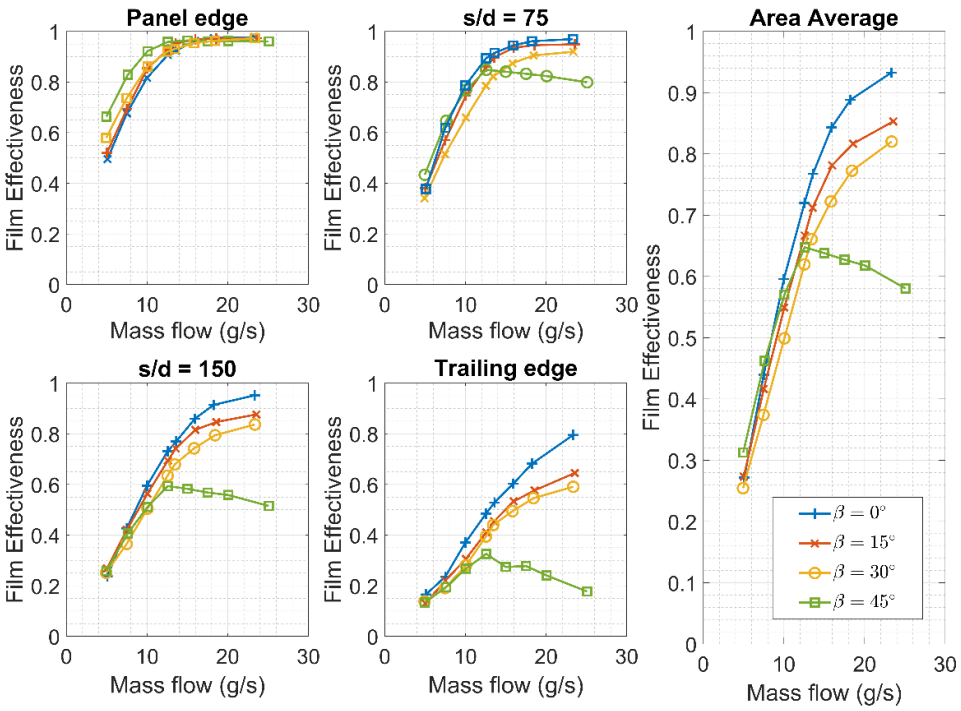


Figure 3-32 Effect of spanwise injection angle β at different streamwise locations on SS

3.2.7. Conclusions

A wide range of high porosity cooling panels have been tested on both the suction surface and pressure surface of a high pressure turbine blade. From the results we can conclude that:

- The optimal blowing ratio for a given mass flow is between 0.2 and 0.3 for the suction surface and between 0.4 and 0.5 for the pressure surface. This is significantly lower than conventional film models but highlights the inefficiencies of these designs. Lift off is partially observed above blowing ratios of 0.6 on the SS and 1 on the PS, at which point films stop improving despite the addition of more mass flow, however complete lift off is avoided.
- Coolant mass flow is the predominant parameter effecting trailing edge film effectiveness. The specifics of the hole geometry are less important as long as film lift off is avoided. This indicates that regardless of the film structures near the panel, these features have been dissipated within the boundary layer.
- Injection geometry is more significant near the panel edge, determining whether or not the film is able to saturate or not. Peak film effectiveness values are determined by number of rows, more specifically the panel length. Between 5 and 7 rows are required to ensure that the films remain

attached at higher blowing ratios. This is also reflected at intermediate positions along the blade as the length of the saturated region also depends on the injection geometry.

- Hole diameter is a significant parameter, particularly near the panel. Smaller holes show lead to better film distribution as well as a more extended film core.
- The interactions between films are seen to be significant as even when the lowest blowing ratio film near the front of the panel are seen to lift off individually, the overall panel is able to generate a well attached film.
- Injection angles are less important as the panel films are resilient and resistant to lift off. Spanwise angles are not particularly helpful as the panels already demonstrate good spanwise coverage and lateral injection induces more secondary flows and vortices which are detrimental to the films.

ACKNOWLEDGMENTS

The authors wish to express their thanks for the ongoing support provided by both Rolls-Royce PLC and the EPSRC through (EP/P000878/1). The authors would also like to thank the technicians at the Oxford Thermofluids Institute for their assistance in the manufacturing of the experimental setup.

4. Transpiration Cooling Film Effectiveness Correlations for Turbine Blade Applications

Following the extensive film effectiveness campaigns detailed in the previous chapter, benchmarking the results to existing film effectiveness correlations provided a natural next step. Understanding how experimental results compared to discrete film hole models versus porous section film cooling models, was believed to be a way to gauge how well transpiration cooling had been recreated.

Matching existing models to the experimental data however, proved to be challenging, even when allowing for variations caused by varying mainstream conditions around the blade, prompting an investigation into other film cooling models. Given the amount of data already collected, it was possible to develop a new film cooling correlation that matched the experimental data, based on a combination of existing film cooling models.

The following paper was presented at the 15th European Turbomachinery Conference (ETC2023-295) in Budapest Hungary April 2023. This paper was written under the supervision of Professor Peter Ireland.

Transpiration Cooling Film Effectiveness Correlations for Turbine Blade Applications

A. Wambersie – P.T. Ireland

Department of Engineering Science, University of Oxford
Oxford OX1 3PJ, UK
Email: augustin.wambersie@eng.ox.ac.uk

Abstract

High porosity film cooling features have demonstrated exceptionally high film cooling performance. However, conventional methods to predict film cooling effectiveness have proved inaccurate for this new class of film. The inaccuracy is particularly true on the suction surface of the aerofoil where film effectiveness significantly exceeds predictions made using conventional correlations. RANS CFD simulations are equally limited beyond the immediate film hole region and generally over-predict the rate of film decay.

A novel approach to correlating these films is attempted in this paper using the similarities between tangential slot cooling distributions and existing experimental film data of porous cooling features. Based on this similarity, a correlation is developed by combining superposition with existing tangential slot injection models.

The success of this model reinforces both the premise that tangential slots and transpiration cooling share similar film distributions, as well as the hypothesis that the high porosity geometries proposed successfully mimic transpiration cooling.

Keywords: Film Effectiveness, PSP, Transpiration cooling, High porosity

Nomenclature

c_p	Heat capacity (J/kgK)	u	Velocity (m/s)
C_1, C_2	Coefficients for Equation 9	x	Streamwise distance (m)
d	Film hole diameter (m)	y	Spanwise distance (m)
h	HTC (W/m^{2}K)	α	Streamwise hole angle (°)
L	Characteristic length (m)	μ	dynamic viscosity (kg/ms)
$\dot{m}_c$	Coolant mass flow (kg/s)	η_{film}	Film effectiveness
M	Blowing ratio	$_{aw}$	Adiabatic wall condition
Pr	Prandtl number	$_c$	Coolant
Re	Reynolds number	$_\infty$	Mainstream
T	Temperature (K)		

4.1. Introduction

Recent experimental results have demonstrated the exceptional performance of high porosity cooling features on turbine blades (Wambersie et al. 2021). These highly effective geometries, rely on arrays of tightly packed film holes with small pitch to diameter ratios of around 2. The local surface porosity within the film hole arrays, defined as the fraction of the outer blade surface approaches 20%. The individual film holes operate at very low blowing ratios, minimizing any penetration of the film intro the mainstream as well as the resultant mixing between the two gas streams. However, efforts to match these results to existing models, both analytical and numerical, has proven unsuccessful.

The ability to predict the film effectiveness, defined by Equation (4-1), of high porosity cooling features would allow for the evaluation of potential usefulness and impact of this technology.

This paper investigates film effectiveness distributions using both 1D and 2D models as a framework. Whilst the use of 1D models is limited within turbine blade applications due to geometric constraints, these nonetheless help demonstrate the overarching trend of high porosity films. The use of 2D models, by comparison, offers a more accurate approach which can be used to develop meaningful correlations. Nonetheless, both offer a great deal of qualitative understanding of cooling films developed using high porosity features.

$$\eta_{film} = \frac{T_\infty - T_{aw}}{T_\infty - T_c} \tag{4-1}$$

Several features of the films generated by high porosity panels, as illustrated by Figure 4-1, deserve particular attention and are summarized here. Moreover, these features serve as the catalyst for this investigation as a whole. The figure illustrates data for both a pressure surface and a suction surface panel geometry, tested within a highspeed cascade with a mainstream mass flow rate of 1.2kg/s. Firstly, the region immediately downstream of the film hole arrays demonstrates a near uniform level of film effectiveness. This is followed by a region of exponential-like decay further away from the point of coolant injection. The region of constant film effectiveness mimics the behavior of tangential slot injections studies, where the region with constant film effectiveness levels of unity is called the core region (Sturgess, 1986). Across both experimental parametric studies on high porosity film arrays as

well as in tangential slot injection literature, the length and mean effectiveness of this core region were seen to be a clear function of the injection geometry. Conversely, the film effectiveness levels close to the trailing edge indicated almost no relationship with the injection geometry suggesting a breakdown in core structure and a return to a conventional mixed out boundary layer where film effectiveness is determined predominantly by the mass balance between injected coolant and hot mainstream gas that has been entrained into the boundary layer. Once again, this behavior draws parallels with previous work on tangential slot injection and its different zones (Simon, 1986) .

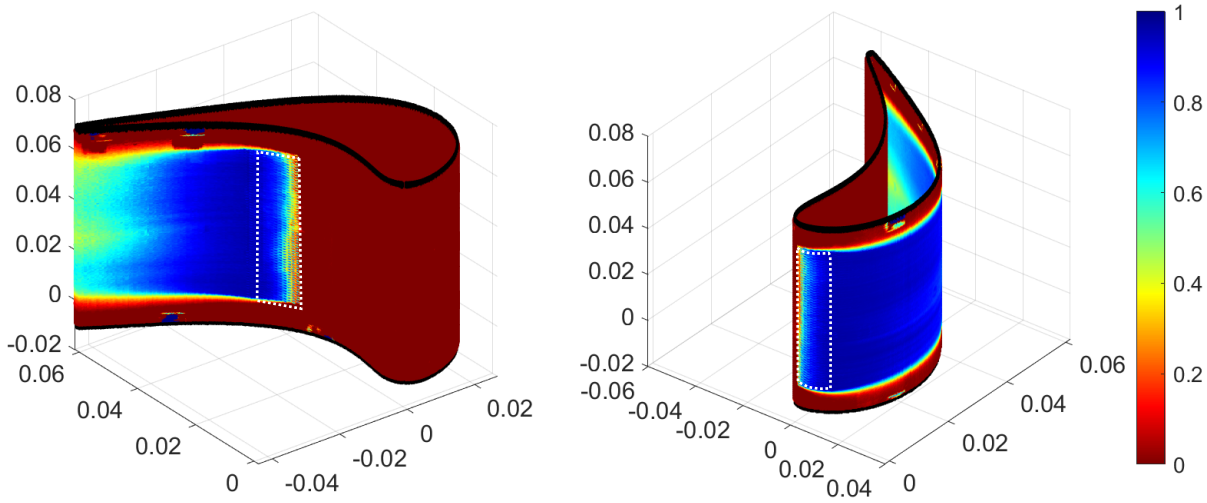


Figure 4-1 Demonstration of film effectiveness data obtained with a high porosity panel using 12.5g/s (1.5% of the mainstream) of coolant on both the pressure surface (left) and suction surface (right). Panels are outlined in white. (Wambersie, et al., 2021)**.**

Figure 4-2 exemplifies these parallels by plotting the film effectiveness of a series of high porosity panels of varying hole diameters. Film effectiveness levels are seen to converge towards the same values at the trailing edge, particularly at lower mass flow rates. As mass flow is increased, film effectiveness levels begin to diverge and then converge. Finally, the film begins to maintain near constant film effectiveness at 15g/s, particularly for smaller mass flows. This trend is only exacerbated at even higher mass flows.

To summarise, the film effectiveness distribution of recent experimental campaigns have pointed towards the need of a new method of predicting film effectiveness by drawing on parallels between these results and previous tangential slot injection studies.

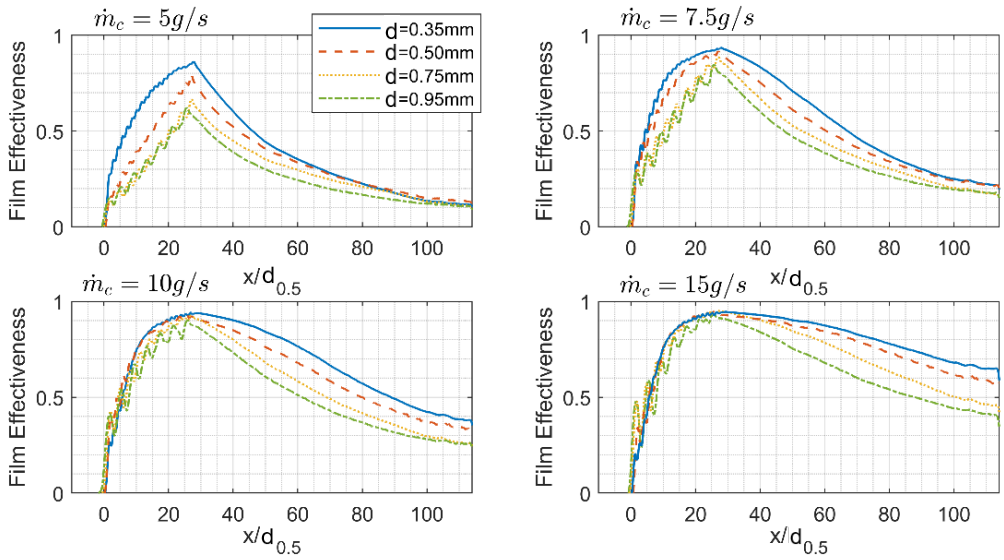


Figure 4-2 Demonstration of the effect of cooling hole diameter on film effectiveness levels at four different mass flow rates for a pressure surface geometry (Wambersie, et al., 2021)

4.2. Literature review

4.2.1. 1D film cooling models

1D film cooling models offer the most basic approach to predicting film effectiveness. Extensively studied and summarised by Goldstein (1971), 2D film correlations are based on a heat balance analogy within the boundary layer between the injected coolant and the entrained mainstream, with coolant simply acting as a heat sink and diluting the enthalpy of the boundary layer Using empirical boundary layer correlations to quantify the temperature profiles as well as entrainment rates, Equation **(4-2)** was developed.

$$\eta_{film} = \frac{1.9\mathrm{Pr}^{2/3}}{1 + 0.329\left(\frac{C_{p\infty}}{C_{pc}}\right)\varepsilon^{0.8}\beta_e} \quad \textbf{(4-2)}$$

Where ε is the dimensionless film cooling parameter

$$\varepsilon = \left(\frac{x}{sM}\right)\left[\frac{\mu_c}{\mu_\infty} Re_2\right]^{-0.25}$$

(4-3)

And β_e is taken as the increase in the rate of entrainment into the boundary layer due to coolant injection.

$$\beta_e = 1 + 1.5 \times 10^{-4} Re_2 \frac{\mu_c}{\mu_\infty} \sin\alpha$$

(4-4)

Equation 2 was seen by Goldstein and Haji-Sheikh to closely correlate flat plate data of both porous sections as well as tangential slot injections where ***s*** refers to either the porous section length or the slot height.

4.2.2. Tangential slot models

Other approaches have been used to specifically correlate tangential slot injection films as these can demonstrate different film cooling distributions, particularly at high blowing ratios.

Sturgess (1986) suggests using a model in which the film can be categorized into three separate regions. The first is the potential core, where film effectiveness levels are effectively maintained at unity. This is followed by a region of decaying film effectiveness known as the wall jet region, where the boundary layer is still dominated by the coolant injection. This region slowly narrows towards the wall as mixing propagates from the interface between coolant and mainstream gas. Finally, the flow becomes fully developed as the boundary layer mixes out completely, at which stage film cooling effectiveness is seen to match the standard heat sink film cooling models. Equation (4-5) describes the overall form of the film effectiveness where x_p is the length of the film core with film effectiveness values of unity given for $x < x_p$. MIX_n is defined as a function of the injection geometry.

$$\eta_{film} = f\left[\frac{\left(x - x_p\right)}{s\bar{M}}, MIX_n\right]$$

(4-5)

Velocity ratio, density ratio, and slot geometry are seen to have important effects on the core length. Simon (1986) similarly categorizes the film into two separate zones with a core and developed region and quantifies the effects of turbulence on the core length.

Hatch and Papell (1959) suggest an alternative approach to modeling tangential slot injections by using a different physical analogy. The mainstream and coolant stream are assumed to remain separate, with the heat transfer between the two driven by a characteristic HTC as given by Equation (4-6). x' is given as the distance travelled by the coolant before heat is able to conduct through the coolant layer. Additional functions to fit the model to varying velocity ratios and injection angles are also included later in subsequent studies (Papell, 1960).

$$\eta_{film} = \exp\left[-\left(\frac{hL(x-x')}{\dot{m}c_p}\right)\right] \tag{4-6}$$

Goldstein (1965) also noted that this approach provides a relatively accurate fit for transpiration sections as well as for tangential slots, indicating that models developed for either type of geometry could be interchanged within reason. However, these models were seen to be less effective beyond streamwise distances x/LM of 100.

4.2.3. 2D models

When modelling cooling features with multiple injection locations, the standard analytical approach involves modelling each individual film hole and superimposing the separate streams using the method defined by Sellers (1963). This approach has the benefit of being extremely simple and relatively accurate for most use cases. An improvement on this approach proposed by Kirollos and Povey (2015) that corrects the energy imbalance however the overall approach remains similar.

$$\eta_{film} = 1 - \prod_{i=1}^{n_{holes}} \left(1 - \eta_{film,i}\right) \tag{4-7}$$

Equation (4-7) can be applied in both streamwise and spanwise directions making it ideal for large banks of individual film holes. This approach also has the benefit of being able to model in between film holes as opposed to solely downstream of the overall feature. The film effectiveness of individual cylindrical film holes can be modelled in 2D as heat sinks using Equation (4-8) (Goldstein, 1971) where y_h and x_{decay} are constants that are functions of blowing ratio. This approach has been demonstrated

by Murray (2018)and Coulton who also suggested improvements to the spanwise distribution term (Coulton, et al., 2022).

$$\eta_{film} = \frac{\mathrm{M}\, \mathrm{u}_\infty \mathrm{d}}{8\alpha(x/d + x_{decay})} \exp - \left(0.693 \frac{y}{y_h}\right)^2 \quad \textbf{(4-8)}$$

Note that this approach provides a local effectiveness that depends on both x and y. This method proves to be a highly effective and efficient approximation for flat plate geometries with pitch-to-diameter ratios of over ten in the streamwise direction. The constraint of large streamwise spacing allows the boundary layer to recover to a uniform velocity distribution and for the vortices developed by the interactions between film and mainstream to begin to dissipate. High blowing ratios increase this distance further as the impact on the boundary layer is more significant.

However, when pitch to diameter ratios are reduced to the order of 2-3, the interactions between films become significant and large variations in individual film behavior can be observed. Chen et al. (2020) demonstrated the potential discrepancies between film superposition and experiments in which two rows are positioned inline with pitch to diameter ratios. Whilst the standard film models can be tuned in an attempt to capture some of these effects, these still fall short when applied to either curved geometries in representative engine flows or when applied to high blowing ratio films that would typically lift off altogether if not for interactions with other films (Jiang, et al., 2018).

Long-standing similarities between the behaviors of tangential injection and transpiration cooling have been discussed. Multiple different approaches to modeling these geometries have also been presented, however, these have yet to be used successfully to predict the film effectiveness of high porosity film cooling features on real turbine blade geometries.

4.3. Overview of film effectiveness data and geometries

Film effectiveness data from a wide range of high porosity panel geometries is used to develop and test the correlations. The experimental setup as well as the initial set of results are detailed by Wambersie, Ireland and Mayo (2021) but have since been greatly expanded to include a much larger range of

variables, including film hole diameter and panel length. Figure 4-3 illustrates the location and types of geometries that were tested. Both the blowing ratio and density ratio are also varied. The results offer high spatial resolution film effectiveness, though this paper will emphasize the streamwise distribution of film effectiveness as this has been the primary area of interest of these geometries, with the spanwise distribution being relatively uniform.

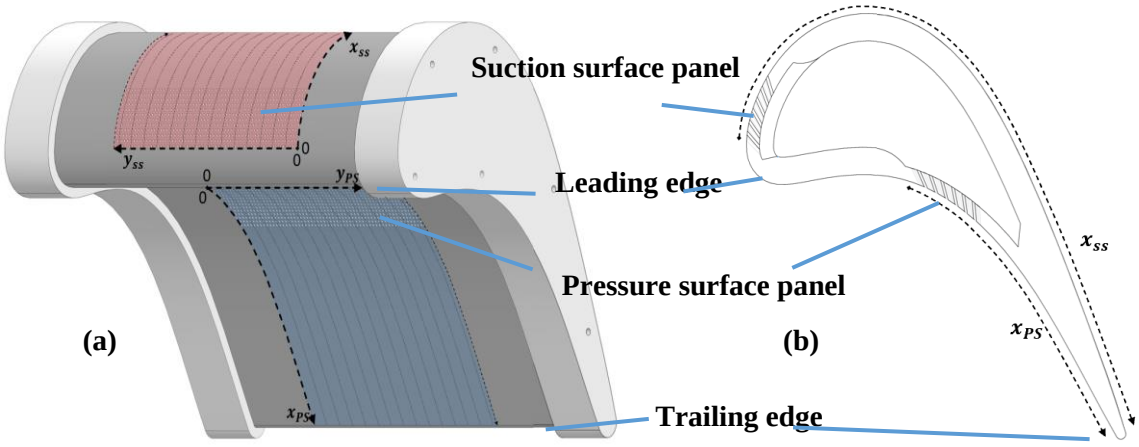


Figure 4-3 Schematic of geometries and locations used in film effectiveness experiments

Whilst both inline and staggered geometry data is available, it was determined that film effectiveness data of inline geometries would not be particularly suitable to model as these films are exacerbated by film lift off. By comparison, staggered rows resulted in a much more robust, attached, and uniform films at all blowing ratios. A critical requirement for the geometries evaluated is that the films are closely packed together with a pitch to diameter ratio close to 2. This results in a feature where the bulk film of the panel array takes on a different distribution relative to that of the individual films.

4.4. 1D film effectiveness investigation

Figure 4-4 demonstrates how the films generated by high porosity features scale with blowing ratio once the abscissa offset by a potential core. As the film effective levels do not begin at unity, the length of the potential core was estimated as the distance between the panel trailing edge and the inflection point of the film effectiveness which could be systematically determined.

Equation **(4-2)** is also included for reference with the geometries modelled as porous sections with no offset, demonstrating that past a core or transitional region, the films behave predictably once the boundary layer becomes fully developed.

This would suggest that given a long enough surface, transpiration panels can be modelled simply as single porous geometries on flat plates with a streamwise offset. Figure 4-5, taken from a geometry on the late suction surface offers a visible representation of the core region as the values of different mass flows diverge and then converge towards Equation 2.

However, due to the length of a turbine blade geometry, a significant region of the relevant blade surface remains upstream of the predictable fully developed film regime for both suction and pressure surfaces. This is particularly true at higher mass flows where the core region extends almost to the trailing edge. Furthermore, the apparent length of the film core stemming from the early suction surface geometries exceeds the blade length altogether, rendering this approach useless for this region of the blade.

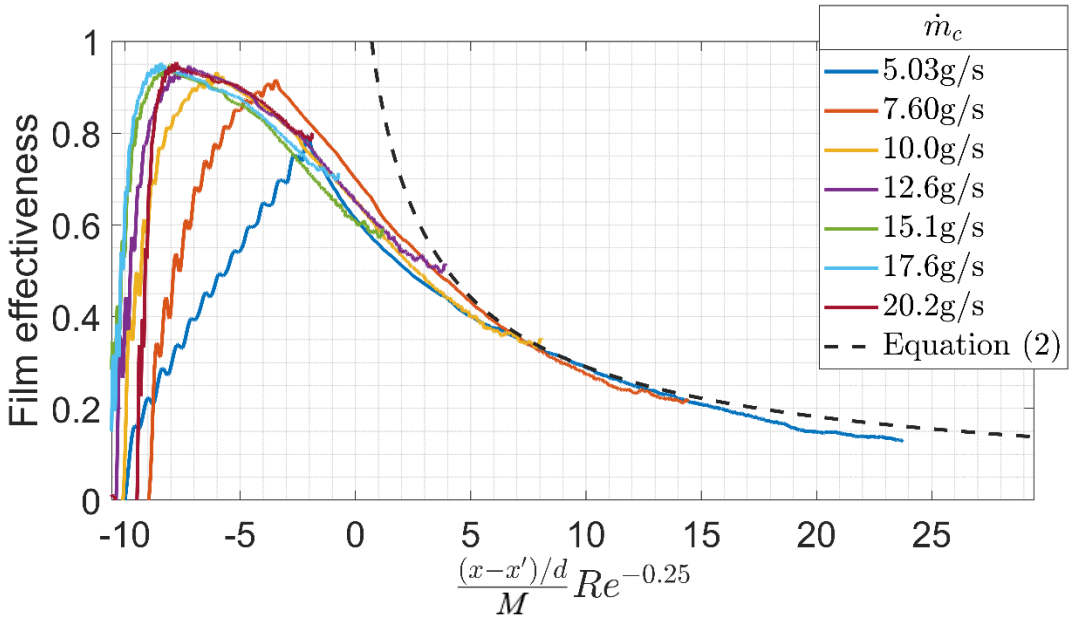


Figure 4-4 Film effectiveness levels plotted against scaled streamwise distance with core offset for 12 row staggered geometry on mid Pressure surface. (Wambersie, et al., 2021)

Overall, it can be concluded that the high porosity panels are able to develop a robust and sufficiently thick layer of coolant such that the effects of boundary layer entrainment are delayed until

the boundary layer becomes fully developed. The potential core length is predominantly a function of the velocity ratio, however, mass flow and blade curvature also play a significant role.

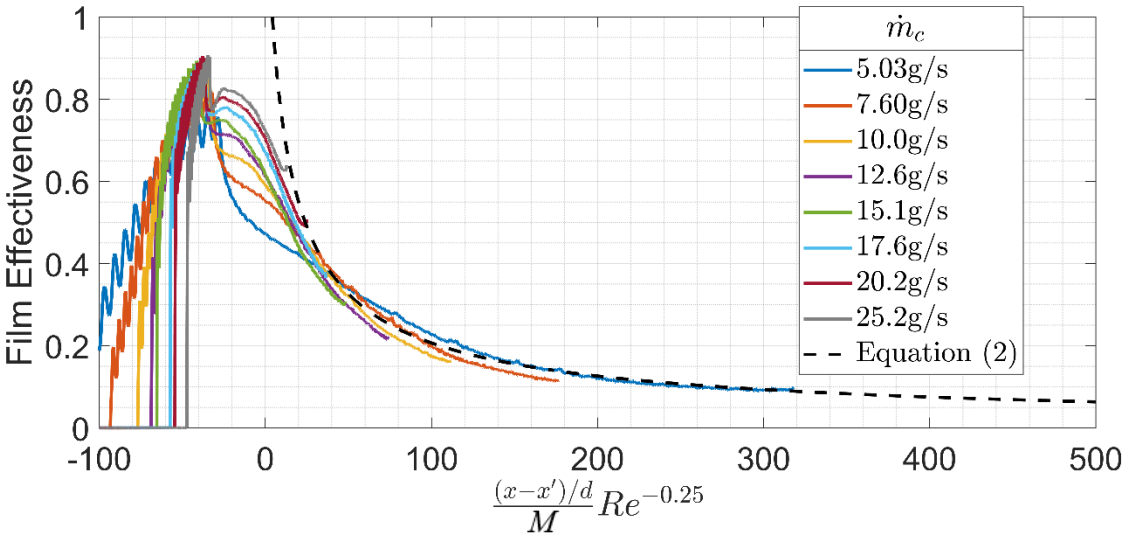


Figure 4-5 Film effectiveness against scaled streamwise distance with core offset for 17 row inline late suction surface panel (Wambersie, et al., 2021)

4.5. 2D Film effectiveness correlation

An alternative approach that attempts to capture the 2D distribution of film cooling combines the streamwise term from Equation (4-6) with the Goldstein approach of Equation (4-8) yielding Equation (4-9)

$$\eta_{film} = \exp\left[-\left(\frac{C_2 h dx}{\dot{m}c_p} + C_1\right)\right] exp\left[-0.693\left(\frac{y}{y_h}\right)^2\right] \quad \textbf{(4-9)}$$

Where h is defined as the flat plate heat transfer coefficient with mainstream flow conditions defined by those at the film hole exit. Similarly to Equation 6, h serves as an analogy for mixing and heat transfer within the boundary layer.

$$h = 0.0287 P_r^{-0.4} Re_x^{-0.2} \rho u c_p \quad \textbf{(4-10)}$$

Two additional parameters, C_1 and C_2 are included. C_1 equates to an offset streamwise distance, whereas C_2 captures the increase in heat transfer due to the disruption in the boundary layer caused by coolant injection. Each film hole is modelled individually and then superimposed using the Sellers

superposition approach described by Equation (4-7). This approach allows for a full 3D film effectiveness distribution starting at the leading edge of the cooling feature to be calculated.

4.5.1. Regression to experimental data

Figure 4-6 and Figure 4-7 illustrate the spanwise averaged film effectiveness values calculated using equation (4-9) plotted against experimental data in which C_1 and C_2 were selected in order to minimize R^2 for 12 and 13-row geometries on both the suction and pressure surface respectively. The mean R^2 value for these geometries is 0.999 with a maximum deviation in film effectiveness values of 0.03 - well within the range of experimental uncertainty. The main inconsistencies between the model and experimental data lie within the panel and the film holes themselves as the model is unable to predict values measured within the holes.

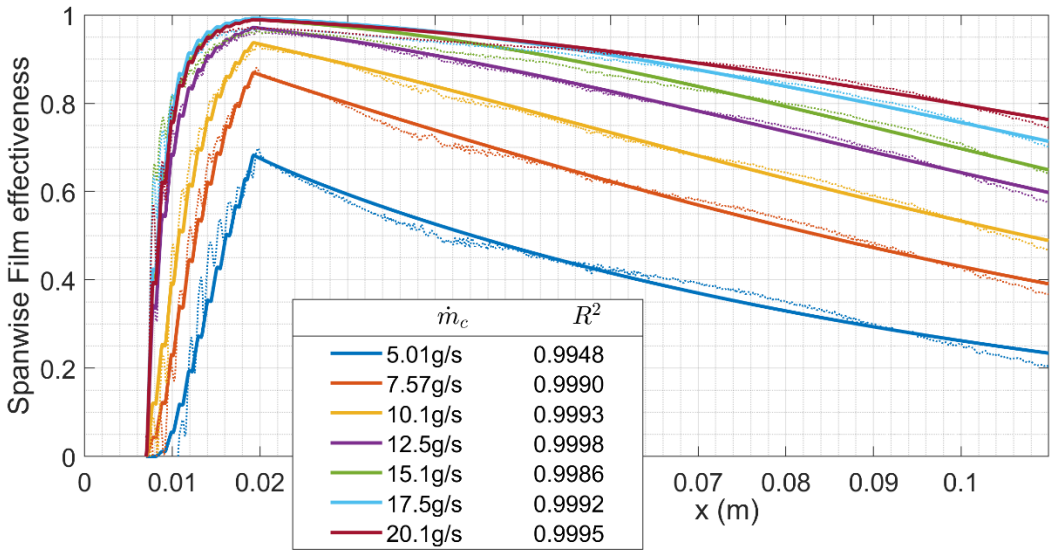


Figure 4-6 Best fit of Equation 9 (solid line) with experimental film effectiveness data (dotted line) of a 12-row staggered panel geometry located on the early suction surface

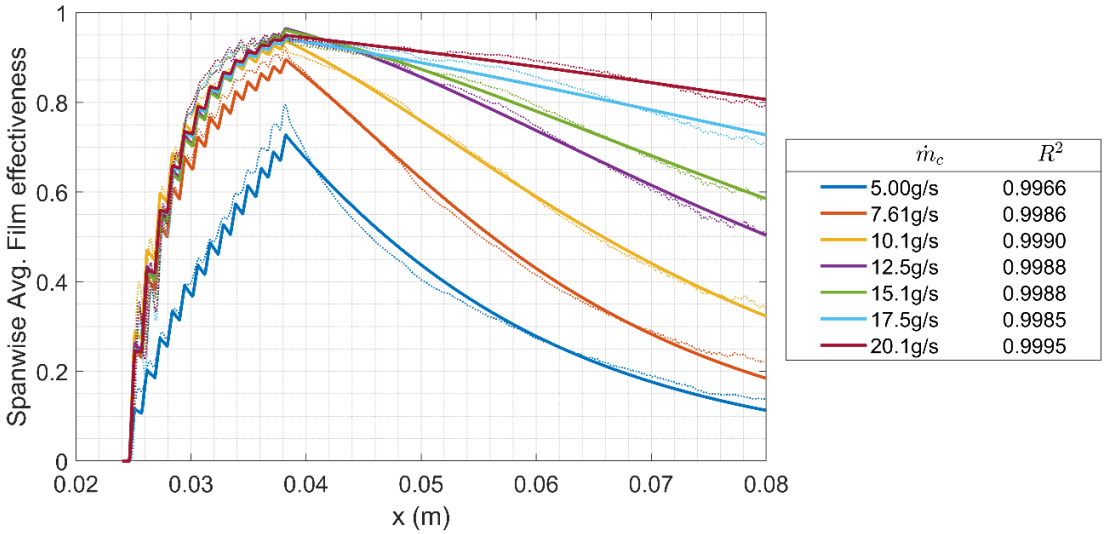


Figure 4-7 Best fit of Equation 9 (solid line) with experimental film effectiveness data (dotted line) of a 13-row staggered panel geometry located on the mid-pressure surface

The best-fit coefficients C_1 and C_2 for all geometries and mass flows are plotted in Figure 4-8 and Figure 4-9 respectively, with a minimum R^2 value of 0.985 across all geometries. This demonstrates that the form of Equation (4-9) is able to fit the film effectiveness data very closely with the greatest discrepancies occurring either at very high or very low blowing ratios where partial ingestion or lift-off could be expected.

C_1 is seen to be a strong function of velocity ratio (VR) as variations in coolant density were able to highlight. C_1, follows a similar trend for both the suction and pressure surface, with C_1increasing exponentially as VR approaches zero. C_1 is approximately 0.75 for intermediate VRs between 0.5 and 1.5 for both surfaces. When C_1 is a positive value, it can be proposed that the films generated by the high porosity features behave as if stemming from an imaginary tangential slot located $C_1 Mcp/hD$ upstream of the panel.

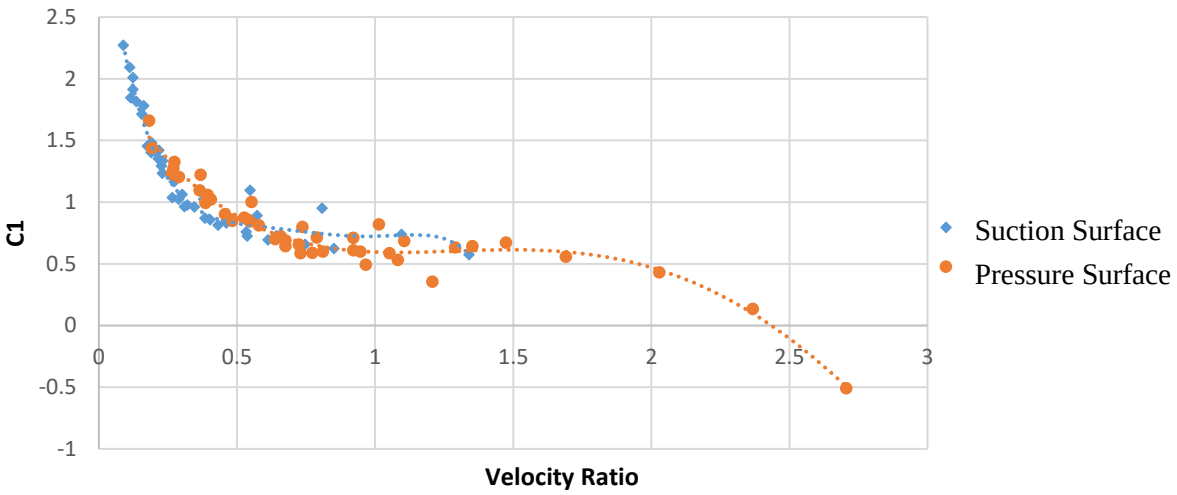


Figure 4-8 C1 values for the suction and pressure surface geometries against velocity ratio (VR)

C_2 values exhibit greater differences between the suction surface and pressure surface than the C1 levels for a range of blowing ratios. C_2 can be considered to capture the effects of coolant injection on the heat transfer coefficient, which in this case serves as a proxy for mixing in the boundary layer. In other words, C_2 acts much like β_e in Equation **(4-2)** and like β_e would be expected to be a function of blowing ratio. At low blowing ratios, C_2 increases logarithmically for both surfaces up to a blowing ratio of 0.6. As the blowing ratio is increased further, C_2 on the suction surface begins to increase again as the surface curvature pulls away from the coolant jets. On the pressure surface, however, the concave curvature allows C_2 to recover at moderate blowing ratios as the increased coolant momentum forces it closer to the blade surface. The discrepancy in magnitudes between the two surfaces however remains to be explained and indicates a fundamental difference in the behaviors of the films.

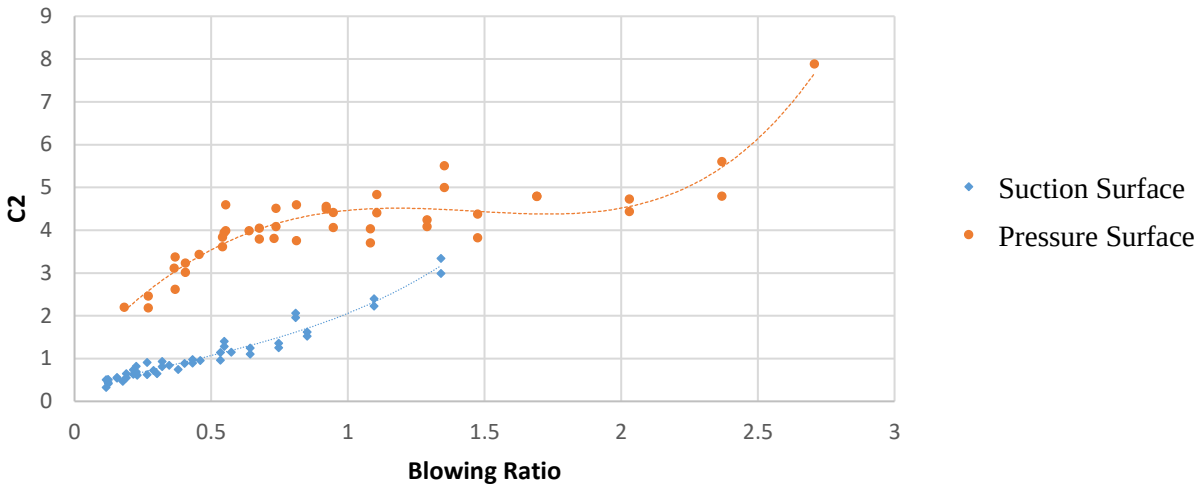


Figure 4-9 C2 values for suction and pressure surface geometries

4.6. General observations on C_1 and C_2

In order to attempt to find a generalised correlation for all the geometries tested for both surfaces, best fit splines were determined for all of the data and the model is run using values taken from the best fit line. With this approach, an average R^2 value of 0.96 was achieved with values ranging between 0.92 and 0.99. The spread of these values is principally determined by the results at the limits of the range of blowing ratios where ingestion or lift-off may occur.

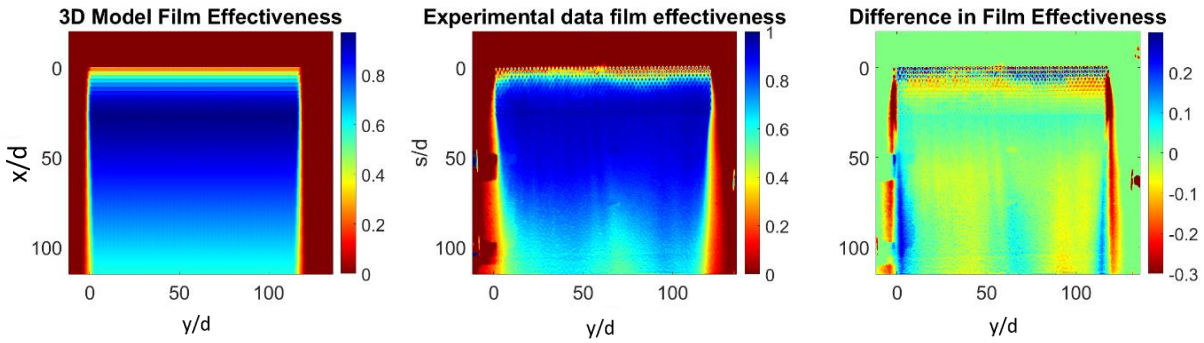


Figure 4-10 Comparison between film effectiveness levels predicted by correlation and experimental data

Figure 4-10 plots the full spatial distribution for an example geometry using the curve fitted C_1 and C_2. Comparison between the experiment and model illustrates the high degree of accuracy of the model. The primary discrepancies between the two, highlighted by the rightmost figure are close to the panel edges where the experiment shows a higher degree of spanwise spreading as well as the development of vortices. As previously mentioned, these effects can be captured to some degree by more

evolved lateral spreading models. However, with the aim of minimizing complexity and concentrating on the overall bulk of the panel, this task has been left as future work. Minor discrepancies are also noticed between the film holes of the first 4 to 7 rows where the lift-off of individual holes (experimental data) as well as variations in individual film holes is observable. Overall, with the exception of regions dominated by secondary flows, this method proves to be highly successful.

4.7. Discussion

A final analysis of the model can be carried out by testing the film effectiveness model on flat plate data taken from another experimental facility. Flat plate data taken from Courtis (Courtis, et al., 2021) was used to generate C_1 and C_2 values in the same manner.

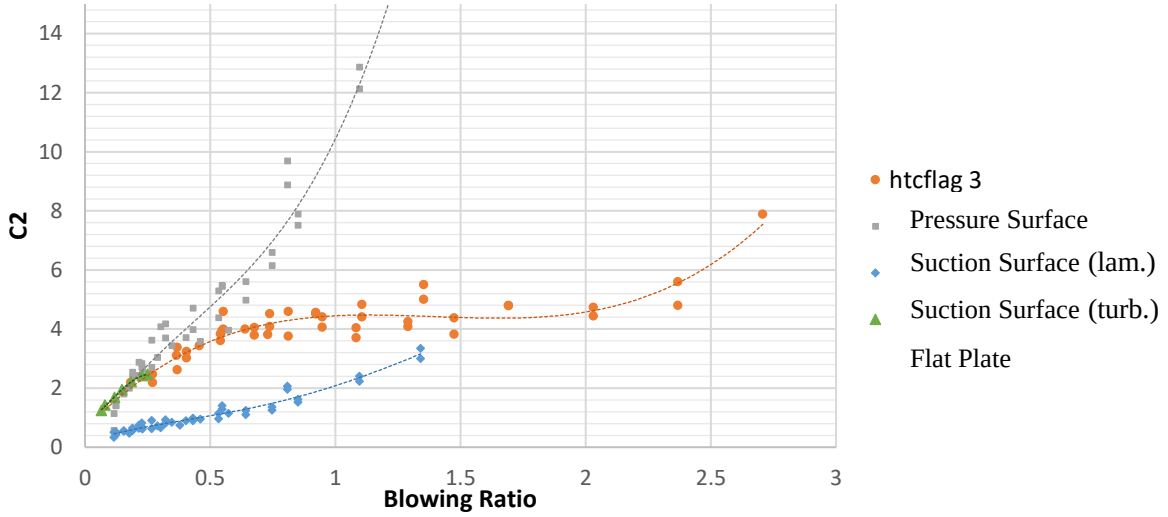


Figure 4-11 C2 values for equivalent geometries across suction surface, pressure surface and flat plate.

Comparing C_2 values from similar panel geometries in all three setups indicates that both the pressure surface and flat plate exhibit a similar trends with blowing ratio (Figure 4-11). The data shows that the C_2 values for the suction surface are significantly lower than that for the pressure surface at low blowing ratios - approximately one-quarter up to a blowing ratio of 0.5. Since C_2 governs the rate at which the film decays with distance, the large difference between the suction surface and the other surfaces offers yet another illustration of how films on the suction surface behave significantly differently from more conventional geometries.

By assuming the suction surface flow is in fact laminar, however, the equation for *h* can be replaced with a laminar alternative given by Equation (4-11) and values for C_2 recalculated. Here, a significantly higher value of C_2 is calculated for the suction surface which lines up closely with pressure surface and flat plate values at low blowing ratios.

$$h_l = 0.332 P_r^{-\frac{2}{3}} Re_{h,x}^{-0.5} \rho_h u_h c_p \tag{4-11}$$

As the blowing ratio is increased, the effect of curvature becomes more significant and the suction surface films are blown further into the mainstream resulting in more mixing. On the concave surface, the effect is reversed and increased blowing ratios push the film closer to the blade surface, minimizing additional mixing. Overall however, the close agreement between the three surfaces at low blowing ratios indicates that the relaminarization of the flow on the suction surface most likely explains the significant reduction in film degradation. Lastly, when using the laminar assumption on the suction surface, all values of C_2 are calculated to be above unity. This better matches the intended description of C_2 being a penalty incurred due to the film injection into the boundary layer. If the turbulent assumption of the suction surface boundary layer were maintained, the addition of films would appear to reduce the heat transfer expected within the boundary layer. In Figure 4-12, C_1 is also seen to shift such that the values for a flat plate lie between the convex surface and concave surfaces indicating a sensitivity to curvature.

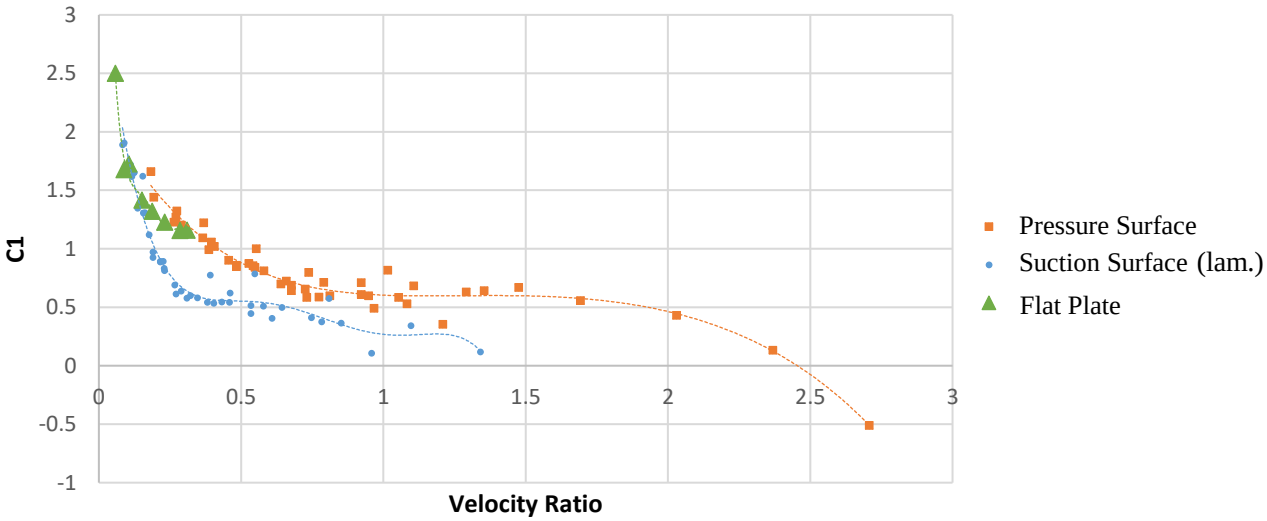


Figure 4-12 C1 values for flat plate data between pressure surface and laminar suction surface

Whilst a significant assumption to make, the acceleration parameter K on the suction surface is known to exceed values required for relaminarization, between 1 and 3.5x10-6 (Kays & Crawford, 1980). Furthermore, the very low blowing ratios and Reynolds numbers within the film cooling holes located at or upstream of this region of strong favorable pressure gradients offer a geometry which minimizes the increase in turbulence within the boundary layer.

4.8. Conclusions

An investigation into the film effectiveness levels of high porosity film cooling features has been carried out. First, it was demonstrated that after a given downstream length, films behave as heat sinks in a fully developed turbulent boundary layer, following the trends of typical 2D film models. However, this region is preceded by a core-like region in which mixing between the mainstream and film coolant is reduced. This core length is increased by reducing individual film hole diameters, blowing ratio, and increasing the overall mass flow.

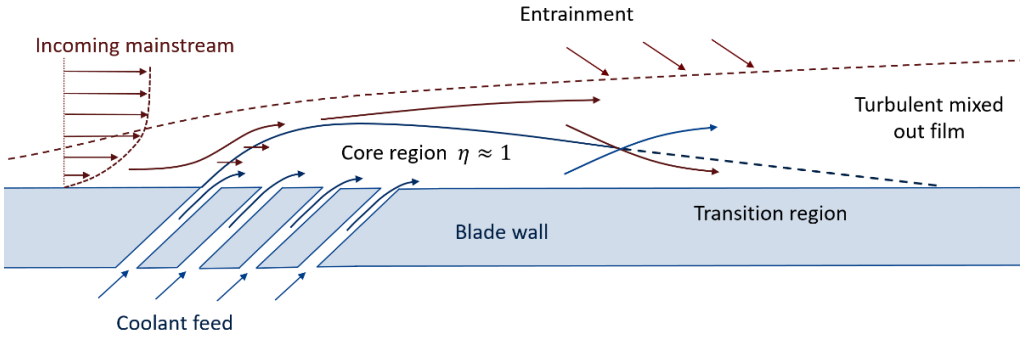


Figure 4-13 Conceptual model of high porosity films

This results in the significant conclusion that like slot cooling, transpiration cooling does not simply reduce the boundary layer temperature but also acts as a physical barrier between the mainstream and blade surface within the core region.

The correlation proposed was successful in predicting the film effectiveness with a high degree of accuracy as well as with a reasonable level of spatial resolution around the individual film features. Secondary effects are not captured, however, the robustness of these panels means that these effects are mostly insignificant. Again, the model points towards the similarities between the panel geometries, tangential injection slots and transpiration cooling.

Comparing results from both the pressure and suction surface has pointed towards the possibility that low-blowing ratio films on the early suction surface remain in the laminar regime due to the high acceleration parameters potentially explaining the exceptional film effectiveness levels observed.

Extensive work remains to be carried out concerning the investigation of turbulence levels within the suction surface boundary layer as well as the effect of very low blowing ratio films being ejected within the region of relaminarization.

The conclusion which can be taken from these modelling approaches lies in the fact that the high porosity panel geometries share the same film cooling trends as both tangential slots and porous sections. Whilst not yet equivalent, the shared trends indicate that the development of transpiration-like cooling features is both achievable and within reach.

Acknowledgments

The authors wish to express their thanks for the ongoing support provided by both Rolls-Royce PLC and the EPSRC through (EP/P000878/1). The authors would also like to thank the technicians at the Oxford Thermofluids Institute for their assistance in the manufacturing of the experimental setup and Dr Matt Courtis for his help with the preparation of Figure 4-11 and 6-12.

5. Study of Interactions between Closely Spaced Films Used in Novel High Porosity Turbine Cooling Designs

After the analysis of a wide range of film effectiveness results of high porosity geometries, certain phenomenon still remained unexplained. Two separate lines of enquiry were taken on in order to further investigate the reason behind the high film effectiveness levels. The first, was whether existing CFD models could predict the film effectiveness levels measured by the PSP experiments. The second, was focused on explaining why the staggered geometries significantly out performed the inline geometries as well as showing little to no sign of film lift off, despite very high blowing ratios.

The first investigation proved very challenging, and eventually, it was concluded that conventional CFD (RANS) models would not be able to adequately model the film effectiveness levels measured within the experiments. Numerical results consistently overpredicted the decay of film effectiveness beyond the immediate film hole region, despite the experimental facility being modelled to a high degree of fidelity. It was hypothesized that this was due to the overprediction of turbulence by the numerical models and the inability to mode the relaminarization hypothesised in the end of the previous chapter. However, as a satisfactory conclusion was not achieved, this section of work has not been included in this document.

The second area of investigation focused on the region that was modelled to a reasonable degree of agreement by the numerical tools at hand. However, as it had already been concluded that the accuracy of CFD could pose a challenge, the paper included in this chapter focuses on investigating and explaining the mechanisms increasing film effectiveness within the high porosity panels as opposed to focusing on obtaining a perfect match with results or developing a new numerical model to better predict the

results. The paper included in this chapter was presented at the 15th European Turbomachinery Conference (ETC2023-297) in Budapest Hungary April 2023. This paper was written under the supervision of Professor Peter Ireland.

Study of Interactions between Closely Spaced Films Used in Novel High Porosity Turbine Cooling Designs

A.Wambersie – P.T. Ireland

Department of Engineering Science, University of Oxford
Oxford OX1 3PJ, UK
Email: augustin.wambersie@eng.ox.ac.uk

Abstract

High porosity arrays of small film cooling holes offer a practical alternative to transpiration cooling whilst also having the potential to be manufactured. As these discrete cooling features are spaced closer together than conventional rows of holes, interactions between individual films become increasingly significant. Experiments by the authors, at engine representative conditions, suggest that local film effectiveness levels can vary by over 30% because of changes in these interactions.

This paper demonstrates how these interactions are governed by the interactions between the counter-rotating vortex pairs that issue from the holes, and the variations in the boundary layer velocity as the coolant film develops. Significantly, film lift-off can either be encouraged or suppressed completely- depending on the hole arrangement selected. An understanding of how films develop can be exploited by turbine blade designers to produce high performance films. The paper shows that the appropriate combination of interactions resulting from carefully engineered hole spacing pushes the hot mainstream gas away from the blade surface completely, resulting in film effectiveness ratios approaching unity. In addition to dramatically improved film effectiveness levels, these results suggest that new geometries should be optimized differently from conventional films as the performance of individual holes is decoupled from that of the hole array.

Keywords: Film effectiveness, Transpiration cooling, High porosity, CRVP, counter-rotating vortex pair

Nomenclature

d	Film hole diameter (mm)	η_{film}	Film effectiveness
P_1	Streamwise hole pitch (mm)	M	Blowing Ratio
P_2	Spanwise hole pitch (mm)	x	Streamwise distance (mm)
W_c	Coolant mass fraction	y	Spanwise distance (mm)

5.1. Introduction

Recent work at Oxford University (Ngetich, 2019) (Jiang, et al., 2019) (Courtis, et al., 2021)(Wambersie et al. 2021) has shown that film cooling systems, that use multiple rows of films, have the potential to deliver much improved film cooling compared to conventional film cooled designs. The increased (relative to conventional) proximity of such multi-holes designs has increased the significance of fluid dynamic interaction between the films issuing from the cooling holes. Therefore the investigation and characterization of these effects if of utmost importance for the further development of high density cooling arrays.

Since the introduction of film cooling in the 1960s, the influence of refinements in the geometry of the film holes (for example through the use of a fan shaped exit, variations in the angle of layback or the use of compound angles) has been carefully studied in order to maximize their individual downstream film effectiveness. The use of a fan-shaped diffuser has been shown to improve lateral coolant distribution as well as to contribute to the dissipation of the counter-rotating vortex pair (CRVP). The suppression of the CRVP helps spread the film across the blade surface and reduce downstream mixing between the coolant and the hot gas as well as significantly reducing film lift off. The success of fan shaped holes (high effectiveness and high discharge coefficient) means that rows of fans are typically spread far (20d-60d) apart in the mainstream flow direction which minimizes the scope for interaction between the rows of films.

With new, closely packed effusion and transpiration-inspired designs however, these interactions can no longer be ignored as film holes are spaced within 2-3 diameters of each other in both the spanwise and streamwise directions. Under such close hole spacing arrangements, the films do not have sufficient flow distance to dissipate and become fully developed before reaching the next film row, meaning coolant streams interact as discrete jets. Even at more moderate pitches (5-10 P/*d*), the velocity profiles and vortices developed by the jets within the boundary layer are enough to significantly change the performance of other films within the wake region of the respective upstream hole. In a review of effusion

cooling research, Krewinkel (2013) similarly noted that the application of fundamental, flat plate understanding of basic cooling features would no longer suffice in fully understanding effusion systems and that these had to be studied directly.

Under these conditions films no longer behave as predicted by single row flat plate experiments, with this difference being heightened at blowing ratios over 0.6 . Murray et al. (2018) demonstrated that the widely used Sellers superposition method (Sellers, 1963) fails to capture any of these interactions and, at best, can only be reliably used for large hole pitches above 10-15*d* and at low blowing ratios. These caveats bring into question the utility of optimizing holes individually as well as modelling them as individual features. The resultant lack of any appropriate analytical representation of the films leaves the cooling designer only experimental and computationally expensive numerical tools.

These same high-density film cooling arrangements have proven to yield exceptionally high film cooling effectiveness levels through the use of low blowing ratios and high porosity. Therefore, the study of film interactions within this context is of great interest with previous studies on such high porosity designs demonstrating that the difference between inline and staggered arrangements on suction surface cooling panels can lead to variations of up to 30% mean film effectiveness (Wambersie, et al., 2021).

Many studies on double-row film cooling designs have demonstrated that certain arrangements can perform better than the sum of two single rows. Jubran and Brown (1985) demonstrated that, the closer the spacing between the two staggered coolant rows, the greater the improvement in film cooling. It was highlighted that the development length was a crucial factor for film-film interactions, which is also influenced by blowing ratios. In a numerical study on similar staggered double row arrangements, Jiang et al. (2018) determined that significant improvements also exist at high blowing ratios where the films are expected to lift off. Under some conditions, the presence of the second row is seen to reattach the first row after it has lifted off, with the second row also reattaching itself shortly after. By comparison, the individual rows did not reattach at all under the same conditions. These effects were largely attributed to vortex interactions. Saumweber and Schulz (2004) highlighted that the geometry and flow conditions at the second row dominated the first in the instigation of the reattachment of films.

An alternative approach exploited these same vortex interactions to reverse the effects of lift-off caused by the CRVP altogether (Kusterer, et al., 2007). By combining two or more holes with compound angles, the vortices interaction can be tuned. This approach was often demonstrated to achieve a certain degree of success with the vortex pair interaction effectively being reversed which promoted coolant attachment to the aerofoil surface as well as lateral distribution of the film (Graf & Kleiser, 2014). Conversely, while immediate film attachment and film cooling is increased, the overall film effectiveness, particularly downstream was seen to suffer due to increased net turbulence and vorticity. For the case of fanned film cooling holes, despite having less significant vortices, these were still demonstrated to interact with each other when spaced sufficiently close. Renze et al. (Renze, et al., 2009) showed that, while the path of the vortices was slightly further apart due to the width of the fan, the films could still interact with staggered holes to form a flow downstream that promoted film attachment.

The interactions between film rows can have significant negative consequences as well. Sinha et al. (1991) found that the presence of film cooling holes upstream of an ejection point increases the boundary layer thickness upstream of the second row. Baldauf et al. (1997) described the length required for the boundary layer velocity distribution to return to normal, as the formation or recovery length and demonstrated its dependence on Blowing Ratio (BR). Beyond this distance, the film was described as having become fully developed. The resultant reduction in apparent incoming mainstream velocity around the hole results in the downstream film penetrating deeper into the mainstream for the same coolant velocity since the tendency of a film to lift off is increased as the ratio of coolant velocity to hot gas velocity is increased. This effect is further magnified for smaller film hole diameters with scales approaching the boundary layer thickness. For smaller pitches of inline holes, Wang et al. (2020) showed that this effect was more pronounced as the downstream hole demonstrated significantly more lift-off and larger CRVPs than the rows upstream. Even at moderate spacings in multi-row geometries, this inline effect was seen to dominate the film behavior, as vortices from adjacent holes were positioned too far apart to bridge the spanwise spacing. For these geometries, the resultant flow field can effectively

be modelled as columns of independent inline holes. As the number of rows is increased in multi-row cooling systems, this effect is compounded as is shown by Jiang et al. (2019)

The negative outcome of lift-off is two-fold: not only does the coolant detach from the surface; the mainstream also becomes energised close to the aerofoil surface in a highly turbulent manner, resulting in an increase in heat transfer coefficient (Baldauf et al, 1999). Each consecutive row further increases the turbulence in the boundary layer and consequent mixing with the mainstream. The difference in possible outcomes resulting from film interactions illustrates the complexity of this highly 3-dimensional problem.

The aim of the research reported in the present paper is to highlight two possible mechanisms through which multiple films interact with each other within an extensive film hole array. The effectiveness data for the geometries used also demonstrates the potential benefits of maximizing these effects. RANS numerical modelling is used in this investigation allowing the fluid domain modelling to be greatly reduced (compared to LES or DNS) and simplified for the purpose of this analysis. The ability to visualise individual streamlines and flow features at a very small scale further warrants the use of numerical simulations over experimental methods for this study.

As mainstream variables such as acceleration, surface curvature, turbulence, and individual hole geometries all have significant impacts on film structures and their potential interactions, engine representative flow conditions and geometries were used in the present study.

5.2. CFD setup and domain

The fluid domain in Figure 5-1 was chosen to match a region of the experimental test facility used by Wambersie et al. (2021). It consisted of the suction surface of a single high-pressure turbine blade with the span of the domain consisting of a single spanwise film hole pitch. Periodic boundary conditions were used on the flat surfaces bounding the domain to represent the periodic (in the spanwise sense) nature of the geometries being tested.

The cooling geometries consisted of arrays of small film cooling holes located on the early suction surface of the blade, 15*d* from the geometric leading edge. This region was chosen as the effects

of the interactions between holes were already known from experiments (Wambersie et al 2021) to be particularly significant when compared to the slower-moving, more turbulent pressure surface.

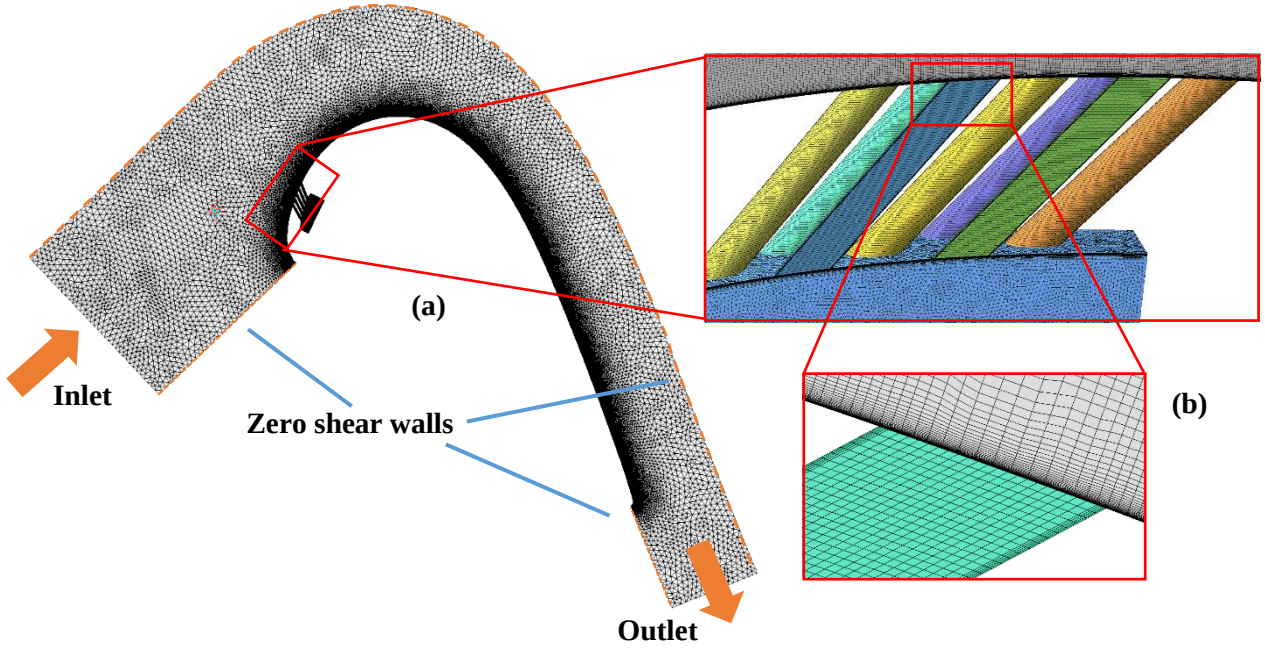


Figure 5-1 (a) Fluid domain and (b) detail of holes and interface

The choice of mesh size was initially informed by previous sensitivity studies by Jiang, et al. (2019) on similar effusion geometries who recommended 26 elements across the hole span to avoid mesh sensitivity issues. This value was dropped however to 20 elements per hole before any mesh sensitivity issues were encountered. The bulk of the mesh was unstructured tetrahedral with prism inflation layers being used in the holes and boundary layers. The turbulence model used was K-ε with enhanced wall treatment and with Y+ values kept below 3. The overall mesh size used was approximately 13M elements.

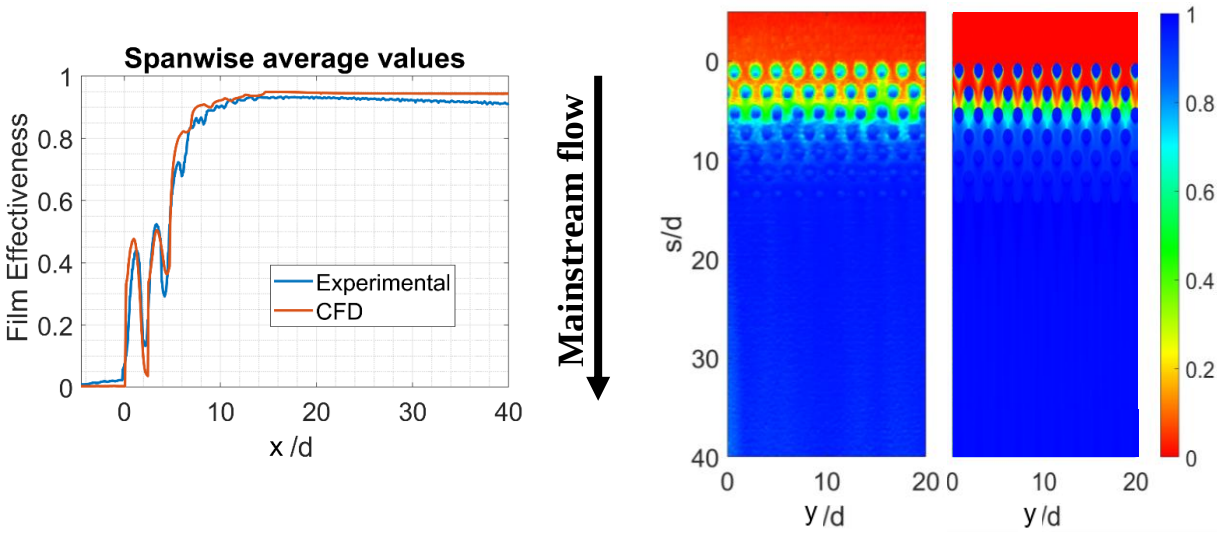


Figure 5-2 Comparison between Experimental (left) and numerical CFD (right) film effectiveness levels on the Suction surface for a 7-row panel at M = 1.06 .

All of the boundary conditions used matched the experimental conditions in Wambersie et al (2021) with the exception of the coolant temperature which was reduced by 50K in order to allow for a non uniform temperature field to be established. Comparison with the experimental data confirms excellent agreement between the CFD results and experimental data close to the film cooling holes, with film effectiveness surface plots indicating similar distributions as shown in Figure 5-2, with the majority of discrepancies being due to the lower resolution achievable with the experimental method. Spanwise averaged values reflect this and illustrate that the overall development of the film is closely matched between experimental and numerical results. However, as the film begins to decay, the models begin to diverge from experimental values regardless of the turbulence model or mesh resolution used. In light of these limitations, results will focus on interactions near the film holes, where numerical models are most accurate.

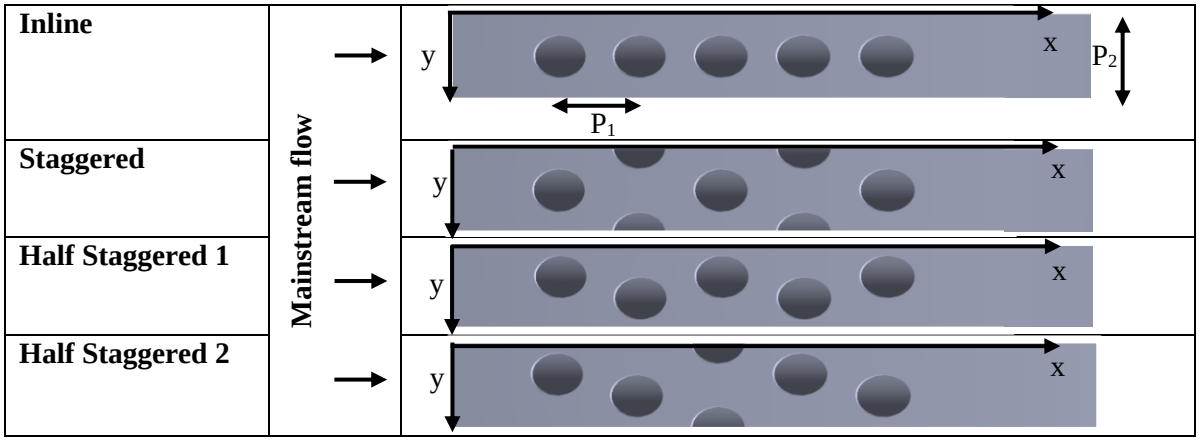


Figure 5-3 Hole positioning of main row geometries

The geometries tested consist of 5, 0.5mm diameter film holes with a streamwise pitch of 2.1 diameters. The relative positions of the film holes are illustrated in Figure 5-3. The holes are inclined at 45 degrees to the blade surface in the streamwise direction. For the inline geometry, holes are positioned in a row, whereas for the staggered geometry, rows 2 and 4 were offset by half the spanwise pitch. Two alternate geometries are also presented, with Half Staggered 1 offsetting rows 2 and 4 by a quarter of the spanwise pitch and Half Staggered 2 offsetting each row by a quarter of the pitch relative to the hole immediately upstream. A small feed plenum was added at the base of the film holes.

5.3. Results

5.3.1. Comparison between basic geometric arrangements

Figure 5-4 plots the area average film effectiveness levels over the region downstream of the film holes across a range of blowing ratios. The plots include the inline, staggered and half-staggered geometries as well as the superposition (Sellers, 1963) of the 5 rows simulated individually which would be effectively identical between geometries.

At low blowing ratios , all geometries match the effectiveness of the predicted superposition closely. Here the films are largely within the mass addition regime and are completely attached to the blade surface. The low blowing ratios also minimize any vortices and potential interactions between them. The superposition hole film effectiveness begins to fall behind other geometries at a blowing ratio

of 0.6 and degrades significantly beyond a blowing ratio of 1 at which point film lift-off occurs. Between blowing ratios of 1 and 1.2, the predicted Sellers superposition are still able to reattach further downstream with a minimal penalty to the downstream film effectiveness. Beyond these blowing ratios the films lift off completely, with film effectiveness only beginning to recover past blowing ratios of 1.7 where excessive mass flow and secondary effects become significant. By comparison, the staggered geometry is effectively unaffected by lift-off as its data forms a smooth continuous curve.

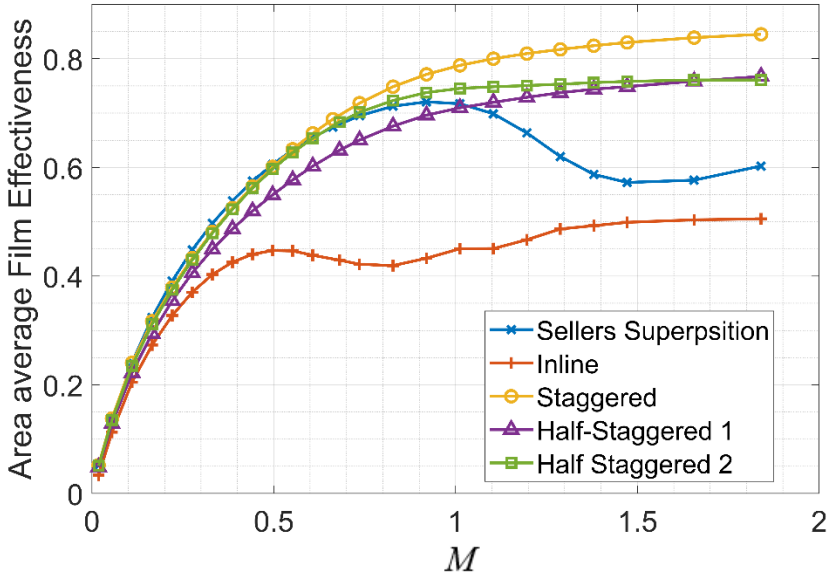


Figure 5-4 Film effectiveness levels of the four basic geometries and superimposed baseline

The inline geometry by comparison begins to drop off significantly in relative performance at a blowing ratio of 0.3, reaching a plateau at a blowing ratio of 0.5. The approximate 30% reduction in film effectiveness matches findings from past experiments comparing these two geometries (Wambersie et al. 2021). Both Half-Staggered geometries appear to be similarly unaffected by film lift-off, but their effective levels remain below the conventional staggered geometry.

Film effectiveness charts plotted in Figure 5-5 offer a means to understand the distribution of films near the cooling holes for each of the geometries. Whilst some films are able to reattach further downstream, focusing on this region best illustrates the differences due to interactions between films. The charts show a periodic repeat to improve legibility. The Inline geometry lifts off immediately above blowing ratios of 0.6, with no film cooling evident for blowing ratios above 0.8 beyond 1d of the last

film hole. Mainstream gas is also seen to be present at the wall between the holes, with film effectiveness levels of zero evident. Film effectiveness levels slowly build up as the mainstream and coolant streams mix. The half-Staggered 1 geometry behaves in the most similar way (to the Inline geometry), however, the outer halves of the film holes are seen to better attach and the mainstream penetration between the holes is much more limited.

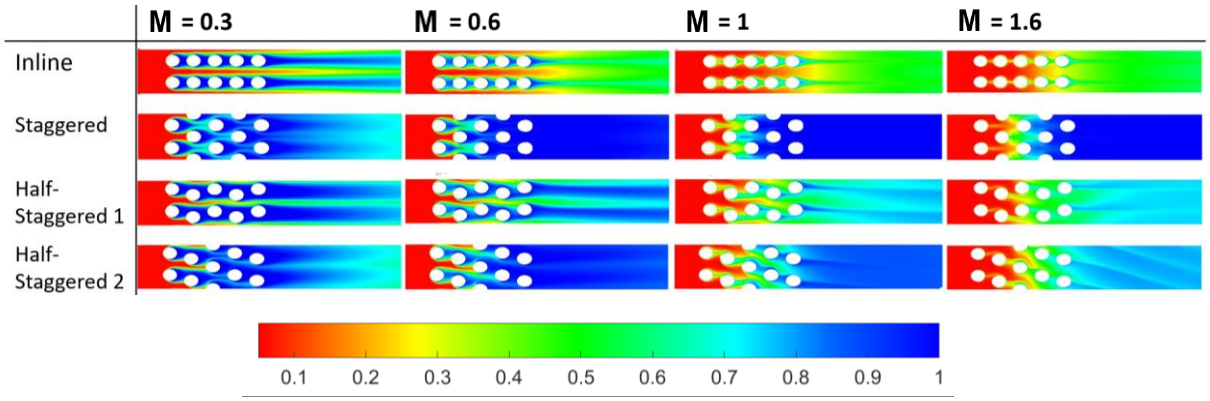


Figure 5-5 Film effectiveness levels of near hole region for different geometric arrangements with $P_1/d = P_2/d = 2.1$

Half-Stagger 2 and the fully Staggered geometry appear to show similar levels of film effectiveness saturation at a blowing ratio of 0.6, with only traces of mainstream gas reaching the surface by the fourth row. When the blowing ratio is increased to 1 and above, the fully staggered geometry is the only one to remain fully attached. Whereas the first row is seen to lift off completely, with film effectiveness levels of zero between rows 1 and 2, the film effectiveness level is nonetheless completely saturated by the fourth row. Meanwhile, Half Staggered 2 begins to lift off as well as to funnel the mainstream into a diagonal direction. Given the equivalent mass flow and streamwise positioning of the individual holes, the large variation in film effectiveness shown in this Figure can be entirely attributed to film-film interactions; something that is particularly relevant when one attempts to superimposed solutions.

5.3.2. Effect of combining film holes – Discussion of the Effective Blowing ratio

The contribution that the respective rows of film holes make for each geometry considered is explored in the simulations summarized in Figure 5-6. Combinations of films at either the coolant or

mainstream temperature are studied for different configurations of double flows (together with the baseline single row) at different blowing ratios.

In the first example (1) of two staggered rows, the first-row temperature is set to match the mainstream, with only the second row being cold in order to isolate its contribution to film effectiveness. Film effectiveness is significantly improved relative to the baseline for all blowing ratios above 0.3. It appears that, as the mainstream is constricted between the holes of the most upstream (1st) row, the freestream is accelerated ahead of the second row, reducing the effective blowing ratio for the second row thereby suppressing lift-off. Meanwhile, the inline arrangement (2), presented in the second row in Figure 5-6, demonstrates the opposite effect, with the downstream row demonstrating an increased propensity to lift off. In this case (2), since the downstream row is inline with the upstream row and experiences the wake from the upstream row, the 2nd row experiences a slower incoming mainstream, equivalent to a thicker boundary layer resulting in an artificially higher blowing ratio.

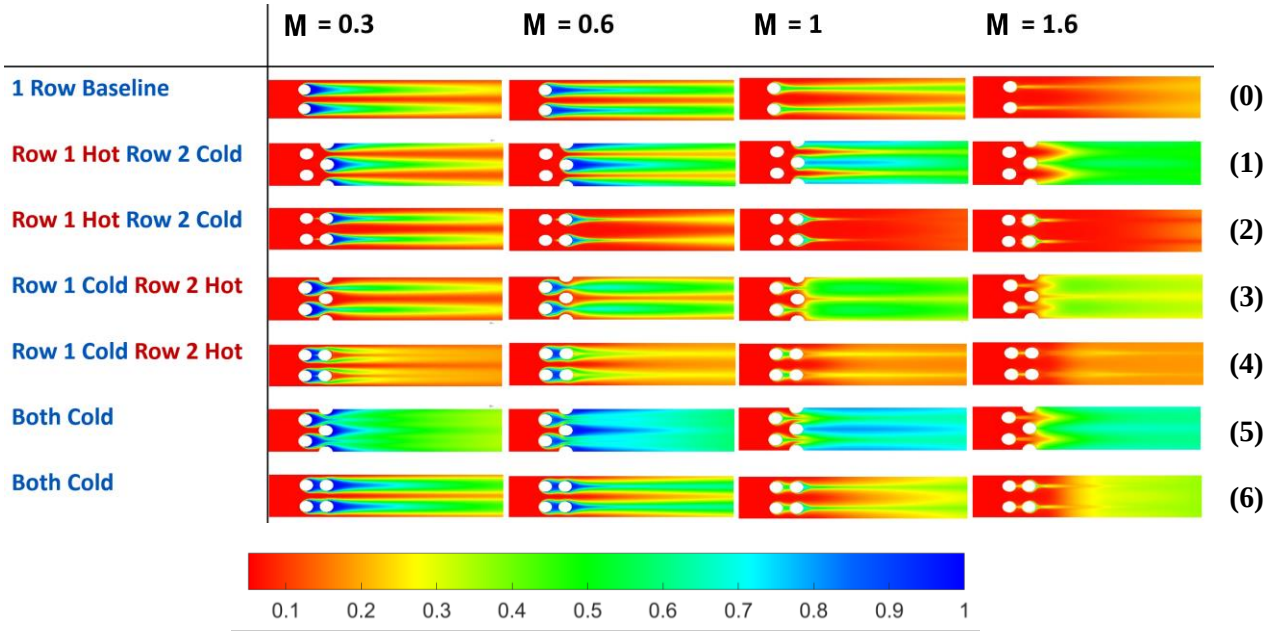


Figure 5-6 Film effectiveness distribution due to different possible interactions between two rows of films

Figure 5-7 summarizes the results of many simulations, for the baseline case, and allows an in-depth analysis of this effect and contains contour plots of the velocity deficit of the mainstream 0.3*d* above the blade surface for different blowing ratios. Figure 5-7(a) indicates the velocity deficit directly

downstream of the hole relative to the same mainstream flow with no hole. The greatest loss is incurred around a blowing ratio of 0.55 immediately downstream of the hole. This is to be expected as this represents the maximum streamwise mass velocity flux deficit added by a coolant hole at 45 degrees. Crucially, any subsequent hole within 40*d* of the upstream film hole will experience a significantly and artificially higher blowing ratio. In practice, secondary effects, such as a reduction in capping will further increase the mass flow through the downstream holes for a fixed feed pressure, further increasing the effective blowing ratio.

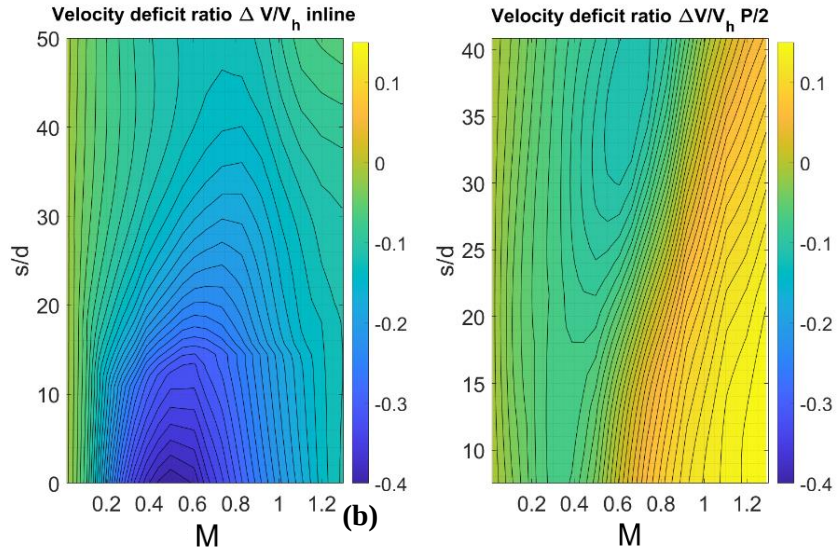


Figure 5-7 Variation in velocity downstream of a single film row 0.3*d* above the blade surface

Values taken half a pitch away from the hole centreline in the span wise direction in Figure 5-7(b) show a different behavior, with little to no effect being observed at low blowing ratios. As the blowing ratio is increased to 0.6, the velocity deficit caused by the injection of slow moving coolant extends spanwise across the pitch and becomes significant over 25*d* downstream. Increasing the blowing ratio above 0.6 however has the effect of accelerating the flow between the two cooling rows as the coolant jets begin to block the mainstream near the blade surface. Holes located in between two upstream films that are lifting off will experience an effective reduction in blowing ratio as the upstream mainstream is accelerated by up to 15%.

When the temperatures of the two rows in Figure 5-6 are reversed, the first staggered row in (3) is minimally affected at low blowing ratios, with the exception of a narrowing of the film between

the second row. However, as the blowing ratio is increased, the film is seen to lift off, but then immediately reattach past the second row. The predominant effects for this behavior are discussed in the next section. For the inline geometry in (4), the first row is merely pushed off the surface by the second, reducing film effectiveness throughout. The combination of these effects result in the differences seen in (5) and (6). The addition of more rows is seen to further enhance all of the effects demonstrated so far. Overall, close-packed films demonstrate the ability either improve or reduce film effectiveness of other films both upstream or downstream.

5.3.3. Effects of interactions between CRVPs

At higher blowing ratios, the film effectiveness distributions can no longer be described by the simple variation in apparent mainstream velocity. Figure 5-6 indicates that even once films have fully lifted off, reattachment still occurs downstream of the second row. This behavior repeats itself to some degree at every combination of staggered film holes. Experimental data in Figure 5-2 reaffirms this effect, with a step in film effectiveness being visible first at row 3, and then again at row 4, where rows 1 and 2 reattach respectively.

This effect has been recreated on both the pressure surface and suction surface and is seen to be independent of hole size (Wambersie, et al., 2021). The location of reattachment is consistent with the location of the low-pressure region created by the second row. These are indicated in Figure 5-8 and are particularly strong at high blowing ratios where the film requires a large force to be turned. Low-pressure regions underneath films typically result in the entrainment of mainstream gas from the sides of the hole into the bottom of the boundary layer, significantly increasing the local heat transfer coefficient and reducing the overall cooling effectiveness. Conversely, by staggering the films appropriately, the low-pressure regions are able to reattach the films as opposed to aspirating mainstream gas.

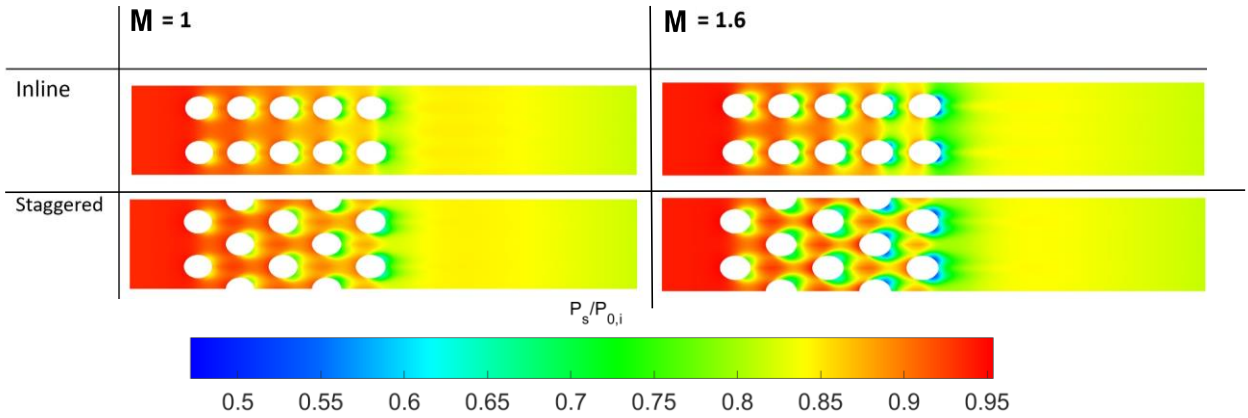


Figure 5-8 Static pressure ratio distribution around film holes at high blowing ratios

In order to better demonstrate this effect, Figure 5-9 illustrates the streamlines of the inline and staggered arrangements. With the inline arrangement, where film lift-off is promoted within each subsequent row, streamlines originating from the mainstream inlet are seen to continuously be pulled under the film and end up below the bulk of the coolant film. As the film lifts off, and the blowing ratio is increased, additional streamlines from beyond the boundary layer are pulled beneath the film. The streamlines originating from the film holes eject right into the upwash of the previous film holes' CRVP, forming an even greater vortex. This has the added effect of pulling mainstream gas into the low-pressure region immediately downstream of the holes below the films.

For the staggered case, the mainstream streamlines are completely removed from the blade surface. Downstream of the feature, streamlines originating from upstream holes are seen to sweep underneath the final film hole which has itself mostly separated. This demonstrates that despite exceeding typical blowing ratios, particularly towards the trailing edge of the panel, film lift-off does not result in a reduction in film effectiveness. Staggering the films with a small pitch-to-diameter ratio allows the upstream films to be pulled in by the low-pressure region formed by its neighboring films. Film holes are also positioned to be located within the downwash of the CRVP of the upstream row.

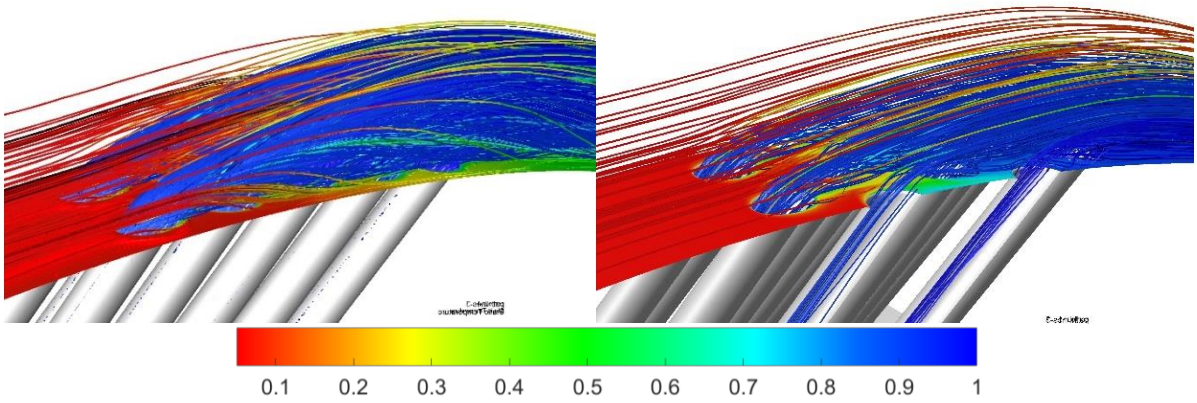


Figure 5-9 Streamlines of inline and staggered holes at M = 1 with colour representing film effectiveness

When plotting the vorticity magnitude downstream of the films (Figure 5-10), the inline arrangement demonstrates a single large feature developing and lifting off the blade surface. Maximum magnitudes are also over 20% higher than for the staggered case. Vortices formed by the staggered arrangement meanwhile completely dissipate within 4*d* of the final film hole. This is likely the result of the various vortices, offset by 1*d* in the spanwise direction being able to cancel each other out.

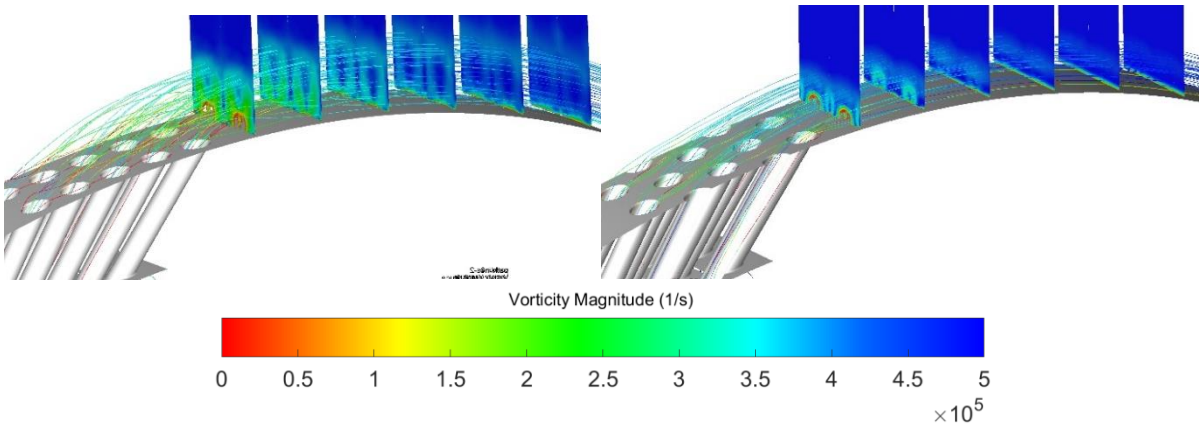


Figure 5-10 Cross section of vorticity downstream of the film holes at M= 1

5.3.4. Implications of interactions on designs: Effect of spacing

The implications of the interactions between film holes are very significant in the context of designing high porosity film cooling arrays. Streamwise spacing will impact both the effective blowing ratio experienced by downstream rows as well as dictate the strength of the vortices when they interact. At large streamwise pitches, the films experience the full velocity of the mainstream, reducing the local blowing ratio. The acceleration of the mainstream along the suction surface further reduces the blowing

ratio for a given mass flow rate. Whilst reducing the blowing ratio also reduces film lift-off, the beneficial interactions between films are also less significant. The combination of these two counter-acting effects results in intermediate spacings yielding the optimal arrangement dependent on the mass flow rate as shown in Figure 5-11. In order to compensate for the variation in mainstream velocity along the blade surface, the geometries were tested at the same coolant mass fraction. This mass fraction is equivalent to that of Figure 5-5. The optimal balance between the two competing effects is also subject to the coolant mass flow rate, with the optimal *P/d* ratio increasing as the mass flow is increased. At higher blowing ratios, the intensity of the CRVPs, velocity deficit and the tendency for individual films to lift off are all increased, favoring increased spacing. For inline holes, the same investigation indicated a strong positive correlation between streamwise pitch and overall film effectiveness as both effects discussed favor increased spacing.

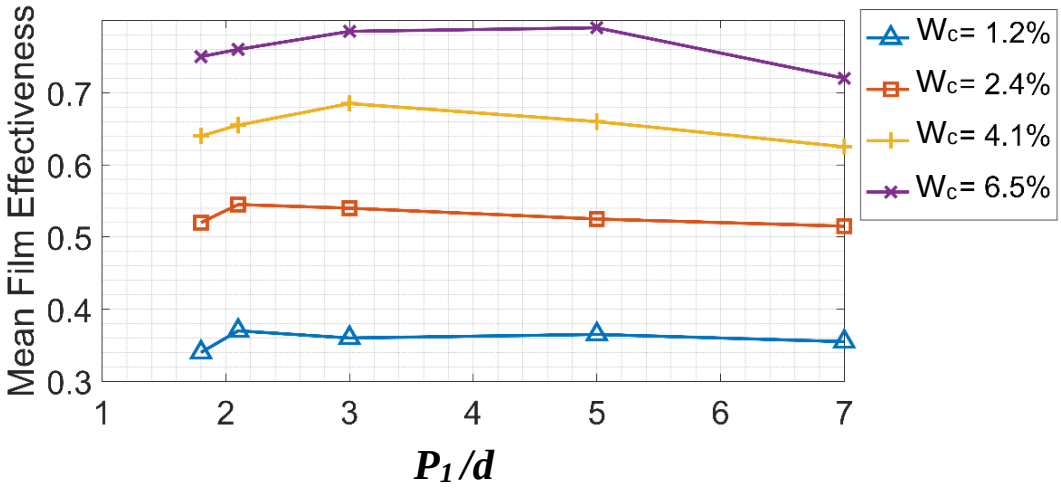


Figure 5-11 Effect of Streamwise spacing on film effectiveness for staggered geometry

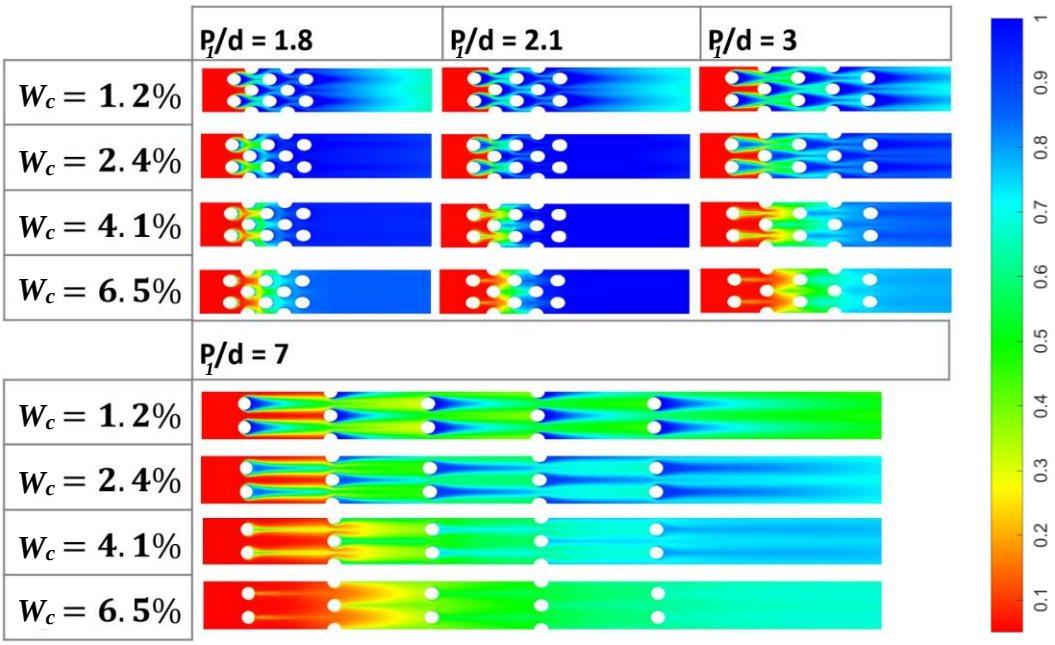


Figure 5-12 Detail of film effectiveness distribution with variation of streamwise pitch for P_2/d=2.1

Similarly, the variation of span wise pitch is closely linked to the interactions between vortices of adjacent holes, explaining the variation in film effectiveness levels shown in Figure 5-13. In order to compensate for the variation in overall domain size, the geometries were tested at the same coolant mass fraction despite this again varying the blowing ratio. At large spanwise pitches, the interactions between vortices are minimal, barring far downstream where the dissipated and weakened vortices are able to bridge the gap set by the spanwise pitch. Nonetheless, the interactions between films with spanwise P_1/d above 3 are closer to those of inline holes and the influence of effective blowing ratio dominates, with the mainstream also being able to penetrate through the rows resulting in an incomplete coverage between holes as shown in Figure 5-14.

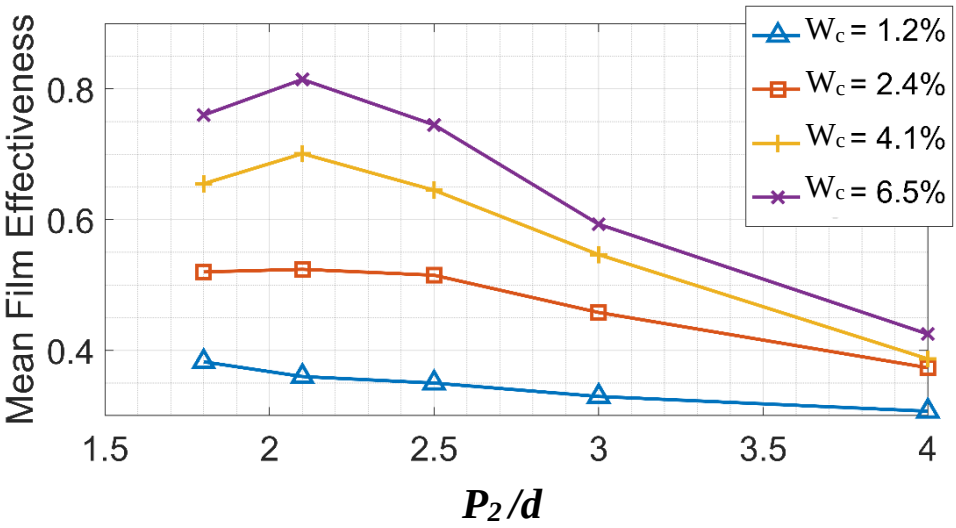


Figure 5-13 Variation of film effectiveness with spanwise pitch

Film effectiveness is seen to increase as the pitch is reduced from *P/d* = 4 to *P/d* = 2. Below this value, the holes begin to overlap with holes in the rows immediately adjacent, effectively halving the streamwise pitch and resulting in a drop in film effectiveness. Whilst not captured within the immediate film hole region, the effect becomes significant further downstream.

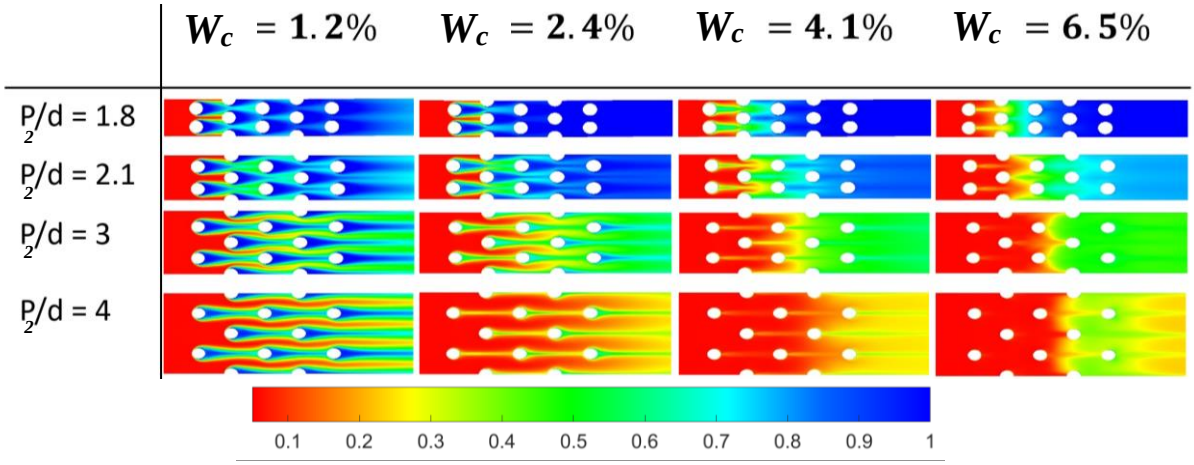


Figure 5-14 Detail of film effectiveness distribution with variation of the spanwise pitch for P_1/d=3

5.3.5. Fan shaped holes

In order to gauge the potential benefit of including fans in these designs, a 25° fan angle with a 7.5° layback was added to the staggered geometry. Fans are designed to effectively suppress the liftoff of an individual hole when compared to its cylindrical equivalent. Figure 5-15 plots the mean film effectiveness of both cylindrical and fanned holes for the 5-hole staggered arrangement. The holes are

simulated both individually and superimposed using the Sellers method, as well as all together, in order to gauge the effect of interactions between film jets. The combination of 5 fans ejecting coolant together lowers film effectiveness relative to the superposition of 5 individual fanned holes by up to 0.03. The destructive interaction between fans may be attributed to the over-packing of large features in a small region, resulting in interactions such as the ones highlighted by the inline geometry. By comparison, the combination of cylindrical holes improves the mean film effectiveness by over of 0.2 (relative to the superposition prediction) at higher blowing ratios.

Whilst the fan geometry remains superior to the cylindrical holes at larger blowing ratios, at low blowing ratios, the cylindrical holes are marginally better. Overall, the similarity in performance between the fans and cylindrical holes stresses both the significance of the cylindrical hole interactions as well as the potential obsolescence of fans. With interactions between fans being quantified as mainly counterproductive, the spacing required to fit multiple fan features may become a hindrance more than a benefit.

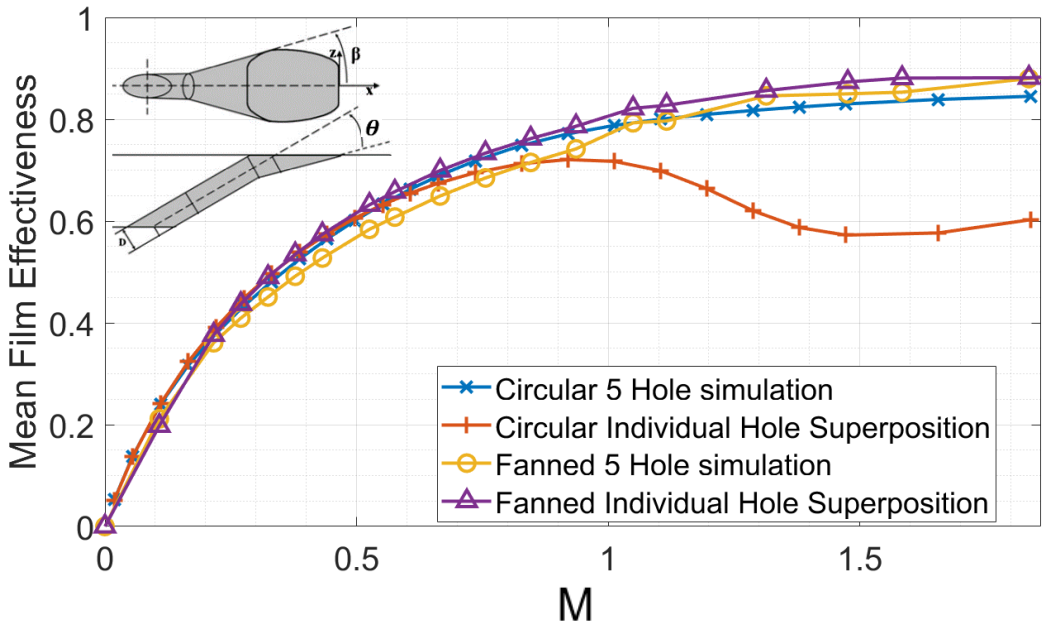


Figure 5-15 Comparison between fanned and circular film holes $\boldsymbol{\beta = 25°,\ \theta = 7.5°}$

5.4. Conclusion

The interactions between films within closely packed high porosity arrangements have been investigated in detail. The change in effective blowing ratio and the interactions between vortices, summarised in Figure 5-16, have been demonstrated to predominantly improve the film effectiveness of the staggered geometry whilst reducing the film effectiveness of inline geometries.

Improvements in the film effectiveness of the first two rows, coupled with the resistance to film lift off at even the highest blowing ratios further point towards the incredible performance and resilience of high porosity geometries. Similarities between the performances of basic cylindrical holes and highly optimized fans justify further investigation into these geometries as removing fans could result in a reduction in manufacturing costs. The present work also indicates the importance of optimizing a cooling scheme as a combined system as opposed to maximising the performance of individual features.

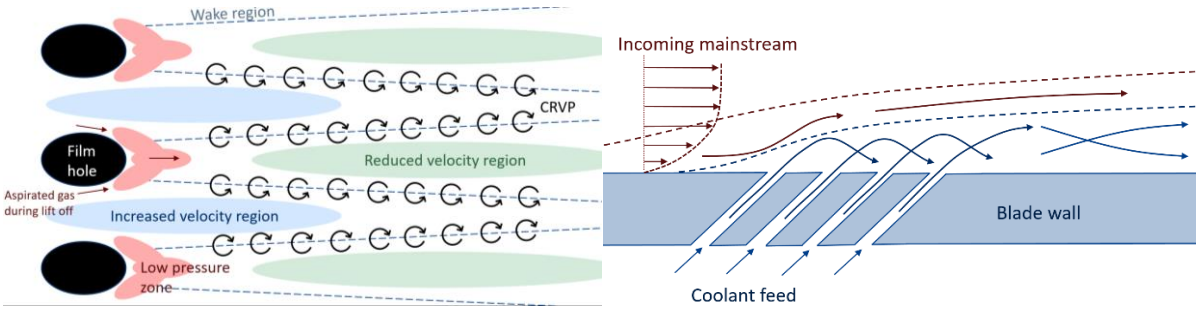


Figure 5-16 (a) Summary of principle factors dominating film interactions and (b) Schematic of staggered interactions removing mainstream from the surface.

Acknowledgments

The authors wish to express their thanks for the ongoing support provided by both Rolls-Royce PLC and the EPSRC through (EP/P000878/1). The authors would also like to thank the technicians at the Oxford Thermofluids Institute for their assistance in the manufacturing of the experimental setup.

6. Demonstration of High Porosity Cooling Systems Using Novel Thermochromic Liquid Crystal Method

Previous chapters summarise a significant development in the understanding of high porosity film cooling features applied to turbine blades. In order to demonstrate the significance and merit of these developments, the paper contained within this chapter consists of a final demonstration of the potential benefits of a high porosity film cooled system. Lessons learned throughout the previous chapters are incorporated into a final design and compared to other cooling schemes. In the context of the overarching research, it serves as a culmination of the work carried out and validation of the overall cooling concept. In order to demonstrate the overall blade metal effectiveness, the test facility is modified to accommodate metal effectiveness tests.

The following paper was presented at the 15th European Turbomachinery Conference (ETC2023-296) in Budapest Hungary April 2023. This paper was written under the supervision of Professor Peter Ireland and experiments were carried out with the assistance of Dr. Tsun Holt Wong.

Demonstration of High Porosity Cooling Systems Using Novel Thermochromic Liquid Crystal Method

A.Wambersie – P.T. Ireland

Department of Engineering Science, University of Oxford
Oxford OX1 3PJ, UK
Email: augustin.wambersie@eng.ox.ac.uk

Abstract

High porosity cooling systems have recently shown promise as a potential option for increasing turbine blade cooling effectiveness. To demonstrate the viability of this approach, a set of turbine blades with a double wall high porosity cooling scheme was manufactured from engine-grade materials. These were tested for metal effectiveness at steady state using a low-temperature high-speed cascade with engine-representative conditions.

Metal effectiveness values were obtained using a novel post-processing technique, based on the response of multiple narrow-band liquid crystals allowing for high-resolution in situ measurements.

Results demonstrated the high cooling potential of such designs as well as their potential implementation within a double-walled system. The comparison between the measured metal effectiveness values to existing state of the art cooling designs suggests that the potential increase in cooling effectiveness exceeds 5-7% at existing mass flows or alternatively, allows for a 15-20% reduction in coolant mass flow for equivalent cooling effectiveness levels.

Keywords: Metal effectiveness, Transpiration cooling, High porosity, double wall cooling, TLCs

Nomenclature

D	Film hole diameter (mm)	PR	Pressure Ratio
h	HTC (W/m^2.K)	T	Temperature
i	Pixel relative intensity	W_c	Coolant mass fraction
k	Conductivity (W/m.K)	x	Streamwise distance (mm)
L	Length (mm)	y	Spanwise distance (mm)
M	Blowing ratio	ε_m	Metal Effectiveness
M*	non-dim. mass flow rate		
$\dot{m}_c$	Coolant mass flow rate		

6.1. Introduction

The ever-increasing demands of turbine inlet temperatures necessary to drive even greater engine performances have fueled research in turbine blade cooling for decades. Open porous structures integrated into the wall of high performance turbine aerofoils have long been identified as very efficient cooling systems. The ability of these structures to generate highly effective and uniform cooling films in the presence of a cross-flow has resulted in transpiration cooling being extensively tested as a solution to turbine blade cooling at a conceptual level. However, manufacturing challenges and sensitivity of these systems to flow blockage has been thought to limit their application.

Recent studies in high porosity film cooling features have demonstrated that a viable intermediate between film cooling and transpiration cooling can be implemented (Wambersie, et al., 2021). These designs operate at blowing ratios far below typical film designs, yet achieve much greater film effectiveness levels for the same coolant mass flow rate. The reduced blowing ratio and uniform spanwise distribution results in a significant reduction in mixing between the coolant and mainstream, minimizing the associated decay in film effectiveness. This is particularly significant on the suction surface of the blade where curvature and a favorable pressure gradient almost suppress mixing altogether. Finally, the interactions between closely packed film holes have been seen to lead to beneficial film-film interactions between counter-rotating vortex pairs, contributing to the film remaining attached to the blade surface, even at high BRs (Jiang, et al., 2017).

Obtaining experimental metal effectiveness data on a full turbine cooling system is typically a very challenging and time-consuming process, with large expensive engine scale rigs required. Alternatively, small-scale experimental facilities such as flat plates or low-temperature cascades have been used to test out various design concepts through analogous measurement techniques such as film effectiveness or HTCs. The present work addresses the gap in fidelity of conditions between these extremes by testing metal aerofoils in a cascade with representative Reynolds and Mach numbers. A similar approach is reported by Nathan et. al. (2012) who demonstrate a similar overall approach relative to this study using an NGV cascade on a traditional film-cooled geometry.

Advances in CFD offer a possible alternative route for investigating new cooling designs, however, newer high porosity cooling systems have proven difficult to accurately predict using standard modelling approaches due to the high number of individual film cooling features. Predictions have failed to progress past the flat plate stage, and struggle to manage curvature and pressure gradients. (Jiang, et al., 2017)

This paper discusses metal effectiveness data, as defined by Equation **(**6-1**)** obtained using an experimental setup that offers a relatively high degree of fidelity despite using straightforward pre-existing tools. In this equation, $\boldsymbol{T_\infty}$, $\boldsymbol{T_m}$ and $\boldsymbol{T_c}$ are defined as the mainstream, metal and coolant feed temperature respectively.

$$\boldsymbol{\varepsilon_m = \frac{T_\infty - T_m}{T_\infty - T_c}} \qquad \textbf{(6-1)}$$

6.2. Method

6.2.1. Rig

Experiments were carried out within a high-speed, low-temperature, single-blade passage, first designed and built by Gurram et al (2016). This earlier setup was modified by the inclusion of a double-layer heater mesh upstream of the test section (Gillespie, et al., 1995), which allowed for the mainstream temperature to be raised by 35K. With the coolant air being approximately 5K colder than atmospheric, a temperature difference of 40K could be developed.

The imaging of the blade was carried out through the use of three CCD cameras as shown by Figure 6-1. These are positioned around the blade so that their overlapping fields of vision cover the entire blade surface. Images were continuously recorded throughout the experiments in order to obtain an intensity history for each pixel.

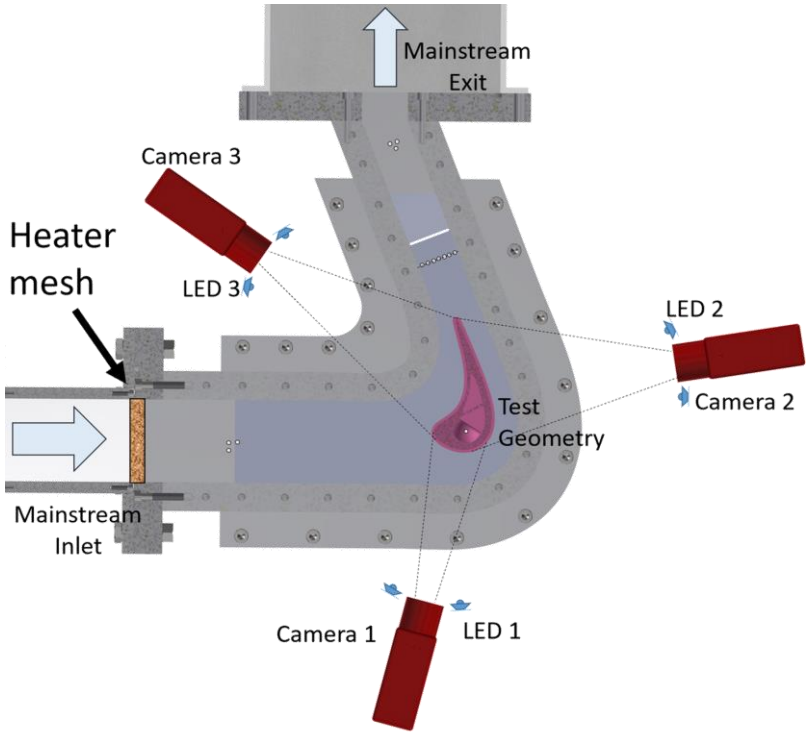


Figure 6-1 Schematic of the experimental facility with heater mesh

6.2.2. Thermochromic liquid crystals

Experiments using Liquid Crystals and metal parts capture the effects of conduction, and internal and external convection when test pieces with engine representative Biot numbers are used. This approach allows for a comprehensive assessment of the blade cooling performance to be evaluated, as opposed to specific film effectiveness or HTC experiments which only measure a component of the driving heat transfer mechanism.

Thermochromic Liquid Crystals (TLCs) offer a non-intrusive approach to determining the metal temperature of the blade surface. TLCs are particularly suited for use in high-speed experiments as they are insensitive to variations in pressure. A comprehensive assessment of TLCs is given by Ireland et. al. (1999). In brief, they can be applied as a coating of temperature-sensitive material that becomes optically active as a function of temperature. For this experiment, narrow-band liquid crystals were used to measure the metal surface temperature.

Narrowband crystals have an optically active temperature range of approximately 1 degree Celsius. Within this temperature band, the reflected light intensity peaks at a specific temperature predetermined by the properties of the crystal, resulting in a color display which identifies an isothermal surface region.

The benefit of this approach is that, while the temperature data obtained is not continuous, the confidence of this data is significantly higher than wideband or infrared methods. Three different liquid crystals were combined to enable multiple temperature contours to be visualized. Figure 6-2 shows an in-situ measurement of the light intensity response of the TLCs used in this investigation achieved using a surface thermocouple. The liquid crystals were chosen with peaks at approximately 25°C, 30°C, and 35°C. By using 3 crystal bands, three contours, indicated by the black vertical lines in Figure 6-2 could be established, resulting in 4 distinct temperature bands. To improve the signal to noise ratio, a combination of warm light with a color temperature of 3000K and green filter with a transmission wavelength of 550nm were added to the lenses.

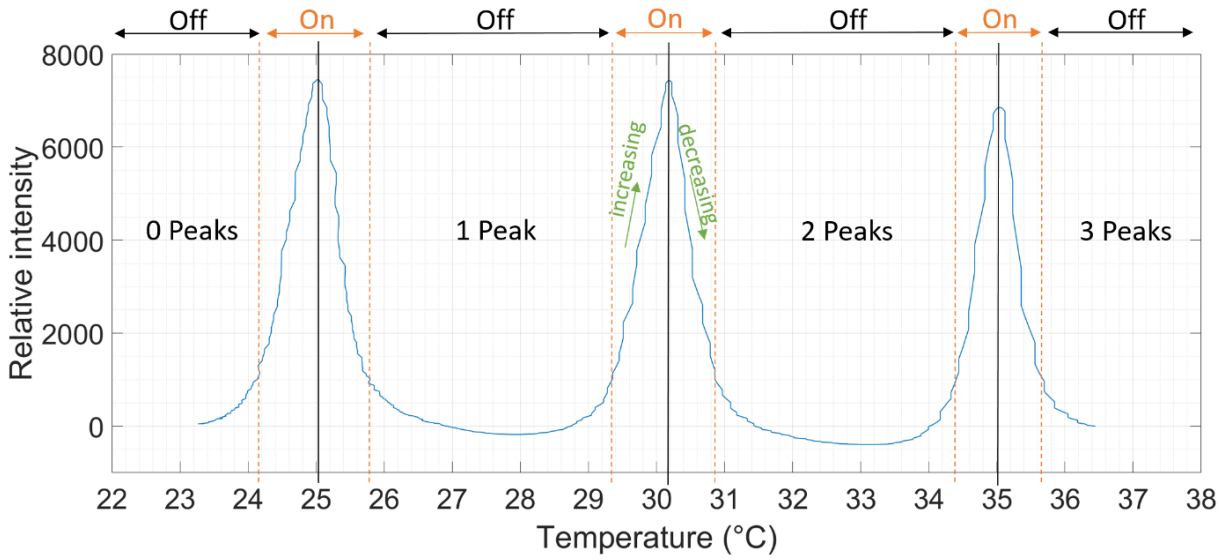


Figure 6-2 Example of narrowband liquid crystal response applied to test aerofoil with temperatures of principle and secondary contours shown in black and orange respectively

Light intensity values at each pixel are first subtracted from a reference image taken when the test pieces are cold and at a uniform temperature below the temperature-sensing range of the TLC coating. These processed images are then normalized by the maximum intensity achievable by each pixel.

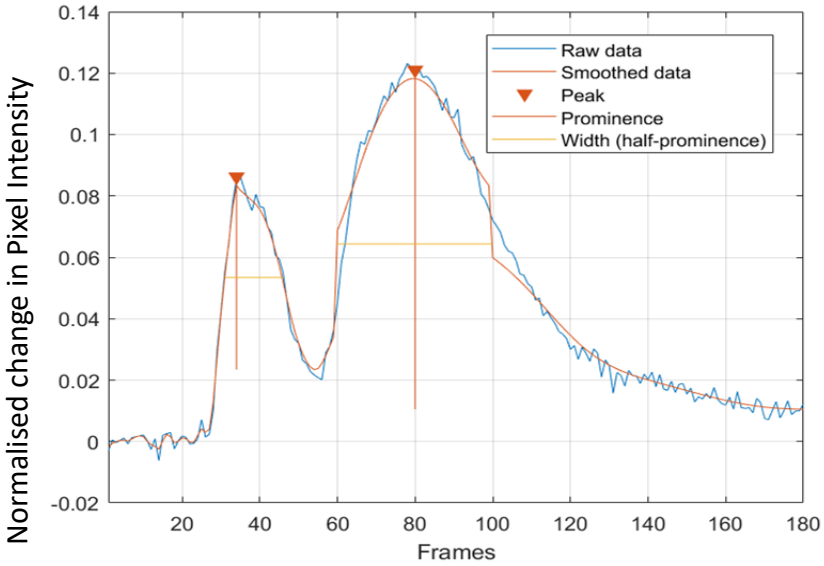


Figure 6-3 Example of signal response of a pixel between 30.9 and 34.4℃

As the three different temperature sensing crystals produced almost identical signals, the different signal peaks had to be systematically discerned by making use of the intensity history of each pixel. During experiments, the test piece was slowly warmed up to its steady state temperature distribution. By starting with the entire blade at a temperature below the measurable temperature range, each pixel transitioned through a different number of identifiable temperatures, dependent on the final steady-state temperature achieved. A peak finding algorithm could be applied to the intensity history of each pixel in order to count the number of peaks that had been passed. An example of a pixel intensity history is shown in Figure 6-3, where the individual peaks of the 25°C and 30°C are identified.

Once sufficient signal strength and image quality was established, additional contour lines could be added around the intensity peaks. By establishing a cut-off relative signal intensity at which the crystal is deemed “on” or “off”, three more temperature bands could be created. These are indicated in Figure 6-2 by the vertical orange dotted lines and were chosen to be at a relative pixel intensity of 0.02, approximately 0.5 degrees on either side of the intensity peaks. These values were selected as the gradient of the crystal temperature-intensity graph remained steep enough to infer values with meaningful confidence intervals. Whilst this results in contours bands of uneven width, the additional temperature levels provide extra data which yields further insight when large portions of the blade are close to the critical TLC temperatures. Finally, the additional three “on” bands can further be divided

into two. As the crystal intensity history is known, it can be determined from the derivative of the pixel intensity-time plot whether the pixel is moving towards or away from an intensity peak. This results in 9 temperature contours and 10 separate temperature bands being established from the use of only 3 crystals.

Variable	Nominal Value	Measurement uncertainty	Sensitivity coef.	Normalized by Result
T_∞	318 K	1	0.013	1.97%
T_c	291 K	1	0.024	3.66%
T_{cali}	300 K	1	0.037	5.70%
$T_{crystal}$	298 K	0.3	0.037	1.71%
			Absolute error	±0.0472
			% Error of calculation	7.26%

Table 6-1 Calculation of errors for a nominal metal effectiveness isothermal contour of 0.65

6.2.3. Uncertainty analysis

The experimental uncertainty in metal effectiveness can be calculated for each isothermal contour line. In this analysis, the perturbation method described by Moffat (1988) is used. These uncertainties stem from the measurements of mainstream, coolant, and crystal calibration temperatures, as well as the measurement of light intensity.

In order to simplify the uncertainty analysis for the light intensity, multiple calibration readings equivalent to Figure 6-2 were taken around the blade at different locations and illuminations. The estimated error in intensity measurements of the liquid crystal response resulted in a maximum variation in temperature of ±0.3K. This is in line with other studies quantifying the accuracy of narrow-band liquid crystals (Sabatino, et al., 2000). Thermocouple measurement errors were estimated to be ±1K once combined with the signal conditioning amplifier following in situ calibrations. Table 6-1 calculates the overall uncertainty to be ±0.047 or approximately 7% for a nominal metal effectiveness of 0.65. It is worth noting that the majority of the error originates from the use of conventional K type thermocouples and the relatively small temperature difference between mainstream and coolant.

6.3. Geometries

6.3.1. Design

The core of the internal geometry used for the transpiration blades is taken from previous studies of double-wall effusion systems (Ngetich, 2019). These systems were seen to provide good convective cooling properties but, more importantly, provided a cooling strategy that the authors could tune to direct tailored quantities of coolant to the appropriate film hole arrays also described as panels.

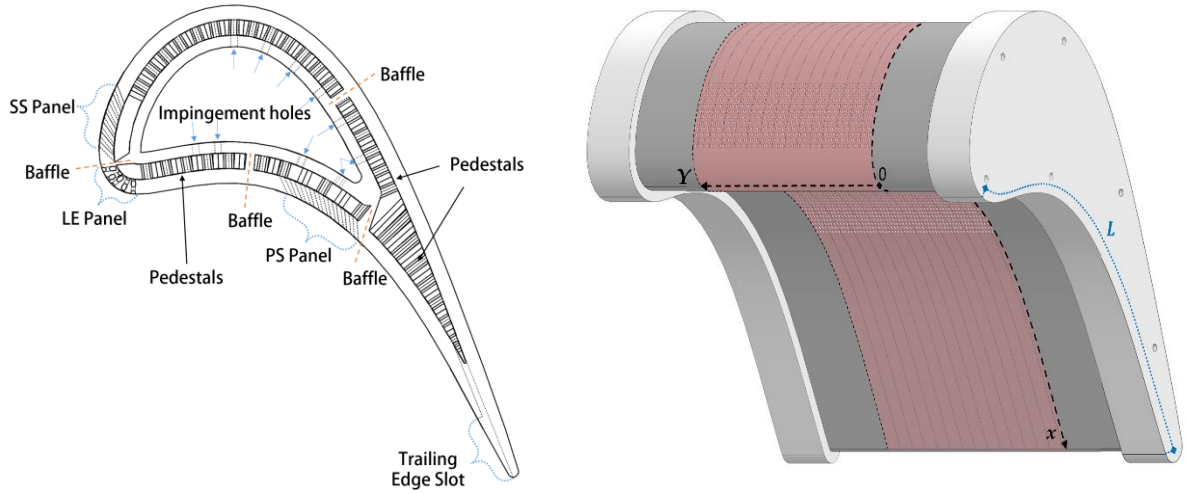


Figure 6-4 (a) Schematic Cross section of TP095TE and (b) blade surface coordinate system

In the double wall geometry, illustrated by Figure 6-4(a), the air is fed to a single inner plenum within the inner wall. The coolant is first directed through a bank of impingement holes within the inner wall. The jets formed by these holes and consequent impingement onto the outer wall contribute significantly to the internal cooling performance. The coolant then migrates through pedestal banks between the walls. The coolant finally effuses through the different arrangements of film cooling holes where it generates an effective external film. As the panels of film cooling holes operate with a relatively low-pressure margin, a wide range of feed pressures is required by the three different panels distributed around the blade. In order to mitigate excessive coolant migration, baffles are included to segment the region between the inner and outer wall. The resultant geometry has three separate cooling modules, each containing its own bank of impingement holes, pedestals, and film cooling holes.

The design point for the coolant mass flow was set at 3.5% of the overall mainstream mass flow rate. The coolant mass flow to each module was chosen to maximize the overall predicted combined film effectiveness over the entire blade. These predictions were made by interpolating and superimposing data from empirical results of individual panels at varying mass flows and blowing rates. This resulted in each panel being designed to operate at a given mass flow and mean blowing ratio, with optimal blowing ratio values expected to lie between 0.3 on the suction surface and 0.4 on the pressure surface as previously determined by Wambersie et al. (2021). Combined with the discharge coefficients determined for each panel, a simple flow net model was developed. For a given inlet pressure, the mass flow and pressure ratio to each module could be set by the impingement hole diameter and number of impingement holes.

As the minimum hole diameter was identified as a potential limit to the implementation of high porosity film cooling designs at engine scales, two-hole sizes were investigated, both above and below existing manufacturing capabilities at engine scale. An additional module was included in either geometry in order to include a trailing edge slot so that the significance of such a feature could be investigated. Further information of the different geometries tested is given in Table 6-2.

Geometry	Film hole *D* (mm)	SS Film rows	PS Film rows	LE Film rows	TE in-cluded	Pitch/D	Impingement *D* (mm)
TP075S	0.75	7	9	5	N	2.1	1.5
TP075TE	0.75	7	9	5	Y	2.1	1.5
TP095S	0.95	5	6	3	N	2.1	1.5
TP095TE	0.95	5	6	3	Y	2.1	1.5

Table 6-2 List of geometries tested with information on film cooling features

6.3.2. Test Piece manufacture

A laser sintered additive manufacture was used to produce the intricate geometries. As the conductivity of the test piece has a significant impact on the metal effectiveness distribution and cooling performance, the Biot number of the experiment, given by Equation (6-2), is matched to engine conditions with blades made of CSMX-4. From the range of different materials available for AM manufacturing, Inconel 625 was selected as it resulted in a Biot number within 2.5% of the target value. Table 6-3 presents the values and constants used to make this assessment. The main assumption made

for this calculation was that the Nusselt number of the rig would match that of the engine. This assumption is valid as by design, both engine and rig share the same Reynolds number, Mach number and similar Prandtl numbers.

$$\boldsymbol{Bi = \frac{h}{k} L_{wall}} \tag{6-2}$$

To minimize any thermal conduction between the test piece and the surrounding test facility, and to eliminate the impact of end wall effects, the test pieces were held in place by uncooled supports made of high-strength ABS plastic with very low thermal conductivity. Analysis showed that the effect of heat lost to the supports had a negligible effect on the aerofoil temperature.

	Engine	**Rig**
Operating temperature (K)	2000	310
Conductivity of air (W/m.K)	0.083	0.0283
Metal material	CMSX-4	Inconel 625
Metal conductivity (W/m.K)	28 Abdul et al. (2007)	9.8
HTC (approximate) (W/m2.K)	8400	1248
Nusselt number	101.2	101.2
Wall thickness (m)	0.001	0.0023
Biot Number	0.3	0.293

Table 6-3 Biot Number scaling

Whilst film hole diameters were chosen based on engine scale manufacturing capabilities, hole diameter was also a concern for manufacturing the test pieces. Additive manufacturing (AM), particularly in the case of laser sintering, results in the contraction of small diameter hole features as the sintered material melts and expands into the hole void. This contraction needs to be accounted for, predominantly through trial and error as these effects are highly dependent on orientation and geometry. Figure 6-5 shows the AM test pieces immediately post-sintering. Measurements of the test pieces showed actual holes sizes to be between 0 and 4% oversized, as holes in the center of the lattice failed to contract as predicted due to the lower bulk density.

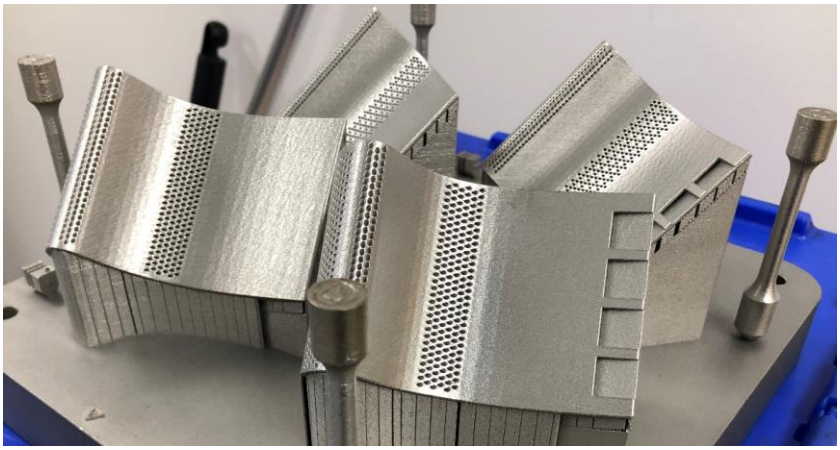


Figure 6-5 Test pieces as manufactured by Laser sintering AM

6.4. TLC results

The metal effectiveness contour plot of the first geometry TP075S is shown in Figure 6-6. The ticks and labels on the color bars indicate the values of each isothermal contour line. The color of each contour band is taken at the mean of these two values. The plots show the leading edge at x/L=0 with the pressure surface and suction surface respectively corresponding to positive and negative values of x/L. Due to the optical constraints of taking measurements within the film holes, no values were assigned to the inside of the film holes.

At the target mass flow and above, high and consistent values of metal effectiveness are achieved from x/L = 0.6 to x/L = -1, representing just under two thirds of the entire blade surface. As expected, the suction surface panel generates a large region of highly effective coolant film, whilst films generated by the leading edge are able to cool the gap between the pressure surface panel. Observations made during the transient warmup period before reaching steady state confirm that the internal impingement holes, particularly those feeding the leading edge and suction surface at x/L=0.2 and x/L=-0.6, contribute to cooling, thereby counteracting any streamwise decay in film effectiveness.

The first geometry also highlights the challenges of cooling the leading edge using a highly porous system at lower mass flows, with sections of the leading edge remaining below the threshold of the highest discernable TLC signal. However, at higher mass flows closer to the expected operating point, the leading edge is cooled to some degree. The coolant is also seen to favor the left side of the blade, with coolant entering the blade from the right-hand side of the images. This is best described by the

increased loss coefficient when the inside cross flow velocity is high. A region of higher static pressure also develops opposite the coolant inlet where the internal flow stagnates. Such behavior is usually observed in manifolds with high small duct to exit area.

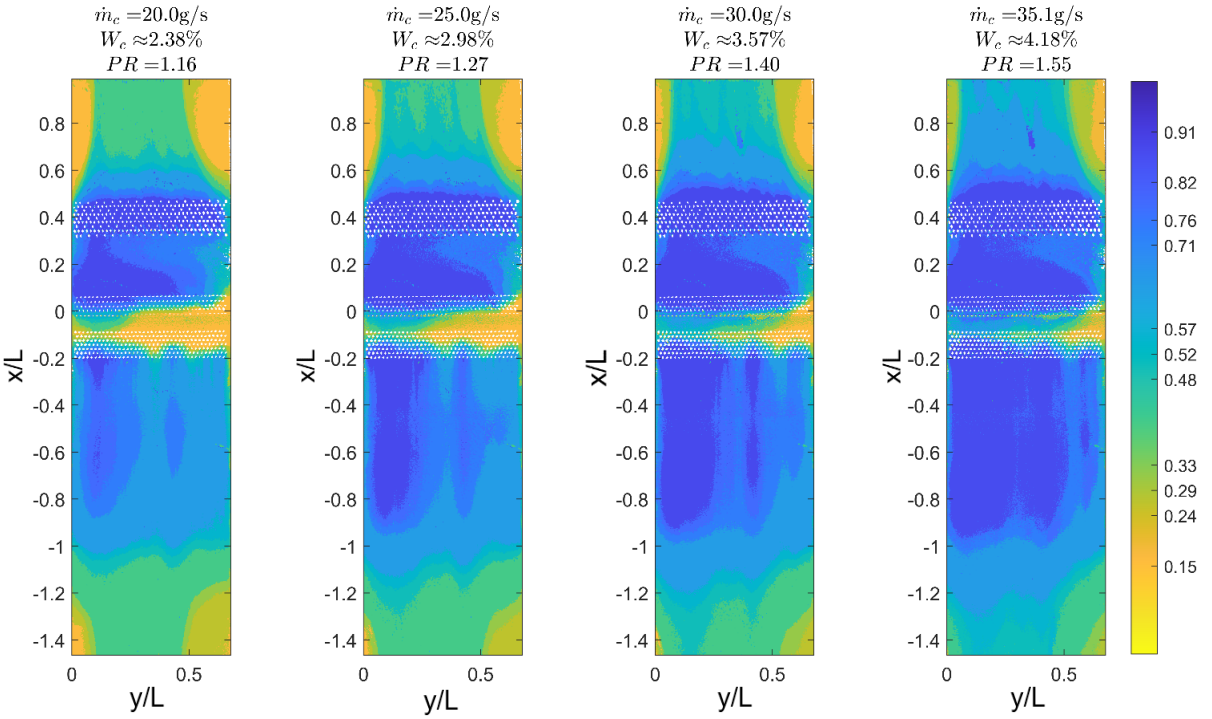


Figure 6-6 Metal effectiveness results for geometry TP075S

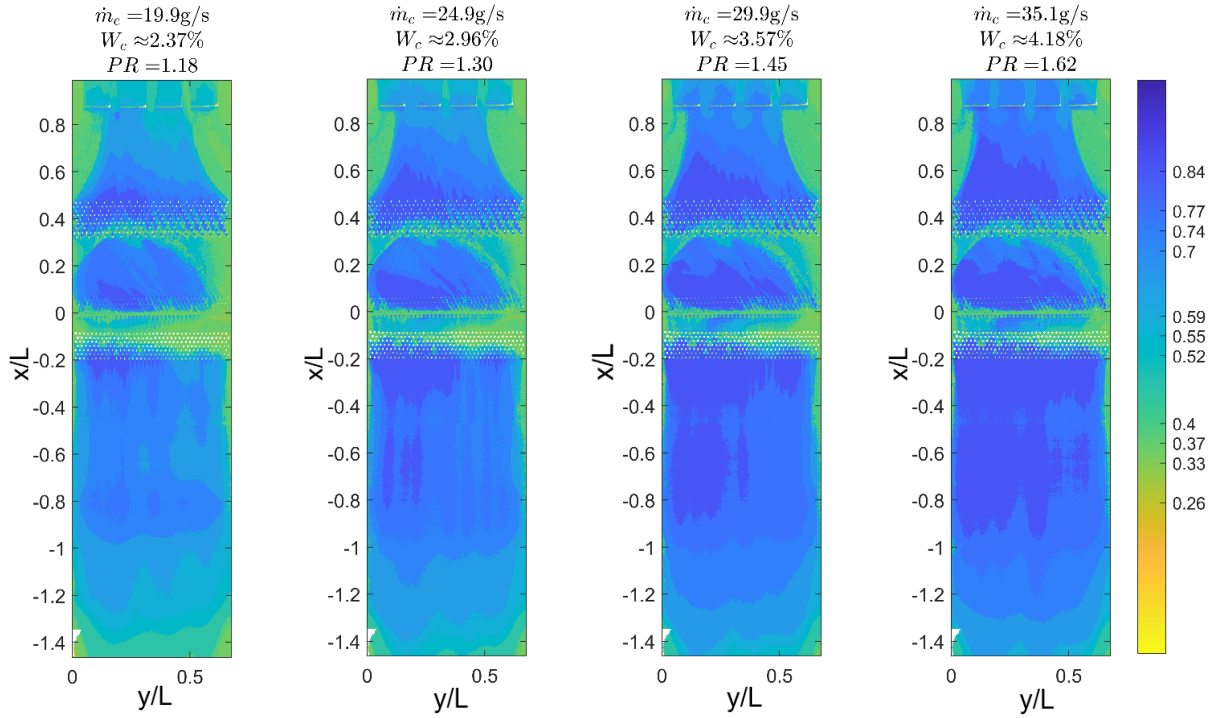


Figure 6-7 Metal effectiveness distribution of TP075TE

An unexpected phenomenon can be observed towards the trailing edge of the results, particularly on the pressure surface with a significant reduction of cooling occurring towards the spanwise edges of the test piece. While the narrowing of the film core has been observed to a limited degree in earlier film effectiveness results (Wambersie et al. 2021), the liquid crystals indicate a much more significant phenomenon. This effect can be seen to conduct through to the suction surface despite the metal effectiveness near the SS panel showing a more conventional full spanwise distribution. A possible explanation for this phenomenon is that the metal effectiveness in these regions is driven by the unprotected corners of the test piece. As the HTCs of this region are relatively high, heat is conducted inward.

6.4.1. TP075TE

The addition of a trailing edge slot to geometry TP075TE results in a marked improvement in metal effectiveness towards the trailing edge on both surfaces. The addition of active cooling to the trailing edge of the blade and associated improvement demonstrates that the film effectiveness of the upstream films is not yet sufficient to passively protect the trailing edge. Improvements in TE effectiveness however come at the expense of reduced cooling towards the early suction surface and mid-pressure surface as the coolant is redirected elsewhere. It is worth noting that the positions of the metal effectiveness bands are slightly different despite indicating the same temperature due to variations in atmospheric conditions which influence the temperature of both mainstream and coolant air.

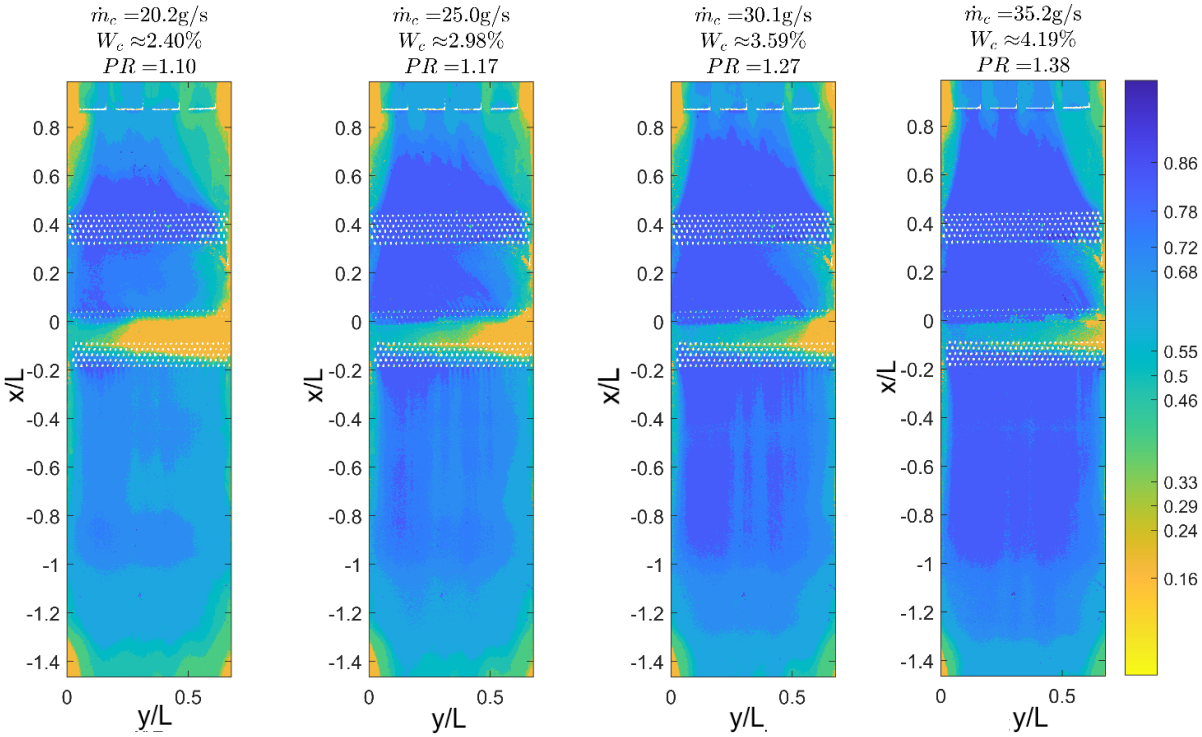


Figure 6-8 Metal effectiveness distribution of TP095TE

6.4.2. TP095TE

Increasing the hole size by slightly over 25% to 0.95mm results in an increase in metal effectiveness around the entire blade (Figure 6-8). While contrary to expectations, the geometry with larger holes and trailing edge is able to maintain larger regions of the blade at or above the maximum measurable temperature band, equating to metal effectiveness levels above 0.86. The slight variation in pressure surface panels may offer some explanation for the different cooling performances, however, this is more likely due to manufacturing challenges associated with the internal blade features leading to uneven coolant distributions throughout the blade. Variations in feed pressure ratios demonstrate how significant these variations can be, with a reduction of up to 0.24 in PR despite the geometries remaining geometrically very similar.

6.4.3. Metal Effectiveness summary plots

As previously mentioned, one of the limitations of the contour plots created using narrow-band liquid crystals is the inability to take accurate numerical linear and area averages. However, by assigning each contour its median value, a qualified average can be determined. This method is best used as a

comparative tool in between test pieces as the fraction of each blade's surface area within a certain metal effectiveness range is still of critical importance to cooling system designs. The average metal effectiveness of several different regions of interest can be taken in order to compare the cooling performances. Averages of the trailing edge region, leading edge region, suction surface, and pressure surface are shown in Figure 6-9.

Data for the trailing edge region was taken between x/L = 0.9 and x/L = 1 which equates to approximately two-thirds of the trailing edge slots. For the leading-edge region, an average was taken over the cylindrical portion of the blade, equating to the region between x/L = -0.05 and x/L = 0.05. For the pressure surface and suction surface, an average was taken from the leading edge to the trailing edge along the respective surfaces.

Average cooling effectiveness was also calculated for the entire blade surface and plotted in Figure 6-10. These values are plotted against the non-dimensional mass flow m* defined by Equation (6-3) allowing for comparisons between test conditions and geometries, where $\boldsymbol{h_o}$ is taken to be the baseline heat transfer coefficient of an uncooled blade.

Reference lines for theoretical internally cooled blades at different internal convective efficiencies are also included as defined by Holland and Thake (1980) and Equation (6-4).

$$\boldsymbol{m^* = \frac{\dot{m} c_p}{\int h_o dA}} \tag{6-3}$$

$$\boldsymbol{\varepsilon_m = \frac{\eta_c m^*}{1 + \eta_c m^*}} \tag{6-4}$$

Results from the current experiment are plotted alongside previous double wall systems taken from Ngetich (2019) and tested in the same manner. More significantly, a modern film cooled quintuple multipass blade, adapted to fit within a 2D cascade was also tested at its theoretical design point, allowing for a direct comparison to the current state of the art.

When examining the trailing edge metal effectiveness, the geometries without trailing edge slots show values at least 0.15 below those with slots. In part, this is driven by the significant edge effects that can be seen in the metal effectiveness contour plots. However, it can be noted that the cooling

effectiveness of these geometries closely matches the film effectiveness levels examined for the pressure surface panels at moderate mass flow rates (Wambersie et al. 2021). Despite the metal effectiveness on the equivalent section of the suction surface being much higher, this does not appear to be sufficient to drive the metal temperature on the pressure surface. By comparison, trailing edge effectiveness of the conventional multipass blade is the highest measured due to the inclusion of many highly inclined film holes with very long length to diameter ratios.

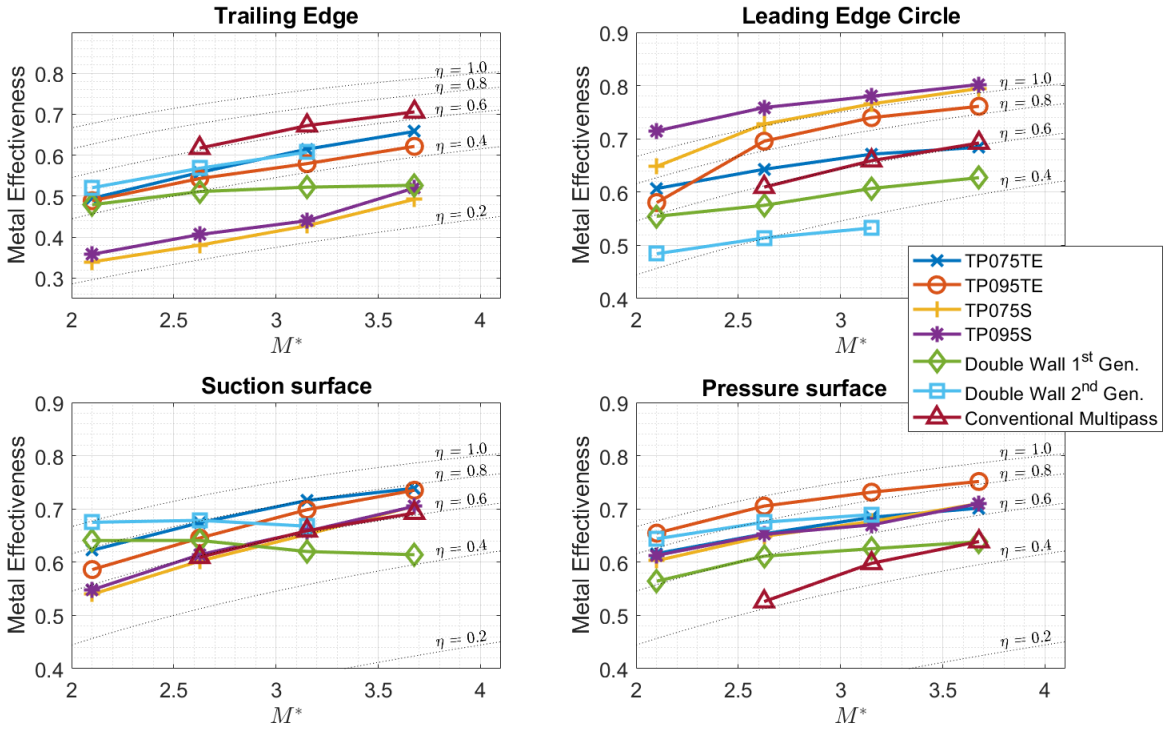


Figure 6-9 Mean metal effectiveness values for leading edge, trailing edge, suction and pressure surfaces

The four geometries with trailing edge slots: the two transpiration geometries as well as the two Double Wall geometries, share a similar trailing edge metal effectiveness level at lower mass flows. As the mass flow is increased, the trailing edge metal effectiveness levels begins to diverge as coolant is fed to different upstream cooling features in varying amounts.

For the leading edge section of the blade, the results are almost inverted. For the geometries without the trailing edge slot, mass flow to the leading edge panel is increased. This panel, when not ingesting provides very high metal effectiveness. Interestingly, the two geometries with the 0.95mm film holes perform better relative to their 0.75mm counterparts despite having a reduced internal surface area. This

is likely due to an increased mass flow to this section of the blade for these two geometries due to inconsistencies in internal features.

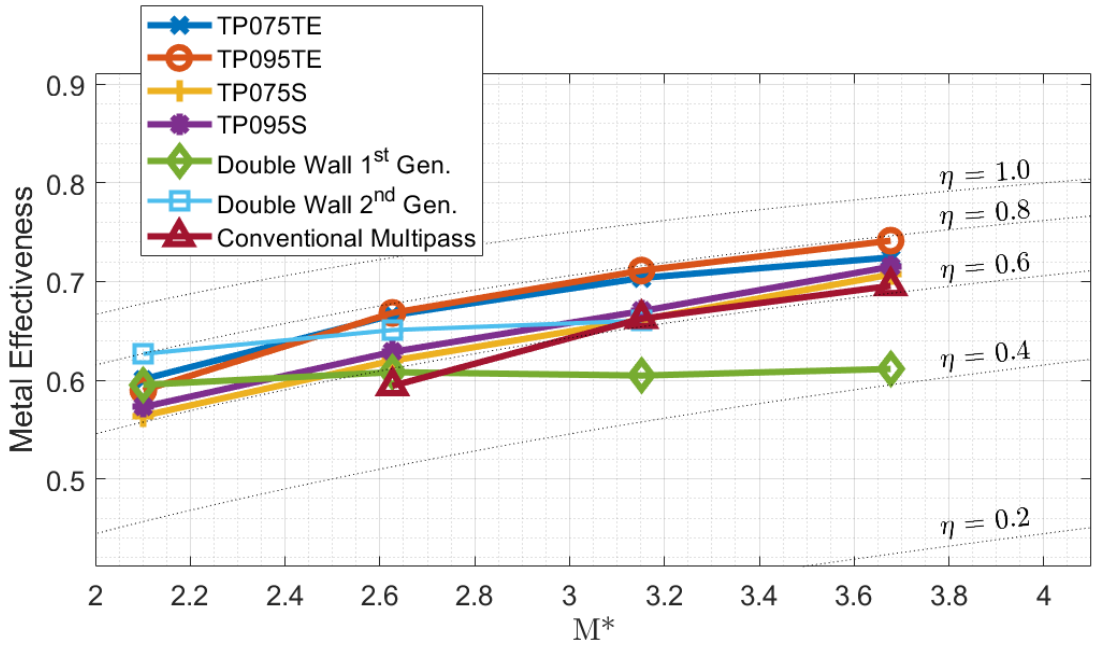


Figure 6-10 Mean metal effectiveness values for entire blade surface with data taken from multipass film cooled blade.

TP075TE performs the worst relative to all the transpiration designs predominantly due to the low mass flow rate of the leading edge panel which can be seen to affect the entire early pressure surface.

On the suction surface, the transpiration-cooled panel geometries result in very high effectiveness levels downstream of the panels, particularly when the internal impingement cooling is able to offset film decay. In contrast to the low porosity effusion systems, the transpiration panels can avoid film lift-off due to the interactions between films.

Similarly, the conventionally multipass is able to avoid film lift off due to its highly optimized hole, featuring fans which keep the film attached at high blowing ratios. However, the low number of films located on the pressure surface, coupled with the relatively simple internal cooling geometry results in the conventional multipass having a much lower pressure surface metal effectiveness.

When examining the overall cooling effectiveness, the geometries with both cooling panels and trailing edge slots can be seen to perform the best, even with large parts of the test blade's cooling performance being under reported by the liquid crystal method. The metal effectiveness of these blades

is equivalent to a theoretical blade with an internal convective cooling effectiveness of 0.8. These are able to achieve much higher metal effectiveness values as the film effectiveness continues to increase significantly at higher mass flow rates. By comparison, the effusion cooling systems perform relatively better at lower mass flow rates but have a very shallow gradient due to the limited film effectiveness and prevalence of film lift off.

Both transpiration cooled geometries with trailing edge slots are able to reliably outperform the conventional multipass, a significant result considering the relative maturity of the two approaches. For a given mass flow rate, the transpiration cooled designs are able to provide an improved metal effectiveness of over 0.05. Alternatively, the transpiration designs are able to provide a reduction in coolant consumption of approximately 25% in order to match the same metal effectiveness. Both of these values are significant and are indicative of the significant gains to be achieved using this type of cooling scheme.

6.5. Conclusion

By combining multiple narrow-band TLCs, a detailed yet reliable surface temperature contour map could be developed. The experimental setup allowed for signal quality to be sufficiently high enough for additional temperature sub-bands to be included in the analysis. Improvements to the method would target increasing the number of bands to add further resolution to the temperature scale. Alternatively, power to the heating element could be varied to produce a range of higher inlet temperatures, with different contours stemming from various inlet temperatures being overlaid.

Most importantly, results from the double wall high porosity geometries indicate that the systems offer a highly effective film cooling design with mean metal effectiveness values exceeding 0.7 at realistic mass flow rates. Matching or exceeding the cooling capabilities of existing designs is made more significant by the relatively low maturity of these designs. Significant improvements are there to be made by refining the designs, particularly with regards to ingestion occurring at the leading edge, as well as spanwise distribution near the trailing edge. Finally, showcasing these results validates previous work on high porosity film cooling features and justifies further investigation into the matter.

ACKNOWLEDGMENTS

The authors wish to express their thanks for the ongoing support provided by both Rolls-Royce PLC and the EPSRC through (EP/P000878/1). The authors would also like to thank the technicians at the Oxford Thermofluids Institute for their assistance in the manufacturing of the experimental setup.

7. CONCLUSIONS AND RECOMMENDATIONS

The present work has successfully broken ground in the field of high porosity film cooling features for turbine blade applications. By beginning with an analysis on a theoretical transpiration cooled blade, this body of research was able to build towards the understanding and development of a high performance film cooling design. Considerable work remains to be done before such a technology is able to reach maturity and find itself within a full scale. In this vein, recommendations for future work can be found at the end of this chapter.

7.1. Summary of major themes

7.1.1. Experimental investigation of high porosity film features

- An extensive volume of high-resolution film effectiveness data was gathered spanning a wide range of geometries, locations and parameters. These facilitated in-depth analysis of the nature of the cooling films.
- Film effectiveness levels were measured to be exceptionally high and long lasting, particularly when stemming from staggered panels located on the early suction surface of the blade.
- The direct comparison with alternative schemes within the same experimental facility, including industry leading multipass designs further reaffirms the significance of these results.

7.1.2. Investigation into the causes of high measured effectiveness

The high performance of the panels can be attributed to 6 major points:

- For a given mass flow, minimizing the blowing ratio results in the best film effectiveness, so long as ingestion does not occur. Lower blowing ratios allow for the coolant to remain within the boundary layer and minimize any mixing between the two fluid streams. The high porosity film cooling panels offer perhaps one of the best methods of sustaining low blowing ratios at reasonable mass

flow rates. This is particularly significant on the suction surface where the film effectiveness for a given mass flow was seen to peak around blowing ratios of 0.2.

- Interactions between films have generally been minimized in the past, if not avoided due to their potentially counterproductive nature. At larger pitch to diameter ratios, once the film development length is exceeded, these can be rightfully ignored. However, these same interactions can also be leveraged to greatly improve the robustness of a film cooling design, with closely packed films interacting in such a way that lift off becomes close to impossible. Mainstream gas also becomes physically pushed from the surface due to the complete spanwise coverage.
- The high porosity, uniformity and span of the features, result in a film with a uniform spanwise distribution. The 2D nature of the films produced results in a significantly reduced surface area between which the film and mainstream gases are able to mix. The smaller scale of the film holes tested further reduce the size of individual film features, with smaller films being more easily turned by the mainstream.
- The combination of low blowing ratio films with favourable mainstream conditions, such as convex curvature and acceleration is particularly influential on the film effectiveness of low BR features.
- As an consequence of the points above, the features are able to develop a relatively stable core of completely saturated film. Much like tangential slot injection, this film only decays due to mixing and conduction occurring between the film-mainstream interface.
- Finally, a significant breakthrough was achieved by developing correlations based on the film effectiveness data. The indication that the high porosity suction surface films behave as if in a laminar regime, offers a potential solution as to why the films far outperform expectations further down the blade surface where turbulence is expected to otherwise rapidly degrade the films.

7.1.3. Feasibility and performance of a full blade design

A full-blade design containing three separate panels was developed using existing research on double wall internal cooling. The design was able to improve upon certain limitations of previous double-walled effusion-cooled systems, such as pressure margins, coolant migration and ingestion by dividing

the blade into separate modular-like regions through the use of baffles. This allowed for a reasonably straightforward design process.

Both film effectiveness and metal effectiveness measurements for these designs were carried out, demonstrating high potential cooling performance, however, the metal effectiveness towards the trailing edge of the blade was not seen as sufficient to go without dedicated trailing edge cooling features.

7.1.4. Challenges

Factors that were identified as potentially troublesome for these designs were investigated:

- Current constraints set on feature sizes due to manufacturing and blockage issues, the sensitivity to hole size was examined. Whilst smaller holes are still seen to be beneficial, film effectiveness levels exceeding existing conventional design performances were still achievable with features within the current design constraints.
- Ingestion of mainstream gas into film cooling holes was observed at lower mass flow rates and pressure ratios. Similarly large variations in spanwise film effectiveness were at times noticed. Pressure margins were measured across the geometries. It was highlighted to be below conventional film designs and ingestion was observed for larger panels. However, the use of baffles and a slight reduction in the number of rows within each panel was able to mitigate ingestion almost completely.

7.2. Recommendations

7.2.1. Turbulence measurements

One of the significant outcomes highlighted towards the end of this research was the potential relaminarization of the suction surface boundary layer due to strongly favourable pressure gradients. This stems from the combination of the analysis of a wide range of film effectiveness data, coupled with an understanding of the film and boundary layer regimes. Due to the late recognition of this development, it was not feasible to develop an experiment to test this hypothesis.

Measurements of the boundary layer turbulence, particularly on the suction surface would easily prove or disprove this hypothesis. Comparisons between a solid blade, high porosity panel blade and

conventional blade running at high blowing ratios would need to be compared. Different flow visualization techniques such as PIV or smoke injection could also be attempted in order to visualize the mixing within the boundary layer.

7.2.2. HTC measurements

Similarly to turbulence measurements, the values of HTCs within and downstream of the high porosity panel would be of great interest. With analytical models suggesting a slight reduction in HTC and experimental and numerical results indicating a range of different interactions between films and the mainstream, these values would also be expected to vary. The addition of thin film gauges within the experimental facility would be straightforward to implement and could also provide supporting evidence of the high performance of the panel cooling features.

7.2.3. Further CFD modelling

Whilst CFD modelling was able to shed light on the nature of the interactions between different closely packed film holes, it was not possible to recreate the full film distribution across the entire blade surface despite significant effort and computation being committed to the problem. Whilst the flow in this region away from the film holes should be straightforward to model, existing commercial solvers were unable to provide a good match. Possible explanations could be related to the previous point, with varying levels of turbulence suppression not being accounted for by the models.

7.2.4. Further Optimization of both individual panels and joint systems

Investigations into the interactions between films yielded significant information on the nature of interactions between films as well as highlighting the significance of spacing. Overall, it was determined that the spanwise spacing with P/d = 2.1 was near optimal yet the streamwise spacing was a compromise between film effectiveness and management of pressure margins. However, a thorough multi-objective optimization of this setup was not yet attempted for either cylindrical or shaped holes. The benefits of this investigation would be immediate and potentially significant as the film effectiveness is seen to be highly sensitive to the hole pitches.

This routine could be relatively straightforward to run using parametric optimization. If better agreement can be achieved between numerical models and experimental data, this could be further expanded to the panel locations and blowing ratios.

Similarly, within a full blade design, the definitions of different panels and interior features result in an extensive list of parameters that can be optimized for. Whilst optimization for internal features has already been carried out for flat plates, the interactions with panel features, requiring a wide range of mass flows and pressure margins would likely result in different outcomes.

7.2.5. Pressure margins

Pressure management across the panels has been highlighted as an issue, as the high porosity results in a low-pressure margin at reasonable mass flows. This can lead to uneven span wise distributions, as well as a high risk of ingestion towards the leading edge of the panels. In order to better control this effect, the pressure losses within the individual holes would need to be increased. Different lattices intersection configurations and shaped holes have been examined by other authors for a similar purpose. Overall, high pressure margins are likely to work against the high effectiveness of the panels as these would result in an increased blowing ratio. However, a compromise between these competing factors would need to be established at which point the benefits of the design would need to be revaluated.

7.2.6. Further investigation into shaped holes

Investigations using CFD determined that at the same spacing, fanned holes would not perform better than cylindrical holes within high porosity features. However, there exists a great range of differently shaped holes with potentially very different interactions between them. Furthermore, fans may have a different ideal spacing based on the external fan size, as opposed to the throat diameter.

7.2.7. Mechanical implications

Due to the nature of high porosity cooling features, the mechanical properties of the outer wall would become significantly affected. Moreover, the reliance on small features increases the likelihood of stress concentrators near hole edges. High cooling effectiveness, if not managed correctly may also increase

thermal stresses in the outer blade wall. Both mechanical and thermal stresses within the blade would need to be revaluated as the designs proposed lie beyond the existing design space.

Appendix A : Analytical analysis of transpiration cooled turbine blades

The first investigations carried out into transpiration cooling during the early stages of this thesis were primarily theoretical ones. The objective was to gain a firm understanding of transpiration cooling and its application to turbine blades. Practical considerations were not prioritized and the research question was aimed at calculating the theoretical maximum cooling performance of transpiration cooling using existing understanding of transpiration cooled flows. Coolant flow around the blade was optimized to achieve a uniform metal temperature distribution across the entire blade. A summary of these findings are contained within a paper that was submitted and accepted to the ASME Turbo Expo 2020 conference (GT2020-15405). This paper was written under the supervision of Professor Peter Ireland.

Approximate Analytic Thermal Solution for Transpiration Cooled Turbine Blades

Augustin Wambersie, Peter Ireland

Dept. of Engineering Science
University of Oxford
Oxford, OX1 3PJ, United Kingdom
Email: augustin.wambersie@eng.ox.ac.uk
peter.ireland@eng.ox.ac.uk

ABSTRACT

Transpiration cooling is known to be a very effective means of achieving high cooling performances. Carrying out a full conjugate CFD analysis on a transpired turbine blade remains both theoretically and computationally quite challenging. In the meanwhile, a computationally simple analytical approach to predicting cooling capabilities of transpired turbine blades is presented. A finite difference boundary layer code was also used as an intermediate alternative to calculating external HTCs.

The analysis is demonstrated on a simulated turbine cascade with real engine conditions. Both methods used show good agreement with each other and predict very high cooling effectiveness for the modeled turbine blade. The method also returns important design parameters such as the coolant distribution required for an isothermal turbine blade.

NOMENCLATURE

B_h	Thermal blowing parameter
c_p	Heat capacity (J/kgK)
h	HTC (W/m^2K)
$\dot{m}_c''$	Coolant mass flux (kg/sm^2)
$\dot{q}''$	Heat flux (W/m^2)
ρ	Density (kg/m^3)
u	Streamwise velocity (m/s)
v	Perpendicular velocity (m/s)
G	Mass velocity ρu (kg/m^2s)
P	Pressure (Pa)
T	Temperature (K)
x	Streamwise distance (m)
y	Perpendicular distance (m)
Re	Reynolds number
St	Stanton number $St = h/\rho u c_p$
Pr	Prandtl number
Nu	Nusselt number
α_H	Molecular thermal diff. (m^2)
ε_H	Eddy diff.for heat transfer (m^2)
Δ_2	Enthalpy thickness (m)

Subscripts

∞	Mainstream
r	Recovery
m	Metal
t	Total
c	Coolant
o	No blowing case
e	Exit conditions
i	Inlet conditions
s	Surface conditions

A.1. INTRODUCTION

Since the early 1950s, the concept of transpiration cooling has been heralded as a method of achieving high metal effectiveness in turbine applications (Eckert & Livingood, 1954). The 1970s saw an extensive amount of flat plate experimental work reported which was aimed at exploring this statement. The high levels predicted cooling performance of transpired surfaces are achieved by the very high internal surface area, the uniform distribution of cooling film and the inflation of the enthalpy thickness (Kays & Crawford, 1980). Nevertheless, in recent years focus has remained on perfecting film and effusion cooling. Transpiration cooling mostly remains of academic interest and limited headway has

been made in introducing transpiration cooling into working gas turbines.

Despite recent renewed efforts in researching casting and production techniques, manufacturing limitations still appear to be the biggest hurdle for implementing transpiration cooled turbine blades. High thermal stresses and the likelihood of pore blockage of the porous wall also add to the difficulties of developing working prototypes. The recent development of porous C/C-SiC and CMC composites has offered the potential application of high temperature ceramics to rocket nozzle cooling (Langener, et al., 2012). The aim of this paper is to demonstrate the importance of developing such a design for gas turbine purposes and hopefully motivate the continuation of development in the field.

An easy to use analytical method to estimate the performance of a transpiration cooled aerofoil would allow for easy preliminary design and modeling of possible transpiration based designs. It could also serve as a bench mark for predications of practical highly cooled systems such as effusion cooled components.

In this paper, an analytical, 2D approach to estimating the performances of a transpiration cooled turbine blade is presented. The approach is a combination of Kays and Crawford's analysis on the effects of transpiration on turbulent heat transfer coefficients (HTCs) (Kays & Crawford, 1980), combined with Ambrok's integral approach to calculating HTCs of turbulent non-isothermal boundary layers (Ambrok, 1957). The approach is derived from first principles which results in a relatively simple and elegant solution to a traditionally computationally complex problem. Laminar flow may occur near the leading edge of a blade and these can be solved using the Pohlhausen solution (Pohlhausen & , 1921). Repeating the procedure over carefully spaced parallel streamlines can then be used to build a 3D model of the blade. A parallel analysis using TEXSTAN, a finite element boundary layer solver code, has also been carried out for comparison.

A.2. LITERATURE REVIEW

Predicting the cooling performance of a particular blade design is of great importance to turbine development. Whilst fully coupled conjugate heat transfer simulations can be used to model a complicated aerothermal system such as a double wall turbine blade, this route can be computationally very demanding (Andersson, et al., 2011). In practice, a cooled turbine blade contains three different sections that require modeling: the mainstream flow, the coolant flow and the metal domain. The majority the work reported in recent literature, targeted at modeling the cooling effectiveness of turbine blades, uses simplified models with at least some portion of fluid boundary conditions being decoupled and determined by analytical or empirical means, leaving only the thermal Fourier equation to be solved numerically.

In a convection cooled blade analysis by Reyhani et. al. (Reyhani, et al., 2013), the internal cooling is simplified as 1D flow through pipes running spanwise across the blade, greatly streamlining the process of solving for the metal temperature. This approach allows both the mainstream fluid temperature and the external HTC to be iterated. The use of 1D heat sinks as a means to simplify heat transfer analyses was evaluated by Krückels et. al. (Kruckels, et al., 2007) and demonstrated very good agreement with a fully meshed cooling passages. Takahashi et. al. (Takahashi, et al., 2000) uses a different method to modeling convection cooled blades, where only the coolant and metal domains are modeled, with the external HTC and mainstream temperature being kept constant. Both these approaches, while providing reasonable results, streamline their respective analyses by greatly simplifying one of the fluid domains.

Certain decoupled conjugate approaches have also found success by modeling the different domains separately. Zecchi et al. [6] developed a 2D decoupled conjugate model for preliminary design of internally cooled turbine vanes. Only the internal and external HTCs and fluid temperatures were required to determine both the metal temperature distribution and the coolant mass flow distribution in the vane. This study was able to match well the experimental results of the same vane from Hylton et al. (Hylton, et al., 1983). These approaches end up being successful due to the fact that the different fluid streams interact very little or not

at all. Combining both streams together in a single domain greatly complicates the analysis.

An approach used to simplifying the analysis of film and effusion cooled blades is by dividing complicated coolant passage designs into repeatable unit cells, whose geometry only needs to be simulated once. In an analysis by Ngetich et. al. (Ngetich, 2018) on double walled effusion cooled blades, the external boundary conditions of the blade are determined by adiabatic film effectiveness models. The external HTC is determined analytically and kept constant throughout the analysis. The internal cooling efficiency is taken from a wall block model developed by Murray et. al. (Murray & al., 2017) for similar flat plate wall geometries, allowing the internal heat transfer to be set as a function of the coolant Reynolds number and metal temperature. This approach benefits from a repeating internal geometry but ignores the effect of metal temperature and coolant injection on HTC.

Due to the complexity of the interactions between film holes and the mainstream, full conjugate analyses that simultaneously model both mainstream and coolant flows have mainly been carried out on single cooling holes as was done by Bohn et. al. (Bohn, et al., 2003) A more developed analysis by Laschet et al. (Laschet, et al., 2013) was able to examine curved sections with multiple holes, but both of these references are limited to basic uniform cold side flows.

Cerri et. al. (Cerri, et al., 2007) attempted to optimize the distribution of coolant holes across a turbine blade of an effusion design based off of Poroform technology. This decoupled approach used a flat plate correlation which was taken from Arcangeli et. al. (Arcangeli, et al., 2008) in order to generate a 2D film cooling model for the blade surface. The internal cooling was determined by a 1D model based on the know heat transfer parameters of a single hole. The surface was then generalized as a generic surface with the internal and external heat transfer defined by functions of hole diameter and density. Again, this approach fails to consider the effects of flow effusion on the HTC, particularly at the densities suggested by the study.

These repeating cell approaches are attractive when dealing with complicated film cooling arrangements yet these approaches all focus solely on the film effectiveness and fail to acknowledge the variations in HTC. The mapping of 2D film distributions onto the curved surface of a blade also fails to acknowledge the possible secondary flows which arise due to curvature. (Schwarz, et al., 1990) Furthermore this approach hinges on the underlying assumption that flows interact with the repeating cells in the same manner at all points of the blade.

By comparison, very few studies decide to tackle porous surfaces in a turbine blade head on. Numerical studies by Dahmen et. al. (Dahmen, et al., 2014) on porous materials intended for combustors have managed to develop coupled conjugate models for flat porous plates. Here the porous volume is modeled as a separate coupled subsystem of fluid and solid medium, which is then coupled to the mainstream by equating boundary conditions. This approach has found close agreement with experimental data by Langener et al. (Langener, et al., 2012), and manages to overcome the issue of modeling both fluid streams and solid at once. Unfortunately this approach is non trivial due to one coupled system being contained within another, meaning this approach would not be as effective for rapid designing and prototyping.

In contrast an analytical method developed by Eckert and Livingood (Eckert & Livingood, 1954) on porous wall blocks was used to estimate the porous metal temperature using the heat transfer reduction model for transpired surfaces. Whilst a very simplistic approach, the method was found to provide an acceptable approximation of flat plate experimental data.

Clearly, the development of these types of conjugate models weigh complexity against fidelity. Additionally, as designers look to effusion cooling with a greater number of holes for better cooling performances, the complexity of the domains will only increase. The overwhelming majority of the studies of the kind mentioned use film cooling models in order to determine external heat transfer. In the case of transpiration cooling, the coolant and metal domains can be calculated together but at a significant computational cost. Consequently heat transfer models which are both simple and accurate enough to carry out a full thermal analysis of a turbine blade are not yet in common use.

A.3. HEAT BALANCE

In the present analysis of an ideal transpiration cooled blade, a heat balance on a simplified wall element is used to estimate the metal temperature. The porous wall block is assumed to be at a uniform temperature, as was demonstrated by Eckert and Cho (Eckert & Cho, 1994). Conduction tangential to the wall is also assumed to be zero as one of the aims of the transpiration cooled design is to obtain a uniform temperature over the entire blade. Radiation from the wall is also neglected as it has been confirmed to have limited effect on the overall analysis (Cerri, et al., 2007). The only two mechanisms for heat transfer are taken to be the external heat transfer from the mainstream and the internal heat transfer into the effusing coolant. Initially, the coolant is assumed to exit the porous medium at the metal temperature. This setup and assumptions have previously been used with success by Eckert and Livingood (Eckert & Livingood, 1954). The approach assumes an internal cooling efficiency of 1, which would be the case for an idealized transpired surface.

The total heat flux into the wall, is equated to the increase in product of enthalpy and mass flow rate of the coolant since the blade is assumed to reach a steady temperature. Thermal conduction to the elements either side of the control volume shown in FIGURE A-1 is assumed negligible. Solving for the metal temperature results in Equation (1), which shows that the wall temperature is solely dependent on the coolant flux and the external HTC. Since the external HTC analysis is dependent on the surface temperature the process of estimating the metal temperature becomes an iterative one. The coolant mass flux is left as an independent variable, assuming the porosity and pressure difference across the blade can be controlled by the designer.

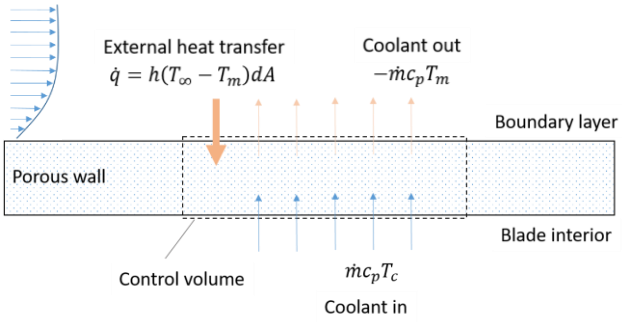


FIGURE A-1:CONTROL VOLUME FOR HEAT BALANCE

$$T_m = \frac{hT_r + \dot{m}'' c_p T_{c,in}}{\dot{m}'' c_p + h} \quad (1)$$

A.4. ANALYTICAL CALCULATION OF HTC

Stanton number reduction due to transpiration

The basis for quantifying the performance of transpiration cooling originates from calculating the effective reduction in Stanton number caused by mass flux through the wall surface. Where the Stanton number is defined as:

$$St = \frac{h}{\rho u c_p} \quad (2)$$

The analysis begins with the Couette flow analysis of the energy equation, shown below. This procedure is taken from Kays and Crawford (Kays & Crawford, 1980) and is reproduced in the Appendix A1.

$$\bar{u}\frac{d\bar{T}}{dx} + \bar{v}\frac{d\bar{T}}{dy} = \frac{d}{dy}\left[(\alpha_H + \varepsilon_H)\frac{d\bar{T}}{dy}\right] \quad (3)$$

The approach navigates around computing the complicated diffusivity terms on the right hand side of Equation (3) by finding the ratio between Stanton numbers with and without blowing as shown below. This statement can be assumed to be valid since it has been proved that transpiration has a negligible effect on the Prandtl mixing length (Kays & Moffat, 1975).

$$\left|\frac{St}{St_0}\right|_x = \left(\frac{\ln(B_h+1)}{B_h}\right) \quad (4)$$

Where the non dimensional thermal blowing parameter is defined as

$$B_h = \frac{v_s/u_\infty}{St} \quad (5)$$

While the assumptions made in the derivation in Appendix A1. are quite significant, data from experiments carried out by Kays and Moffat (Kays & Moffat, 1975) support the relation very well, including for cases with significant favorable pressure gradients and moderate adverse pressure gradients as shown in FIGURE A-2.

The testing setup that was used is described by Moffat (Moffat, 1967) and involved segments of sintered bronze plate. The surface heat flux was controlled by heating elements embedded within the bronze. Whilst heating the coolant inverts the direction of heat transfer this allows for better control of the heat flux. The surface temperature was measured using temperature probes, calibrated to account for radiation and lateral conduction. By assuming the mainstream temperature as constant and that the coolant exit temperature matches the wall temperature, the external HTC can be determined by the same heat balance as Equation (1). This makes the data particularly relevant as it was collected using the same assumptions as the model described in Section 2.

While Equation (4) in itself is significant, the 1-dimensional nature of the analysis means it is only applicable for constant B_h. Therefore another approach which accounts for the effect of variations in B_h on the heat transfer must be used in order to be applicable as an effective model.

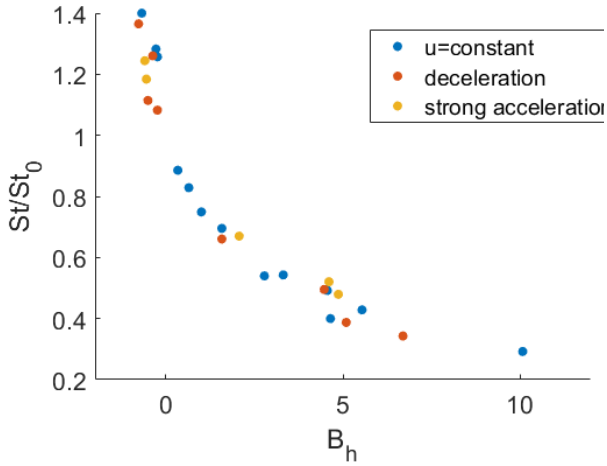


FIGURE A-2: EXPERIMENTAL DATA OF STANTON NUMBER AGAINST B_h KAYS AND MOFFAT (Kays & Moffat, 1975)

Determining the Stanton number with variations in freestream velocity and B_h

In order to account for the variations in freestream and coolant distribution which occur around a turbine blade, a modified integral approach first developed by Ambrok (Ambrok, 1957) for calculating the heat transfer coefficients of a non-isothermal surface is used and briefly described below.

Starting from empirical observations taken from Reynolds et. al. (Reynolds, et al., 1958), Equation (6) is used to define the Stanton number for solid flat plates with uniform free stream velocities as a function of streamwise length Reynolds number.

$$St_0 = 0.0287 Pr^{-0.4} {Re_x}^{-0.2} \quad (6)$$

Equation (6) is multiplied by Equation (4) to give the St for porous flat plates with blowing. The product is then redefined as a function of enthalpy thickness using Equation (7). The resulting Equation (8) defines the Stanton number in terms of the local enthalpy thickness Reynolds number and B_h.

$$St = \frac{d\Delta_2}{dx} \quad (7)$$

$$St = 0.0125 Pr^{-0.5} {Re_{\Delta_2}}^{-0.25} R \quad (8)$$

Where

$$R = \left(\frac{\ln(1+B_h)}{B_h}\right)^{1.25} (1+B_h)^{0.25} \quad (9)$$

This proves to be the critical step as it has been assumed that the Stanton number can be defined only in terms of the behavior of the local enthalpy thickness. This implies that the following results are applicable to non uniform velocity flows as well.

Finally, the equation for the conservation of energy in the boundary layer is introduced in the form of Equation (10).

$$\frac{\dot{q}_s''}{G_\infty(T_s-T_\infty)c_p}+\frac{v_s\rho_s}{G_\infty}=\frac{1}{G_\infty(T_s-T_\infty)}\frac{d}{dx}[\Delta_2 G_\infty(T_s-T_\infty)] \quad (10)$$

The first term is substituted with Equation (8), and the result is solved for $\Delta_2 G_\infty$.

$$(\Delta_2 G_\infty)^{-0.25}=(T_s-T_\infty)^{0.25}\left[0.0156Pr^{-0.5}\int_0^x \mu^{0.25}G_\infty(T_s-T_\infty)^{1.25}R(1+B_h)dx\right]^{0.2} \quad (11)$$

The resulting Equation (11) is substituted back into Equation (8), with the result shown below if solved for *St*. The viscosity is removed from the integral since it is assumed to be constant.

$$St=\frac{0.0287Pr^{-0.4}\mu^{0.2}(T_s-T_\infty)^{0.25}R}{\left[\int_0^x G_\infty(T_s-T_\infty)^{1.25}R(1+B_h)dx\right]^{0.2}} \quad (12)$$

Since Equation (12) is an implicit function, with St, hidden within the R and B_h terms, it must be solved sequentially along the streamline. By marching downstream and assuming that all the positions upstream of a certain point are defined and unaffected by downstream variations, the bottom integral can be broken into two sections: the first from 0 to x_{i-1} whose value is known, and the second at x_i. The result can easily be solved to provide the local Stanton number.

A known limitation to the Ambrok integral approach that must not be overlooked is difficulties which arise in modeling strong pressure gradients as these will affect the boundary layer shape, which until this point has been assumed as constant.

This method works well for all points except x_0, at the LE, where a different model given by Equation (13) is used to estimate the HTCs in the stagnation zone. The similarity solution assumes the leading edge behaves like an infinitely long cylinder of radius r. This well understood approach taken from Reshotko and Cohen (Reschotko & Cohen, July 1955) provides a starting place for the integral which can then be built upon as x increases.

$$Nu=0.81{Re_r}^{0.5}Pr^{0.4} \quad (13)$$

A.5. NUMERICAL CALCULATION OF HTC

In parallel to the analytical method just described, a two-dimensional, boundary layer, finite difference code called TEXSTAN (Crawford, 2008) was also used to calculate the HTC. The code works by solving the continuity, momentum and energy differential equations, with the possibility of also solving the kinetic energy and turbulence energy diffusion equations. This code was chosen for its versatility of inputs and ability to easily vary every parameter found in the code. The code contains several transition and turbulence models as well as predetermined starting boundary layer profiles designed for turbine blades. A full description of the code's predecessor STAN5 can be found in reference (Kays, 1976), which is still applicable to TEXSTAN. A MATLAB2019a [1] script was written around the code in order to rapidly send inputs and read outputs within an iterative loop.

Domain and Mesh

The flow was separated into two separate and independent streams, one on the pressure surface and one on the suction surface. The domain is contained between the leading edge, trailing edge, no slip surface and the free stream. As the velocity profile at the leading edge is zero, TEXSTAN provides an analytical starting velocity profile taken from the Faulkner-Skan velocity profile of an infinitely long cylinder in crossflow, similar to the methodology used in the previous section.

The mesh parameters used in order to obtain mesh-independent results are suggested by Crawford (Crawford, 2008). The streamwise integration step size was set to be 5% of the velocity boundary layer 99% thickness. The initial crossflow step size was set at 0.005% of the velocity boundary layer 99% thickness and the consequent growth rate was 9%.

[1] www.matlab.com

Inputs

TEXSTAN inputs needed to be carefully formatted into a text file containing a number of flags, boundary conditions and thermodynamic parameters. Input boundary conditions would include the free stream velocity, streamwise position, wall temperature, wall curvature and transpiration rate. The total inlet values of the flow were also provided as well as whichever fluid properties that were to be kept constant.

Turbulence modeling

The flow was assumed to be entirely turbulent and the primary turbulence model used was the mixing length model, primarily for the purpose of speed and simplicity. The one equation Hassid-Poreh model as well as the two equation Launder-Sharma turbulence models were used only for comparison and close agreement was found between all three.

Fluid Properties

For this analysis, heat capacity, viscosity, Prandtl number and the heat capacity ratio were maintained constant in order to match the same procedure used in the analytical model. Density was left as a variable in order to account for compressibility. Variable fluid properties could be programmed into TEXSTAN as could be the case for the analytical model but this was avoided since the free stream temperature undergoes only small variations in temperature along a single streamline.

Adjustments of inputs

One of the limitations that come with the simplicity of TEXSTAN is that it cannot solve for certain flows such as stagnation points. Furthermore, it cannot calculate through flow separation and recirculation bubbles. This is mainly due to the parabolic nature of the solver and the fact that it cannot solve for reversed flows. (Gaugler, 1981)

This limitation plays an important role in transpired boundary layers as transpiration tends to destabilize boundary layers and promote separation, meaning the coolant mass flux was required to be limited. The max value for the blowing ratio was limited to 0.007, lower than the value suggested by Kays and Crawford (Kays & Crawford, 1980)in order to account for less stable segments in the boundary layer. Since blow off caused by injecting coolant can lead to significant aerodynamic and cooling performance penalties, it is generally avoided at all costs and the inability to solve blown off transpired flows is therefore not an issue.

On the other hand, the inability to solve separated flows can become troublesome near the leading edge of the pressure surface on a turbine blade. Here the velocity peaks very rapidly and drops again into the midsection of the blade, often leading to a small separation zone. In order to work around this setback, previous workers of TEXSTAN have suggested modifying the velocity input to smooth out the initial velocity peak (Gaugler, 1981).

A.6. ITERATIVE PROCESS

Since the surface temperature is used as a boundary condition for TEXSTAN as well as in Equation (12), it is necessary to iterate around the turbine blade in order to obtain the correct temperature and HTC for a steady state system. A convergence criterion for the mean metal temperature was arbitrarily chosen to be $\Delta 0.1$K between iterations.

An additional goal was to achieve a quasi-uniform blade temperature. The reasoning behind this decision is that simply finding the average metal temperature would not be an appropriate means of measuring cooling effectiveness if there were large temperature variations across the blade. Therefore, another iterative loop was added which varied the local coolant mass flux rate proportionately to the difference between the local metal temperature and the average metal temperature.

The criterion for a uniform blade temperature was that the standard deviation of the metal temperature be below 5 K, once the points immediately adjacent to the trailing edge were removed. This caveat was due to the singularities that could arise at the leading and trailing edge. This criterion would be met within 3 to 4 redistributions in coolant.

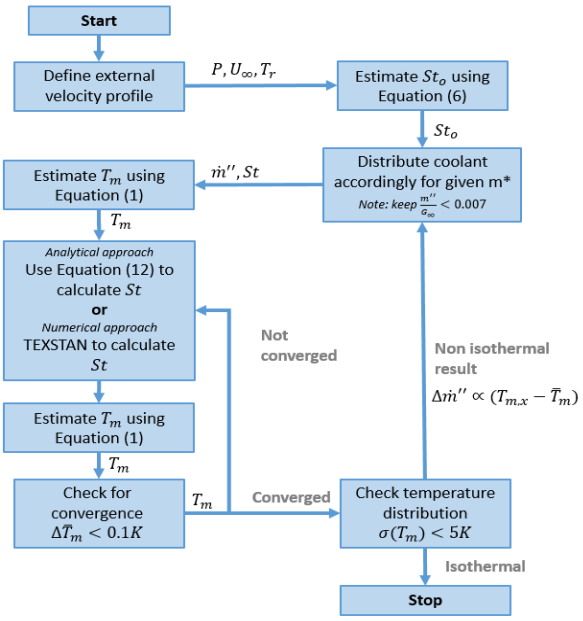


FIGURE A-3-3: ITERATIVE LOOP USED TO FIND ISOTHERMAL BLADE TEMPERATURE

The first analytical iteration would use the criterion given by Equation (14) to distribute coolant around the blade as this was found to already produce very even temperature distributions.

$$\dot{m}'' \propto h_o(T_r - T_c) \qquad (14)$$

Since the analytical solution is computationally very easy, it would serve as the first guess for the finite difference method.

A.7. EXAMPLE FLOW FIELD

The approximate pressure and velocity fields around a body such as turbine blade are typically first calculated quite trivially using inviscid solvers with basic corrections for viscous effects. In order to demonstrate the validity of the models, a 2D turbine blade cascade quickly simulated in ANSYS Fluent 19[2] using a real blade geometry, as shown in FIGURE A-4. Static pressure and Mach number values were calculated along the surface and imported to MATLAB, from which all other thermodynamic properties could be calculated via isentropic relations. Real engine conditions were used and are described in Table (1). The coolant feed pressure was set at 103% of the mainstream total pressure. It was also assumed that the addition of coolant would not have a significant impact on the overall flow field.

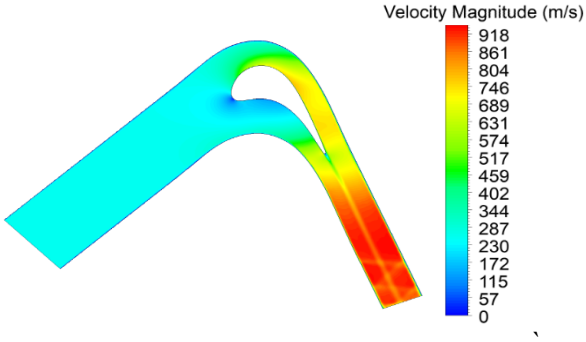


FIGURE A-4: SIMULATED CASCADE FLOW FIELD SHOWING STATIC PRESSURE

To properly account for Mach effects, the mainstream temperature is adjusted using a recovery factor as shown in Equation (15). The recovery temperature is used as an effective local gas static temperature in all subsequent calculations.

$$T_r = T_\infty + \sqrt[3]{Pr}(T_t - T_\infty) \qquad (15)$$

Property (unit)	Value
Entry $\boldsymbol{P_t}$ (bar)	34.5
Entry $\boldsymbol{P_s}$ (bar)	34
Entry $\boldsymbol{T_t}$ (K)	1970
Entry Mach	0.333
Entry Velocity (m/s)	300
Exit $\boldsymbol{P_s}$ (bar)	20
Pressure ratio	1.681
$\boldsymbol{C_p}$ (j/kg-K)	1249.58
Entry Density (kg/m3)	6.08
Dynamic viscosity (kg/m-s)	6.683E-05
Mass flow (kg/s)	2.985
Conductivity of air (W/m-K)	0.0083
Coolant $\boldsymbol{T_t}$ (K)	800

TABLE A-1:ENGINE OPERATING CONDITIONS

A.8. RESULTS

Both models converged towards an isothermal blade very quickly even without modeling conduction. The metal temperature predictions of both models are in strong agreement with each other, with a difference of just under 10°C for the demonstrated case of a nondimensional coolant flow rate of m^*=0.9. The numerical and analytical methods predicted a metal

[2] www.ansys.com

temperature of 983°C and 993°C respectively.

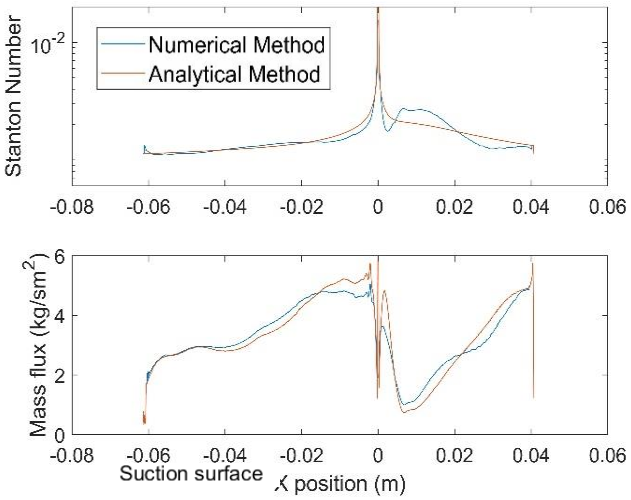


FIGURE A-5: FINAL NUMERICAL AND ANALYTICAL SOLUTIONS AT m=0.9 FOR ISOTHERMAL BLADE*

FIGURE A-5 displays the solutions of analytical and numerical finite difference methods. The numerical Stanton number plot diverges more noticeably with respect to the analytical model, demonstrating a higher sensitivity to the variations in free stream velocity, particularly on the pressure surface. This reiterates the difficulty of accurately calculating the HTCs through analytical means for regions with large pressure gradients. Both approaches are in closer agreement on the suction side. The differences in predicted Stanton number are mirrored by the differences in what is predicted to be the ideal coolant mass flux distribution for an isothermal blade. Nevertheless, both models share a very similar overall distribution.

These results demonstrate that whilst analytical approximations may have certain limitations in predicting local values to a high degree of accuracy, the overall result obtained is an accurate enough result to provide a preliminary understanding of the effect transpiration cooling has on blade cooling performances.

In order to bring the results into perspective, the coolant flow rate and blade temperature can be respectively nondimentionalized using m^*, as shown in Equation (16) and the cooling effectiveness as given by Equation (17).

$$m^* = \frac{\dot{m}_c C_p}{h_o A} \tag{16}$$

$$\varepsilon_m = \frac{T_\infty - \bar{T}_m}{T_\infty - T_c} \tag{17}$$

In FIGURE A-6, the temperature and cooling effectiveness predicted by both methods are plotted against m^*. Both predict a very similar trend in performance for values below an m^* of 1.5. Above this, the numerical methods begins to predict smaller improvements. The numerical method was only predicted up to an m^* of 2 because higher values would lead to flow separation in the uniform blade solution.

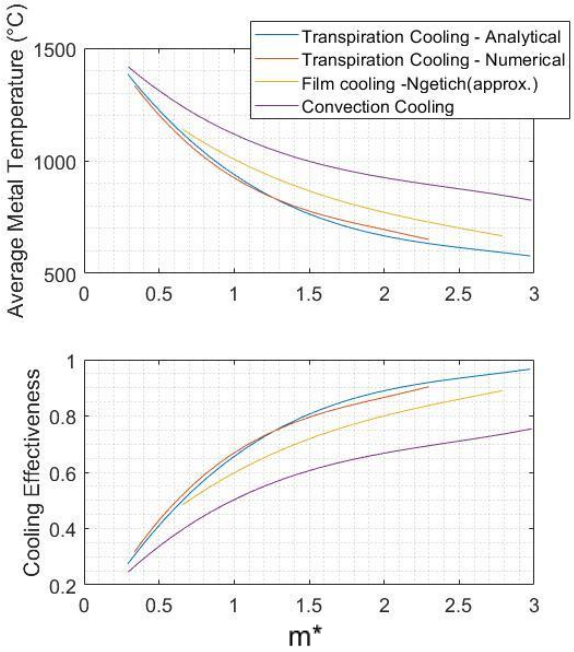


FIGURE A-6: PREDICTED COOLING PERFORMANCE OF TRANSPIRATION MODELS COMPARED TO CONVENTIONAL COOLING ARRANGMENTS

The temperature and effectiveness of internal and film cooling blades are also plotted. In both cases, internal cooling effectiveness is assumed to be perfect, as has been the case with transpiration cooling. Achieving cooling effectiveness near unity in convection and film cooled blades would be much more challenging than for transpired blades but this scenario allows for an easy theoretical comparison. For the convection cooled blade, the coolant leaves the blade through the trailing edge at the metal temperature, providing no additional thermal protection. For the film cooled blade, the adiabatic wall temperature has been varied as typical in film cooling analyses using the

method described by Ngetich et.al. (Murray & al., 2017).

The advantages of the transpiration cooling model are very clear. For typical values of *m**, between 1 and 2, transpiration cooling requires approximately 15-20% less coolant for the same average metal temperature. Alternatively, for the same coolant fraction, the metal temperature is predicted to be about 100 degrees lower than typical film cooling designs. These benefits are compounded by the fact that the blade can be designed to be isothermal, assuming the entire surface is porous

A.9. CONCLUSION

A very simple approach for predicting transpired turbine blade temperatures has been presented. Both analytical and numerical methods of predicting the external HTC yield very similar cooling performance predictions given the heat balance model. The cooling effectiveness predicted also incites a great deal of excitement in the possibilities that transpiration cooling may provide.

The next step of investigation should examine the effect of varying the coolant exit temperature in greater detail, allowing for the model to account for reduced internal heat transfer. The ability to properly model the internal heat transfer will allow for the full conjugate model to be developed.

Experimental work must still be carried out to confirm the true cooling capabilities of transpiration based blade designs as well as to confirm the validity of both numerical and analytical models, particularly around curved surfaces. Further studies must also be carried out on the physical bounds which define a transpired surfaced from an effusion cooled surface. With current development focused on increasing the number of film cooling holes and increasing the effective surface porosity, manufacturers will no doubt enjoy a continuous trend in cooling improvements that will slowly converge towards the performances predicted within this paper.

Overcoming the engineering difficulties posed by manufacturing and operating porous turbine blades will still be a major hurdle to overcome but the legitimacy of embarking on such a challenge has undoubtedly been validated.

AA1. APPENDIX

Equation (3) can be derived through the following procedure:

Starting with the energy equation for the turbulent boundary layer:

$$\bar{u}\frac{d\bar{T}}{dx} + \bar{v}\frac{d\bar{T}}{dy} = \frac{d}{dy}\left[(\alpha_H + \varepsilon_H)\frac{d\bar{T}}{dy}\right]$$

Where $\dot{q}''$ can be defined as:

$$\dot{q}'' = \rho c_p(\alpha_H + \varepsilon_H)\frac{d\bar{T}}{dy}$$

Applying Couette flow assumptions the first term is dropped.

$$\bar{v}\frac{d\bar{T}}{dy} = \frac{d}{dy}\left[(\alpha_H + \varepsilon_H)\frac{d\bar{T}}{dy}\right]$$

Integrating with respect to *y* using the following boundary conditions:

$y = 0$	$y = \delta$
$\bar{T} = T_s$	$\bar{T} = T_\infty$
$\dot{q}'' = \dot{q}_s''$	

Yeilds:

$$v_s(T_\infty - T_s) = (\alpha_H + \varepsilon_H)\frac{d\bar{T}}{dy} - \frac{\dot{q}_s''}{\rho c_p}$$

Rearranging and integrating

$$\int_{T_s}^{\bar{T}} \frac{d\bar{T}}{\left(v_s(T_\infty - T_s) + \frac{\dot{q}_s''}{\rho c_p}\right)} = \int_0^\delta \frac{dy}{(\alpha_H + \varepsilon_H)}$$

$$\frac{1}{v_s}\ln\left(v_s(T_\infty - T_s)\rho c_p + \dot{q}_s''\right) - \frac{1}{v_s}\ln(\dot{q}_s'') = \int_0^\delta \frac{dy}{(\alpha_H + \varepsilon_H)}$$

Collecting terms

$$\frac{1}{v_s}\ln\left(\frac{v_s(T_\infty - T_s)\rho c_p}{\dot{q}_s''} + 1\right) = \int_0^\delta \frac{dy}{(\alpha_H + \varepsilon_H)}$$

Combining the following definitions:

$$B_h = \frac{v_s/u_\infty}{St}\, St = \frac{h}{u_\infty \rho c_p} \qquad h = \frac{\dot{q}_s''}{(T_\infty - T_s)}$$

$$B_h = \frac{v_s(T_\infty - T_s)\rho c_p}{\dot{q}_s''}$$

Substituting $B_h$back in

$$\frac{1}{v_s}\ln(B_h + 1) = \int_0^\delta \frac{dy}{(\alpha_H + \varepsilon_H)}$$

Rearranging and solving for St

$$\ln(B_h + 1) = B_h u_\infty St \int_0^\delta \frac{dy}{(\alpha_H + \varepsilon_H)}$$

$$St = \frac{1}{u_\infty}\frac{\ln(B_h + 1)}{B_h}\left(\int_0^\delta \frac{dy}{(\alpha_H + \varepsilon_H)}\right)^{-1}$$

By l'Hopital's theorem:

$$\lim_{B_h \to 0}\left(\frac{\ln(B_h + 1)}{B_h}\right) = 1$$

Therefore the ratio of Stanton number with blowing to Stanton number without blowing (at the same x location) is equal to:

$$\left|\frac{St}{St_0}\right|_x = \left(\frac{\ln(B_h + 1)}{B_h}\right)$$

A.10. REFERENCES

[1] E. Eckert and J. Livingood, "Comparison of Effectiveness of Convection-, Transpiration-, and Film-Cooling Methods With Air as Coolant," *NACA Report 1182*, 1954.

[2] W. Kays and M. Crawford, Convective Heat and Mass Transfer 2nd Edition, McGraw Hill, 1980.

[3] T. Langener, J. v. Wolfersdorf, M. Selzer and H. Hald, "Experimental investigations of transpiration cooling applied to C/C material," *International Journal of Thermal Sciences*, vol. 54, pp. 70-81, 2012.

[4] G. Ambrok, "Approximate solution of equations for the thermal boundary layer with variations in boundary layer structure," *Soviet Physics - Technical Physics*, vol. 2, pp. 1979-86, 1957.

[5] E. Pohlhausen and v. 1. p. 1.-1. 1. , *Math. Mech.*, vol. 1, pp. 115-121, 1921.

[6] B. Andersson, A. R., L. Håkansson, M. Mortensen, R. Sudiyo and B. van Wachem, Computational Fluid Dynamics for Engineers, Cambridge University Press, 2011.

[7] M. R. Reyhani, M. Alizadeh, A. Fathi and H. Khaledi, "Turbine blade temperature calculation and life estimation - a sensitivity analysis," *Propulsion and Power Research*, vol. 2, no. 2, pp. 148-161, 2013.

[8] J. Kruckels, T. Arzel, T. Kingston and M. Schnieder, "Turbine Blade Thermal Design Process Enhancements for Increased Firing Temperatures and Reduced Coolant Flow," *ASME Expo*, pp. GT2007-27457, pp. 445-455, 2007.

[9] T. Takahashi, K. Watanabe and T. Takahashi, "Thermal Conjugate analysis of a first stage blade in a gas turbine," *ASME Turbo Conference Paper*, Vols. 2000-GT-251, 2000.

[10] L. Hylton, M. Mihelc, E. Turner, D. Nealy and R. York, "Analytical and experimental evaluation of the heat transfer distribution over the surfaces of turbine vanes.," 1983.

[11] G. Ngetich, "A 3D Conjugate Approach for Analysing a Double Walled Effusion Cooled Turbine Blade," in *ASME Turbo*

Expo GT 2018-76534, Olso Norway, 2018.

[12] A. Murray and e. al., "An Integrated Conjugate Computational Approach for Evaluating the Aerothermal and Thermomechanical Performance of Double Walled Effusion Cooled Systems," in *ASME Turbo Expo GT 2017-64711*, Charlotte, 2017.

[13] D. Bohn, J. Ren and K. Kusterer, "Conjugate Heat Transfer Analysis for Film Cooling Configurations with Different Hole Geometries," *ASME Turbo Conference Paper*, 2003.

[14] G. Laschet, R. Krewinkel, D. Hul and D. Bohn, "Conjugate analysis and effective thermal conductivities of effusion cooled mulitlayer blade sections," *International Journarl of Heat and Mass Transfer*, vol. 57, no. 2, pp. 812-821, 2013.

[15] G. Cerri, A. Giovannelli, L. Battistia and R. Fedrizzi, "Advances in effusive cooling techniques of gas turbines," *Applied thermal engineering*, vol. 27, no. 4, pp. 692-698, 2007.

[16] L. Arcangeli, B. Facchini, M. Surace and T. Lorenzo, "Correlative Analysis of Effusion Cooling Systems," *ASME j. Turbomachinery*, vol. 130, no. 1, pp. 11-16, 2008.

[17] S. G. Schwarz, R. Goldstein and E. Eckert, "The Influence of Curvature on Film Cooling Performance," *ASME Expo*, pp. 90-GT-010, 1990.

[18] W. Dahmen, T. M. S. Gotzen and M. Rom, "Numerical simulation of transpiration cooling through porous material," *International Journal for Numerical Methods in Fluids*, vol. 76, pp. 331-365, 2014.

[19] E. Eckert and H. Cho, "Transition from Transpiration to Film Cooling," *Int. J Heat Mass Transfer*, vol. 37, no. 1, pp. 3-8, 1994.

[20] W. M. Kays and R. J. Moffat, "Behaviour of Transpired and Turbulent Boundary Layers," in *Studies in Convection*, vol. 1, Academic Press, 1975, pp. 223-319.

[21] R. J. Moffat, "The Turbulent Boundary Layer on a Porous Plate: Experimental Heat Transfer with Uniform Blowing and Suction," Ph.D. Thesis, 1967.

[22] W. Reynolds, W. Kays and S. Kline, "NASA Memo 12-2-58W," Washington, 1958.

[23] E. Reschotko and C. Cohen, NACA TN 3513, Washington, July 1955.

[24] M. Crawford, "TEXSTAN," 2008. [Online]. Available: http://www.texstan.com/index.php. [Accessed 21 May 2019].

[25] M. C. W. Kays, "STAN5 - A Program for Numerical Computation of Two-dimensional Internal and External Boundary Layer Flows," 1976.

[26] R. Gaugler, "Some Modifications to, and Operational Experiences with, the Two-Dimensional, Finite-Difference, Boundary-Layer Code, STAN5," ASME, 1981.

[27] E. Eckert, "Analysis of Film Cooling and Full Coverage Film Cooling of Gas Turbine Blades," *ASME GT*, vol. 106, pp. 207-211, 1984.

[28] A. S. Dorfman, Conjugate Problems in Convective Heat Transfer, CRC Press, 161-227.

[29] W. M. Kays, M. Crawford and W. B., Convective Heat and Mass Transfer 4th Edition, McGraw-Hill, 2005.

Appendix B Experimental facility and methods

The experiments presented in this thesis were all carried out within a single, yet highly versatile, experimental facility. This chapter details the apparatus as well as the two different data capturing methodologies used to evaluate and develop the novel cooling geometries. The facility itself is a high-speed, low temperature single blade passage, first designed and built by by Gurram et al (2016) and then modified by Ngetich et al (2019). The present author was responsible for some additional modifications to the ancillary systems which have allowed for an expansion in test types that can be carried out as well as a large increase in the rate of testing that could be achieved by the rig and its operators. The first subsection details the basic rig design and function whereas the following subsections detail the different types of tests carried out within the rig.

B.1. Rig Description

The blow-down rig's test section, shown in Figure B-1 is designed around a fixed high pressure turbine blade profile. The inner surfaces of the passage are contoured to match the mid-span streamline between two adjacent rotor blades of an infinite 2D cascade. The blade passage has a rectangular profile and a constant width of 100mm with the inlet and outlet areas normal to the flow. The rig operating conditions can be found in Table B-1 Engine and Rig operating conditions. which includes both the design intent as well as the actual operating conditions. The curved cascade walls of the test section are made entirely of clear 20mm thick Perspex to allow for an unimpeded view of the entire blade surface. Both end walls, initially made of Perspex, were replaced with aluminium to allow for greater strength and adaptability due to Perspex's propensity to crack when machined.

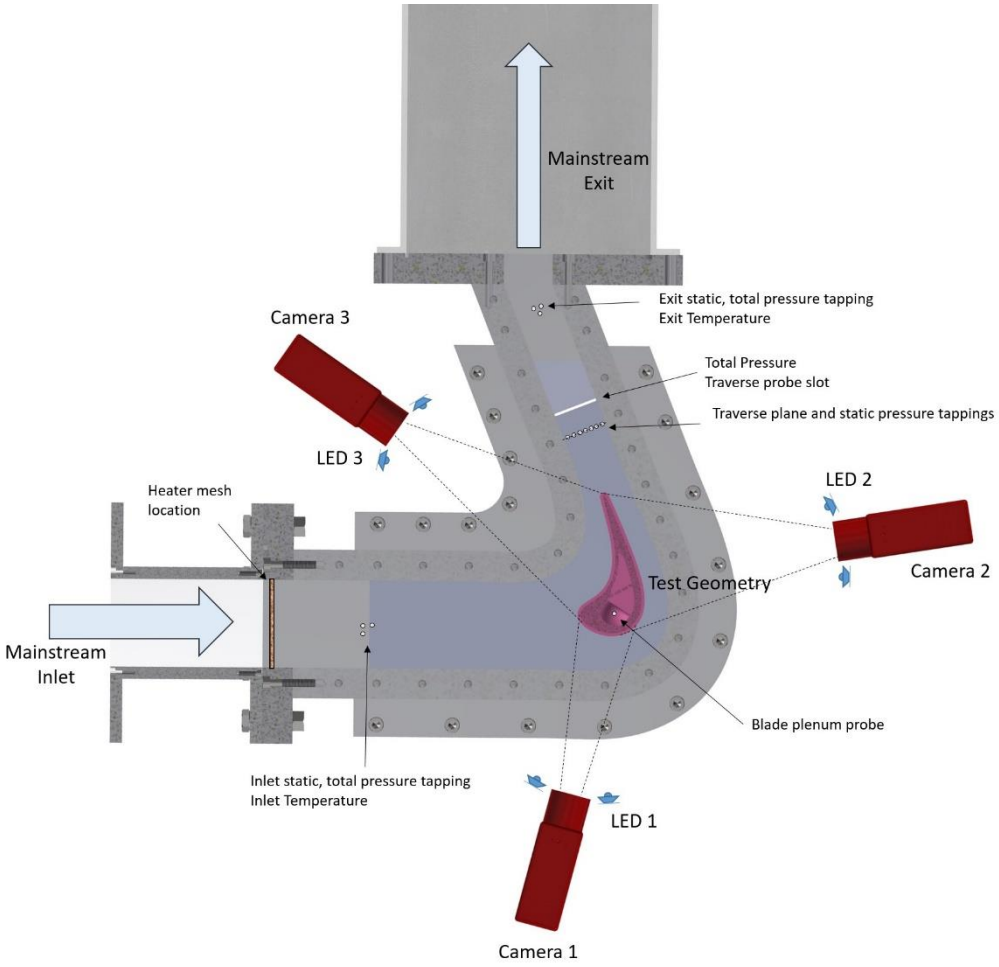


Figure B-1 Schematic of Cascade Test Section

The rig mainstream flow is fed by a 400 psi compressed air line which is triggered by a large pneumatic ball valve. The air pressure is first dropped by a large regulator to 10 bar and then fed through a mass restrictor plate which chokes the flow. This setup allows for the mainstream mass flow to be set by the regulator and kept constant between runs and not be affected by the downstream geometries or by the addition of heating elements.

		Engine	PSP	TLC
P_o	bar	34.50	1.842	1.901
P_s exit	bar	20.520	1.150	1.200
Pressure ratio		1.681	1.600	1.583
T_0	K	1977	291	316
c_p	j/kg-K	1249.58	1004.17	1006.28
Density	kg/m^3	6.08	2.20	2.09
Dynamic viscosity	kg/m-s	6.683e-05	1.815e-05	1.921e-05
Scale		1	2.3	2.3
Chord length	mm	33.832	77.81	77.81
Mass flow	kg/s	141.80	104.28	103.33
N blades		68	1	1
Mass flow /passage	kg/s	2.0853	1.4064	1.3937
Heat input	kW		0.00	35.06
Entry Mach		0.3342	0.324	0.324
Entry velocity	m/s	297.89	110.80	115.46
Entry P_s	bar	31.80	1.705	1.760
Entry angle	^{o}	43.4451	43.45	43.45
Entry area	mm^2	1151.49	5762.66	5762.66
Entry passage width	mm	25.06	57.63	57.63
Passage pitch	mm	34.51	79.37	79.37
Passage height	mm	45.96	100.00	100.00
H/P ratio		1.33	1.26	1.26
Exit angle	^{o}	65.8280	65.83	65.83
Exit passage width	mm	14.13	32.50	32.50
Exit passage area	mm^2	649.43	3250.09	3250.09
Reynolds		935085	1067296	999319
Corrected $\dot{m}/A$		0.02334	0.02263	0.02263

Table B-1 Engine and Rig operating conditions.

A flow straightener is also included upstream of the test section. The rig exhausts to atmosphere through a large cylindrical pipe. The rig section is geometrically scaled up in order to facilitate accurate data capture and resolution. The overall size of the rig was limited by the mass flow that can be provided by the test facility's compressed air supply. The scaling was therefore set at 2.3x engine scale, with a mass flow of 1.4 kg/s. At this rate runs can be sustained for up to 8 minutes. During the initial design

intent, stage pressure ratio, dimensionless mass flow and mainstream Reynolds number, defined by Equation **(B-1** and Equation **(B-2** respectively, are maintained between the engine and experimental conditions. The Mach number and pressure ratio across the cascade are also maintained. P_{atm}, μ and T_0 where all set by environmental conditions. However, due to the finite nature of the rig as well as the additional losses incurred by the presence of the mid pitch walls, the required inlet pressure increased in order to match inlet Mach numbers as well as the pressure distribution around the blade as is demonstrated in the following section.

$$Q = \frac{\dot{m}\sqrt{T_o}}{AP_o} \tag{B-1}$$

$$Re = \frac{\rho u d}{\mu} \tag{B-2}$$

Air for the coolant flow stream is drawn from either a 100 psi line or a set of compressed gas cylinders depending on the coolant gas of choice. Both sources are controlled by the use of a remote pressure regulator which can be operated throughout the rig's operation. The coolant stream mass flow is monitored by the use of an orifice plate as described by ISO 5167 (International Organization for Standardization, 2020)with mass flow measurements being calculated in real time. In order to increase the flexibility and control of the rig, a system of manifolds and parallel orifice plates was expanded to allow for up to 5 distinct controllable coolant streams. The coolant is fed through one of the end walls of the rig and into the root of the blade.

Additional safety features to the rig include a pressure release valve and burst disc exhaust which have been calibrated to avoid any over pressurization of the test section. For further safety, the rig is encased in a Plexiglas and aluminium box, which serves to physically shield the rig from its operators during runs at all times.

B.1.1. Rig Validation

In order to ensure the flow on the blade surface is properly representative of engine conditions despite minor variations from the design intent, static pressure measurements were taken along the midspan of the blade surface using both pressure tappings as well as pressure sensitive paint described later un this section. From these values, the Mach number distribution around the blade can be plotted and compared to the intended infinite cascade distribution. Close agreement is seen around the entire blade surface with the sole exception of the late suction surface, where the presence of the added boundary layer on the Perspex walls prevents the flow from accelerating as intended, resulting in a lower Mach numbers in this region. Figure B-2 demonstrates the ideal, predicted and actual static pressure distributions around the blade.

Further CFD simulations of the full cascade volume also indicate the presence of vortices originating from where the endwalls meet the convex surfaces in the passage as seen in Figure B-3. These slowly migrate inward along the suction surface of the blade, encroaching 15mm towards the midspan at the trailing edge. In order to avoid these endwall effects as well as any boundary layers or velocity profiles caused by the finite nature of the rig, the actual test region is

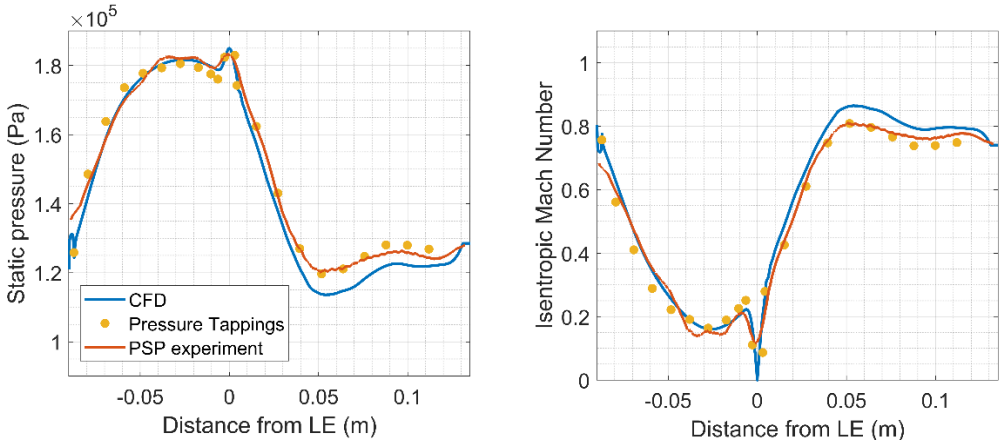
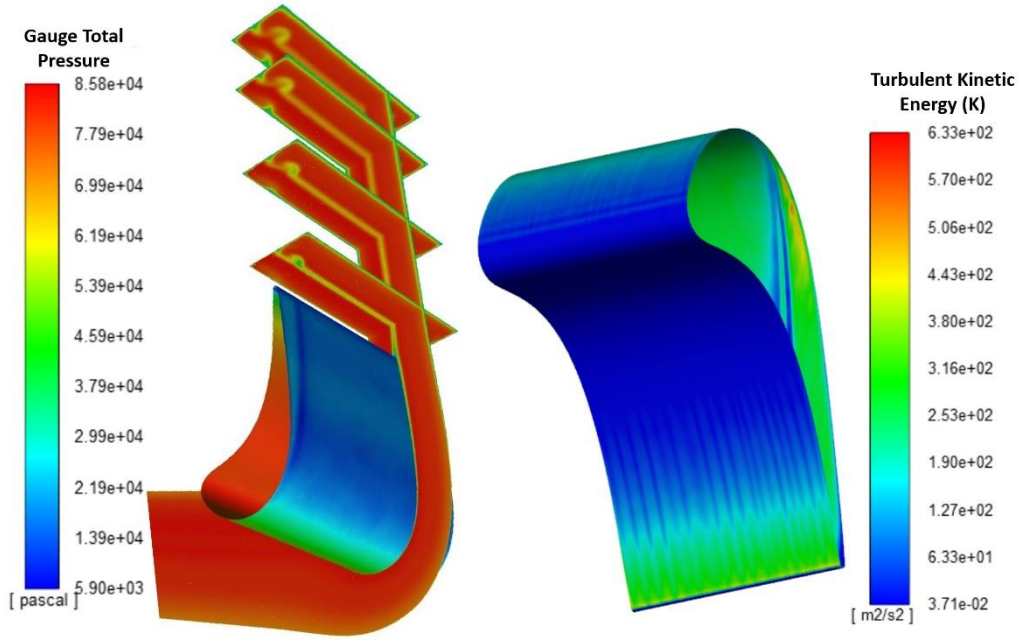


Figure B-2 Static pressure and resulting isentropic Mach number distribution of Rig and compared to design intent.

limited to the 60% midspan of the test blades. Taylor-Görtler vortices were also detected on the entire span of pressure surface of the blade.



(a) Suction Surface and wake (b) Pressure surface and Taylor-Görtler Voritces

Figure B-3 Visualization of secondary flows within test section at operating conditions using CFD

B.1.2. Sensor arrays and camera Setup

In order to monitor and control the rig's operation, a large bank of temperature and pressure sensors is attached to the rig. Static and total pressure measurements are taken at several locations both upstream and downstream of the blade using miniature amplified HCE and HDI pressure transducers. The coolant feed inlet total pressure is also measured as well as the test blade plenum static pressure. Temperature measurements are also taken at these locations through the use of K-type thermocouples. Monitoring these values ensures the inlet velocity and Mach number of the rig remain correct. Data acquisition systems NI 9205 and NI 9214 from National instruments are used for collecting pressure and temperature measurements respectively.

The imaging of the blade is carried out through the use of three AVT BigEye G-283B cooled CCD cameras. These are positioned around the blade so that their overlapping fields of vision cover the

entire blade surface. These cameras were selected for their high sensitivity and range. In order for the relevant light intensity data to be mapped onto the blade surface, a geometric transform was generated for each camera depending on its position relative to the blade. These transforms scale the images so that they remain area representative through the use of a reference checkerboard pattern, flattening out the blade surface and allowing data to be accurately plotted on 2D axes. This scaling also allows for the three cameras' images to be scaled to the same size so they can be stitched together into a single accurate representation of the entire blade surface. Figure B-4 demonstrates the transformation of the leading edge region of the aerofoil geometry.

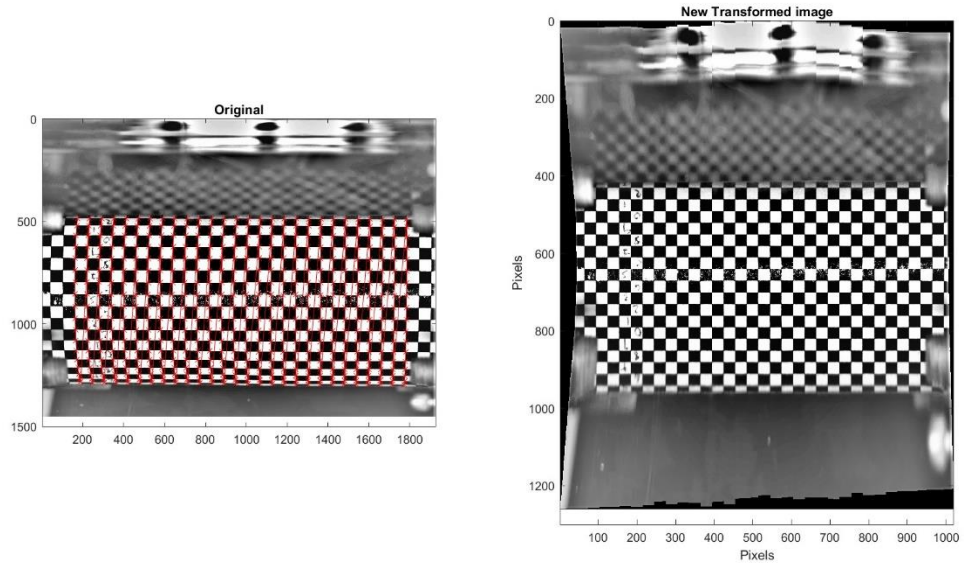


Figure B-4: Original input with detected checkerboard locations and corresponding transformed image

In order to reduce any noise for the cameras, the entire rig is enclosed in thick blackout curtains which prevents any variation in external light to affect the test section. These curtains have the added benefit of shielding the operators of the rig from any potentially hazardous low energy light sources.

B.2. Pressure Sensitive Paint methodology for Film Effectiveness measurements

Due to its reliability and ease of use, PSP was the predominant method used to evaluate the film effectiveness of different parametric film cooling geometries. This non-intrusive high resolution approach, originally conceived for static pressure measurements, can be repurposed for adiabatic film effectiveness measurements allowing for full effectiveness maps to be constructed, offering a great level of detail over alternative methods. As extensive literature and research exists on PSP, this section will only serve as an overview of its basic function with a focus on its specific application and implementation within this research.

B.2.1. Description

PSP's properties are derived from the behaviour of luminophores. These compounds have specific light emission and absorption spectra due to their distinct electronic energy states. However, when excited, a luminophore can also follow a non-radiative pathway when in the presence of oxygen molecules. Due to the existence of this pathway, also known as oxygen quenching, the paint's emission intensity can be used as a measure of the oxygen partial pressure in contact with the paint. Further information about specifics of luminophores and their use in sensitive paints can be found in (Gregory, et al., 2008).

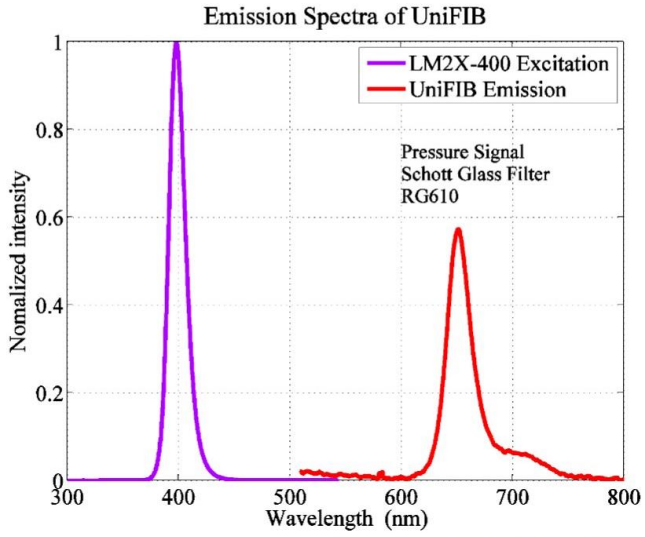


Figure B-5 Emission and absorption spectra of UniFIB PSP (Innovative Science Solutions Inc., 2016)

The specific PSP used in this research is called UniFIB and is manufactured to perform consistently across different applications and runs. The luminophore in UniFIB is called platinum tetra(pentafluorophyneyl)porphine (PtTFPP) and it's absorption and emission spectra are characterised by Figure B-5. The paint also includes a white pigment, a gas permeable binder to allow oxygen to diffuse into the paint and a volatile solvent to allow for easy application. Additional properties of the paint that need to be taken into consideration are the rapid photo-degradation of the paint which can be as high as 1% per hour when exposed to light as well as a sensitivity to temperature. The full specifications of the paint can be found in (Innovative Science Solutions Inc., 2016).

B.2.2. PSP Characterisation

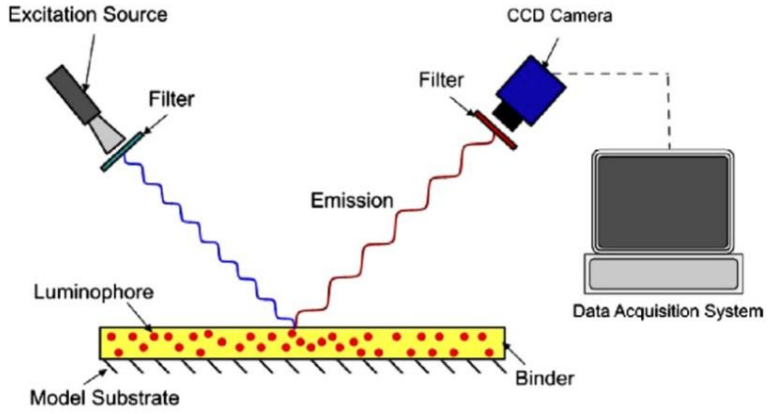


Figure B-6 Basic PSP experimental set-up (Quinn, et al., 2013)

$$\frac{I_{ref} - I_b}{I - I_b} = A(T) + B(T) + \frac{p(O_2)}{p(O_2)_{ref}} \quad \textbf{(B-3)}$$

The specific characterisation of PSP with respect to its light emitting properties is described by the Stern-Volmer Equation (B-3) (Quinn, et al., 2013) where $p(O_2)$ refers to the oxygen partial pressure and I refers to the measured light intensity. Both the partial pressure and intensity values are normalised by a reference value typically taken at atmospheric conditions. The intensity values are further adjusted by removing background noise captured by the I_b term.

In practice, instead of attempting to determine the Stern-Volmer constants, empirical calibration is typically the preferred method of characterising the PSP. While a default correlation is provided by the manufacturers, the complex nature of the paints sensitivity and rapid photo-degradation warrants further and constant validation. An example generated using a calibration rig is shown in Figure B-7. Here a paint sample is subjected to a full range of temperatures and pressures within a controlled chamber. By comparing the light intensity of the paint at a reference pressure, and at the test pressure, the ratio of oxygen partial pressures can be determined. The temperature sensitivity, which is due to the gas permeable binder's temperature sensitivity as well as the thermal quenching of the luminophores, can also be accounted for using this approach.

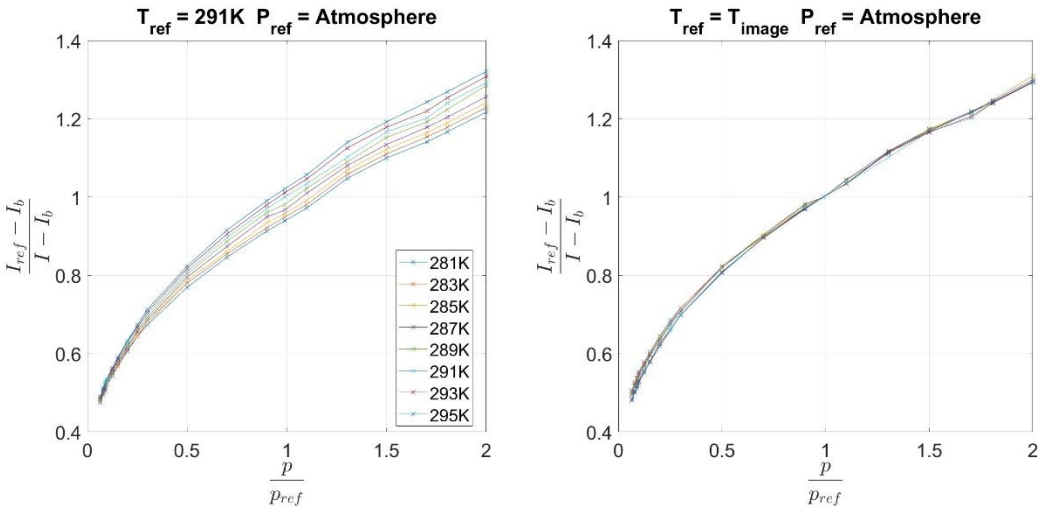


Figure B-7 Example Calibration Curves taken from UniFIB

In order to minimize the uncertainty caused by the temperature sensitivity, the reference and test measurements can also be taken at the same temperature. With this approach, the intensity curves collapse onto each other. During experiments, this can be often be achieved by taking the reference intensity immediately after the test is complete. However, as this cannot always be perfectly accomplished due to the nature of compressible transonic flows, the paint surface temperature can be measured insitu through the use of embedded thermocouples, allowing for the temperature variation to be directly accounted for when necessary.

Through this approach, every single pixel of a CCD camera pointed at a PSP sample can be used as an oxygen partial pressure sensor. As intensities are always calculated as a ratio to a reference image, local variations in lighting, paint application and positioning relative to the camera should not have an effect on the results. This is a major advantage of PSP over other imaging techniques, making it particularly suited to examining complicated shapes with intricate cooling geometries and film distributions.

Given that the concentration of oxygen in air is always constant at 21%, the overall static pressure can be inferred from the oxygen partial pressure. Alternatively, if the static pressure is known, we can infer the concentration of oxygen in the gas around the PSP which serves as the basis for the following section.

B.2.3. Mass transfer analogy for film effectiveness measurements

By making use of the mass transfer analogy, PSP can also be applied to make adiabatic wall film cooling measurements as explained by the following derivation.

The 2D turbulent boundary layer heat transfer equation for a homogenous fluid is given by Equation **(B-4)** (Kays & Crawford, 1980)

$$G_x \frac{\partial T}{\partial x} + G_y \frac{\partial T}{\partial y} = \rho(\epsilon_t + \alpha)\frac{\partial^2 T}{\partial y^2} \quad \textbf{(B-4)}$$

where the ϵ_t and α are the turbulent thermal and molecular thermal diffusivities respectively. If we assume an adiabatic wall, where the heat transfer between the wall and the boundary layer is zero, the boundary conditions are

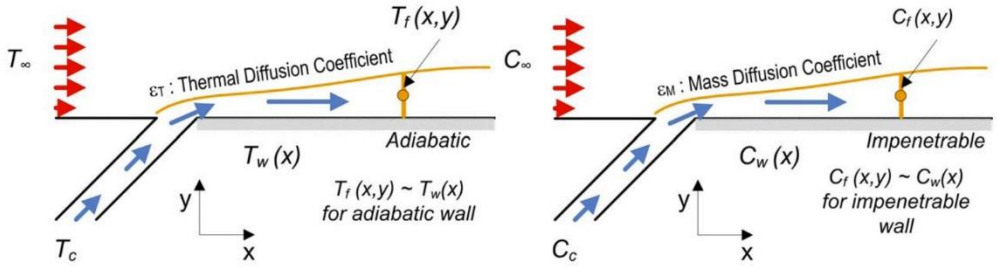


Figure B-8 2D Film Cooling model showing mass transfer analogy (Han & Rallabandi, 2010)

$$y = 0, \frac{\partial T}{\partial y} = 0, T = T_{aw}$$
$$y > \delta_f, T = T_\infty$$
$$x = 0, T = T_c \tag{B-5}$$

The corresponding 2D turbulent boundary layer mass transfer equation dictating the mass fraction of a specific gas is Equation (B-6) where ϵ_M and Γ are the turbulent mass and molecular mass diffusivities respectively.

$$G_x \frac{\partial C}{\partial x} + G_y \frac{\partial C}{\partial y} = \rho(\epsilon_M + \Gamma) \frac{\partial^2 C}{\partial y^2} \tag{B-6}$$

Given an impermeable wall, the boundary conditions are

$$y = 0, \frac{\partial T}{\partial y} = 0, C = C_w$$
$$y > \delta_f, C = C_\infty$$
$$x = 0, C = C_c \tag{B-7}$$

For turbulent flows in gases, the ratio of diffusivities, known as the Lewis number is close to 1.

$$\frac{\epsilon_t + \alpha}{\epsilon_M + \Gamma} = Le_T \approx 1 \tag{B-8}$$

With this assumption, the two governing equations for the thermal and concentration boundary layers become identical. While the boundary layer near the leading edge can be laminar or transitory, the

presence of films typically triggers a turbulent flow regardless. Provided these assumptions hold true, it can be stated that the adiabatic film effectiveness is equivalent to the ratio of mass fractions of a specific gas, as given by Equation **(B-9)**.

$$\eta = \frac{T_\infty - T_{aw}}{T_\infty - T_c} \approx \frac{C_\infty - C_w}{C_\infty - C_c} \tag{B-9}$$

If C is chosen as the mass fraction of oxygen and the coolant gas used is an oxygen free foreign gas, such as Nitrogen or argon, the film effectiveness can be rearranged to Equation (B-10) as $C_{O2,fg} = 0$.

$$\eta \approx \frac{C_{O_2,air} - C_{O_2,w}}{C_{O_2,air} - C_{O_2,fg}} = 1 - \frac{C_{O_2,w}}{C_{O_2,air}} \tag{B-10}$$

However from the ideal gas law, the partial pressure of gases are a function of the molar fraction of gases X, not the mass fraction . Equation (B-11) relates these two values through the molecular weight MW.

$$C_i = X_i \left(\frac{MW_i}{MW_{mix}} \right) \tag{B-11}$$

Where MW_{mix} is the molar average molecular mass as given by

$$MW_{mix} = X_i MW_i \tag{B-12}$$

Substituting back into Equation (B-10)

$$\eta \approx 1 - \frac{X_{O_2,w} \left(\frac{MW_{O_2}}{MW_{mix}} \right)}{X_{O_2,air} \left(\frac{MW_{O_2}}{MW_{air}} \right)} \tag{B-13}$$

As experiments are always run on the premise that a foreign gas is added to air in order to form the mixture

$$MW_{mix} = X_{air} MW_{air} + X_{fg} MW_{fg} \tag{B-14}$$

Where

$$X_{air}MW_{air} \approx X_{O_2}MW_{O_2} + X_{N_2}MW_{N_2} \quad \textbf{(B-15)}$$

Since the ratio of oxygen to nitrogen in air is known, as are their molecular masses, it can be stated that

$$X_{air} = 4.74X_{O_2} \quad \textbf{(B-16)}$$

As the mole factions must add up to unity

$$X_{air} + X_{fg} = 4.74X_{O_2} + X_{fg} = 1 \quad \textbf{(B-17)}$$

$$X_{fg} = 1 - 4.74XO_2 \quad \textbf{(B-18)}$$

Substituting back into Equation

$$\eta \approx 1 - \frac{X_{O_2,w}\left(\frac{MW_{O_2}}{X_{air}MW_{air}+X_{fg}MW_{fg}}\right)}{X_{O_2,air}\left(\frac{MW_{O_2}}{MW_{air}}\right)} = \quad \textbf{(B-19)}$$

$$= 1 - \frac{X_{O_2,w}MW_{air}}{X_{O_2,air}\left(4.74X_{O_2,w}MW_{air} + (1 - 4.74X_{O_2,w})\,MW_{fg}\right)}$$

Which simplifies to

$$\eta = 1 - \frac{1}{4.74X_{O_2,air} + \left(\frac{X_{O_2,air}}{X_{O_2,w}} - 4.74X_{O_2,air}\right)\frac{MW_{fg}}{MW_{air}}} \quad \textbf{(B-20)}$$

Given that

$$4.74X_{O_2,air} = X_{air,air} = 1 \quad \textbf{(B-21)}$$

$$\eta \approx 1 - \frac{1}{1 + \left(\frac{X_{O_2,air}}{X_{O_2,w}} - 1\right)\frac{MW_{fg}}{MW_{air}}} \quad \textbf{(B-22)}$$

As the mole fraction of oxygen in a gas is equivalent to the ratio of partial pressure of oxygen to the overall gas pressure

$$\eta \approx 1 - \frac{1}{1 + \left(\frac{p(O_2)_{air}/p_{tot}}{p(O_2)_w/p_{tot}} - 1\right)\frac{MW_{fg}}{MW_{air}}} =$$

$$= 1 - \frac{1}{1 + \left(\frac{p(O_2)_{air}/p_{ref}}{p(O_2)_w/p_{ref}} - 1\right)\frac{MW_{fg}}{MW_{air}}} \quad \textbf{(B-23)}$$

When the foreign gas used has a similar molecular weight to air, such as nitrogen, the equation can further be simplified to

$$\eta \approx 1 - \frac{p(O_2)_w/p_{ref}}{p(O_2)_{air}/p_{ref}} \quad \textbf{(B-24)}$$

In this form, the equations can be related directly to the intensity measurements obtained from the PSP. The $p(O_2)_w/p_{ref}$ term can be determined from the intensities taken when running the experiment with the foreign gas coolant. In order to obtain $p(O_2)_{air})/p_{ref}$ which is in effect the static pressure away from the wall, the experiment can be run with air as a coolant instead of the foreign gas.

B.2.4. Implementation

In order to implement the PSP method within the experimental rig, 2 UV LED panels were setup adjacent to each camera. This allowed for the entire test piece surface to be exposed to the UV. A 610nm wavelength filter to match the PSP emmission spectra was installed in front of each camera in order to reduce noise.

Test pieces were manufactured from high strength ABS like plastics using an AM printer due to its high resolution, strength and adaptability to complicated geometries. These were sprayed with multiple fine coats of PSP in order to ensure thorough coverage. A base layer of white primer was also added in order to improve the signal quality as well as protect the plastic test pieces from any potential chemical effects of the PSP.

Test pieces were also fitted with multiple embedded thermocouples at regular 20mm intervals along the surface midspan which measured the paint surface temperature. These would be used to

determine an interpolated temperature distribution around the blade and measure any temperature variations between the reference and experiment images.

When running experiments, the following procedure would be carried out in order to maximize repeatability and rig time. First the lighting system would be switched on in advance in order to allow the lighting ample time to warm up and reach a constant intensity. Once the mainstream was switched on, a series of 30 images of the blade were taken in rapid succession using first air then the foreign gases at a given mass flow rate, measured using the orifice plate. This was repeated for all mass flow rates for a given geometry. Both the mainstream and coolant streams would then be switched off and reference images would be taken. Finally the lighting would be switched off and a final dark image would be taken as a measure of background noise.

After averaging each set of images, each pixel would have a measured value for I, I_{ref}, I_b and an interpolated value for T and T_{ref}. P_{ref}, the atmospheric pressure, was also measured and recorded. By using the most recent calibration data to match the paint application, a new intensity-temperature-pressure surface, much like the curves in Figure B-7, could be generated for each pixel. This allows any potential variation in temperature between the experiment and reference image to be accounted for. Finally a simple lookup function on the surface could be implemented to determine p/p_{ref}. By repeating the process for both the air and nitrogen, the film effectiveness for each pixel could be determined.

B.2.5. Benefits of PSP

- Accounts for variation in lighting and paint application
- High signal to noise ratios makes for clear results
- Experiments can be carried out at low temperatures
- Plastic test pieces can cheaply and rapidly be designed and tested allowing for a quick turnaround between design conception and experimental validation.

B.2.6. Limitations of PSP

- Lighting intensity needs to be constant in between different images

- Paint degradation can be significant and quick, particularly when in the presence of UV light as this leads to photobleaching. This requires test pieces to be tested as quickly as possible once painted and constant calibrations to be carried out.
- The sensitivities to temperature are can be more significant when measuring minor variations in pressure. This can be important when using cooling gases from multiple sources each of which can be at a different temperature.
- The paint has a typical response time of 300ms meaning experiments need to be steady state.
- The physical operating range of the selected paint brand is limited 2 bar and 50 degrees Celsius, meaning it cannot be applied to high pressure, high temperature experiments.
- The flow needs to be turbulent in order for the mass transfer analogy to be valid
- When using coolants of varying densities in large quantities, the static pressure flow field may be different to that of the case measured when using air as a coolant.

Thermochromic liquid crystals can offer a valid alternative for film effectiveness measurements. However, as temperature is measured directly, conductivity and internal cooling effects also need to be considered. When carrying out simpler parametric studies, this is not always preferable. These can be overcome to some degree by using a material with very low conductivities such as dense foams or plastics but not entirely. Therefore, corrections typically have to be overlayed onto the results. For these reasons, TLCs are used instead in the following section for overall cooling effectiveness measurements.

B.3. TLC Crystals for Metal effectiveness measurements

In order to capture the overall cooling effectiveness of a design, metal effectiveness measurements are required. By measuring temperature directly, Thermochromic Liquid Crystals (TLCs) offer a non-intrusive approach to determining these values on the blade surface. In these experiments, the effects of conduction, internal and external convection are accounted for. By using test pieces with representative conductivities as well as relevant internal cooling geometries, an overall measure of cooling ability can be determined. While offering the possibility of a higher fidelity study, at possibly a lower cost, the

complexities of producing accurate and quality test pieces of out of metal mean that this method can only be used in the later stages of this investigation.

B.3.1. Method Overview

Thermochromic liquid crystals are organic compounds structured in several layers of molecules. Each layer is oriented in a certain direction relative to its neighbours, with the directors forming a spiral over multiple layers. When submitted to specific temperatures, the angle between different layer orientations is changed, altering the pitch of the director helix. The crystals become optically active when the pitch of the helix matches the wavelength of visible light. When layered over a black substrate, white visible light reflected off the active liquid crystals can be quantified to form a temperature reading. TLCs are particularly suited for use in high speed experiments as they are insensitive to pressure. Commercially available TLCs are micro-encapsulated by a protective polymer. The capsules, ranging between 10-15 μm, help to protect the TLCs from contaminants such as dust, moisture and shear effects, prolonging the useful life of the TLC coating.

TLCs can be categorized to either be narrow band or wide band thermochromic crystals, depending on the range of temperatures at which the crystals are optically active. In wide band crystals, the temperature sensing range is between 20 and 30 degrees. As the spiral pitch is slowly modified, so does the wavelength and colour of light reflected. The temperature can then be inferred by the hue of the crystals. This method allows for continuous spatial temperature measurements to be taken making it popular for many low temperature experiments, particularly on flat surfaces where uniform lighting and data capture can be achieved.

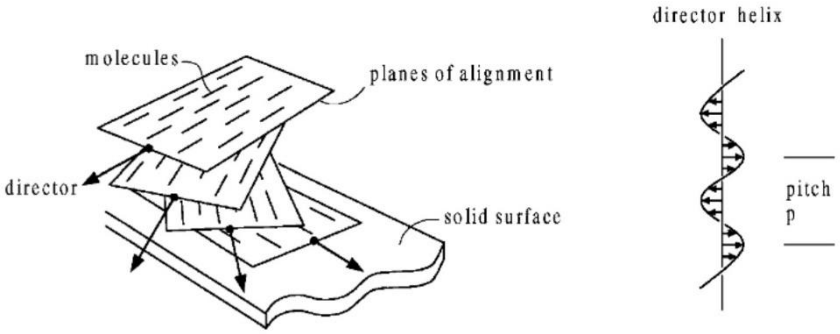


Figure B-9 Schematic of TLC and director orientation (Ireland, et al., 1999)

However, as the hue of light can also be affected by a range of other optical effects such as lighting orientation and reflections from the base substrate, a full calibration needs to be carried out insitu which can be complicated to achieve for an intricate geometry.

Narrow band crystals in comparison have a range of approximately 1 degree. At this critical point, the reflected light intensity peaks at a specific temperature predetermined by the properties of the crystal, resulting in a discrete contour of isothermal surface temperatures. The benefit of this approach is that while less information can be obtained, the confidence of this data is significantly higher as measurements can be taken relative to a reference image when the blade is cold.

B.3.2. Implementation

When compared to the previous method, the experimental rig requires only minor adjustments. Firstly, a heater mesh is installed upstream of the test section in order to provide a temperature increase relative to the coolant stream. At full power, a temperature step of 35K can be achieved. Second, the light sources used are large diffuse white LED lighting panels spaced out to illuminate the surface as best as possible.

In order to minimize any lateral conduction of the test piece to the surrounding rig, the test pieces are held in place by plastic holders made of high strength AM ABS plastic. These parts have low thermal conductivities, isolating the test piece from the rest of the rig. Results from the experiments

show no signs of visible lateral conduction to the side walls with the surface temperature at the interface being very discontinuous.

In order to improve the signal quality as well as reduce the level of noise caused by unwanted reflections from the light source, a green filter with a transmission wavelength of 550nm can be added to the camera system as this is the predominant hue of the crystals at peak intensity. Further trials with different lighting combinations also indicated that warmer lighting reduces the glare and reflections as narrow band crystals keep a blue hue once above their critical temperature. Much like in the case of PSP, the images are taken relative to reference images in order to account for variations in lighting and orientation. Intensity values are also normalized by the maximum value achieved at peak intensity. Three different liquid crystals were combined together to add more temperature contours to the test piece. Figure B-10 shows a calibration plot for the light intensity response of the TLCs used in this investigation. Crystals were chosen with peaks at approximately 25°C, 30°C and 35°C. Through the use of 3 different crystal bands, 4 separate levels can first be established.

As the different crystals in effect produce almost identical signals, in order to systematically discern between the different peaks, the test piece can be slowly brought to the operating condition from cold and held until it reaches steady state temperature. By starting with the entire blade outside of the measurable temperature range the crystals will transition through a different number of critical points depending on the steady state temperature at which they finish. By plotting the pixel intensity against time these peaks can easily be identified and counted.

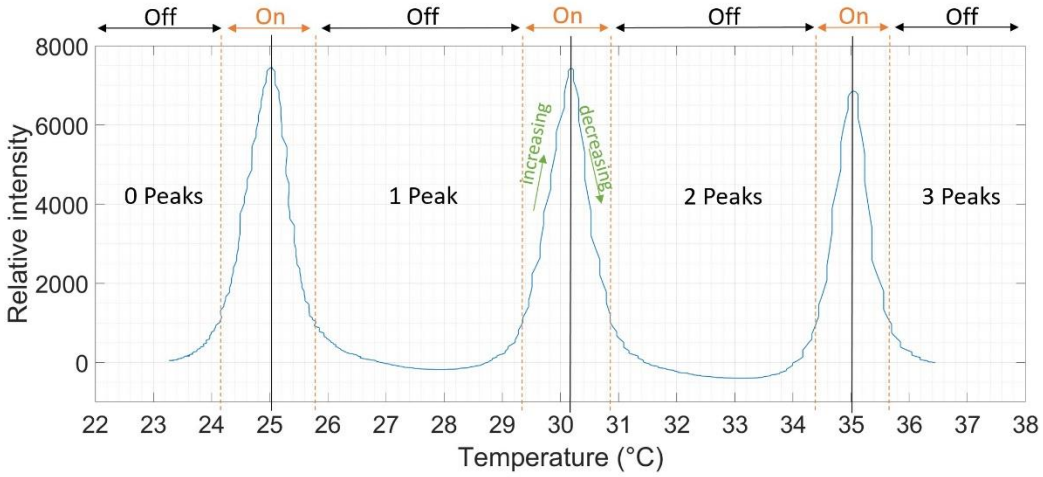


Figure B-10: TLC reference intensity response relative to temperature

If sufficient signal strength and quality can be established, additional contour levels can be added around the intensity peaks. By establishing an arbitrary relative signal intensity at which the crystal is deemed on or off, three more bands can be created. These are indicated in Figure B-10 by the red dotted lines. Whilst this results in contours of uneven width, the additional levels can yield further insight when large portions of the blade are close to the critical temperatures. Finally the additional three bands can further be divided into two. As the crystal intensity history is known, it can be determined from the derivative of the pixel intensity-time plot whether the pixel is moving towards or away from an intensity peak. This results in 10 separate temperature bands being established from the use of only 3 crystals.

	Engine	Rig
Operating temperature (K)	2000	300
Conductivity of air (W/m.K)	0.083	0.0283
Metal material	CSMX-4	Inconel 625
Metal conductivity (W/m.K)	28	9.8
HTC (approximate) (W/m^2.K)	8400	1248
Nusselt number (based on wall thickness)	101.2	101.2
Wall thickness (m)	0.001	0.0023
Biot Number	0.3	0.293

Table B-2 Biot number scaling for material selection

B.3.3. Test piece material choice

As the conductivity of a turbine blade has a significant impact on the metal effectiveness distribution and cooling performance, the Biot number of the experiment, given by Equation (B-25), is matched to engine conditions. From the range of different materials available for AM manufacturing, Inconel 625 was selected as it would lead to a Biot number within 2.5% of the target value. Table B-2 presents the values and constants used to make this assessment. One of the principle assumptions made was that the Nusselt number of the rig would match that of the engine. This assumption is valid as by design, both engine and rig share the same Reynolds number and similar Prandtl numbers.

$$B_i = \frac{h}{k} L \tag{B-25}$$

B.3.4. Benefits of TLCs

- TLCs are low cost and easy to apply
- TLCs show minimal pressure sensitivity
- Allow for full surface metal effectiveness to be measured
- Limitations of other methods such as infra red and wide band, make it very hard to calibrate for when it comes to complicated geometries.

B.3.5. Limitations of TLCs

- Low cost of TLC crystals is offset by the high cost and complexity of manufacturing one off metal test pieces, with additional complications stemming from AM such as hole shrinkage playing an important role in the final geometry.
- The discrete nature of the temperature bands measured. This is particularly significant when comparing different geometries of similar effectiveness as it is not possible to assign accurate numerical values for the cooling effectiveness. Local and area averages will carry high uncertainties.
- The source light and measured light are of similar wavelengths, unlike for PSP. Therefore lighting and camera angles must account for reflections and glare which can result in a tradeoff against the overall signal strength.
- As the incoming mainstream air temperature is predominantly determined by outdoor environmental factors due to the location of the supply tank, the temperatures of both the mainstream and coolant stream cannot be precisely controlled. However, the critical points of the narrow band TLCs are by defined fixed, meaning the values for the cooling effectiveness contours are not necessarily consistent from run to run.
- The relatively narrow temperature difference that can be generated between the mainstream and coolant air also result in any uncertainties being magnified in the final metal effectiveness calculation.

B.4. Uncertainty Analysis

In order to determine the uncertainty of the different experimental methods, the perturbation method of Moffat (1988)was used. In this method, a series of measurements with associated uncertainties $S_j(\pm\delta_{Sj})$ are used to calculate a certain result R.

$$R = f(S_1, S_2, S_3, \ldots, S_N) \tag{B-26}$$

If the uncertainty in a single measurement is given by δS_j, then the uncertainty in the final result due to this particular measurement is given by

$$\delta R_{S_j} = \frac{\partial R}{\partial S_j}\delta S_j \tag{B-27}$$

where the partial derivative of R with respect to S_j is called the sensitivity coefficient. Multiple independent variables are then combined using the root-sum square method

$$\delta R = \left[\sum_{i=1}^{N}\left(\frac{\partial R}{\partial S_j}\delta S_j\right)^2\right]^{1/2} \tag{B-28}$$

The principle results in this study are listed below

$$\dot{m}_c = f(d_{ori}, d_{pipe}, T_{ori}, p_{atim}, p_{ori,u}, \Delta p_{ori}, \epsilon_{ori}, C_{d,ori}) \tag{B-29}$$

$$\eta_{film} = f(I_{ratio,fg}, I_{ratio,air}, T_{ref}, T) \tag{B-30}$$

$$\eta_{metal} = f(T_c, T_m, i_m, T_{cali}, T_{crystal}) \tag{B-31}$$

Applying the perturbation method to the orifice meter calculations used to obtain coolant mass flow rate at a nominal mass flow of 20g/s yielded an uncertainty of 2.86%. In addition to uncertainties due to the measurements, uncertainties stemming from the C_d as stated in ISO 5167:2003 (International Organization for Standardization, 2020)were included. The main contributions in uncertainty are from the pressure difference across the orifice as well as the orifice hole sizing. The calculation is shown in Table B-3. Nominal $\dot{m}_c = 20g/s$

Measurement	Nominal Value	Measurement uncertainty	Sensitivity coef.	Normalized by Result
D_{ori}	10	0.1	4.285	2.14%
D_{pipe}	20.3	0.1	0.514	0.26%
T_{ori}	290.8	1	0.0337	0.17%
p_{atm}	101230	100	3.97e-5	0.02%
$p_{ori,1}$	110000	1000	4.49e-5	0.22%
Δp_{ori}	27000	1000	3.474e-4	1.74%
ϵ_{ori}	0.972	0.61%	17.146	0.51%
C_{dori}	0.6124	0.50%	27.219	0.42%
		absolute error		0.5723
		% error of calculation		2.86%

Table B-3 Uncertainty calculation in coolant mass flow evaluated at $\dot{m}_c$= 20g/s

The uncertainty in film effectiveness is given as a function of the uncertainty in I_{ratio} which given by Equation (B-3). The uncertainty is variable, as the sensitivity coefficient is not constant given the inverse relationship between intensity and p/p_{ref}. The sensitivity coefficient was calculated for a range of η_{film} values between 0 and 1. Sample images were taken across a range of nominal effectiveness values and the standard deviation in intensity ratio across all pixels was used as the measurement uncertainty for the perturbation method. Results are given in Table B-4. The uncertainty at high film effectiveness is very low but increases exponentially at lower values as shown by Figure B-11.

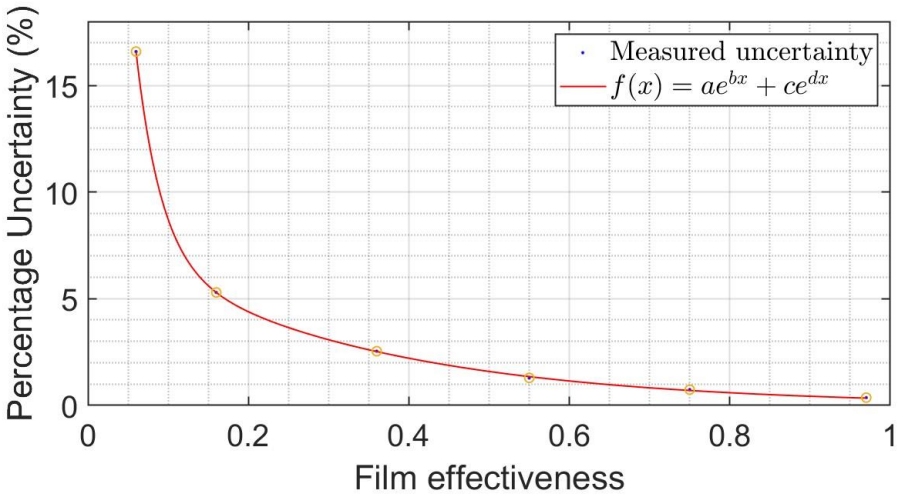


Figure B-11: Variation in PSP error against film effectiveness

Uncertainties at given η_{film}

	Nominal Value	Nominal η_{film}	Measurement uncertainty	Sensitivity coef. With respect to $p/pref$	Uncertainty in η_{film}
I_{ratio}	0.3789	0.97	0.0058	0.6	0.36%
I_{ratio}	0.7325	0.75	0.0103	0.7	0.74%
I_{ratio}	0.9548	0.55	0.0146	0.75	1.29%
I_{ratio}	1.127	0.36	0.0176	0.78	2.54%
I_{ratio}	1.3024	0.16	0.0221	0.83	5.29%
I_{ratio}	1.3677	0.06	0.0242	0.88	16.6%

Table B-4 Uncertainty calculation in film effectiveness evaluated at multiple η_{film} values

Metal effectiveness uncertainty are largely dictated by the size of the induced temperature difference relative to the measurement error. The most significant contributions stem from the thermo-couple uncertainty rather than the uncertainty in the liquid crystal response. In order to quantify the crystal response uncertainty, the crystals where cycled through the range of temperatures multiple times with reference thermocouples installed in multiple locations. The lateral shift in the crystal response was limited to ±0.3 degrees. Results from the perturbation method are given in Table B-5. Nominal ε_m= 0.65.

	Nominal Value	Measurement uncertainty	Sensitivity coef.	Normalized by Result
$T_{o,m}$	318	1	0.01282	1.97%
$T_{o,c}$	291	1	0.02381	3.66%
T_{cali}	300	1	0.03704	5.70%
T_{TLC}	300	0.3	0.03704	1.71%
		absolute error	0.0472	
		% error of calculation	7.26%	

Table B-5 Uncertainty calculation in Metal effectiveness evaluated at ε_m = 0.65

REFERENCES

- 3D Systems, 2020. *Plastic 3D Printers: SOLUTIONS FOR PROTOTYPING TO PRODUCTION IN PLASTICS.* [Online]
  Available at: https://www.3dsystems.com/3d-printers/plastic
  [Accessed 20 September 2022].

- Abdul Abas, R., Hayashi, M. & Seetharaman, S., 2007. Thermal Diffusivity Measurements of CMSX-4 Alloy by the Laser-Flash Method. *Int. J. of Thermophysics Vol. 28 No. 1.*

- Abdul, A. R., Hayashi, M. & Seetharaman, S., 2007. Thermal Diffusivity Measurements of CMSX-4 Alloy by the Laser-Flash Method. *Int. J. of Thermophysics Vol. 28 No. 1.*

- Acosta, W. A., 1987. *Liner cooling research at NASA Lewis Research Center.* Army Aviation Research and Development Command, Cleveland Ohio., United States: NASA TM - 100107.

- Adair, D., Kirka, M. & Ryan, D., 2019. Additive Manufacture of Prototype Turbine Blades for Hot-Fired Engine Performance Validation Trials. *Proceedings of the ASME Turbo Expo 2019: Turbomachinery Technical Conference and Exposition. Volume 6: Ceramics; Controls, Diagnostics, and Instrumentation; Education; Manufacturing Materials and Metallurgy. Phoenix, Arizona, USA,* p. V006T24A012. ASME.

- Albert, J. E., Bogard, D. G. & Cunha, F., 2004. *Adiabatic and Overall Effectiveness for a Film cooled blade.* Vienna Austria, ASME.

- Ambrok, G., 1957. Approximate solution of equations for the thermal boundary layer with variations in boundary layer structure. *Soviet Physics - Technical Physics,* Volume 2, pp. 1979-86.

- Andersson, B. et al., 2011. *Computational Fluid Dynamics for Engineers.* s.l.:Cambridge University Press.

- Andrews, G. E., Asere, A. A., Gupta, M. L. & Mkpadi, M. C., 1985. Full coverage Discrete Hole Film Cooling: The Influence of Hole Size. *ASME Journal on Gas Turbines,* Volume 47.

- Andrews, G. E., Asere, A. A., Mkpadi, M. C. & Tirmahi, A., 1986. Transpiration Cooling: Contribution of Film Cooling to the Overall Cooling Effectiveness. *International Journal of Turbo and Jet Engines,* Volume 3, pp. 245-256.

- Andrews, G. E., Khalifa, I. M., Asere, A. A. & Bazdidi-Tehrani, F., 1995. *"Full Coverage Effusion Cooling With Inclined Holes".* Houston, Texas, USA, V004T09A045. ASME.

- Andrews, G. E., Khalifa, I. M., Asere, A. A. & Bazdidi-Tehrani, F., 1995. *"Full Coverage Effusion Cooling With Inclined Holes.* Houston Texas, Proceedings of the ASME 1995 International Gas Turbine and Aeroengine Congress and Exposition. Volume 4: Heat Transfer; Electric Power; Industrial and Cogeneration.

- Arai, M. & Suidzu, T., 2013. Porous Ceramic Coating for Transpiration Cooling of Gas Turbine Blade. *Journal of Thermal Spray Technology*, Volume 22, pp. 690-698.
- Arcangeli, L., Facchini, B., Surace, M. & Lorenzo, T., 2008. Correlative Analysis of Effusion Cooling Systems. *ASME j. Turbomachinery,* 130(1), pp. 11-16.
- Arcangeli, L., Facchini, B., Surace, M. & Tarchi, L., 2008. Correlative Analysis of Effusion Cooling Systems. *ASME. J. Turbomach.,* 130(1), p. 011016.
- Baldauf, S., Scheurlen, M., Schulz, A. & & Wittig, S., 2002. *Correlation of Film Cooling Effectiveness From Thermographic Measurements at Engine Like Conditions.* Amsterdam The Netherlands, Proceedings of the ASME Turbo Expo 2002: Power for Land, Sea, and Air. Volume 3: Turbo Expo 2002, Parts A and B..
- Baldauf, S., Schulz, A. & Wittig, S., 1997. *An Overall Correlation of Film Cooling Effectiveness From One Row of Holes.* Orlando, Florida, USA, ASME.
- Baldauf, S., Schulz, A. & Wittig, S., 1999. *High Resolution Measurements of Local Heat Transfer Coefficients by Discrete Hole Film Cooling.* Indianapolis, Indiana, ASME, p. V003T01A017.
- Baldauf, S., Schulz, A., Wittig, S. & Scheurlen, M., 1997. "An Overall Correlation of Film Cooling Effectiveness From One Row of Holes.". *Proceedings of the ASME 1997 International Gas Turbine and Aeroengine Congress and Exhibition. Volume 3: Heat Transfer; Electric Power; Industrial and Cogeneration.,* 2-5 June.
- Battisti, L., 2002. *Boundary Layer control of aerodynamic airfoils.* US, Patent No. US6682022B2.
- Battisti, L., Fedrizzi, R. & Cerri, G., 2006. *Novel Technology for Gas Turbine Blade Effusion Cooling.* Barcelona Spain, Proceedings of GT2006 ASME Turbo Expo 2006: Power for Land, Sea and Air .
- Bayley, F., Cornforth, J. & Turner, A., 1973. Second Paper: Experiments on a Transpiration Cooled Combustion Chamber. *Proceedings of the Institution of Mechanical Engineers,,* Volume 187, pp. 158-169..
- Bayley, F. J. & Turner, A. B., 1968. The Heat Transfer Performance of Porous Gas Turbine Blades. *The Aeronautical Journal of the Royal Aeronautical Society*, Volume 72, pp. 1087-1094.
- Behning, F. P., Prust, H. W. & Moffit, T. P., 1971. *Cold Air Investigation of Stator with wire mesh shell blading,* Lewis Research Center Clevland Ohio: NASA TM-X-2166.
- Bohn, D., Ren, J. & Kusterer, K., 2003. Conjugate Heat Transfer Analysis for Film Cooling Configurations with Different Hole Geometries. *ASME Turbo Conference Paper.*
- Bons, J. P., MacArthur, C. D. & Rivir, R. B., 1994. The Effect of High Free Stream Turbulence on Film Cooling Effectiveness. *ASME Paper 94-GT-51.*

- Broomfield, R. W. et al., 1998. Development and Turbine Engine Performance of Three Advanced Rhenium Containing Superalloys for Single Crystal and Directionally Solidified Blades and Vanes. *ASME. J. Eng. Gas Turbines Power,* 120(3), pp. 595-608.

- Bunker, R. S., 2005. A Review of Shaped Hole Turbine Film-Cooling Technology. *ASME J. Heat Transfer.,* 127(4), pp. 441-453.

- Bunker, R. S., 2006. Gas Turbine Heat Transfer: Ten Remaining Hot Gas Path Challenges. *ASME. J. Turbomach.,* 129:(2), p. 193–201.

- Bunker, R. S., 2017. *Evolution of Turbine Cooling.* Charlotte NC USA, Proceedings of ASME Turbo Expo 2017: Turbomachinery Technical Conference and Exposition.

- Calderon, L., Curbelo, A., Gupta, G. & Kapat, J., 2018. *Adiabatic Film Cooling Effectiveness of a LAM Fabricated Porous Leading Edge Segment of a Turbine Blade.* Oslo, Norway., Proceedings of the ASME Turbo Expo 2018: Turbomachinery Technical Conference and Exposition. Volume 5B: Heat Transfer.

- Campbell, C. & Morrison, J., 2012. *A. Turbine Airfoil With a Compliant Outer W.* s.l. Patent No. US Patent 8,147,196 B2.

- Cerri, G., Giovannelli, A., Battistia, L. & Fedrizzi, R., 2007. Advances in effusive cooling techniques of gas turbines. *Applied thermal engineering,* 27(4), pp. 692-698.

- Chen, Z., Li, Y., Su, X. & Yuan, X., 2020. *Accuracy Assessment of the Sellers Model in Predicting the Multi-Row Film Cooling Performance.* Virtual, Online September , s.n., p. V07BT12A010.

- Choe, H., Kays, W. M. & Moffat, R., 1976. *Turbulent boundary layer on a full-coverage film-cooled surface: An experimental heat transfer study with normal injection,* Stanford University California: NASA CR-2642.

- Cho, H. H. & Goldstein, R. J., 1997. Total-Coverage Discrete Hole Wall Cooling. *ASME. J. Turbomach.,* Volume 119(2), p. 119(2): 320–329.

- Cho, H. H. & Goldstein, R. J., 1997. Total-Coverage Discrete Hole Wall Cooling. *ASME. J. Turbomach.,* Volume 119(2), p. 320–329.

- Colban, W. F., Thole, K. A. & Bogard, D., 2010. A Film-Cooling Correlation for Shaped Holes on a flat-plate Surface. *ASME J. Turbomach.,* 133(1), p. 011002.

- Coulton, B., Murray, A. V. & Ireland, P., 2022. *A Computational Approach to Aerothermal Analysis of Complex Internal Turbine Cooling Geometries.* Rotterdam, AMSE GT, p. 81928.

- Courtis, M. et al., 2021. Influence of Spanwise and Streamwise Film Hole Spacing on Adiabatic Film Effectiveness for Effusion-Cooled Gas Turbine Blades. *nt. J. Turbomach. Propuls. Power ,* pp. 6(3), 37.

- Courtis, M. et al., 2021. Influence of Spanwise and Streamwise Film Hole Spacing on Adiabatic Film Effectiveness for Effusion-Cooled Gas Turbine Blades. *Int. J. Turbomach. Propuls. Power,* pp. 6(3), 37.

- Courtis, M. et al., 2021. Influence of Spanwise and Streamwise Film Hole Spacing on Adiabatic Film Effectiveness for Effusion-Cooled Gas Turbine Blades. *Int. J. Turbomach. Propuls. Power,* pp. 6,37.

- Crawford, M., 2008. *TEXSTAN.* [Online]
  Available at: http://www.texstan.com/index.php
  [Accessed 21 May 2019].

- Crawford, M. E., Kays, W. M. & and Moffat, R. J., 1980. Full-Coverage Film Cooling—Part I: Comparison of Heat Transfer Data for Three Injection Angles. *ASME J. Eng. Power, 102(4),* p. pp. 1000–1005.

- Crawford, M. E., Kays, W. M. & and Moffat, R. J., 1980. Full-Coverage Film Cooling—Part II: Heat Transfer Data and Numerical Simulation. *ASME. J. Eng. Power.,* 102(4), pp. 1006-1012.

- Crawford, M. E., Kays, W. M. & Moffat, R. J., 1980. Full-Coverage Film Cooling—Part I: Comparison of Heat Transfer Data for Three Injection Angles. *ASME J. Eng. Power, 102(4),* p. pp. 1000–1005.

- Cumpsty, N. A., 1997. *A Simple Guide to the Aerodynamic and Thermodynamic Design and Performance of Jet Engines.* 2nd ed. Cambridge: Cambridge University Press.

- Dahmen, W., Gotzen, T. M. S. & Rom, M., 2014. Numerical simulation of transpiration cooling through porous material. *International Journal for Numerical Methods in Fluids,* Volume 76, pp. 331-365.

- Dahmen, W., König, V., Müller, S. & Rom, C. M., 2017. *Numerical investigation of transpiration cooling with uniformly and non-uniformly simulated injection.* Milan, Italy, s.n.

- Devore, M. & Paauwe, C., 2009. *Turbine Airfoil with Improved Cool.* USA, Patent No. U.S. Patent 7,600,966 B2.

- Dorfman, A. S., 161-227. *Conjugate Problems in Convective Heat Transfer.* s.l.:CRC Press.

- Eckert, E., 1984. Analysis of Film Cooling and Full Coverage Film Cooling of Gas Turbine Blades. *ASME GT,* Volume 106, pp. 207-211.

- Eckert, E. & Cho, H., 1994. Transition from Transpiration to Film Cooling. *Int. J Heat Mass Transfer,* 37(1), pp. 3-8.

- Eckert, E. & Livingood, J., 1954. Comparison of Effectiveness of Convection-, Transpiration-, and Film-Cooling Methods With Air as Coolant. *NACA Report 1182.*

- Eckert, E. R. G., 1953. *Transpiration cooled turbine blade manufactured from wires.* US, Patent No. US3011760A.
- El-Jummah, A. M., Nazari, A. & Andrews, G. E. J. E. J., 2017. *Impingement/Effusion Cooling Wall Heat Transfer: Reduced Number of Impingement Jet Holes Relative to the Effusion Holes.* Charlotte, North Carolina, Proceedings of the ASME Turbo Expo 2017: Turbomachinery Technical Conference and Exposition. Volume 5C: Heat Transfer.
- Ellis, G., 2016. *Britain's Jet Age: From the Meteor to the Sea Vixen.* 1st ed. Stroud, Gloucestershire: Amberly Publishing.
- Esgar, J. B., 1970. *Turbine Cooling - Its Limitations And Its Future,* s.l.: NASA TM- X-52801.
- Esgar, J., Colladay, R. & Kaufman, A., 1970. *An analysis of the capabilities and limitations of turbine air cooling methods.* NASA: s.n.
- Fantozzi, G. et al., 2019. Experimental Study on Pressure Losses in Porous Materials. *ASME. J. Eng. Gas Turbines Power,* 141(2), p. 021037.
- Fletcher, D. A., 1997. *Internal Cooling of Turbine Blades: The Matrix Cooling Method - Doctoral Thesis.* Department of Engineering Science, University of Oxford: Oxford UK.
- Friedman, J., 1949. A Theoretical and Experimental Investigation of Rocket Motor Sweat Cooling. *Jour. Am. Rocket Soc.,* Volume 79, pp. 147-154.
- Gao, Z. & Han, J., 2009. "Influence of Film-Hole Shape and Angle on Showerhead Film Cooling Using PSP Technique. *Journal of Heat Transfer,* 131(6), p. 061701.
- Gao, Z., Narzary, D. P., Mehtras, S. & Han, J., 2008. Full-Coverage Film Cooling for a Turbine Blade with Axial-Shaped Holes. *J. Thermophysics and Heat Transfer,* 22(1), pp. 50-61.
- Gaugler, R., 1981. *Some Modifications to, and Operational Experiences with, the Two-Dimensional, Finite-Difference, Boundary-Layer Code, STAN5,* s.l.: ASME.
- Georgiou, D. P. & Louis, J. F., 1985. The Transpired Turbulent Boundary Layer in Various Pressure Gradients and the Blow-Off Condition. *ASME. J. Eng. Gas Turbines Power,* 107(3), pp. 636-641.
- Gillespie, D. & Ireland, P., 1999. *Leading edge intersecting hole flow and heat transfer - Matrix Cooling Report,,* s.l.: Oxford University Engineering Laboratory, University of Oxford.
- Gillespie, D., Ireland, P. & Dailey, G., 2000. *Detailed Flow and Heat Transfer Coefficient Measurements in a Model of an Internal Cooling Geometry Employing Orthogonal Intersecting Channels.* Munich, Germany, Proceedings of the ASME Turbo Expo 2000: Power for Land, Sea, and Air. Volume 3: Heat Transfer; Electric Power; Industrial and Cogeneration.

- Gillespie, D., Wang, Z. & Ireland, P., 1995. *Heating Element.* s.l. Patent No. British Patent Application PCT/GB96/2017.
- Glass, D. E., 2008. *Ceramic Matrix Composite (CMC) Thermal Protection Systems (TPS) and Hot Structures for Hypersonic Vehicles.* Dayton, Ohio, USA, AIAA International Space Planes and Hypersonic Systems and Technologies Conference.
- Glassman, A. J., 1975. *Turbine Design and Application, Volume 3.* NASA Lewis Research Center Cleveland, OH, United States: NASA-SP-290-VOL-3.
- Goldstein, R. J., 1971. Film Cooling. *Advances in Heat Transfer,* pp. (pp. 321-379)..
- Goldstein, R. J., Shavit, G. & Chen, T. S., 1965. Film-Cooling Effectiveness With Injection Through a Porous Section. *ASME. J. Heat Transfer. August,* p. 87(3): 353–359.
- Graf, L. & Kleiser, L., 2014. Film Cooling Using Antikidney Vortex Pairs: Effect of Blowing Conditions and Yaw Angle on Cooling and Losses. *J. Turbomach.,* pp. Vol. 136 - 011008.
- Gregory, J. W. et al., 2008. A review of pressure-sensitive paint for high-speed and unsteady aerodynamics. *Proceedings of the Institution of Mechanical Engineers, Part G: Journal of Aerospace Engineering.,* 222(2), pp. 249-290.
- Grylls, R. J., Austin, C. M., O'Hara, K. & Company, G. E., 2002. *Airfoild with leading edge pockets for reduced heat transfer.* NY, US, Patent No. U.S. Patent 6,443,700.
- Gunston, B., 2006. *World Encyclopedia of Aero Engines: From the Pioneers to the Present Day.* 5th Edition ed. s.l.:Sutton.
- Guo, S. et al., 1998. The application of thin-Ælm technology to measure turbine-vane heat transfer and effectiveness in a film cooled engine simulated environment. *nternational Journal of Heat and Fluid Flow,* Volume 19, pp. 594-600.
- Gurram, N., Ireland, P., Wong, H. & Self, K. P., 2016. *"Study of film cooling in the trailing edge region of a turbine rotor blade in high speed flow using PSP".* Seoul, South Korea., V05CT19A023. ASME.
- Gurram, N., Ireland, P., Wong, H. & Self, K. P., 2016. *Study of film cooling in the trailing edge region of a turbine rotor blade in high speed flow using PSP.* Seoul, South Korea., V05CT19A023. ASME.
- Han, J.-C., 2005. Turbine Blade Cooling Studies at Texas A&M: 1980-2004. *The 2004 AIAA Thermophysics Award Lecture.*
- Han, J. C. & Rallabandi, A. P., 2010. Turbine Blade Film Cooling Using PSP Technique. Volume 1(1) pp. 1–21.
- Han, J. C. & Rallabandi, A. P., 2010. Turbine Blade Film Cooling Using PSP Technique. *Frontiers in Heat and Mass Transfer,* Volume 1(1) pp. 1–21, pp. 1-013001.

- Harrington, M. K. et al., 2001. Full-Coverage Film Cooling With Short Normal Injection Holes. *ASME. J. Turbomach.,* 123(4), pp. 798-805.
- Hartsel, J., 1972. *Prediction of Effects of Mass-Transfer Cooling on the Blade-Row Efficiency of Turbine Airfoils.* San Diego USA, s.n.
- Hatch, J. E. & Papell, S. S., 1959. *Use of a Theroretical FLow Model to Correlate Data for Film Cooling Or Heating an Adiabatic Wall by Tangential Injection of Gases of Different Fluid Properties.* s.l.:s.n.
- He, W. et al., 2019. Film cooling and aerodynamic performances of a turbine nozzle guide vane with trenched cooling holes. *Applied Thermal Engineering,* Volume 150, pp. 150-163.
- Hickel, R. O., Warren, E. L. & Kaufman, A., 1972. *Experimental investigation of the flow, oxidation, cooling, and thermal-fatigue characteristics of a laminated porous sheet material.* NASA Lewis Research Center Cleveland, OH, United States: NASA-TN-D-6664.
- Holgate, N. E., Ireland, P. T. & Romero, E., 2020. Coolant Jets Blowing Across the Airfoil Stagnation Line to Enhance Film Effectiveness. *ASME. J. Turbomach.,* 142(6), p. 061005.
- Holland, M. J. & Thake, T. F., 1980. Rotor Blade Cooling in High Pressure Turbines. *J. Aircraft AIAA Vol. 17, No.6,* pp. 412-418.
- Holrock, J. H., Watson, D. T. & Jones, T. V., 2001. Limitations on Gas Turbine Perfomance Imposed by Large Turbine Cooling Flows. *Journal of Engineering for Gas Turbines and Power,* Volume 123, pp. 487-494.
- Huang, G. & He, L., 2019. Influence of inhomogeneous porosity on effusion cooling. *International Journal of Heat and Mass Transfer,* Volume 144, p. 118675.
- Huang, Z. & al., e., 2015. Experimental investigation of full-coverage effusion cooling through perforated flat plates. *Journal of Applied Thermal Engineering,* Volume 76, pp. 76-85.
- Hylton, L. et al., 1983. Analytical and experimental evaluation of the heat transfer distribution over the surfaces of turbine vanes..
- Innovative Science Solutions Inc., 2016. *UniFib Sensitive paint.* [Online] Available at: https://www.ara.co.uk/assets/DocumentLibrary/ISSI/UniFIB-Data-Sheet.pdf [Accessed 09 02 2022].
- International Organization for Standardization, 2020. *ISO5167 2020: Measurement of fluid flow by means of pressure differential devices inserted in circular-cross section conduits running full -Part 2: Orifice plates,* s.l.: International Organization for Standardization.
- Ireland, P. T., Neely, A. J., Gillespie, D. R. H. & and Robertson, A. J., 1999. Turbulent Heat Transfer Measurements Using Liquid Crystals. *Int. J. Heat Fluid Flow 20,* p. pp. 355–367.

- Jackowski, T. et al., 2021. Experimental Study of Impingement Effusion Cooled Double-Wall Combustor Liners: Aerodynamic Analysis with Stereo-PIV. *Energies*, 14(19), p. 6191.

- Jiang, P.-X.et al., 2017. Experimental investigation of combined transpiration and film cooling for sintered metal porous struts. *International Journal of Heat and Mass Transfer*, 108(A), pp. 232-243.

- Jiang, Y., Capone, L., Ireland, P. & Romero, E., 2017. "A Detailed Study of the Interaction Between Two Rows of Cooling Holes.". *Proceedings of the ASME Turbo Expo 2017: Turbomachinery Technical Conference and Exposition. Volume 5A: Heat Transfer. Charlotte, North Carolina, USA. June 26–30, 2017. V05AT12A009. ASME.*.

- Jiang, Y., Capone, L., Ireland, P. & Romero, E., 2018. A detailed Study of the Interaction Between Two Rows of Cooling Holes. *J. Turbomach.AMSE*, p. 140(4): 041008 (10 pages).

- Jiang, Y., Murray, A., Ireland, P. & di Mare, L., 2019. *Coolant Jets Interaction in Effusion Cooling System: Experimental and Numerical Study*. Phoenix, Arizona, USA, ASME, p. V05AT12A003.

- Johnson, P. L., Nguyen, C. Q., Ho, S. H. & Kapat, J. S., 2010. Sensitivity Analysis of Domain Considerations for Numerical Simulations of Film Cooling. *Proceedings of the 14th International Heat Transfer Conference August 8-13, 2010, Washington, DC, USA.*

- Jubran, B. & Brown, A., 1985. Film Cooling From Two Rows of Holes inclined in the Streamwise and Spanwise Directions. *J. Eng. Gas Turbines Power.*, pp. 84-91.

- Kalghatgi, P. & Acharya, S., 2014. Modal analysis of inclined film cooling jet flow. *J. Turbomach*, Volume 136, pp. 81007–1–11,.

- Kasagi, N., Hirata, M. & and Kumada, M., 1981. *Studies of Full-Coverage Film Cooling: Part 1—Cooling Effectiveness of Thermally Conductive Wall,*. Houston, Texas, Proceedings of the ASME 1981 International Gas Turbine Conference and Products Show. Volume 3: Heat Transfer; Electric Power.

- Kaufman, A., Poferl, D. J. & Richards, H. T., 1972. *Coolant Pressure and Airflow Distribution in a Strut-Supported Transpiration Cooled Vane for a gas turbine. ,* Lewis Research Center Cleveland Ohio: Nasa TN D-6916.

- Kays, M. C. W., 1976. *STAN5 - A Program for Numerical Computation of Two-dimensional Internal and External Boundary Layer Flows*, s.l.: s.n.

- Kays, W. & Crawford, M., 1980. *Convective Heat and Mass Transfer 2nd Edition.* s.l.:McGraw Hill.

- Kays, W. M., Crawford, M. & B., W., 2005. *Convective Heat and Mass Transfer 4th Edition.* s.l.:McGraw-Hill.

- Kays, W. M. & Moffat, R. J., 1975. Behaviour of Transpired and Turbulent Boundary Layers. In: *Studies in Convection.* s.l.:Academic Press, pp. 223-319.

- Kelly, G. & Bogard, D., 2003. An Investigation of the Heat Transfer for Full Coverage Film Cooling. *Proceedings of the ASME Turbo Expo 2003, collocated with the 2003 International Joint Power Generation Conference. Volume 5: Turbo Expo 2003, Parts A and B,* pp. 581-590.

- Kelly, J. B. & L'Ecuyer, M. R., 1966. *Transpiration Cooling - Its Theory and Application,* s.l.: NASA-CR-76367.

- Kim, M. et al., 2021. Experimental investigation of effusion and transpiration air cooling for single turbine blade. *J. Applied Thermal Engineering,* Volume 182, p. 116156.

- Kim, M., Shin, D. H., Lee, B. J. & Lee, J., 2022. Experimental and numerical investigation of micro-scale effusion and transpiration air cooling on cascaded turbine blades. *Case Studies in Thermal Engineering,* Volume 32, p. 101892.

- Kirollos, B. & Povey, T., 2015. An Energy-Based Method for Predicting the Additive Effect of Multiple Film Cooling Rows. *ASME. J. Eng. Gas Turbines Power December,* p. 137(12): 122607.

- Krewinkel, R., 2013. A review of gas turbine effusion cooling studies. *International Journal of Heat and Mass Transfer,* Volume 66, pp. 706-722.

- Krewinkel, R. et al., 2020. Design and Characterization of Additively Manufactured NGVs Operated in a Small Industrial Gas Turbine. *International Journal of Gas Turbine, Propulsion and Power Systems,* 11(4).

- Kruckels, J., Arzel, T., Kingston, T. & Schnieder, M., 2007. Turbine Blade Thermal Design Process Enhancements for Increased Firing Temperatures and Reduced Coolant Flow. *ASME Expo,* pp. GT2007-27457, pp. 445-455.

- Kusterer, K., Bohn, D., Sugimoto, T. & Tanaka, R., 2007. Double-Jet Ejection of Cooling Air for Improved Film Cooling. *J. Turbomach.,* pp. 809-815.

- Land, C. C., Joe, C. & Thole, K. A., 2010. Considerations of a Double-Wall Cooling Design to Reduce Sand Blockage.. *ASME. J. Turbomach.,* 132(2), p. 031011.

- Langener, T., Von Wolfersdorf, J., Kuhn, M. & Steelant, J., 2010. Transpiration cooling with supersonic flows and foreign gas injection. *46th AIAA/ASME/SAE/ASEE Joint Propulsion Conference and Exhibit.*

- Langener, T., Wolfersdorf, J. v., Selzer, M. & Hald, H., 2012. Experimental investigations of transpiration cooling applied to C/C material. *International Journal of Thermal Sciences,* Volume 54, pp. 70-81.

- Laschet, G., Krewinkel, R., Hul, D. & Bohn, D., 2013. Conjugate analysis and effective thermal conductivities of effusion cooled mulitlayer blade sections. *International Journarl of Heat and Mass Transfer,* 57(2), pp. 812-821.

- Lauziere, N., 1960. *Testing of Transpiration Air Cooled Turbine Blades Volume 2 - CWR Report no 700-9-II,* s.l.: Department of the Navy Bureau of Weapons.

- Le Brocq, P., Launder, B. & Priddin, C., 1973. Experiments on Transpiration Cooling First Paper: Discrete hole injection as a means of transpiration cooling; an experimental study. *https://doi.org/10.1243/PIME_PROC_1973_187_095_02,* Volume 187, pp. 149-157.

- Le Grives, E., Nicolas, J. J. & Genot, J., 1979. Internal aerodynamics and heat transfer problems associated to film cooling of gas turbines. *Proceedings of the ASME Turbo Expo, ASME Paper No. 79-GT-57.*

- Ligrani, P. et al., 2019. Double Wall Cooling of a Full Coverage Effusion Plate With Cross Flow Supply Cooling and Main Flow Pressure Gradient. *ASME. J. Eng. Gas Turbines Power,* 141(3), p. 031015.

- Ling, J., Ireland, P. & Tumer, L., 2002. Full Coverage Film Cooling for Combustor Transition Sections.. *Proceedings of the ASME Turbo Expo 2002: Power for Land, Sea, and Air. Volume 3: Turbo Expo 2002, Parts A and B. Amsterdam, The Netherlands.,* Volume 1021, p. 1011.

- Liu, R., Wang, Z., Sparks, T. L. F. & Newkirk, J., 2017. Aerospace applications of laser additive manufacturing. *Laser Additive Manufacturing,* pp. Pages 351-371.

- Liu, Y.-Q. & al., e., 2013. Experimental and numerical investigation of transpiration cooling for sintered porous flat plates. *Journal of Applied Thermal Engineering,* Volume 50, pp. 997-1002.

- Livingood, J. N. B., Ellerbrock, H. H. & Kaufman, A., 1971. *Nasa Turbine Cooling Research Status Report,* s.l.: NASA - TM-X-2384.

- Li, W., Li, X., Ren, J. & Jiang, H., 2018. Experimental investigation of wall thickness and hole shape variation effects on full-coverage film cooling performance for a gas turbine vane. *Applied Thermal Engineering,* Volume 144, pp. 349-361.

- Luque, S. et al., 2014. Full Thermal Experimental Assessment of a Dendritic Turbine Vane Cooling Scheme. *ASME. J. Turbomach.,* 136(2), p. 021011.

- Martiny, M., Schulz, A. & Wittig, S., 1995. *Full-Coverage Film Cooling Investigation: Adiabatic Wall Temperatures and Flow Visualization.* Houston; TX, ASME Paper No. 95-WA/HT-4..

- Mayle, M. E. & Camarata, F. J., 1975. Multihole Cooling Film Effectiveness. *ASME J. Heat Transfer 97(4),*, p. pp. 534–538.

- Meitner, 1978. *Analysis of Metal Temperature and Coolant Flow on a Full Coverage Film Cooled Turbine Blade,* s.l.: NASA Technical Paper 1310.

- Metzger, D. E., Takeuchi, D. I. & Kunestler, P. A., 1975. Effectiveness and heat transfer with full-coverage film cooling. *J. Eng. Power,* 95(3), pp. 180-184.

- Mhetras, S. & Han, J.-C., 2006. *Effect of Unsteady Wake on Full Coverage Film-Cooling Effectiveness for A Gas Turbine Blade.* San Francisco, California, 9th AIAA/ASME Joint Thermophysics and Heat Transfer Conference.

- Min, Z. et al., 2019. Experimental Investigation on Additively Manufactured Transpiration and Film Cooling Structures. *ASME. J. Turbomach,* 141(3), p. 031009.

- Moffat, R. J., 1967. *The Turbulent Boundary Layer on a Porous Plate: Experimental Heat Transfer with Uniform Blowing and Suction,* s.l.: Ph.D. Thesis.

- Moffat, R. J., 1988. Describing the uncertainties in experimental result. *Experimental Thermal and Fluid Science,* 1(1), pp. 3-17.

- Moffit, T. P., Stepka, F. S. & Rohlik, H. E., 1976. *Summary of Nasa Aerodynamic and Heat Transfer studies in Turbine vanes and Blades,* Lewis Research Center Clevland Ohio: NASA TM X-73518.

- Moore, J., Easterby, C. & Bogard, D., 2021. *Effects on Film Cooling Performance in the Showerhead From Geometric Parameterization of Shaped Hole Designs.* Virtual, Online, Proceedings of the ASME Turbo Expo 2021: Turbomachinery Technical Conference and Exposition. Volume 5A: Heat Transfer — Combustors; Film Cooling.

- Moskowitz, S. L. & Lombardo, S., 1971. 2750 Deg F Engine Test of a Transpiration Air-Cooled Turbine. *ASME. J. Eng. Power. ,* 93(2), pp. 238-248.

- Murray, A. & al., e., 2017. *An Integrated Conjugate Computational Approach for Evaluating the Aerothermal and Thermomechanical Performance of Double Walled Effusion Cooled Systems.* Charlotte, s.n.

- Murray, A. et al., 2018. High Resolution Experimental and Computational Methods for Modelling Multiple Row Effusion Cooling Performance. *Int. J. Turbomach. Propuls. Power,* pp. 3, 4. https://doi.org/10.3390/ijtpp3010004.

- Murray, A. V., 2017. *An Integrated Conjugate Computational Approach for Evaluating the Aerothermal and Thermomechanical Performance of Double Walled Effusion Cooled Systems.* Charlotte, s.n.

- Murray, A. V., Ireland, P. T. & Romero, E., 2020. Experimental and Computational Methods for the Evaluation of Double-Wall, Effusion Cooling Systems. *ASME. J. Turbomach.,* 142(11), p. 1110033.

- Murray, A. V., Ireland, P. T. & Romero, E., 2021. An Experimentally Validated Low-Order Model of the Thermal Response of Double-Wall Effusion Cooling Systems for High-Pressure Turbine Blades. *ASME. J. Turbomach. ,* 143(11), p. 111015.

- Naik, S., Krueckels, J., Gritsch, M. & Schnieder, M., 2014. Multirow Film Cooling Performances of a High Lift Blade and Vane. *Journal of Turbomachinery ASME,* Volume 136, p. 051003.

- Najmon, J. C., S., R. & Tovar, A., 2019. Review of additive manufacturing technologies and applications in the aerospace industry. *Additive Manufacturing for the Aerospace Industry*, pp. 7-31.

- Narzary, D., Liu, K., Rallabandi, A. P. & Han, J., 2012. Influence of Coolant Density on Turbine Blade Film-Cooling Using Pressure Sensitive Paint Technique. *ASME. J. Turbomach.*, 134(3), p. 031006.

- Nathan, M. L., D. T. E., Bogard, D. G. & Bradshaw, S. D., 2014. Adiabatic and Overall Effectiveness for the Showerhead Film Cooling of a Turbine Vane. *ASME. J. Turbomach.*, 136(3), p. 031005.

- Nathan, M. L., Dyson, T. E., Bogard, D. G. & Bradshaw, S. D., 2012. *Adiabatic and Overall Effectiveness for the Showerhead Film Cooling of a Turbine Vane.* Copenhagen Denmark, s.n.

- Natsui, G., Claretti, R. & Kapat, J., 2012. Experimental Evaluation of Large Spacing Compound Angle Full Coverage Film Cooling Arrays: Adiabatic Film-Cooling Effectiveness. *Proceedings of the ASME Summer Heat Transfer Conference, ASME Paper No. HT2012-58131*.

- Natsui, G. et al., 2012. *Experimental Evaluation of Large Spacing Compound Angle Full Coverage Film Cooling Arrays: Adiabatic Film-Cooling Effectiveness.* Rio Grande, Puerto Rico, USA, ASME.

- Natsui, G., Little, Z., Kapat, J. S. & Dees, J. E., 2017. Adiabatic Film Cooling Effectiveness Measurements Throughout Multirow Film Cooling Arrays. *ASME. J. Turbomach.*, 139(10), p. 101008.

- Natsui, G. et al., 2016. Adiabatic Film Cooling Effectiveness Measurements Throughout Multi-Row Film Cooling Arrays.. *Proceedings of the ASME Turbo Expo 2016: Turbomachinery Technical Conference and Exposition. Volume 5C: Heat Transfer Seoul, South Korea*, p. V05CT19A006.

- Natsui, G., Little, Z., Kapta, J. S. & Dees, J. E., 2017. Adiabatic Film Cooling Effectiveness Measurements Throughout Multirow Film Cooling Arrays. *ASME Journal of Turbomachinery*, Volume 139(10): 101008.

- Nealy, D. A., Anderson, R. D. & Hufford, A. A., 1969. *Design and Experimental Evaluation of a Turbine Vane Fabricated From Laminated Porous Material. (EDR-6296, General Motors Corp., NAS3-7913),*, s.l.: NASA CR-72649,.

- Ngetich, G., 2018. *A 3D Conjugate Approach for Analysing a Double Walled Effusion Cooled Turbine Blade.* Olso Norway, s.n.

- Ngetich, G., 2019. *Study of film cooling effectiveness on a double walled effusion cooled turbine blade in a high speed flow using pressure sensative paint.* Phoenix, Arizona, USA, V05BT19A008. ASME.

- Ngetich, G. C., 2019. *Study of Double-Wall Effusion Cooling Scheme for Gas Turbine Blade Applications,* University of Oxford: PhD Thesis .
- Ngetich, G. I. P. &. R. E., 2019. *Study of Film Cooling Effectiveness on a Double-Walled Effusion-Cooled Turbine Blade in a High-Speed Flow Using Pressure Sensitive Paint.* Phoenix, Arizona, USA, ASME.
- Nowlin, S. R., 2009. *The use of Intersecting Film cooling Passages for Nozzle Guide Vane Cooling, Doctoral Thesis.* Department of Engineering Science Univeristy of Oxford: Oxford UK.
- Oguntade, H. et al., 2015. *The Influence the Number of Holes on Effusion Cooling Effectiveness for an X/D of 4.7.* Montreal, Quebec, Canada., Proceedings of the ASME Turbo Expo 2015: Turbine Technical Conference and Exposition. Volume 5A: Heat Transfer.
- Papell, S. S., 1960. *Effect on Gaseous Film Cooling of Coolant Injection Through Angled Slots and Normal Holes.* s.l.:s.n.
- Pohlhausen, E. & v. 1. p. 1.-1. 1., 1921. *Math. Mech.,* Volume 1, pp. 115-121.
- Quinn, M. K., Gongora-Orozco, N., Kontis, K. & Ireland, P., 2013. Application of pressure-sensitive paint to low-speed flow around a U-bend of strong curvature. *Experimental Thermal and Fluid Science,* Volume 48, pp. 58-66.
- Raj, R., 1983. Deposition Results of a Transpiration Air-Cooled Turbine Vane Cascade in a Contaminated Gas Stream. *J. Engineering Power ASME,* Volume 105, pp. 826-833.
- Rannie, W. D., 1947. *"A simplified Theory of Porous Wall Cooling" ,* California Institute of Technology, Pasadena California: Progress Report No. 4-50 Jet Propulsion Laboratory.
- Renze, P., Schroder, W. & Meinke, M., 2009. *Large-Eddy Simulation of Interacting Film Cooling Jets.* Orlando, Florida, USA, s.n., pp. 81-90.
- Reschotko, E. & Cohen, C., July 1955. *NACA TN 3513.* Washington: s.n.
- Reyhani, M. R., Alizadeh, M., Fathi, A. & Khaledi, H., 2013. Turbine blade temperature calculation and life estimation - a sensitivity analysis. *Propulsion and Power Research,* 2(2), pp. 148-161.
- Reynolds, W., Kays, W. & Kline, S., 1958. *NASA Memo 12-2-58W,* Washington: s.n.
- Rogers, N. et al., 2017. Effects of Double Wall Cooling Configuration and Conditions on Performance of Full-Coverage Effusion Cooling. *ASME. J. Turbomach.,* 139(5), p. 051009.
- Rolls Royce Plc, 2021. *Investor Presentation.* [Online]
  Available at: https://www.rolls-royce.com/~/media/Files/R/Rolls-Royce/documents/investors/investor-presentation-may-2021.pdf
  [Accessed 3 September 2022].

- Rolls-Royce plc, 1986. *The Jet Engine.* Fifth Edition ed. Derby, England: Renault Printing Co Ltd.

- Rubesin, M. W., 1954. *An Analytical Estimation of the Effect of Transpiration Cooling on the Heat Transfer and Skin Friction Characteristics of a Compressible, Turbulent Boundary Layer,* s.l.: NACA TN-3341.

- Sabatino, D. R., Praisner, T. J., Smith, C. R. & ab, 2000. A high-accuracy calibration technique for thermochromic liquid crystal temperature measurements. *Experiments in Fluids,* Volume vol. 28, no. 6,, p. pp. 497–505.

- Sasaki, M., Takahara, K., Kumagai, T. & Hamano, M., 1979. Film Cooling Effectiveness for Injection From Multirow Holes. *J. Eng. p[ower,* 101(1), pp. 101-108.

- Saul, A. J. et al., 2019. An Experimental Investigation of Adiabatic Film Cooling Effectiveness and Heat Transfer Coefficient on a Transonic Squealer Tip. *ASME. J. Turbomach,* p. 141(9): 091005.

- Saumweber, C. & Schulz, A., 2004. Interaction of Film Cooling Rows: Effects of Hole Geometry and Row Spacing on the Cooling Performance Downstream of the Second Row of Holes. *J. Turbomach.,* pp. 237-246.

- Schmidt, D. L., Sen, B. & Bogard, D. G., 1996. Film cooling with compound angle holes: Adiabatic effectiveness. *ASME Journal of Turbomachinery,* Volume 118, pp. 807-813.

- Schwarz, S. G., Goldstein, R. & Eckert, E., 1990. The Influence of Curvature on Film Cooling Performance. *ASME Expo,* pp. 90-GT-010.

- Sellers, J. P., 1963. Gaseous film cooling with multiple injection slots. *AIAA,* 1(9), pp. 2154-2156.

- Simon, F. F., 1986. *Jet Model for Slot Film Cooling with Effect of Free-Stream and Coolant Turbulence.* s.l.:NASA.

- Sinha, A. K., Bogard, D. G. & Crawford, M. E., 1991. Gas Turbine Film Cooling: Flowfield Due to a Second Row of Holes. *J. Turbomach. ASME,* pp. 450-456.

- Skamniotis, C. & Cocks, A. C. F., 2021. Minimising stresses in double wall transpiration cooled components for high temperature applicaitons. *International Journal of Mechanical Sciences,* Volume 189, p. 105983.

- Snyder, J. A. & Thole, K. A., 2020. Effect of Additive Manufacturing Process Parameters on Turbine Cooling. *ASME Journal of Turbomachinery,* Volume 142, p. 051007.

- Snyder, J. C., Stimpson, C. K., Thole, K. A. & Mongillo, D., 2016. Build Direction Effects on Addtively Manufactured Channels. *ASME. J. Turbomach.,* 138(5), p. 051006.

- Snyder, J. C. & Thole, K. A., 2020. Performance of Public Film Cooling Geometires produced through Additive Manufacturing. *ASME J. of Turbomachinery,* Volume 142, p. 051009.

- Sohn, S., 2019. Effect of cooling hole arrangements of micro-effusion cooling on. *Journal of Mechanical Science and Technology,* Volume 33(10), pp. 5103-5112.

- Song, Y. J., Park, S. H., Kang, Y. J. & Kwak, J. S., 2021. Effects of trench configuration on the film cooling effectiveness of a fan-shaped hole. *International Journal of Heat and Mass Transfer,* Volume 178, p. 121655.

- Spalding, D. B., Auslander, D. M. & T. R. Sundarum, 1964. *"The Calculation of Heat and Mass-TransferThroughtheTurbulent Boundary Layer on a Flat Plate at High Mach Numbers, with and without Chemical Reaction Supersonic Flow, Chemical Process and Radiative transfer,* s.l.: Pergamon-MacMillan,.

- Stepka, F. S., 1981. *Thermal and flow analysis of a convection air-cooled ceramic coated porous metal concept for turbine vanes,* NASA Lewis Research Center Cleveland, OH, United States: NASA TM-81749.

- Stimpson, C. K., Snyder, J. C., Thole, K. A. & Mongillo, D., 2018. Effectiveness Measurements of Additively Manufactured Film Cooling Holes. *ASME. J. Turbomach.,* 140(1), p. 011009.

- Sturgess, G. J., 1980. Account of Film Turbulence for Predicting Film Cooling Effectiveness in Gas Turbine Combustors. *ASME. J. Eng. Power. July*, p. 102(3): 524–534..

- Sturgess, G. J., 1986. Design of Combustor Cooling Slots for High Film Effectiveness: Part I—Film General Development. *ASME. J. Eng. Gas Turbines Power. April*, p. 108(2): 354–360.

- Sweeney, P. C. & Rhodes, J. F., 2000. An Infrared Technique for Evaluating Turbine Airfoil Cooling Designs. *ASME. J. Turbomach,* 122(1), pp. 170-177.

- Takahashi, T., Watanabe, K. & Takahashi, T., 2000. Thermal Conjugate analysis of a first stage blade in a gas turbine. *ASME Turbo Conference Paper,* Volume 2000-GT-251.

- Unnikrishnan, U. & Yang, V., 2022. A review of cooling technologies for high temperature rotating components in gas turbines. *Propulsion and power research,* pp. 1-18.

- van de Noort, M. & Ireland, P., 2022. A Low Order Flow Network Model for Double-Wall Effusion Cooling Systems. *Int. J. Turbomach. Propuls. Power*, 7(1:5).

- Wambersie, A., Ireland, P. & Mayo, I., 2021. Experiments of Transpiration Cooling Inspired Panel Cooling on a Turbine Blade Yielding Film Effectiveness Levels over 95%. *Int. J. Turbomach. Propuls. Power,* pp. 6(2), 16.

- Wambersie, A., Ireland, P. & Mayo, I., 2021. Experiments of Transpiration Cooling Inspired Panel Cooling on a Turbine Blade Yielding Film Effectiveness Levels over 95%. *Int. J. Turbomach. Propuls. Power,* pp. 6(2), 16.

- Wang, L., Li, X., Ren, J. & Jiang, H., 2020. The interaction between upstream and downstream film cooling rows in. *International Journal of Thermal Sciences,* pp. Volume 149 - 106176.

- Wang, L., Li, X., Ren, J. & Jiang, H., 2020. The interaction between upstream and downstream film cooling rows in flow field and heat transfer. *International Journal of Thermal Sciences,* pp. Volume 149 - 106176.

- Wang, W., Cui, J. & Qu, S., 2022. Effects of hole arrangement and trenched hole on multirow film cooling. *AIP Advances,* Volume 12, p. 045205.

- Waye, S. K. & Bogard, D. G., 2007. High-Resolution Film Cooling Effectiveness Comparison of Axial and Compound Angle Holes on the Suction Side of a Turbine Vane.. *ASME. J. Turbomach.,* 129(2), pp. 202-211.

- Whittle, F., 1930. *Improvements relating to the propulsion of aircraft and other vehicles.* s.l. Patent No. British patent no. 347,206.

- Wilkins, P. H. et al., 2021a. Experimental Heat Transfer and Boundary Layer Measurements on a Ceramic Matrix Composite Surface. *ASME. J. Turbomach.,* 143(6), p. 061010.

- Wilkins, P. et al., 2021b. Experimental Heat Transfer and Boundary Layer Measurements on a Ceramic Matrix Composite Surface. *J. Turbomach.,* 6(061010), p. 143.

- Wolf, J. & Moskowitz, S., 1983. Development of the Transpiration Air cooled Turbine for High Temperature Dirty Gas Streams. *J. Engineering Power,* Volume 105, pp. 821-825.

- Wolf, J. & Moskowitz, S., 1983. Development of the Transpiration AirCooled Turbine for High-Temperature Dirty Gas Streams. *ASME J. Eng. Power,* Volume 105, pp. 821-825.

- Wong, T., Ireland, P. & Self, K., 2016. Film Cooling Effectiveness Downstream of Trailing Edge Slots Including Cutback Surface Protuberances. *Int. J. Turbomach. Propuls. Power,* pp. 1, 4. https://doi.org/10.3390/ijtpp1010004.

- Xu, G. et al., 2015. Experimental investigation of transpiration cooling for sintered woven wire mesh structures. *International Journal of Heat and Mass Transfer,* Volume 91, pp. 898-907.

- Yoon, C., Moore, J. & Bogard, D., 2019. *Evaluation of Film Cooling Superposition Predictions Using Shaped Holes on the Suction Side of a Blade Model.* Pheonix Arizona, Proceedings of the ASME Turbo Expo 2019: Turbomachinery Technical Conference and Exposition. Volume 5B: Heat Transfer.

- Zhang, F. et al., 2021. Experimental Investigation on Cooling Performance of Impingement–Effusion Full Coverage Film on Suction Surface of a Vane. *ASME. J. Turbomach.*, 143(12), p. 121007.

- Zhang, G., Liu, J., Sundén, B. & Xie, G., 2020. Improvements of the Adiabatic Film Cooling by Using Two-Row Holes of Different Geometries and Arrangments. *J. Energy Resour. Technol.* , p. 142(12): 122101 .

- Zhao, L. et al., 2014. An experimental investigation on transpiration cooling under supersonic condition using a nose cone model. *International Journal of Thermal Sciences,* Volume 84, pp. 207-213.

- Zhong, F. & Brown, G., 2005. Experimental and Numerical Studies of Multi-Hole Cooled Ceramic Matrix Composite Liners. *43rd AIAA Aerospace Sciences Meeting and Exhibit Reno Nevada*.